

# Magnetic Properties of Antiferromagnetic $\text{Mn}_2\text{Au}$ : Exchange Interaction and Domain Manipulation



**Dissertation**

for the degree of

"Doktor der Naturwissenschaften"

Faculty 08:

Physics, Mathematics and Computer Science

Johannes Gutenberg-University Mainz

Submitted April 25, 2018 by

Alexey Sapozhnik

born May 8, 1991

in Irkutsk (USSR)



# Abstract

Antiferromagnets, unlike their ferromagnetic counterparts, have their magnetic properties concealed in a compensated spin structure. For this reason, antiferromagnetic materials remained a scientific curiosity for many years without practical applications. The situation changed in the early 90s when antiferromagnetic thin films were used to impede the magnetization reversal of ferromagnetic layers via exchange coupling at their common interface. This so-called exchange bias effect is used in tunneling magnetoresistance devices implemented in read-heads of hard disk drives. Only recently antiferromagnets have become the focus of scientific and technological interest for their own right because of their intriguing properties and potential applications in antiferromagnetic spintronic devices. This is due to their much faster spin dynamics in the THz regime as compared to GHz frequencies in ferromagnets and their insensitivity to external magnetic fields, allowing a much higher information storage density. However, new concepts for manipulating the antiferromagnetic state have to be developed for reading and writing information bits. One of the prominent materials for this purpose is the metallic antiferromagnetic  $\text{Mn}_2\text{Au}$ .

In this thesis, we report on a detailed investigation of the antiferromagnetic properties of epitaxial  $\text{Mn}_2\text{Au}$  thin films. Most of the results were obtained by application of x-ray magnetic linear and circular dichroism (XMLD and XMCD) either in spectroscopic or in imaging mode, using instrumentation at the synchrotrons BESSY II (Helmholtz Zentrum Berlin, Germany) and Diamond (Rutherford Appleton Laboratory, UK). In addition, in-house facilities were used for magnetic hysteresis measurements and domain imaging via the magneto-optic Kerr effect.

The main results of the thesis are as follows. In the as-grown state, the  $\text{Mn}_2\text{Au}$  antiferromagnetic domains have a size of  $\sim 1\ \mu\text{m}$ . The Néel vector within the domains points along one of the  $\langle 110 \rangle$  easy axes. Exposure to very high magnetic fields causes a reorientation of the domains. The spin-flop field necessary to rotate the Néel vector is between 16 T and 30 T. From these values, the four-fold in-plane anisotropy constant is inferred to be in the range from 5 to  $17.5\ \mu\text{eV}/\text{f.u.}$ , in agreement with theoretical predictions. The upper limit for the domain wall width was determined to be about 80 nm, but the actual value may be much less. From the perpendicular susceptibility measurements, the effective exchange coupling constant was determined to be  $(22 \pm 5)\ \text{meV}$ . These experiments also revealed a much larger Mn orbital moment than expected, an effect that can be explained by a much weaker spin-orbit coupling compared to the spin-spin exchange coupling. Finally, we demonstrate that elastic strain affects the antiferromagnetic domain distribution in a fashion similar to magnetostriction in ferromagnets. The XMLD spectroscopy measurements confirmed that application of a 0.1% tensile strain along an easy-axis causes a reorientation of the Néel vector in thin  $\text{Mn}_2\text{Au}$  films. This shows that a magnetoelastic effect also exists in antiferromagnets.

# Kurzfassung

Antiferromagnete, im Unterschied zu Ferromagnete, verbergen ihre magnetischen Eigenschaften in der kompensierten Spinstruktur. Daher blieben Antiferromagnete über viele Jahre eine wissenschaftliche Kuriosität ohne praktische Anwendung. Die Situation änderte sich erst in den frühen 90-iger Jahren, als antiferromagnetische Schichten zum Unterdrücken der Magnetisierungskehr in ferromagnetischen Schichten gebraucht wurde, ein Effekt, der über die Austauschwechselwirkung an einer gemeinsamen Grenzfläche bewerkstelligt wurde. Diese sogenannte Austauschverschiebung wird überall bei Tunnelmagnetwiderständen genutzt, die z. B. in Leseköpfe von magnetischen Festplatten eingebaut sind. Erst kürzlich haben Antiferromagnete selber sehr großes wissenschaftliches und technologisches Interesse wegen ihrer faszinierenden Eigenschaften und möglichen Nutzung im Rahmen einer antiferromagnetischen Spintronik geweckt. Dies beruht einerseits auf einer viel schnelleren Spindynamik im THz Bereich im Vergleich zu GHz Frequenzen bei Ferromagneten und andererseits auf der Unempfindlichkeit gegenüber magnetischen Streufeldern, die eine viele höhere Datenspeicherdichte ermöglicht. Allerdings müssen neue Konzepte für die Veränderung des antiferromagnetischen Zustands sowie das Schreiben und Lesen von Information in Datenbits entwickelt werden. Ein vielversprechendes Material für diesen Zweck ist die metallische antiferromagnetische Legierung  $\text{Mn}_2\text{Au}$ .

In dieser Dissertation wird über eine detaillierte Untersuchung der antiferromagnetischen Eigenschaften von epitaktischen  $\text{Mn}_2\text{Au}$  dünnen Schichten berichtet. Die meisten Resultate wurden durch Anwendung des linearen und zirkularen magnetischen Röntgen-Dichroismus (XMLD und XMCD) entweder durch Spektroskopie oder Mikroskopie gewonnen. Die Experimente wurden an Instrumenten durchgeführt, die an den Synchrotron Strahlungsquellen BESSY II (Helmholtz Zentrum Berlin, Germany) und Diamond (Rutherford Appleton Laboratory, UK) zur Verfügung stehen. Darüberhinaus wurden Labor-Instrumente verwendet um mittels des magnetooptischen Kerr Effekts magnetische Hysteresen zu messen und magnetische Domänen abzubilden.

Die wichtigsten Ergebnisse der Dissertationsarbeit sind wie folgt zusammengefasst. Im ursprünglichen Zustand nach Wachstum haben die antiferromagnetischen Domänen in  $\text{Mn}_2\text{Au}$  eine Größe von  $\sim 1 \mu\text{m}$ . Der Néel Vektor in den Domänen ist entlang der leichten  $\langle 110 \rangle$ -Achsen ausgerichtet. Anwendung sehr hoher Magnetfelder erzeugt eine Umorientierung der Domänen. Das Spin-Flop Feld, welches für die Umorientierung mindestens benötigt wird, liegt zwischen 16 T und 30 T. Mit diesen Feldern kann die vierzählige Anisotropiekonstante mit Werten im Bereich 5 bis  $17.5 \mu\text{eV}/\text{f.u.}$  abgeschätzt werden, was auch mit theoretischen Voraussagen übereinstimmt. Die obere Grenze für die Domänenwandbreite wurde zu 80 nm ermittelt, der tatsächliche Wert mag weit darunter liegen. Durch Messung der senkrechten Suszeptibilität wurde die effektive Austausch - Kopplungskonstante zu  $(22 \pm 5) \text{meV}$  bestimmt. Diese Experimente offenbarten außerdem ein unerwartet hohes orbitales magnetisches Moment in Mn. Dieser Effekt kann durch die Annahme einer deutlich schwächeren Spin-Bahn Wechselwirkung im Vergleich zur Spin-Spin Wechselwirkung erklärt werden. Schließlich wurde der Einfluß elastischer Verzerrung auf die antiferromagnetische Domänenverteilung untersucht, ähnlich der Magnetostraktion in Ferromagneten. Mittels der XMLD-Spektroskopie konnte bestätigt werden, dass bei einer Verzerrungsamplitude von 0.1 % entlang der leichten Achse eine Umorientierung des Néel-Vektors in  $\text{Mn}_2\text{Au}$  stattfindet. Damit konnte nachgewiesen werden, dass ein magnetoelastischer Effekt auch in Antiferromagneten existiert.

# Contents

<b>1</b>	<b>Introduction</b>	<b>1</b>
<b>2</b>	<b>Theoretical foundations and literature review</b>	<b>5</b>
2.1	Classification of antiferromagnetic materials . . . . .	5
2.1.1	Insulators . . . . .	5
2.1.2	Semiconductors and semimetals . . . . .	7
2.1.3	Conductors . . . . .	8
2.2	Interactions determining the spin order in a magnetic material . . . . .	10
2.2.1	Hubbard model . . . . .	10
2.2.2	Direct kinetic exchange . . . . .	11
2.2.3	Superexchange . . . . .	12
2.2.4	RKKY exchange . . . . .	14
2.2.5	Itinerant magnetism and Stoner criterion . . . . .	14
2.3	Spin dependent Hamiltonian and mean field approximation . . . . .	16
2.4	Energy functional of a magnetic material . . . . .	19
2.5	Susceptibility of different magnetic substances . . . . .	21
2.6	Ferromagnetic and antiferromagnetic domains . . . . .	23
2.7	Hysteresis curves of FM and AFM/FM heterostructures . . . . .	25
2.8	Spin-flop transition in antiferromagnets . . . . .	27
<b>3</b>	<b>Experimental methods</b>	<b>29</b>
3.1	Synchrotron radiation . . . . .	29
3.2	X-ray absorption spectroscopy . . . . .	33
3.2.1	X-ray magnetic circular dichroism . . . . .	36
3.2.2	X-ray magnetic linear dichroism . . . . .	37
3.3	Experimental methods for measuring X-ray absorption spectra . . . . .	40
3.3.1	Determining the absorption coefficient from transmission measurements . . . . .	40
3.3.2	Determining the absorption coefficient from total electron yield measurements . . . . .	42
3.3.3	Determining the absorption coefficient from fluorescence measurements . . . . .	43
3.4	Experimental setup for X-ray absorption spectroscopy and X-ray resonant magnetic scattering studies . . . . .	44

3.5	Low-energy electron microscopy and photoemission electron microscopy . . . . .	45
3.5.1	Interaction of low-energy electrons with matter . . . . .	45
3.5.2	Interaction of X-rays with matter . . . . .	46
3.5.3	Instrumentation of a LEEM/PEEM microscope . . . . .	46
3.5.4	XMCD and XMLD spectromicroscopy . . . . .	50
<b>4</b>	<b>Determination of the exchange constant and the loose spin concentration in Mn<sub>2</sub>Au epitaxial thin films</b>	<b>53</b>
4.1	Introduction . . . . .	53
4.2	Experimental details . . . . .	54
4.3	Determination of the exchange constant and the loose spin concentration in Mn <sub>2</sub> Au	55
4.3.1	Estimation of the loose spin contribution to the perpendicular susceptibility at different temperatures . . . . .	56
4.3.2	Room temperature measurements . . . . .	56
4.3.3	Low temperature measurements . . . . .	59
4.4	Conclusion . . . . .	60
<b>5</b>	<b>Investigation of antiferromagnetic properties of Mn<sub>2</sub>Au via a ferromagnetic tracer layer</b>	<b>63</b>
5.1	Introduction . . . . .	63
5.2	Experimental details . . . . .	64
5.3	Exchange bias in epitaxial Mn <sub>2</sub> Au/Fe heterostructures . . . . .	66
5.3.1	Investigation of high-quality Mn <sub>2</sub> Au/Fe films . . . . .	66
5.3.2	Dependence of the exchange bias field on the Mn <sub>2</sub> Au grain size . . . . .	69
5.3.3	Spin glass theory of coupled antiferromagnet/ferromagnet heterostructures	73
5.3.4	Fitting of experimental data using theoretical models . . . . .	74
5.4	Exchange bias induced by Mn <sub>2</sub> Au deposited on an Fe layer . . . . .	75
5.5	Investigation of ferromagnetic domains in Mn <sub>2</sub> Au/ferromagnet heterostructures .	77
5.5.1	Kerr microscopy investigation of ferromagnetic domains in Mn <sub>2</sub> Au/Py . .	77
5.5.2	XMCD-PEEM investigation of ferromagnetic domains in Mn <sub>2</sub> Au/Fe . . .	78
5.6	Conclusion . . . . .	80
<b>6</b>	<b>Antiferromagnetic domains in Mn<sub>2</sub>Au and domain reorientation in a high magnetic field</b>	<b>83</b>
6.1	Introduction . . . . .	83
6.2	Experimental details . . . . .	85
6.3	Orienting the Néel vector of a Mn <sub>2</sub> Au thin film by a spin-flop transition in a high magnetic field . . . . .	87
6.4	Imaging AFM domains in an as-prepared Mn <sub>2</sub> Au . . . . .	88

6.5	Spin-flop induced changes in the AFM domain structure in Mn <sub>2</sub> Au epitaxial thin films . . . . .	89
6.6	Domain walls in Mn <sub>2</sub> Au . . . . .	93
6.7	Transport measurement of spin-flop in Mn <sub>2</sub> Au . . . . .	96
6.8	Conclusion . . . . .	98
<b>7</b>	<b>Magnetoelastic effect in Mn<sub>2</sub>Au epitaxial thin films</b>	<b>101</b>
7.1	Introduction . . . . .	101
7.2	Methods . . . . .	102
7.3	Investigation of the magnetoelastic effects by transport measurements . . . . .	104
7.3.1	Optimization of the sample geometry for achieving a homogeneous strain	104
7.3.2	Magnetoelastic effects in a Ni thin film . . . . .	105
7.3.3	Magnetoelastic effects in a Mn <sub>2</sub> Au thin film . . . . .	106
7.4	Investigation of the magnetoelastic effects in Mn <sub>2</sub> Au by XMLD measurements . .	108
7.5	Conclusion . . . . .	110
<b>8</b>	<b>Summary and Outlook</b>	<b>113</b>
<b>9</b>	<b>Appendix</b>	<b>117</b>
9.1	The list of samples . . . . .	117
9.2	Collective magnonic modes in a tetragonal easy plane antiferromagnet . . . . .	119
9.3	Density functional theory calculation of density of states and of X-ray magnetic linear dichroism in Mn <sub>2</sub> Au . . . . .	120
9.3.1	A short introduction to density functional theory . . . . .	120
9.3.2	A short introduction to the linear augmented plane wave method . . . . .	122
9.3.3	The results obtained for Mn <sub>2</sub> Au . . . . .	123
9.4	Technical drawings of the equipment for the bending experiments . . . . .	125
	<b>List of used abbreviations</b>	<b>129</b>
	<b>Bibliography</b>	<b>131</b>
	<b>Publications</b>	<b>143</b>
	<b>Curriculum Vitae</b>	<b>145</b>





# 1 Introduction

The phenomenon of magnetism is known to humans at least for two thousand years. It is not possible to name the discoverer of ferromagnetism (FM), who for the first time noticed that iron is attracted by natural mineral magnetite<sup>1</sup>. However, the theory, able to comprehensively explain this phenomenon, appeared only in the beginning of the last century after the introduction of quantum mechanics. Approximately at the same time, new magnetic states of matter were described including ferrimagnets and antiferromagnets (AFM). Antiferromagnets, in other words, materials with the alternating magnetic moments at neighboring atoms, were proposed by L. Néel [1; 2]. Interestingly, the name "antiferromagnet" was given to this class of materials later by F. Bitter [3]. First experimental evidence of an AFM order was provided in 1949 when C. G. Shull and J. S. Smart determined the magnetic structure of MnO by neutron diffraction [4]. The research on AFMs resulted in two Nobel Prizes. One of them was awarded to Louis Néel in 1970 "for fundamental work and discoveries concerning antiferromagnetism and ferrimagnetism which have led to important applications in solid state physics"<sup>2</sup> and another one to Clifford G. Shull jointly with Bertram N. Brockhouse in 1994 "for the development of neutron spectroscopy"<sup>3</sup>.

In his Nobel lecture, L. Néel declared that the materials he discovered "are extremely interesting from the theoretical viewpoint, but do not seem to have any applications" (from the Nobel lecture by L. Néel, 1970). However already at that time, experimental results existed, which subsequently would lead to an important application of AFMs. In 1957, W.H. Meiklejohn and C.P. Bean discovered exchange anisotropy in heterostructures AFM/FM [5], which manifests itself in a displacement of the FM hysteresis loop along the field axis. This phenomenon named exchange bias was later used in spin valves [6; 7] for pinning one of the FM layers [8] and resulted in giant magnetoresistance (GMR)<sup>4</sup> and tunnel magnetoresistance (TMR) read-heads implemented in modern hard disk drives (HDD). The above-mentioned effects, GMR and TMR together with spin-transfer torques (STT) [9] and spin Hall effect (SHE) [10] are at the base of modern spintronics, which stands for SPIN transport elecTRONICS. As follows from the name, the essence of this concept is in utilizing not only the charge of the electrons but also their spin. To this extent, magnetic phenomena determined by the electron spin play a very important role in spintronics.

The next step envisioned for the development of non-volatile data storage is the realization of the magnetoresistive random-access memory (MRAM), where writing and reading operations are

---

<sup>1</sup>A Greek legend tells that this happened to shepherd Magnes when he was pasturing his sheep at mount Ida

<sup>2</sup>taken from [https://www.nobelprize.org/nobel\\_prizes/physics/laureates/1970/](https://www.nobelprize.org/nobel_prizes/physics/laureates/1970/)

<sup>3</sup>taken from [https://www.nobelprize.org/nobel\\_prizes/physics/laureates/1994/](https://www.nobelprize.org/nobel_prizes/physics/laureates/1994/)

<sup>4</sup>Peter Grünberg and Albert Fert received the Nobel Prize in physics in 2007 for the discovery of GMR

performed by currents. In contrast to the current HDD technology, where AFMs are used only as a passive element for pinning the FM magnetization, MRAM can make full use of the outstanding properties of AFMs and implement them as active parts carrying bits of information. The advantages of AFMs for the new generation storage devices are hard to overestimate. AFMs do not produce stray fields due to compensated magnetic moments at an atomic scale, which makes them insensitive to external field perturbations. Furthermore, AFM memory cells are expected not to disturb the magnetic moments in the neighboring cells, which allows for increasing the information storage density. In comparison to FMs, where the characteristic resonance frequency is proportional to the applied external field  $f_{FM} \propto H$ , resonance frequencies in AFMs depend on the product of the exchange field ( $H_E$ ) and the anisotropy field ( $H_A$ ),  $f_{AFM} \propto \sqrt{H_E H_A}$ . While  $H$  cannot exceed several Tesla, the exchange interaction is equivalent to a magnetic field of  $H_E \sim 1000$  T. This enhancement means that  $f_{AFM}$  is to be expected in the THz regime in contrast to the ferromagnetic resonance frequencies in the GHz range. These exceptional properties provide a vision of reliable future data storage devices with a high areal bit density operating at extremely high frequencies.

The potential of AFMs is not limited to data storage only. Several new applications were already proposed for AFMs including THz emitters [11] and detectors [12], AFM-based spin current generators in spin-orbitronics [13], and spin-caloritronics [14]. This list is by far not complete and interested readers are referred to several recent reviews on advances in the AFM research area [15; 16; 17; 18; 19].

Scientists who intend to probe the magnetic state of AFMs experience considerable difficulties. Direct investigation of the AFM order usually requires large-scale facilities like neutron sources or synchrotrons. The anisotropic magnetoresistance measurements are limited to conductive AFMs [20; 21; 22]. The recently discovered spin Hall magnetoresistance (SMR) allows performing transport experiments of insulating AFMs with a heavy-metal layer deposited on top [23]. However, this effect provides small signals of the order of 0.01%. Another approach for studying AFMs is based on the exchange bias effect in a FM/AFM bilayer where the FM is used as a tracer for extracting information on the AFM domains [24; 25]. In spite of a high activity in this research area, AFMs still remain *terra incognita* among the magnetic materials. Consequently, obtaining information about properties of AFMs and elaborating ways for manipulating the Néel vector are of prime importance for stimulating progress in the field of AFM spintronics.

In the framework of this thesis, we report on magnetic characterization and reorientation of magnetic moments for the epitaxial  $\text{Mn}_2\text{Au}$  thin films, a novel metallic AFM material with a high potential for applications. The characterization involves measuring the exchange constant and the loose spin concentration in thin epitaxial  $\text{Mn}_2\text{Au}$  films. These values are determined by detecting the spin and orbital magnetic moments induced by an out-of-plane magnetic field (perpendicular susceptibility) extracted from the X-ray magnetic circular dichroism (XMCD) spectra. Investigation of hysteresis loops in  $\text{Mn}_2\text{Au}/\text{Fe}$  heterostructures sheds light on the

spin structure at the interface. For the first time, irreversible reorientation of AFM domains via a spin-flop transition was evidenced by measuring the domain images in  $\text{Mn}_2\text{Au}$  samples after applying strong magnetic fields. This result together with the field dependent transport data provided the range for the spin-flop field and for the anisotropy constant. In addition, the domain wall width was estimated by fitting the intensity profiles across a domain wall image according to the proposed model. Direct experimental evidence of strain manipulation of the AFM Néel vector was obtained by measuring the strain-dependent X-ray magnetic linear dichroism (XMLD) spectra in  $\text{Mn}_2\text{Au}$ .

This thesis is structured as follows:

In **Chapter 2**, we introduce the basics of the AFM physics, including a material review, which presents the most relevant AFMs for modern science and technology, magnetic interactions responsible for the characteristic antiparallel alignment of magnetic moments, and the energy functional for AFM materials. Also, such phenomena as exchange bias, susceptibility, and spin-flop fields are discussed.

In **Chapter 3**, we explain the experimental techniques employed in this work focusing on the synchrotron radiation based methods. The description starts with the general aspects of the interaction of X-rays with matter and physical base of XMCD and XMLD, which is followed by an introduction to the instrumentation used for spectroscopy and microscopy studies.

Chapters from 4 to 7 present the results obtained in the present work.

In **Chapter 4**, we report on the determination of the exchange interaction constant and of the loose spin concentration in epitaxial  $\text{Mn}_2\text{Au}$  films by field-dependent XMCD spectroscopy.

In **Chapter 5**, we demonstrate the possibility of generating exchange bias in  $\text{Mn}_2\text{Au}/\text{FM}$  heterostructures and present investigation of exchange bias dependence on the  $\text{Mn}_2\text{Au}$  grain size and film thickness. The feasibility of using an exchange coupled FM film as a tracer layer for investigating the  $\text{Mn}_2\text{Au}$  domain structure by Kerr microscopy and XMCD photoemission electron microscopy (PEEM) is proven.

In **Chapter 6**, we show the domain images in as-prepared epitaxial  $\text{Mn}_2\text{Au}$  thin films and after a spin-flop transition in a high magnetic field measured by XMLD-PEEM. An estimation of the domain wall width in  $\text{Mn}_2\text{Au}$  is also provided.

In **Chapter 7**, we discuss the magnetoelastic effect in  $\text{Mn}_2\text{Au}(001)$  epitaxial thin films. A strain of 0.1% applied along an in-plane easy direction causes a reorientation of the Néel vector and changes the domain distribution within the AFM, favoring the magnetic moment orientation perpendicular to the strain axis.

In **Chapter 8**, we summarize the results obtained in this work and provide the conclusions, which follow from the analysis of the results.



## 2 Theoretical foundations and literature review

### 2.1 Classification of antiferromagnetic materials

Antiferromagnetic materials have versatile crystallographic and magnetic structures. For example, the collinear spin order in a primitive cubic lattice can be classified according to seven types of magnetic arrangements shown in Figure 2.1. One of them, B-type, is FM and the rest corresponds to AFM orders with A-type, C-type, and G-type being the most common structures among the AFMs. An A-type AFM is characterized by the ferromagnetically oriented xy-planes stacked along the z-axis. C-type and G-type ordered materials have a compensated net moment in the xy-planes. The moments located in different xy-planes above each other point in the same direction in a C-type AFM and in the opposite directions in a G-type AFM.

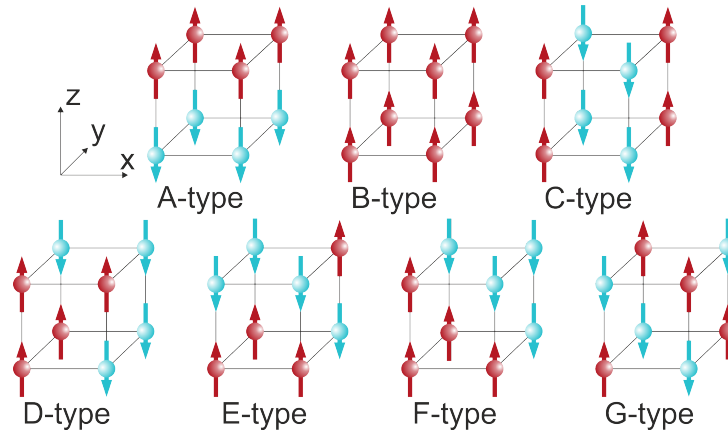


**Figure 2.1:** Seven types of magnetic moment arrangements in a primitive cubic lattice. For a better visibility, red and blue colors are used for up and down spins, respectively.

In the following, some representatives of insulating (Subsection 2.1.1), semiconducting and semimetallic (Subsection 2.1.2), as well as conductive AFMs (Subsection 2.1.3) are listed. The focus is set on AFMs having a collinear order with some exceptions.

#### 2.1.1 Insulators

The AFMs having the rock-salt structure include several divalent oxides of 3d transition elements. The magnetic moments in such compounds are ferromagnetically ordered within the  $\{111\}$  planes. The easy anisotropy directions are material dependent as shown in Table 2.1.

This class of materials marks many important milestones in the AFM research field. MnO is mentioned above in connection with the first neutron diffraction studies [4]. The pioneering experiments on exchange bias were performed on Co/CoO nanoparticles [5]. The resonant excitation of AFM magnons by terahertz pulse magnetic field was demonstrated in NiO [26].

Crystal structure	Unit cell	Chemical formula	Néel temperature	Easy axes
Rock salt		MnO	120 K	$\langle 11\bar{2} \rangle$
		FeO	198 K	$\langle 111 \rangle$
		CoO	293 K	$\approx \langle 100 \rangle$
		NiO	525 K	$\langle 11\bar{2} \rangle$
from [27]				
Rutile		MnF <sub>2</sub>	67 K	$\langle 001 \rangle$
		FeF <sub>2</sub>	78 K	$\langle 001 \rangle$
from [28]				
Perovskites		BiFeO <sub>3</sub>	653 K	$\langle 001 \rangle$
		LaFeO <sub>3</sub>	740 K	$\langle 001 \rangle$
from [29]				

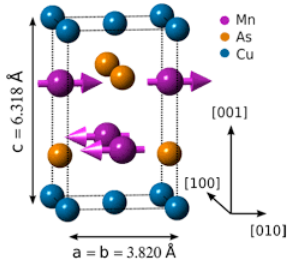
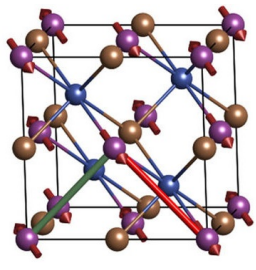
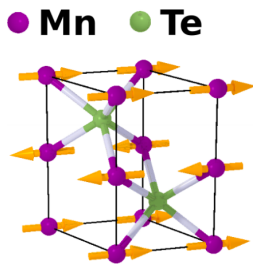
**Table 2.1:** Representatives of insulating antiferromagnetic materials

The archetypal AFM halides MnF<sub>2</sub> and FeF<sub>2</sub> were widely studied in the past, which includes the experimental identification of the spin-flop transition [30] and of antiferromagnetic resonances [31; 32]. Moreover, a positive exchange coupling was for the first time observed in a FeF<sub>2</sub>/Fe heterostructure [33]. However, as shown in Table 2.1, these materials have very low Néel temperatures, which excludes them from candidates for technical applications.

The perovskites are known for their multiferroic properties, which provide additional means for

control of their magnetism. In Ref. [34], electric field induced changes in the AFM domain structure of BiFeO<sub>3</sub> are demonstrated. Nolting et al. employed another material of this family, for investigating the alignment of FM domains by an underlying AFM in a LaFeO<sub>3</sub>/Co heterostructure [24]. Other prominent results are the detection of the optically driven AFM moment reorientation in TmFeO<sub>3</sub> [35] and the inertial spin dynamics in AFM HoFeO<sub>3</sub> [36].

### 2.1.2 Semiconductors and semimetals

Crystal structure	Unit cell	Chemical formula	Néel temperature	Easy axes
Tetragonal	 <p>from [37]</p>	CuMnAs	480 K	$\langle 100 \rangle$
Half-Heusler	 <p>from [38]</p>	CuMnSb	50 K	$\langle 11\bar{2} \rangle$
Wurzite	 <p>from [39]</p>	MnTe	323 K	$\langle 1000 \rangle$

**Table 2.2:** Representatives of semiconductive and semimetallic antiferromagnetic materials

A remarkable semimetallic AFM CuMnAs has magnetic sublattices with broken inversion symmetry. These are the necessary prerequisites for the emergence of the Néel spin-orbit torque

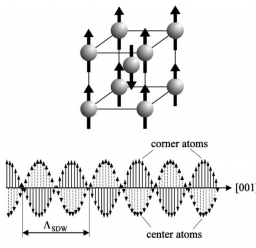
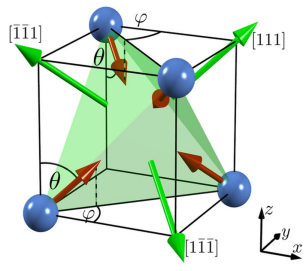
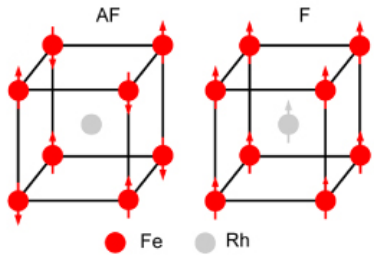
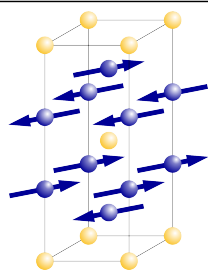
(NSOT) theoretically predicted in Ref. [40], which provides a possibility to reorient the magnetic moments by a charge current. The first experimental demonstration of this effect was published in Ref. [21] followed by other works on switching the Néel vector via NSOT by ultra-short current pulses [41] and THz radiation [42]. These findings suggest CuMnAs as a candidate for magnetic random access memory (MRAM). The main obstacle to implement this material in applications is a relatively low Néel temperature typical for semiconductors and semimetals. The semimetallic compound CuMnSb is another member of CuMnX family. It has a layered magnetic structure with the ferromagnetically oriented  $\{111\}$ -planes [43]. The Néel temperature of this material is 50 K, which excludes any possible applications. The reason for such low  $T_N$  is the frustrated exchange coupling shown by red and green lines in the corresponding figure in Table 2.2. Therefore, AFM order is stabilized only at low temperatures. The magnetic anisotropy of CuMnSb can be varied by changing the lattice symmetry, which makes this material interesting for researchers [37].

The magnetic structure of MnTe was firstly revealed by neutron diffraction in Ref. [44]. The study indicated the ferromagnetically coupled  $ab$ -planes with alternating direction of moments along the  $c$ -axis. Kriegner et al. [39] demonstrated a concept of a multiple-level memory based on the material. Different magnetic states were achieved by cooling MnTe films in different magnetic fields from above  $T_N$ . Afterward, the domain distribution in the final state was monitored by anisotropic magnetoresistance (AMR). It is worth mentioning that AMR in this AFM was found to follow the  $\sin^2 \phi$ -law, similar to FMs. An exceptional stability of the magnetic order below the Néel temperature was also proven.

### 2.1.3 Conductors

Chromium is the only known single element antiferromagnet among the 3d transition metals. In the AFM phase, bcc-Cr has a magnetic order with the oppositely oriented moments of the central atom and of the corner atoms within one unit cell. In a bulk single crystal, the magnetic moments are modulated along one of the  $\langle 001 \rangle$  directions forming an incommensurate spin-density wave with a wavelength of  $\sim 25$  lattice constants [45]. The material undergoes a first order phase transition at about 311 K as was shown by neutron diffraction studies in Ref. [46]. Alloys of Mn usually have a complex non-collinear magnetic structure (e.g. 3Q order of FeMn and IrMn with the spins pointing to the center of the tetrahedron formed by the magnetic atoms) and are characterized by very high Néel temperatures. Currently, they are widely used in the read-heads of modern hard disks, which makes them the most technologically relevant AFMs. Park et al. studied tunneling anisotropic magnetoresistance (TAMR) in NiFe/IrMn/MgO/Pt heterostructures while changing the direction of AFM moments via the exchange spring effect at the interface NiFe/IrMn [20]. They demonstrated TAMR reaching 100 % at a temperature of 4 K, however, the effect was reduced to a few percent already at 100 K. In Ref. [50], the authors investigated the value of spin Hall angle (SHA) in different Mn alloys. The result indicated that



Crystal structure	Unit cell	Chemical formula	Néel temperature	Easy axes
Body-centered cubic	 <p>from [47]</p>	Cr	311 K	$\langle 001 \rangle$
Face centered cubic	 <p>from [48]</p>	Fe <sub>50</sub> Mn <sub>50</sub> PtMn <sub>3</sub>	500 K 475 K	3Q-structure
Bulk centered cubic	 <p>from [49]</p>	FeRh	380 K	$\langle 001 \rangle$
Bulk centered tetragonal		Mn <sub>2</sub> Au	~1500 K	$\langle 110 \rangle$

**Table 2.3:** Representatives of conductive antiferromagnetic materials

the alloys containing heavy metals with a larger atomic weight are characterized by a larger SHA. The strongest spin Hall effect is observed in PtMn, which is comparable to that of Pt. These findings indicate a correlation between the SHA and the spin-orbit coupling.

An interesting property of FeRh is a FM-AFM transition that takes place at about 380 K, with the G-type spin ordering in the AFM state. This fact was utilized in Ref. [51] to illustrate the concept of the memory resistor based on an AFM. The authors cooled a FeRh thin film through the transition point in differently oriented magnetic fields and subsequently measured AMR, which was found to depend on the magnetic field direction. Recently, it was shown that FM/AFM transition in FeRh can be influenced by epitaxial strains [52]. This finding opens more opportunities for tuning the magnetic order in the material and for possible applications. Metallic AFM Mn<sub>2</sub>Au is in the focus of the present research. Its crystallographic structure was firstly described by Wells in 1970 [53]. Neutron and X-ray diffraction studies revealed that the material has the tetragonal symmetry with spatial group I4/mmm and the lattice constants  $a = 3.328 \text{ \AA}$  and  $c = 8.539 \text{ \AA}$ . Based on the temperature dependent susceptibility measurements, Abe et al. concluded that the material exhibited weak itinerant magnetism in contrast to Au-rich MnAu-alloys [54]. A recent powder neutron diffraction study by Barthem et al. [55] proved the AFM nature of this alloy. Mn<sub>2</sub>Au exhibits a layered AFM structure with the moments lying in the basal planes. The ferromagnetically arranged sheets of Mn atoms are antiferromagnetically stacked along the c-axis. The easy axes of bulk Mn<sub>2</sub>Au are  $\langle 110 \rangle$ , which was evidenced theoretically [56] as well as experimentally [57]. The bulk Mn<sub>2</sub>Au Néel temperature reaches about 1500 K [55].

## 2.2 Interactions determining the spin order in a magnetic material

For this variety of materials shown above, it is important to address the question of physical mechanisms determining the magnetic order. Subsection 2.2.1 introduces the Hubbard model, which is then employed for addressing different exchange mechanisms in Subsections 2.2.2 - 2.2.5.

### 2.2.1 Hubbard model

The Hubbard model is used for describing an ensemble of strongly correlated electrons. It is based on the following Hamiltonian written in the basis of the Wannier functions:

$$\mathcal{H} = \sum_{\langle ij \rangle \sigma} -t(c_{i\sigma}^+ c_{j\sigma} + h.c.) + \sum_i U n_{i\uparrow} n_{i\downarrow}, \quad (2.1)$$

where  $c_{i\sigma}^+$  ( $c_{i\sigma}$ ) are the creation (annihilation) operators for the electron at the cite  $i$  with the spin  $\sigma = \uparrow$  or  $\downarrow$  and  $n_{i\sigma} = c_{i\sigma}^+ c_{i\sigma}$  is the number operator. Both terms in Eq. (2.1) have a clear physical meaning. The first term corresponds to kinetic energy and describes the motion of an electron as hopping between the cites  $i$  and  $j$ . The second term accounts for the Coulomb repulsion energy, which counts if two electrons occupy the same site. Please note that the Hamiltonian

in Eq. (2.1) is written in the single band approximation and includes hopping only between the nearest neighbors (NN), which is denoted by the angle brackets ( $\langle ij \rangle$ ).

### 2.2.2 Direct kinetic exchange

The kinetic exchange is illustrated for a system of two atoms with two electrons. The fundamentally different configurations of the system correspond to parallel and antiparallel electron spins (Fig. 2.2). The energy of the former is equal to zero since Pauli principle forbids hopping and double occupancy. The latter corresponds to four possible states  $|\uparrow, \downarrow\rangle$ ,  $|\downarrow, \uparrow\rangle$ ,  $|\downarrow\uparrow, 0\rangle$ , and  $|0, \downarrow\uparrow\rangle$ .



**Figure 2.2:** The states, which can be realized in a system of two atoms, each having a single unpaired electron. The spins of the electrons are (a) antiparallel and (b) parallel. The Pauli principle prevents hopping in (b).

In this basis, the matrix form of the Hamiltonian in Eq. (2.1) is

$$\mathcal{H} = \begin{pmatrix} 0 & 0 & -t & -t \\ 0 & 0 & t & t \\ -t & t & U & 0 \\ -t & t & 0 & U \end{pmatrix} \quad (2.2)$$

This matrix has the following eigenvalues:

$$E_{1,2} = \frac{U}{2} \pm \frac{\sqrt{U^2 + 16t^2}}{2},$$

$$E_3 = U, \quad (2.3)$$

$$E_4 = 0,$$

with the eigenfunctions:

$$\psi_{1,2} = -\frac{1}{\sqrt{2 + E_{1,2}^2/(2t^2)}} \left( |\uparrow, \downarrow\rangle - |\downarrow, \uparrow\rangle - \frac{E_{1,2}}{2t} (|0, \uparrow\downarrow\rangle + |\uparrow\downarrow, 0\rangle) \right),$$

$$\psi_3 = \frac{|0, \uparrow\downarrow\rangle - |\uparrow\downarrow, 0\rangle}{\sqrt{2}}, \quad (2.4)$$

$$\psi_4 = \frac{|\downarrow, \uparrow\rangle + |\uparrow, \downarrow\rangle}{\sqrt{2}}.$$

For a strong Coulomb coupling ( $U \rightarrow \infty$ ), the system has the minimal energy  $E_2 = -\frac{4t^2}{U}$  corresponding to the state  $\psi_2 \approx \frac{|\uparrow, \downarrow\rangle - |\downarrow, \uparrow\rangle}{\sqrt{2}}$ , which indicates that the kinetic exchange favors the antiparallel (AFM) spin alignment.

### 2.2.3 Superexchange

Superexchange plays an important role in magnetic oxides where the direct exchange between the remote magnetic ions is suppressed. Here, this mechanism is demonstrated for a system consisting of two 3d atoms separated by an oxygen atom. Each of the periphery atoms has one unpaired electron at a 3d orbital and the central atom has two electrons occupying the same 2p level. Looking ahead, the coupling type, namely AFM or FM, depends on the relative positions of the ions and the symmetries of the 3d electronic orbitals.

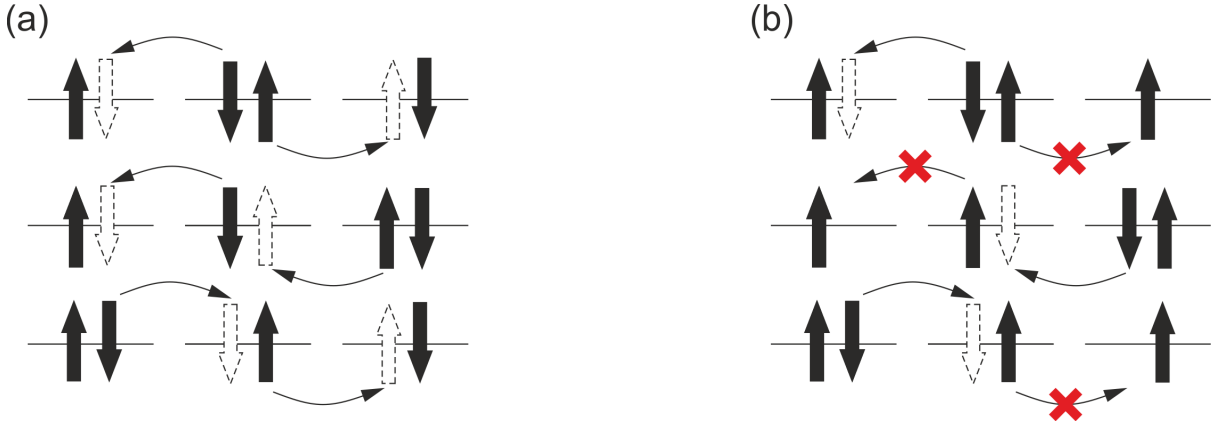


**Figure 2.3:** The states, which can be realized in a system of two (magnetic) ions having one unpaired electron each separated by another ion with two paired electrons. The periphery spins are (a) antiparallel and (b) parallel. The Pauli principle imposes restrictions on hopping in (b).

1) *AFM coupling*: the typical case of AFM coupling corresponds to all three ions located in one line with the 3d orbitals having the same symmetry. In analogy with the kinetic exchange, two cases are compared, namely the parallel and the antiparallel alignment of the 3d electron spins.

The former corresponds to a  $3 \times 3$ -Hamiltonian matrix, and the latter to a  $9 \times 9$ -Hamiltonian matrix (Fig. 2.3). A rigorous treatment of this problem can be found in Ref. [58], which results in the lowest energy for the antiparallel configuration.

The coupling strength depends on the mutual orientation of the electronic orbitals, in other words, on the degree of their overlap. The configuration shown in Fig. 2.4(a) is characterized by a stronger coupling than that in Fig. 2.4(b).

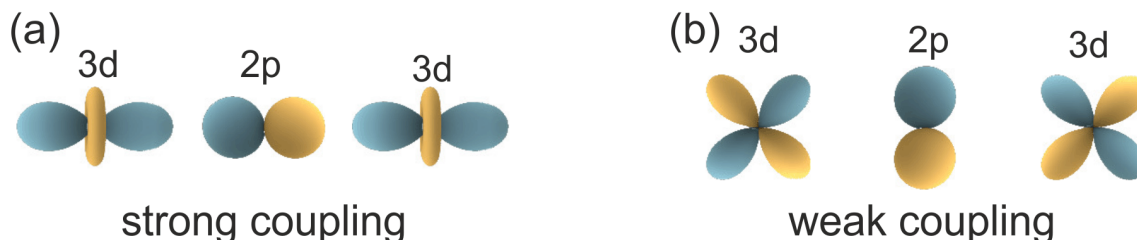


**Figure 2.4:** Examples of electronic configurations with (a) strong and (b) weak anti-ferromagnetic superexchange interaction.

2) *FM coupling*: since not only oxide AFMs are present in nature, but also a number of oxide FMs, a mechanism favoring parallel spin arrangement has to exist as well. The FM superexchange coupling is realized in a system of atoms arranged at an angle of  $90^\circ$  (Fig. 2.5(a)) or involving different kinds of 3d orbitals (Fig. 2.5(b)). Here, hopping occurs only between the overlapping 3d and 2p orbitals, such that the electrons from one 3d site cannot come to the other one. FM superexchange coupling is a particular case of the double exchange, which is a combination of the kinetic exchange between the 3d and 2p atoms and the Coulomb exchange at the oxygen site. A more detailed treatment of this problem can be found in [58] indicating the parallel (FM) ground state.

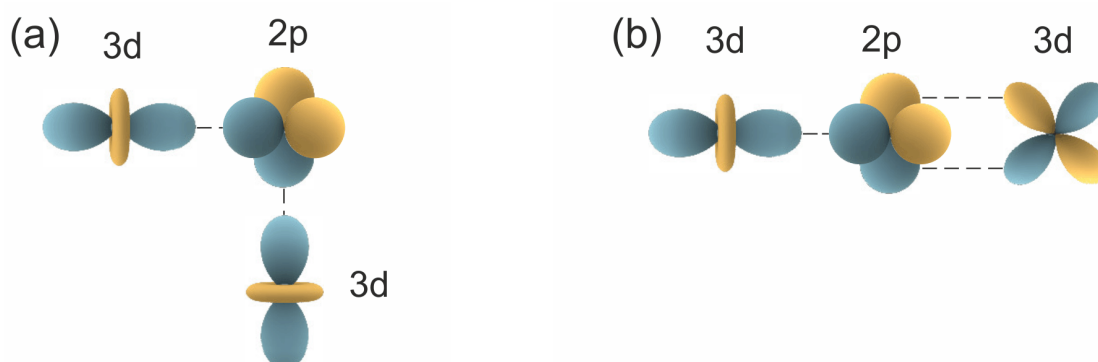


**Figure 2.5:** Examples of electronic configurations resulting in a ferromagnetic superexchange coupling. The dashed lines show the hopping paths.

### 2.2.4 RKKY exchange

In rare-earth (RE) metals, the magnetic properties are mainly determined by the electrons in the unfilled 4f-shell. They are strongly localized in the vicinity of the nucleus and their wave functions almost do not overlap with the 4f electrons of the neighboring atoms. This renders the direct exchange in RE very weak. The Ruderman-Kittel-Kassiyama-Yoshida (RKKY) mechanism is important in this case, where the coupling is mediated by conduction electrons. The free 5d6s-electrons, polarized by the 4f-electrons via direct exchange, transfer the polarization to the neighboring atoms. The character of the coupling depends on the distance between the interacting atoms as

$$\mathcal{H}_{RKKY} \propto \frac{2k_F R_{ij} \cos(2k_F R_{ij}) - \sin(2k_F R_{ij})}{(k_F R_{ij})^4} = \mathcal{F}(R_{ij}), \quad (2.5)$$

where  $k_F$  is the Fermi momentum [59]. The sign of  $\mathcal{F}(R_{ij})$  determines the coupling type, which is FM at short distances and then changes sign with a period of  $\sim \pi/(2k_F)$  (Fig. 2.6). Due to a long range nature of the RKKY exchange and interplay with other magnetic interactions and anisotropies, multiple exotic spin configurations can exist in a RE metals, including helical and conical spin structures.

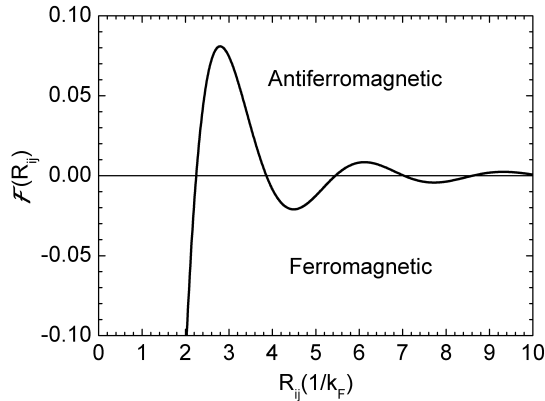


**Figure 2.6:** Dependence of the RKKY exchange parameter  $\mathcal{F}(R_{ij})$  on the distance between the atoms  $R_{ij}$  according to Eq. (2.5).

### 2.2.5 Itinerant magnetism and Stoner criterion

The mechanism discussed in this subsection is relevant for conductive FM and AFM materials, where the electronic structure is described in terms of continuous bands rather than discrete levels. The density of states (DOS) is the quantity determining the number of available states per interval of energy. In the non-relativistic approximation, the DOS has two branches corresponding to spin-up and spin-down electrons. In a non-magnetic material, these branches are degenerate and all states below the Fermi energy  $E_F$  are occupied at  $T = 0$ .

In some cases, it can be energetically favorable to promote electrons within an energy interval  $\delta E$  in the vicinity of Fermi level to the other spin sub-band resulting in an asymmetric DOS. The number of electrons in this interval is  $\delta n = \rho(E_F)\delta E$ . The kinetic energy increase is given by

$$\delta E_{kin} = \delta n \delta E = \rho(E_F)(\delta E)^2. \quad (2.6)$$

At the same time, the change of the Coulomb energy (see Eq. (2.1)) is

$$\delta E_{Coulomb} = U(n + \delta n)(n - \delta n) - Un^2 = -U(\delta n)^2, \quad (2.7)$$

where  $n$  is the equilibrium electron density.

For a stable configuration, the total energy gain has to be less than zero:

$$\rho(E_F)(\delta E)^2 - U\rho(E_F)^2(\delta E)^2 < 0 \quad (2.8)$$

$$U\rho(E_F) > 1$$

The last expression is called Stoner criterion, which decides whether spontaneous spin order is energetically favorable.

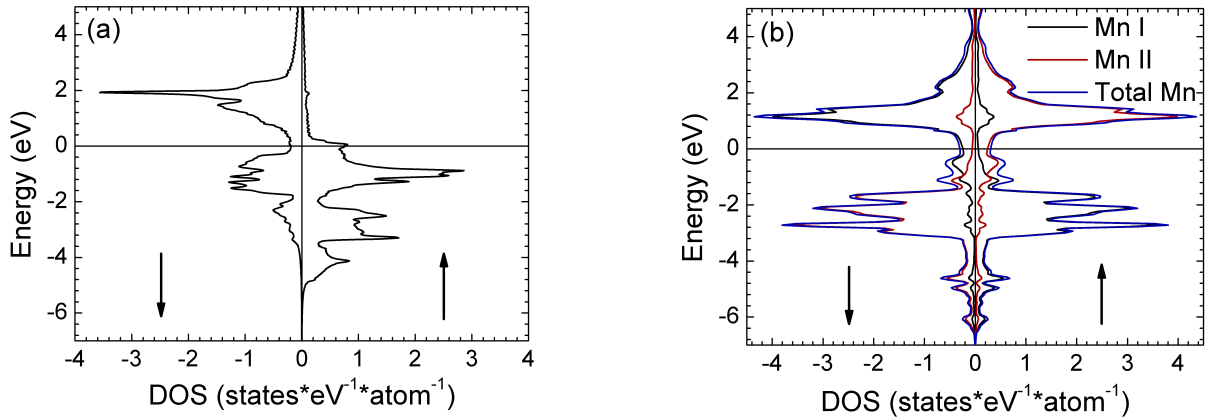


**Figure 2.7:** (a) Density of states of bcc-Fe calculated with FP-LAPW ELK code. Zero energy corresponds to the Fermi level. (b) The same for  $Mn_2Au$ .

The considerations given above are supported by density functional theory calculations performed with the FP-LAPW ELK software [60]. Indeed, the DOS of Fe exhibits shifted bands (Fig. 2.7(a)). The DOS of  $Mn_2Au$ , which is one of the very few itinerant AFM, is shown in Fig. 2.7(b). The partial DOS of the Mn-I and Mn-II atoms belonging to the different sublattices with opposite magnetic moments are asymmetric (Fig. 2.7(b)), while the branches of the total Mn DOS are identical.

## 2.3 Spin dependent Hamiltonian and mean field approximation

The previous section mainly deals with the Hubbard Hamiltonian, which implicitly depends on the electron spins. However, it seems more natural to discuss the magnetic properties of a material dealing with spin-dependent Hamiltonians and corresponding wave functions. A "toy-model" Hamiltonian generalizing the above-listed exchange mechanism was proposed by Heisenberg [61]:

$$\mathcal{H} = \sum_{ij} 2\mathcal{J}_{ij} \mathbf{S}_i \mathbf{S}_j, \quad (2.9)$$

where  $i$  and  $j$  enumerate the atoms and  $\mathbf{S}_i$  denotes the spin of the corresponding atom. In this representation,  $\mathcal{J}_{ij}$  is called exchange constant and is proportional to the overlap of the spatial wave functions of the electrons located at the atoms  $i$  and  $j$ . This quantity also considers the short-range nature of the exchange interaction, since it rapidly decreases as the distance between the corresponding atoms becomes larger. Therefore, for many problems, the summation in Eq. (2.9) is confined to the nearest coordination sphere with a single constant  $\mathcal{J}$ .

Two qualitatively different cases are distinguished depending on the sign of  $\mathcal{J}$ . The ground state of the Hamiltonian with  $\mathcal{J} < 0$  is the FM state with the parallel spins. Within the 1D Ising model, it is either  $|\psi_{FM1}\rangle = |\uparrow\uparrow\uparrow\dots\rangle$  or  $|\psi_{FM2}\rangle = |\downarrow\downarrow\downarrow\dots\rangle$ . However for  $\mathcal{J} > 0$ , a sign-changing ensemble of spins in the form  $|\uparrow\downarrow\uparrow\downarrow\dots\rangle$  is not the ground state of the Heisenberg Hamiltonian, which seems counterintuitive. The actual AFM ground state is a linear combination of vectors having the form  $|S_1 S_2 S_3\dots\rangle$ , where each  $S_i = \uparrow$  or  $\downarrow$  [19]. This fact evidences a crucial role of correlations in quantum AFMs.

A practical simplification of the Heisenberg Hamiltonian is called mean field approximation (MFA) which implies representing the interaction with the neighboring atoms in terms of the average spin  $\langle S \rangle$ :

$$\mathcal{H} = \mathcal{J} \sum_i \mathbf{S}_i \sum_{\delta} \mathbf{S}_{i+\delta} \approx \mathcal{J} Z \sum_i \mathbf{S}_i \langle \mathbf{S} \rangle = \mu_0 g \mu_B \sum_i \mathbf{S}_i \mathbf{H}^W, \quad (2.10)$$

where  $\delta$  represents summation over NN with their number amounting to  $Z$ . The last equality introduces the effective magnetic field proportional to the average spin  $\mu_0 \mathbf{H}^W = \mathcal{J} Z \langle \mathbf{S} \rangle / (g \mu_B)$ , which is known as the Weiss field.

Due to a collinear spin arrangement, a FM is characterized by the single order parameter called magnetization ( $\mathbf{M}$ ), which is the magnetic moment per unit volume. Using the fact that  $\mathbf{M} = g \mu_B n \langle \mathbf{S} \rangle$  gives<sup>1</sup>:

$$\mathbf{H}^W = \frac{\mathcal{J} Z}{\mu_0 (g \mu_B)^2 n} \mathbf{M} = \alpha^{FM} \mathbf{M}, \quad (2.11)$$

---

<sup>1</sup>This equation is correct in solids, where the orbital moment ( $L$ ) is quenched. In other cases, magnetization is proportional to the total moment  $M \propto J$ .



where  $g$  is the gyromagnetic ratio, and  $n$  is the number of magnetic atoms per unit volume.

In an AFM, the crystallographic lattice can be split into magnetic sublattices, each characterized by the sublattice magnetization vector ( $\mathbf{M}_i$ ). Since the sublattices interpenetrate each other, the interaction between different sublattices is to be considered. The analog of Eq. (2.11) for an AFM with two collinear sublattices is

$$\begin{aligned}\mathbf{H}_A^W &= \alpha_{AA}\mathbf{M}_A + \alpha_{AB}\mathbf{M}_B, \\ \mathbf{H}_B^W &= \alpha_{BA}\mathbf{M}_A + \alpha_{BB}\mathbf{M}_B,\end{aligned}\tag{2.12}$$

where  $\mathbf{M}_A$  and  $\mathbf{M}_B$  are the magnetizations of the corresponding sublattices. The coefficients  $\alpha_{AB}$  and  $\alpha_{BA}$  are negative and ensure the antiparallel coupling of different sublattices, while  $\alpha_{AA}$  and  $\alpha_{BB}$  are greater than zero and determine the parallel coupling within one sublattice. Inversion symmetry requires that  $\mathbf{M}_A = -\mathbf{M}_B$ ,  $\alpha_{AA} = \alpha_{BB}$ , and  $\alpha_{AB} = \alpha_{BA}$ . With this in mind, Eq. (2.12) becomes

$$\mathbf{H}_{A(B)}^W = \alpha^{AFM}\mathbf{M}_{B(A)},\tag{2.13}$$

where  $\alpha^{AFM} = \alpha_{AB} - \alpha_{AA}$ . Please note that  $\alpha^{AFM} < 0$ .

A different set of vectors is commonly introduced for an AFM, which for the case of two sublattices is

$$\begin{aligned}\mathbf{L} &= \frac{\mathbf{M}_A - \mathbf{M}_B}{2}, \\ \mathbf{M}_{AFM} &= \frac{\mathbf{M}_A + \mathbf{M}_B}{2},\end{aligned}\tag{2.14}$$

where  $\mathbf{L}$  is called the Néel vector and  $\mathbf{M}_{AFM}$  is the magnetization. In equilibrium,  $\mathbf{M}_A = -\mathbf{M}_B$ ,  $\mathbf{M}_{AFM} = 0$ , and the magnetic state of the AFM is described solely by the Néel vector with  $L = M_A = M_B = M$ . A finite  $\mathbf{M}_{AFM}$  appears in a non-equilibrium state, e.g. at spin pumping into the AFM [16], and usually  $M_{AFM} \ll L \approx M$ . Therefore, the Néel vector plays the role of an order parameter in AFMs.

The temperature dependence of the magnetic order parameter can be found from the Brillouin function:

$$\frac{M}{M_S} = B_J(y) = \frac{2J+1}{2J} \coth\left(\frac{2J+1}{2J}y\right) - \frac{1}{2J} \coth\left(\frac{1}{2J}y\right),\tag{2.15}$$

where  $J$  is the total orbital moment of the magnetic atom,  $M_S = gJ\mu_B n$  is the saturation magnetization. The dimensionless argument  $y = M\mu_0 H / (nk_B T)$  includes the magnetic field  $H$  and the temperature  $T$ . In order to find the spontaneous magnetization, which appears in the absence of external fields,  $H$  in Eq. (2.15) is substituted by the Weiss field resulting in [62]

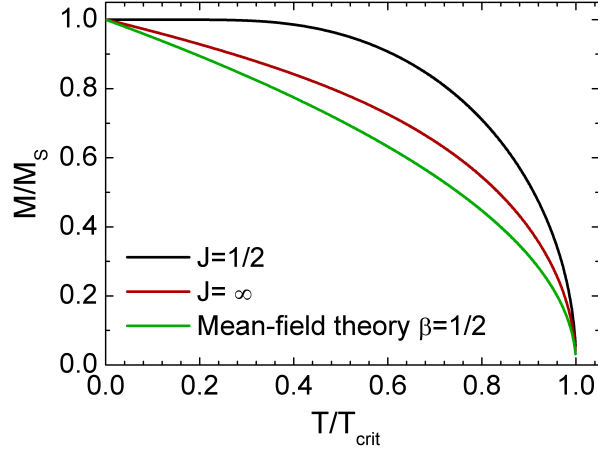


**Figure 2.8:** The temperature dependence of the order parameter calculated according to Eq. (2.16) and to Eq. (2.17).

$$\frac{M}{M_S} = B_J \left( \frac{3J}{J+1} \frac{M/M_S}{T/T_{crit}} \right), \quad (2.16)$$

where  $M_S$  is the saturation magnetization,  $J$  is the total moment, and the critical temperature is given by  $T_{crit} = (J+1)g\mu_B\alpha M_S/3k$ , where  $\alpha$  is either  $\alpha^{FM}$  or  $\alpha^{AFM}$ . Solving Eq. (2.16) provides the dependence of  $M/M_S$  on  $T/T_{crit}$  (Fig. 2.8). The order parameter decreases at higher temperatures and becomes zero at  $T_{crit}$  called Curie temperature ( $T_C$ ) for FM and Néel temperature ( $T_N$ ) for AFM. The existence of the phase transition is dictated by increasing entropy (disorder) in a magnetic system included in the free energy  $F = E - TS$ . For temperatures  $T > T_C$  ( $T_N$ ) the Weiss field cannot sustain the magnetic order and the compound becomes paramagnetic. Another model, usually used for describing the phase transitions, represents a power law relationship between the reduced order parameter and the reduced temperature:

$$\frac{M}{M_S} = \left( 1 - \frac{T}{T_{crit}} \right)^\beta, \quad (2.17)$$

where  $\beta$  is called critical exponent of the order parameter. Mean-field theory provides  $\beta = 1/2$ . In practice, the critical exponent ranges from  $1/3$  to  $1/2$  [63]. A good qualitative agreement between the two models is observed for a large  $J$  (Fig. 2.8).

The magnetization of a ferromagnet can be measured by a variety of techniques, including superconducting quantum interference device (SQUID), vibrating sample magnetometry (VSM), and magneto-optic Kerr effect (MOKE). In contrast, the experimental determination of the Néel vector in an AFM is not easy and usually requires large-scale facilities like synchrotrons and neutron sources.

## 2.4 Energy functional of a magnetic material

This paragraph is devoted to the free energy functional of FM and AFM materials. Only the terms relevant for the present study are considered in this section, therefore such contributions as surface anisotropy [64] and Dzyaloshinskii-Moriya interaction (DMI) [65; 66] are omitted. The former is relevant in films with a thickness of a few monolayers and the latter is important in twisted topological magnetic structures, e.g skyrmions [67], which are beyond the scope of this research.

The energy density functional used for analyzing the results of the present thesis contains six terms, which are explained in more detail below:

$$\epsilon = \epsilon_{exch} + \epsilon_{MAE} + \epsilon_{shape} + \epsilon_{m-e} + \epsilon_{el} + \epsilon_{Zeeman}. \quad (2.18)$$

1) The exchange energy having the form  $E_{exch} = \sum_{ij} 2\mathcal{J}_{ij} \mathbf{S}_i \mathbf{S}_j$  is discussed in detail in Section 2.3. It can be rewritten as

$$\epsilon_{exch} = \frac{1}{V} \sum_{ij} 2\tilde{\mathcal{J}}_{ij} (\beta_{ix}\beta_{jx} + \beta_{iy}\beta_{jy} + \beta_{iz}\beta_{jz}) \quad (2.19)$$

where  $\beta_{ix}$ ,  $\beta_{iy}$ , and  $\beta_{iz}$  are the directional cosines of  $\mathbf{S}_i$ .  $S$  is the absolute value of  $\mathbf{S}_i$ ,  $\tilde{\mathcal{J}}_{ij} = \mathcal{J}_{ij} S^2$ , and  $V$  is the sample volume.

2) The second term in Eq. (2.18) is called magnetocrystalline anisotropy energy (MAE). The origin of MAE lies in spin-orbit coupling (SOC) of the 3d electrons in the transition metals and 4f electrons in the rare-earth elements. Due to SOC, the electronic orbitals rotate upon reorienting the spin of an atom. It leads to change in the energy of electrostatic interaction between the electrons and the nuclei of the neighboring atoms. The  $\epsilon_{MAE}$  is usually written in the phenomenological form. In the case of axial symmetry:

$$\epsilon_{MAE} = \frac{1}{V} \sum_i K \beta_{iz}^2 = \frac{1}{V} \sum_i K \cos^2 \theta_i, \quad (2.20)$$

For tetragonal symmetry,  $\epsilon_{MAE}$  takes the form:

$$\begin{aligned} \epsilon_{MAE} &= \frac{1}{V} \sum_i (K_{2\perp} \beta_{iz}^2 + K_{4\perp} \beta_{iz}^4 + 4K_{4\parallel} (\beta_{ix}^4 + \beta_{iy}^4)) = \\ &= \frac{1}{V} \sum_i (K_{2\perp} \cos^2 \theta_i + K_{4\perp} \cos^4 \theta_i + K_{4\parallel} \sin^4 \theta_i \cos 4\phi_i), \end{aligned} \quad (2.21)$$

where  $\theta$  and  $\phi$  are the axial and polar angles of the corresponding spin, and  $K$  are the anisotropy constants. The directions of magnetic moments for which the  $\epsilon_{MAE}$  reaches its minimum and maximum are called easy and hard axes, respectively.

3) The shape anisotropy energy density, which is the third term in Eq. (2.18), arises from the stray fields produced by a magnetic body. If it has the form of a thin film, the produced, a significant demagnetizing field appears inside the film for the out-of-plane magnetization direction. In this case, the corresponding energy density term is proportional to the square of the out-of-plane magnetization component [68]:

$$\epsilon_{shape} = \frac{1}{2}\mu_0 M_z^2 = \frac{1}{2V^2}\mu_0(g\mu_B S)^2 \left(\sum_i \beta_{iz}\right)^2. \quad (2.22)$$

For AFMs, the shape anisotropy is usually small because of vanishing net magnetization. However, the shape effects can be significant in AFM nanoparticles with a large surface-to-volume ratio (see paragraph 2.6).

4) The fourth term called magnetoelastic energy connects the magnetic and the mechanical properties of a material. As in the case of magnetocrystalline anisotropy, this energy contribution is also related to spin-orbit coupling. The non-spherical electronic orbitals rotate together with the spins of electrons inducing changes in the crystal dimensions. This effect can be illustrated by a simple model of elongated electron clouds in a FM which change their orientation following the external field. As a result, the sample length increases from  $l_1$  to  $l_2$  (Fig. 2.9). Since the elongation is invariant with respect to the magnetic moment inversion, magnetostriction energy has the same form and is usually of the same order of magnitude in FM and AFM.

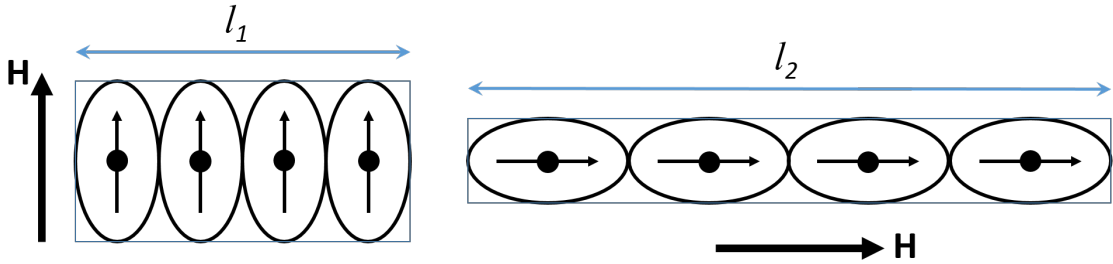


**Figure 2.9:** Schematic illustration of the origin of magnetoelastic effect in a ferromagnet. The black arrows represent the magnetic moments of each atom.

The form of the magnetoelastic energy density functional is derived from the phenomenological expression:

$$\epsilon_{m-e} = \frac{1}{V} \sum_{k,l=x,y,z}^i B_{kl} \epsilon_{kl} \beta_{ik} \beta_{il}, \quad (2.23)$$

where  $B_{kl}$  are the magnetoelastic coupling coefficients,  $\epsilon_{kl}$  is the strain tensor. There are two types of strain: normal strain with  $\epsilon_{kk} \neq 0$  and shear strain with  $\epsilon_{kl} \neq 0$  for  $k \neq l$ , characterized by different coupling coefficients  $B^{long}$  and  $B^{trans}$ , respectively [69]. For a tetragonal crystal

with the xy-basal plane Eq. (2.23) is written as

$$\begin{aligned} \epsilon_{m-e} = \frac{1}{V} \sum_i B_1^{long} (\epsilon_{xx} \beta_{ix}^2 + \epsilon_{yy} \beta_{iy}^2) + B_2^{long} \epsilon_{zz} \beta_{iz}^2 + \\ + 2 B_1^{trans} \epsilon_{xy} \beta_{ix} \beta_{iy} + 2 B_2^{trans} (\epsilon_{xz} \beta_{ix} \beta_{iz} + \epsilon_{yz} \beta_{iy} \beta_{iz}). \end{aligned} \quad (2.24)$$

5) The elastic energy density is purely mechanical and is attributed to any deformed physical body:

$$\epsilon_{el} = \sum_{k,l,m,n} C_{klmn} \epsilon_{kl} \epsilon_{mn}, \quad (2.25)$$

where  $C_{ijkl}$  are elastic stiffness constants.

In a tetragonal crystal with the xy-basal plane, Eq. (2.25) in the Voigt notation takes the form

$$\begin{aligned} \epsilon_{el} = \frac{1}{2} C_{11} (\epsilon_{xx}^2 + \epsilon_{yy}^2) + \frac{1}{2} C_{33} \epsilon_{zz}^2 + \frac{1}{2} C_{44} (\epsilon_{xz}^2 + \epsilon_{yz}^2) + \\ + \frac{1}{2} C_{66} \epsilon_{xy}^2 + C_{13} (\epsilon_{xx} \epsilon_{zz} + \epsilon_{yy} \epsilon_{zz}) + C_{12} \epsilon_{xx} \epsilon_{yy} \end{aligned} \quad (2.26)$$

6) A magnetic moment in an external field minimizes its energy when pointing along the field. The energy gain due to interaction with the external magnetic field is given by the Zeeman term:

$$\epsilon_{Zeeman} = -\mu_0 \mathbf{M} \mathbf{H} = \frac{g \mu_0 \mu_B J}{V} \sum_i \beta_i \mathbf{H}. \quad (2.27)$$

## 2.5 Susceptibility of different magnetic substances

Susceptibility ( $\chi$ ) is an important characteristic of a magnetic material, which determines its response to an external field. According to the definition,  $\chi = dM/dH|_{H \rightarrow 0}$ . At first, the paramagnetic state is considered since it is relevant for FM and AFM above the ordering temperature. The magnetization of a paramagnet is described by the Brillouin function (Eq. (2.15)). Expanding it at high temperatures results in the Curie-Weiss law:

$$\chi = \frac{g^2 \mu_B^2 N J(J+1)}{3k_B T} = \frac{C}{T}, \quad (2.28)$$

where  $C$  is called the Curie-Weiss constant.

For a FM above the Curie temperature, the Weiss field has to be added to the external field

$H \rightarrow H + \alpha^{FM} M$ . Using the fact that  $H^W$  is proportional to  $M$  (Eq. (2.10)) results in

$$\chi = \frac{C}{T - \tilde{T}_C}, \quad (2.29)$$

where  $\tilde{T}_C = C\alpha^{FM}/\mu_0$ . A FM material can be recognized in the paramagnetic state by positive extrapolated Curie-Temperature. It is not practical to assign a susceptibility to a FM below  $T_C$  due to a non-linear  $M(H)$  dependence. Instead, FMs are characterized by the temperature dependent order parameter, which is discussed in more detail above.

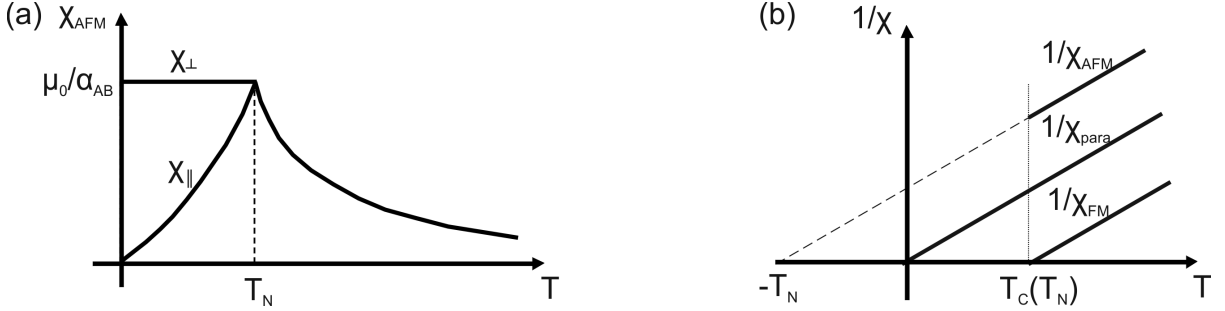


**Figure 2.10:** (a) The temperature dependent susceptibility of an AFM. (b) Inverse susceptibilities for different kinds of magnetic materials. The FM and AFM susceptibilities are shown for the region above the ordering temperature.

Considering only interaction with the NNs in an AFM at a  $T > T_N$  results in a negative addition to the external field  $H \rightarrow H - |\alpha_{AB}|M$  (see Eq. 2.12). This leads to the following expression:

$$\chi = \frac{C}{T + \tilde{T}_N}, \quad (2.30)$$

where  $\tilde{T}_N = C|\alpha_{AB}|/\mu_0$ . This dependence is equivalent to a FM with a "negative" ordering temperature.

For an AFM below  $T_N$ , the susceptibilities for the external field oriented perpendicular ( $\chi_{\perp}$ ) and parallel ( $\chi_{\parallel}$ ) to the magnetic moments are to be distinguished. In the approximation of vanishing anisotropies,  $\chi_{\perp}$  of a uniaxial AFM is determined by an interplay between the exchange interaction favoring the antiparallel spin alignment and the external magnetic field. The energy functional in this case is  $\epsilon = \alpha_{AB}\mathbf{M}_A\mathbf{M}_B - \mu_0\mathbf{H}(\mathbf{M}_A + \mathbf{M}_B)$ , which results in

$$\chi_{\perp} = \frac{\mu_0}{\alpha_{AB}}. \quad (2.31)$$

An external field oriented along the magnetic moment direction changes the sublattice magnetizations, such that they become  $M_A = M_0 + \Delta M$  and  $M_B = M_0 - \Delta M$ :

$$M_0 + \Delta M = g_J J \mu_B N B_J \left( \frac{g_J J \mu_B (\mu_0 H + \alpha_{AB} (M_0 - \Delta M))}{k_B T} \right), \quad (2.32)$$

Expanding Eq. (2.32) to the first order results in

$$\chi_{\parallel} = \frac{2\mu_0(gJ\mu_B)^2NB'_J(y_0)}{k_B T + \mu_0gJ\mu_B M_0|\alpha_{AB}|B'_J(y_0)}, \quad (2.33)$$

where  $y_0 = \mu_0gJ\mu_B M_0|\alpha_{AB}|/k_B T$ . Please note that  $\chi_{\parallel} = 0$  at  $T=0$  due to  $B'_J(y_0 \rightarrow \infty) \rightarrow 0$ . At  $T = T_N$ , both  $\chi_{\parallel}$  and  $\chi_{\perp}$  approach  $\mu_0/\alpha_{AB}$  (see Fig. 2.10(a)).

## 2.6 Ferromagnetic and antiferromagnetic domains

Formation of FM domains allows for reducing the stray fields generated at the surfaces of magnetization discontinuity and reducing the magnetoelastic energy. The magnetoelastic coupling coefficients ( $B^{long}$ ) of Ni and Fe are  $+6.2 \times 10^6$  and  $-2.9 \times 10^6$  J/m<sup>3</sup>, respectively. In comparison, the magnetocrystalline anisotropy constants of these materials are  $-0.45 \times 10^4$  and  $4.8 \times 10^4$  J/m<sup>3</sup>, respectively [70]. A strain reaching 1% is necessary for generating a magnetoelastic contribution comparable to the magnetocrystalline anisotropy. In epitaxial single crystals, the former can usually be omitted being much less than the latter.

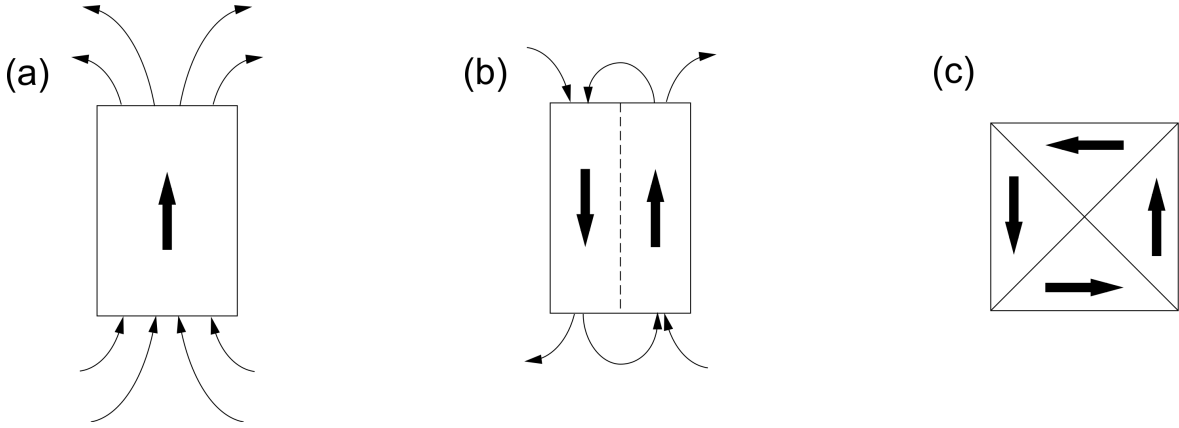


**Figure 2.11:** (a) Schematic illustration of the stray fields produced by a FM in the single domain state. (b) The same after dividing the sample into two domains. (c) A closure domain configuration, known as Landau pattern. The thick arrows are the magnetization vectors and the thin arrows represent the stray fields.

The single domain state of a rectangular FM sample shown in Fig. 2.11(a) is characterized by strong stray fields. In the multidomain state (Fig. 2.11(b)), the magnetic field lines close on the neighboring domains reducing the stray fields. The Landau pattern (Fig. 2.11(c)) is an example of a closed domain structure, where stray fields are very much suppressed in all space except the domain walls and the singularity point in the middle [71]. The magnetization is homogeneous within one domain and changes its direction in a region separating two domains, which is called a domain wall (DW). The DWs are divided into Bloch type walls and Néel type

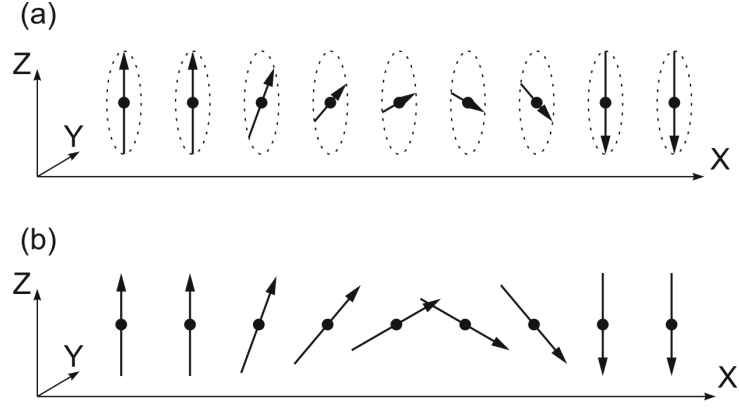


**Figure 2.12:** (a) Schematics of a  $180^\circ$ -Bloch domain wall in a uniaxial ferromagnet. (b) The same for a  $180^\circ$ -Néel domain wall.

walls, which correspond to the magnetic moments rotating parallel and perpendicular to the wall plane, respectively (Fig. 2.12). Due to a non-collinear arrangement of moments, the presence of a DW increases the exchange energy, characterized by the exchange constant ( $A$ ), and the anisotropy energy, characterized by the anisotropy constant ( $K$ ). Minimizing the total energy of a  $180^\circ$  Bloch type DW in a FM provides a DW width of  $w_{DW} = \pi\sqrt{\frac{A}{K}}$  [72]. Thus the widest DW are observed in materials with a strong exchange interaction and low anisotropy. The AFMs also form magnetic domains with a domain size varying within several orders of

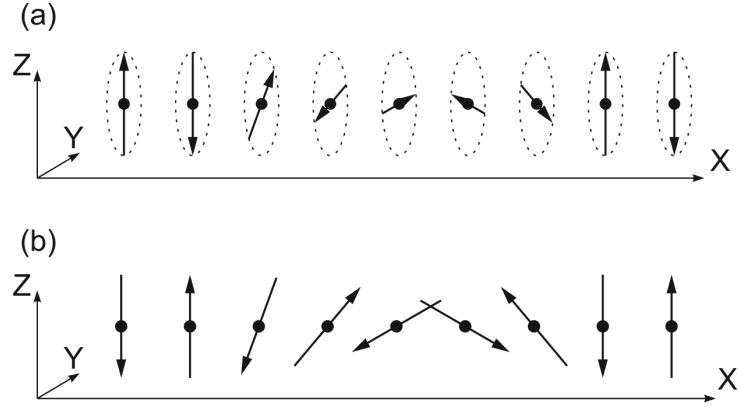


**Figure 2.13:** (a) Schematics of a  $180^\circ$ -Bloch domain wall in a uniaxial antiferromagnet. (b) The same for a  $180^\circ$ -Néel domain wall.

magnitude. It can reach 1 mm in a bulk single crystalline NiO [73], be around  $1\mu\text{m}$  in AFM thin films [74; 75; 76], and appear as small as 4 nm in NiO nanoparticles [77]. The mechanisms governing domain formation in AFMs are not as straight-forward as in FMs. Antiferromagnetic materials do not possess a bulk net magnetization and are not expected to create stray fields. Thus, magnetoelastic coupling plays a crucial role in the formation of AFM domains because



of the lack of other contributions, and minimization of the elastic energy is the main reason for the Néel vector reorientation and the creation of AFM domains.

In a continuous AFM thin film, magnetoelastic effects originate from a lattice mismatch between the AFM film and the substrate/buffer layer. Properties of strained AFM were investigated in films grown on substrates (buffer layers) with different lattice constants. In this case, the magnetoelastic effects result in an enhancement of the exchange bias for a  $\text{Fe}/\text{Fe}_x\text{Mn}_{1-x}$  heterostructure [78] and in a reorientation of the Néel vector of a strained CoO film [79].

The magnetoelastic effects in finite-size AFMs were scrutinized by Gomonay and Loktev [80; 81]. The Néel vector boundary conditions in such AFMs are defined by its geometry. The long-range magnetoelastic coupling transfers the boundary conditions into the bulk. Finally, the magnetic state corresponds to the minimal value of the Néel vector ( $\mathbf{L}(\mathbf{r})$ ) dependent energy functional ( $W[\mathbf{L}(\mathbf{r})]$ ) including the contributions of the bulk and the boundary of the nanostructure. The resulting domain distribution is determined by the size and the shape of a nanostructure as well as by the relative orientation of the AFM easy axes and the boundary. Moreover in nanostructures with a significant surface-to-bulk ratio, a small magnetic moment can exist due to the presence of uncompensated spins at the defect sites, which contributes to the stray fields [82; 83].

The domain walls in an AFM can also be attributed either to the Néel type or to the Bloch type (Fig. 2.13) depending on the plane in which the rotation of magnetic moments takes place.

## 2.7 Hysteresis curves of FM and AFM/FM heterostructures

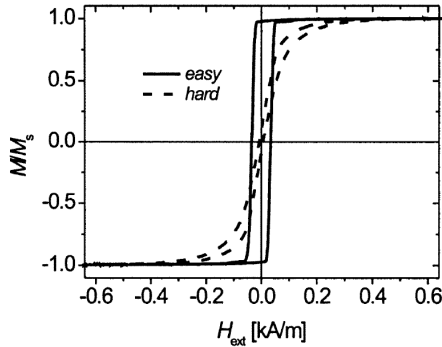


**Figure 2.14:** The hysteresis loops measured in a Sendust sheet along easy and hard magnetic axes. Adapted from [84].

Due to different types of anisotropies, not all magnetization directions in a magnetic material are equivalent, and magnetic moments tend to orient themselves along energetically favorable easy directions. It is necessary to overcome a potential barrier determined by a combination of anisotropies and domain wall pinning for changing the magnetization direction of a FM from a saturation state to the opposite one, which is called a remagnetization process. This causes the magnetization switching not to take place at  $H = 0$  but at a higher coercive field  $|H_C| > 0$ .

The shape and the width of a hysteresis curve depend on the magnetic properties of the material and the relative orientation of the external field with respect to the easy directions. Hysteresis loops are very narrow in magnetically "soft" polycrystalline materials, such as permalloy, in contrast to wide loops in materials with a high anisotropy. A square hysteresis

loop with the remanent magnetization ( $M_r$ ) close to the saturation magnetization ( $M_S$ ) is observed when the external field is swept along an easy axis. The hysteresis loop becomes more rounded if the magnetic field approaches a hard direction. The easy- and hard axis hysteresis loops are illustrated in Figure 2.14.

In a FM/AFM heterostructure, an additional anisotropy stems from the interfacial exchange coupling (Fig. 2.15). In case of a small-anisotropy AFM, the AFM spins at the interface are rotatable, which results in an additional uniaxial anisotropy and broadening of the hysteresis loop [85; 86]. If the anisotropy is large, the AFM spins are fixed causing a shift of the loop [87].

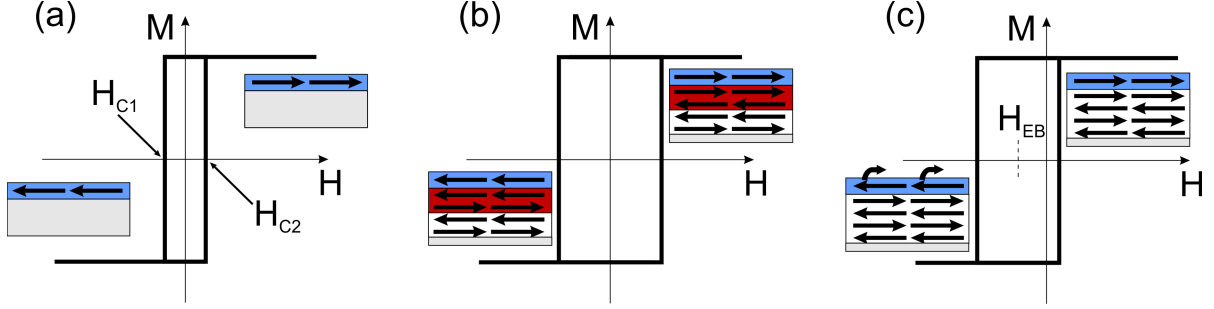


**Figure 2.15:** (a) Sketch of the hysteresis loop of a FM layer (blue) grown on a non-magnetic substrate (gray). (b) The same for a FM deposited on a magnetically soft AFM with rotatable spins in the interface region (red). (c) The same for a FM on a magnetically hard AFM (white). The exchange anisotropy results in a broadening (b) and a shift (c) of the hysteresis loop.

Quantitatively, a hysteresis loop is characterized by the width ( $H_C$ ) and the exchange bias field ( $H_{EB}$ ), which is the shift value. The following notation is usually used:

$$H_C = \frac{H_{C1} + H_{C2}}{2}, \quad (2.34)$$

$$H_{EB} = \frac{H_{C1} - H_{C2}}{2},$$

where  $H_{C1}$  is the left coercivity, and  $H_{C2}$  is the right coercivity (see Fig. 2.15)

The simplest model for estimating  $H_{EB}$  was proposed by Meiklejohn and Bean [5] for cubic FM and AFM materials with one atom in a unit cell and the lattice constant  $a$ . The interfacial exchange and the Zeeman energy density are given by

$$\epsilon_{exch}^{FM-AFM} = \frac{\mathcal{J}_{FM-AFM} \mathbf{S}_{FM} \mathbf{S}_{AFM}}{a^2 t}, \quad \epsilon_{Zeeman} = \frac{g_{FM} \mu_B \mathbf{S}_{FM} \mathbf{H}}{a^3}, \quad (2.35)$$

where  $t$  is the FM layer thickness, and  $\mathcal{J}_{FM-AFM}$  is the interfacial exchange constant. Combining these two expressions in Eq. (2.35), the exchange coupling can be represented as an effective magnetic field directed along the topmost layer of AFM spins:

$$H_{EB} = \frac{\mathcal{J}_{FM-AFM} S_{AFM} a}{g_{FM} \mu_B t}. \quad (2.36)$$

The exchange bias calculated according to Eq. (2.36) is usually much larger than the experimentally determined values [88]. Nevertheless, the model predicts the correct  $1/t$  dependence of  $H_{EB}$  on the FM thickness, indicating the interfacial nature of the effect.

## 2.8 Spin-flop transition in antiferromagnets

Spin-flop is a sudden reorientation of the Néel vector in an AFM caused by a strong magnetic field applied along an easy direction. Firstly, the spin-flop effect is illustrated for a uniaxial AFM at  $T = 0\text{K}$ . Based on Eq. (2.19) and Eq. (2.20), the energy density in the initial antiparallel state can be written as

$$\epsilon = -nZ\mathcal{J}_{eff} - K, \quad (2.37)$$

where  $n$  is the volume density of atoms,  $Z$  is the number of NN, and  $K$  is the volume anisotropy constant. Rotating the moments towards the field decreases the Zeeman contribution but increases the exchange term and the anisotropy energy. Upon increasing the external field, the magnetic moments reorient themselves if the energy of a new configuration is less than in the initial state. The energy density of the final configuration after spin flop results in

$$\epsilon_{fin} = nZ\mathcal{J} \cos 2\theta - 2M_S B \cos \theta + K \cos^2 \theta, \quad (2.38)$$

where  $M_S$  is the sublattice magnetization. Please note that the angles between the sublattice magnetizations and the magnetic field are equal due to the two-fold symmetry with respect to the field axis. Taking into account that usually  $nZ\mathcal{J} \gg K$ , the value of  $\epsilon_{fin}$  in Eq. (2.38) reaches a minimum equal to

$$\epsilon_{fin-min} = \frac{(M_S \mu_0 H)^2}{2nZ\mathcal{J}} - nZ\mathcal{J}, \quad (2.39)$$

at the angle  $\theta$ , for which one obtains

$$\cos \theta = \frac{M_S \mu_0 H}{nZ\mathcal{J}}. \quad (2.40)$$

From the condition  $\epsilon_{fin-min} < \epsilon_{init}$ , the spin-flop field results in

$$\mu_0 H_{SF} = \frac{\sqrt{nZ\mathcal{J}K}}{M_S}. \quad (2.41)$$

It is worth mentioning that there is no spin-flop in an isotropic medium since with  $K = 0$  the Néel vector can freely rotate and orient itself perpendicular to external magnetic field. Substituting

Eq. (2.41) in Eq. (2.40) yields  $\cos \theta = \sqrt{K/nZ\mathcal{J}}$  for the angle directly after reorientation. If  $K < nZ\mathcal{J}$ , the spin-flop transition occurs with a non-zero angle between sublattice magnetizations. In a high anisotropy compounds with  $K > nZ\mathcal{J}$ , the magnetic moments instantly orient themselves parallel at  $H_{SF}$  resulting in the spin-flip transition (Fig. 2.16).

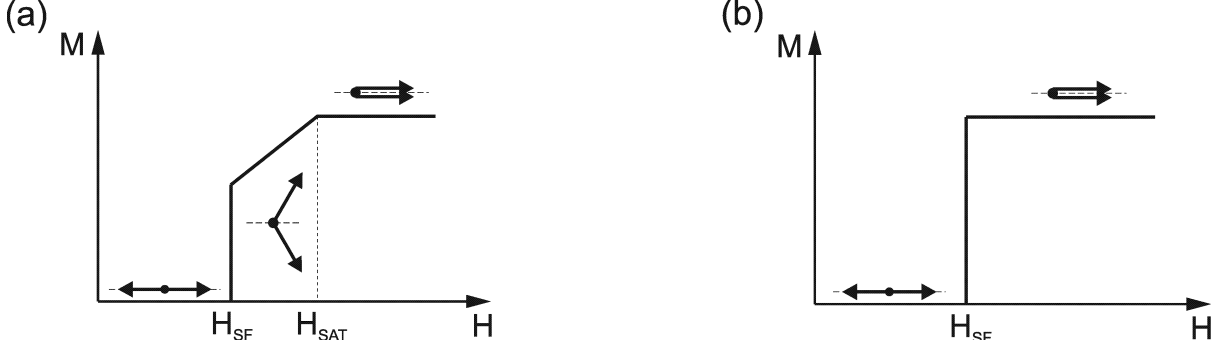


**Figure 2.16:** (a) Schematics of a spin-flop transition in a uniaxial AFM. The magnetic moments form a non-zero angle in the field interval from  $H_{SF}$  to  $H_{SAT}$ . Saturation occurs at  $H > H_{SAT}$ . (b) The same for a spin-flip transition in a uniaxial AFM. Saturation is achieved already at  $H_{SF}$ .

The spin-flop field can also be found from the dependence of the  $\mathbf{k}=0$  magnonic mode frequency of the AFM on the external field [89]. In a tetragonal easy plane AFM, there are two modes associated with the out-of-plane anisotropy and with the in-plane anisotropy (see Appendix 2). For the anisotropy functional in the form of Eq. (2.21), the corresponding spin-flop fields are

$$\begin{aligned} \mu_0 H_{spin-flop}^{oop} &= \frac{\sqrt{4n\mathcal{J}_{eff}K_{2\perp}}}{M_S}, \\ \mu_0 H_{spin-flop}^{ip} &= \frac{\sqrt{8n\mathcal{J}_{eff}K_{4\parallel}}}{M_S}. \end{aligned} \tag{2.42}$$

# 3 Experimental methods

## 3.1 Synchrotron radiation

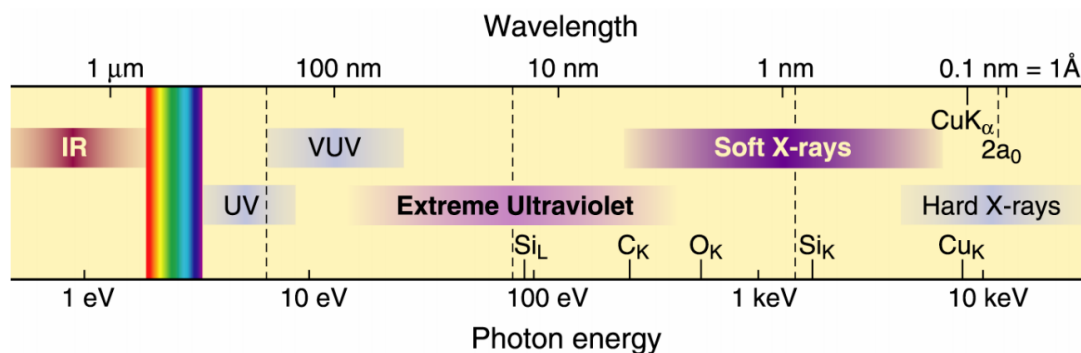


**Figure 3.1:** Electromagnetic spectrum specifying different spectral ranges from infrared (IR) to hard X-rays [90].

The X-ray region of the electromagnetic spectrum is of high importance for material science (Fig. 3.1). X-rays are crucial for investigating the structural properties of materials since the atomic distances are usually of the order of X-ray wavelengths. Moreover, availability of powerful X-ray sources allows studying the electronic properties of different materials investigating the electronic excitations from the core states with binding energies from  $\sim 100$  eV to  $\sim 10$  keV.

Nowadays, intense X-ray radiation is generated by electron bunches accelerated to relativistic velocities in linear accelerators (LINAC) and booster rings and kept at these velocities in storage rings (synchrotrons). A typical synchrotron layout is presented in Figure 3.2. The electrons produced by the electron gun are accelerated in the LINAC (1) to an energy of several MeV. Afterward, the electrons are supplied to the booster (2), which increases the energy by several orders of magnitude up to the GeV range. The booster injects the electrons to the main storage ring (3). In order to keep them on the curved track, magnets with different configurations of the field are used. Dipole (bending) magnets deflect the electron trajectories and quadrupole magnets are used for focusing. One quadrupole magnet focuses electrons along one direction and defocuses along the other. Therefore, two quadrupole magnets work in tandem to reduce both the height and the width of a bunch. The magnetic field configurations of higher orders (e.g. sextupole magnets) provide fine corrections to the trajectories. Radio frequency (RF) cavities installed at a storage ring recover the energy that electrons lose by photon emission and keep them on the track in concentrated bunches around the ring.

An accelerated relativistic electron radiates in the forward direction within a small angle, which

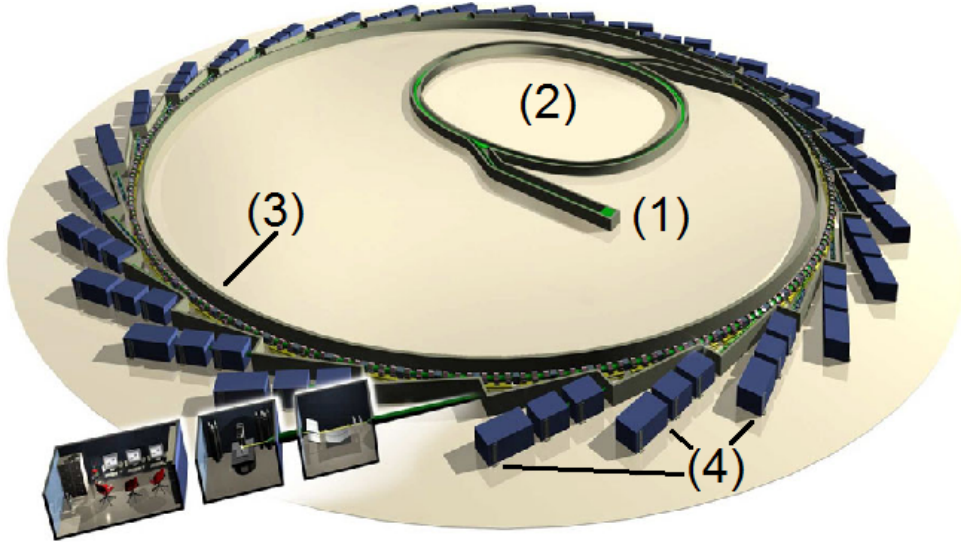


**Figure 3.2:** Layout of a modern synchrotron: (1) - LINAC; (2) - Booster ring; (3) - Storage ring; (4) - Beamlines. Adapted from [91]

is inversely proportional to the relativistic factor  $\sim 1/\gamma$  [92]. Thus in a synchrotron, X-rays are emitted tangentially to the ring and many experimental end-stations (4) can be installed around it. The modern synchrotrons (e.g. BESSY II at Helmholtz-Zentrum Berlin (HZB) and Diamond Light Source) operate in the top-up mode when the ring current losses are compensated by periodically supplying additional electrons to the bunches by the booster without interrupting the facility operation.

Three types of X-ray radiation sources are utilized at synchrotrons:

1) **Bending magnet.** Bending magnets installed at a storage ring perform two jobs simultaneously. They guide particles in the ring and simultaneously produce X-rays with a continuous spectrum. The radiation power of ultrarelativistic electrons moving along a trajectory with a curvature radius  $R$  is given by the Schwinger equation [93]:

$$P = n \frac{2 e^2 c}{3 R^2} \left( \frac{E}{m_e c^2} \right)^4 = \frac{4\pi e^2}{3 R} \left( \frac{E}{m_e c^2} \right)^4 I, \quad (3.1)$$

where  $n$  is the number of electrons,  $I$  is the ring current, and  $E$  is the kinetic energy. The photons emitted in the ring plane are 100 %-linearly polarized. The photons emitted above and below the the ring plane have partially left ( $\sigma-$ ) and right ( $\sigma+$ ) circular polarization, respectively. At higher angles, the circularity degree becomes larger, while the X-ray intensity decreases. One has to take into account both effects while choosing the beamline settings.

2) **Wiggler.** Increase in intensity can be achieved by installing a periodic array of magnets creating the regions with alternating vertical magnetic fields, which induces an additional swaying in the ring plane. The X-ray intensity becomes proportional to the product of the pole number

( $N$ ) and the ring current:

$$P \propto I \times N. \quad (3.2)$$

The swaying also leads to an increased emittance  $\gg 1/\gamma$  and results in a broadening of the X-ray beam.

3) **Undulator.** An undulator also employs spatially varying magnetic fields for enhancing the X-ray intensity. The distance between the magnetic poles in an undulator can be tuned to satisfy the constructive interference condition for the chosen wavelength, which results in a discrete emission spectrum. Due to interference, the generated intensity is proportional to the squared number of poles times the ring current:

$$P \propto I \times N^2. \quad (3.3)$$

By changing the configuration of poles, the X-ray polarization can be chosen between  $\sigma+$ ,  $\sigma-$ , and a set of linear polarization with variable electric field direction.

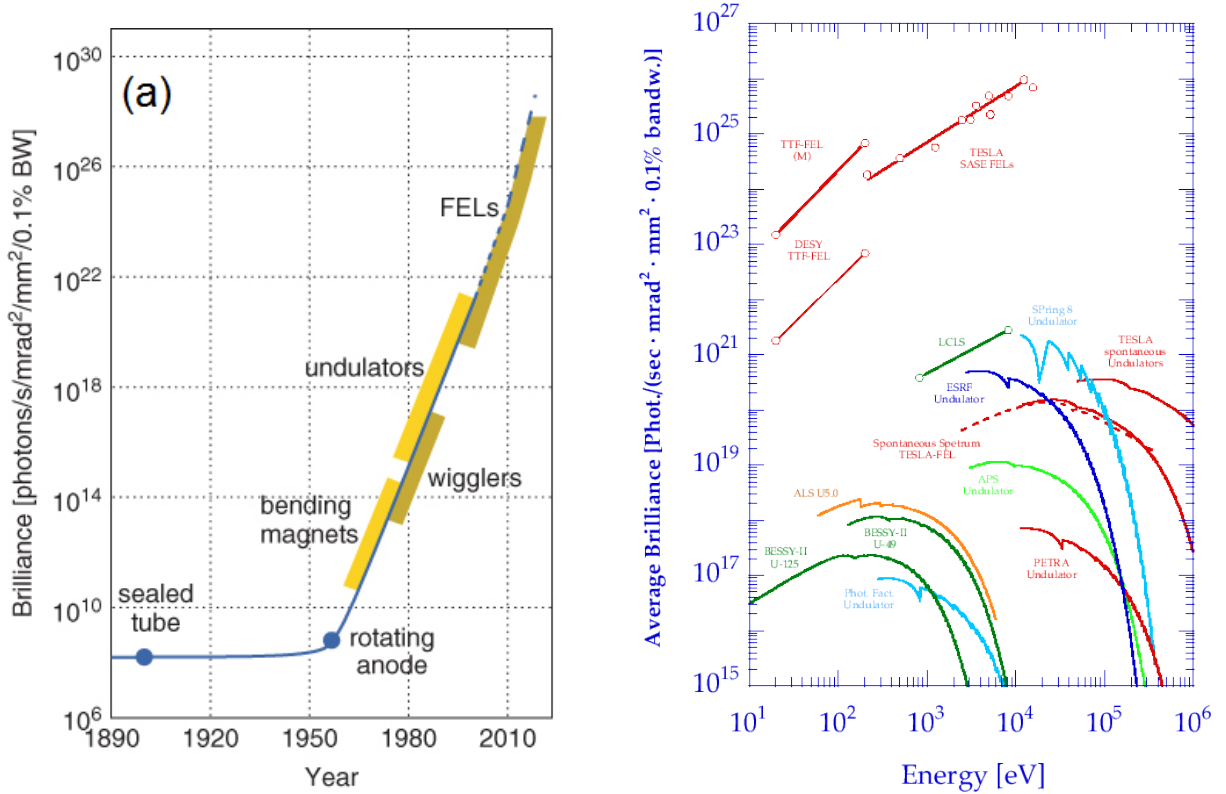


**Figure 3.3:** (a) The brilliance of different X-ray sources [94]. (b) Emission spectra of some modern synchrotrons and free electron lasers [95].

An important characteristic of an X-ray source is called brightness or brilliance. According to

the definition, brightness is the number of photons emitted per second from a  $1\text{ mm}^2$  of the emitter surface in a solid angle of  $1\text{ mrad}^2$  per  $0.1\%$  of the bandwidth. The brilliance of different X-ray sources is plotted in Fig. 3.3(a). Bending magnets, wigglers, and undulators mark three generations of the X-ray sources. The dashed line in Fig. 3.3(a) represents free electron lasers (FEL), which are attributed to the fourth generation. Since FELs are out of the scope of this research, they are not discussed in this chapter.

The energy distribution of the emitted photons depends on the electron kinetic energy. A threshold frequency exists, which marks the photon distribution cut-off [96]. One synchrotron usually does not cover the whole X-ray part of the spectrum, and different machines are used for generating soft and hard X-rays (see Fig. 3.3(b)). Among the former are BESSY II (Germany) and ALS (USA); among the latter are ESRF (France) and SPring8 (Japan).

The generated X-ray beam is guided to the experimental chamber within a beamline. As an example, the layout of the beamline UE52\_SGM at BESSY II (HZB, Berlin) is shown in Fig. 3.4. This beamline often hosts the ALICE chamber [97], which provided many results presented in this thesis.

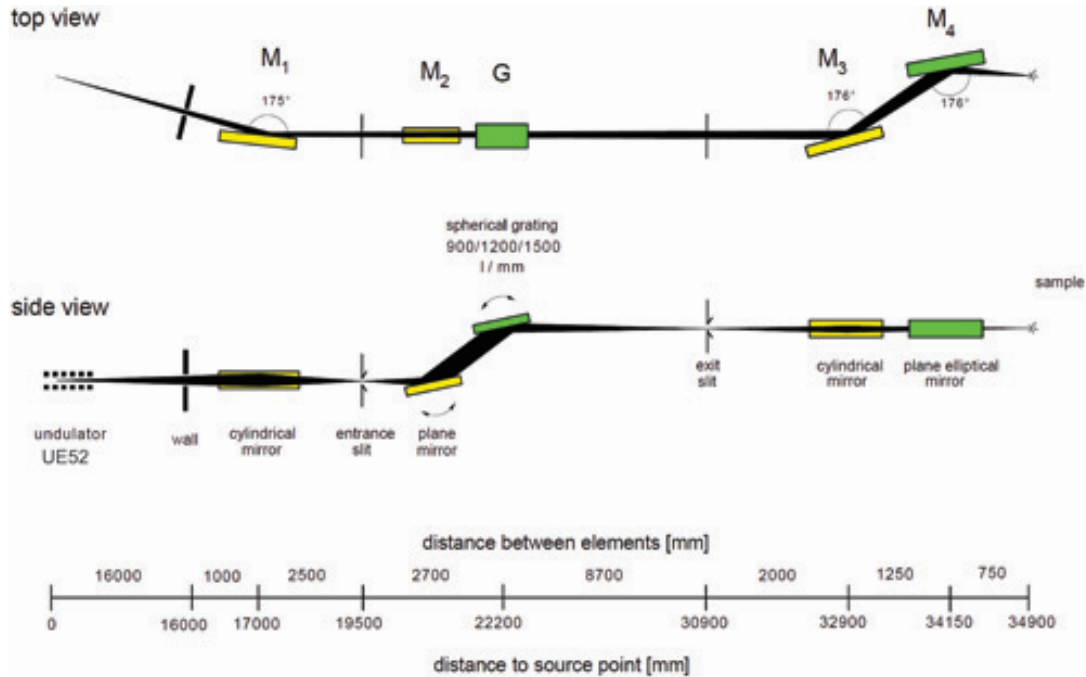


**Figure 3.4:** Layout of beamline UE52\_SGM at BESSY II [98].

An X-ray mirror is made from a substrate covered by a reflective coating with a large atomic number  $Z$ . Due to the fact that X-rays are absorbed in a medium, the refractive index of the coating is a complex number:

$$n = 1 - \delta + i\beta, \quad (3.4)$$



with  $\delta, \beta \ll 1$  and  $Re[n] < 1$ . For this form of the refractive index, the total external reflection occurs at small grazing angles. The Snell's law results in the following expression for critical angle  $\theta_{crit} = \sqrt{2\delta} \propto \sqrt{Z}/(\hbar\omega)$  if  $\beta$  is neglected [90]. The refractive index is close to unity at  $\theta < \theta_{crit}$  and decreases dramatically for  $\theta > \theta_{crit}$ . Multilayer mirrors provide an increase of  $\theta_{crit}$  and are very practical for hard X-rays. Focusing of the beam is realized by curved mirrors. A cylindrical mirror focuses the beam along one direction and an elliptical mirror focuses along both axes perpendicular to the k-vector.

Diffraction gratings are used for monochromatizing the X-rays. They operate according to the Bragg law  $\cos(\theta_i) + \cos(\theta_r) = n\lambda N$ , where  $n$  is the diffraction order and  $N$  is the line density.  $\theta_i$  and  $\theta_r$  are the angle of incidence and the angle of reflection, respectively. It is worth mentioning that a grazing incidence angle enables using gratings with typically  $\sim 1000$  lines/mm, in spite of the small X-ray wavelength. A diffraction grating usually operates in tandem with a mirror (Fig. 3.4).

The entrance slit and the exit slit confine the beam determining the spot size and the bandwidth [99].

## 3.2 X-ray absorption spectroscopy

Synchrotrons provide all necessary prerequisites for investigating the properties of different kinds of materials by X-ray absorption spectroscopy (XAS). A whole spectrum of different non-destructive techniques exists, which are based on the fact that the X-ray absorption coefficient ( $\mu_A$ ) depends on the crystal structure and on the magnetic order of the material. Polarization dependent XAS includes two methods, X-ray magnetic circular dichroism (XMCD) and X-ray magnetic linear dichroism (XMLD). Implementation of both methods requires polarized soft X-rays in order to excite initial states with strong spin-orbit splitting, such as the L-shells of 3d transition metals or the M-shells of 4f rare-earth elements.

Within a single particle approximation, absorption of a photon causes the transitions from the occupied initial state  $|i\rangle$  having the energy  $E_i$  to the unoccupied final state  $|f\rangle$  with an energy of  $E_f$ . The absorption coefficient for a material can be derived from Fermi's golden rule:

$$\mu_A \propto \sum_{if} |\langle f|\hat{O}|i\rangle|^2 \rho(E_f)\rho(E_i)\delta(E_f - E_i - \hbar\omega), \quad (3.5)$$

where  $\hat{O}$  is the transition operator and  $\rho(E)$  is the density of states. Energy conservation, represented in terms of the delta-function<sup>1</sup> implies the resonant nature of absorption, which is very much enhanced if the photon energy is tuned to the difference of two electronic levels.

A resonant peak in the absorption spectrum is characterized by the type of the shell  $|i\rangle$ , from which the electron is excited. The letter denotes the main quantum number (K for  $n=1$ , L for

<sup>1</sup>The delta-function become the Lorentzian in the case of a finite life-time of the corresponding initial and final states.

$n=2$ , M for  $n=3$ , etc.) and the additional index indicates the angular moments corresponding to  $|i\rangle$  (1 for  $s$ , 2 for  $p_{1/2}$ , 3 for  $p_{3/2}$ , etc.). One  $K$ -peak, three  $L$ -peaks, and five  $M$ -peaks can be present in an absorption spectrum. As an example, the energy dependence of the mass absorption coefficient for Sm is shown in Fig. 3.5(a).

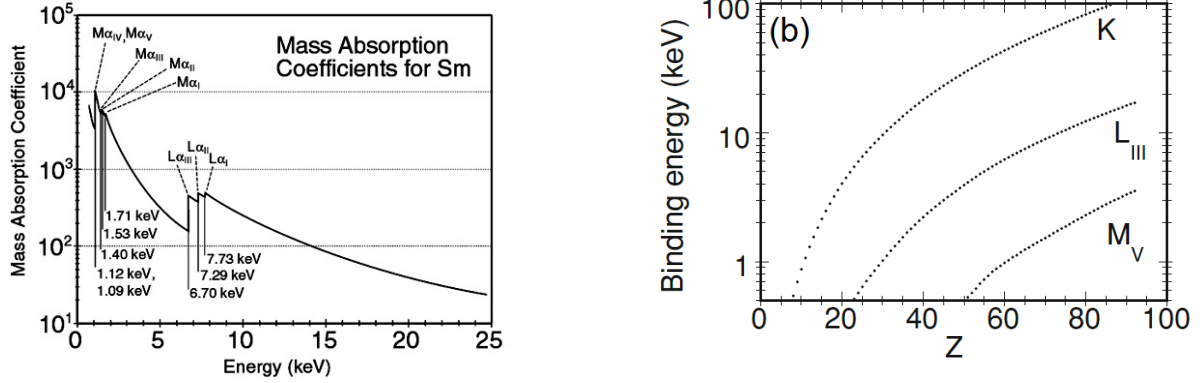


**Figure 3.5:** (a) Energy dependent mass absorption coefficient for Sm [100]. (b) Binding energies for the electrons in K, L, and M shells of atoms with different atomic numbers [101].

According to the selection rules for the strongest electric dipole transition, the total momenta of  $|f\rangle$  and  $|i\rangle$  can differ not more than by 1:  $j_f = j_i \pm 1, 0$ . In the case of LS-coupling, this rule can be expressed in terms of orbital  $l$  and spin moment  $s$  as  $l_f = l_i \pm 1$  (parity change) and  $s_f = s_i$ . The selection rules provide the means for determining the possible final states  $|f\rangle$ .

The presence of resonant peaks in XAS causes the element specificity of the technique by tuning the photon energy to the binding energy of an element of interest. The binding energies for some 3d transition metals and 4f rare-earth elements are provided in Tables 3.1 and 3.2, respectively. The localized core states are split by spin-orbit coupling (SOC) according to the total momentum projection. Typically, this splitting amounts to  $\sim 10$  eV, which determines the difference in energy between the edges with the same principal quantum number [64]. The tables also show that the binding energies for the  $L_{2,3}$ -shells of the transition metals and for the  $M_{4,5}$ -shells of the rare-earths are in the soft X-ray range (see also Fig. 3.5(b)).

	25 Mn	26 Fe	27 Co	28 Ni	29 Cu
$L_3$ -shell (eV)	638.7	706.8	778.1	852.7	932.7
$L_2$ -shell (eV)	649.9	719.9	793.2	870.0	952.3

**Table 3.1:** Electron binding energies for some 3d transition metals.

The single particle approximation provides good results for conductive materials, where the final

	62 Sm	63 Eu	64 Gd	65 Tb	66 Dy	67 Ho
M <sub>5</sub> -shell (eV)	1083.4	1127.5	1189.6	1241.1	1292.6	1351
M <sub>4</sub> -shell (eV)	1110.9	1158.6	1221.9	1276.9	1333	1392

**Table 3.2:** Electron binding energies for some 4f rare-earth elements.

states form a continuous band. However, for describing X-ray absorption in insulating materials, having discrete levels, one has to consider individual transitions of the form  $2p^63d^n \rightarrow 2p^53d^{n+1}$ . In this case, interaction with the core hole, crystal field, and SOC play an important role and have to be taken into account. This results in additional peaks at the absorption edges in comparison with the smooth absorption spectra of metallic compounds having a single peak at each edge (Fig. 3.6). In the case of rare earth elements, the exchange splitting of the initial state also contributes to the multiplet feature of the absorption edges.

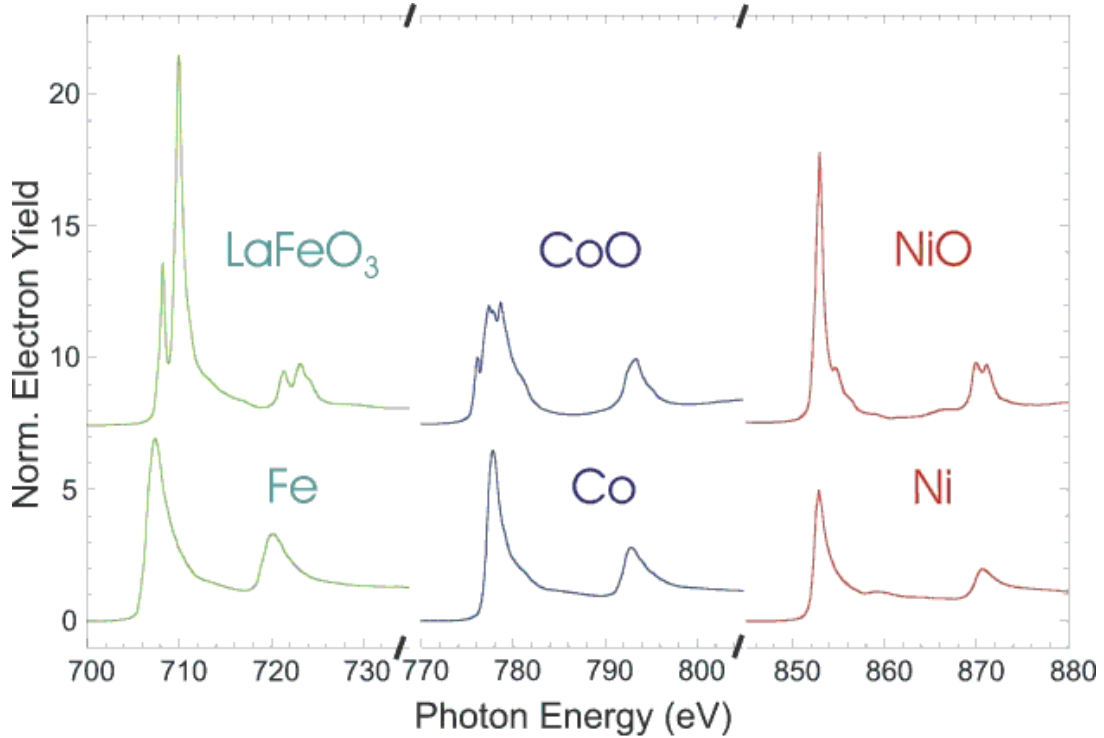


**Figure 3.6:** XAS measured in metallic Fe, Co, and Ni and in oxides containing these elements. Taken from [102] (see also [64])

The following sections provide an introduction to XMCD (Subsection 3.2.1) and XMLD (Subsection 3.2.2). The description of the experimental techniques for measuring these effects is given in Subsection 3.3.

### 3.2.1 X-ray magnetic circular dichroism

The theoretical prediction of the XMCD effect dates back to 1975 [103] and the first experimental proof was published by Schütz et al. in 1987 [104]. Here, the XMCD effect is illustrated using a ferromagnetic 3d transition metal as an example (Fig. 3.7). Due to a strong exchange coupling between neighboring atoms, an effective Weiss magnetic field appears, which shifts the 3d electron density of states (DOS) corresponding to the spin-up electrons (majority) and the spin-down electrons (minority) (see also Fig. 7(a) in Section 1.2).

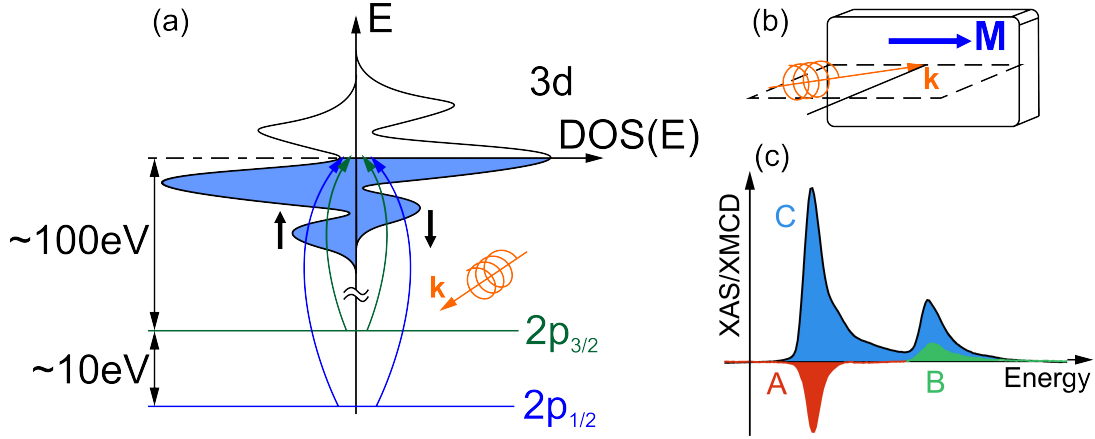


**Figure 3.7:** (a) Schematic representation of the DOS of a magnetic 3d transition metal with the indicated transitions from 2p states to 3d states. (b) Experimental geometry for measuring XMCD.  $\mathbf{M}$  is the magnetization of the sample and  $\mathbf{k}$  is the wave vector of the incoming photons. (c) XAS averaged over  $\sigma+$  and  $\sigma-$  and the corresponding XMCD spectrum measured in an Fe thin film.

According to Fermi's Golden rule (Eq. (3.5)), the probability of an electronic excitation is the product of the squared matrix element and the density of the final states. Thus, the X-ray absorption can be described as a two-step process. The first step is the excitation of an electron from a 2p to a 3d state, governed by the matrix element, and the second step is "filtering" the electrons according to the spin projection due to the different DOS at the Fermi level. It leads to a difference in absorption of  $\sigma+$  and  $\sigma-$  photons:

$$XMCD(E) = XAS_{\sigma+}(E) - XAS_{\sigma-}(E). \quad (3.6)$$

By tuning the photon energy, the technique allows obtaining element specific magnetic properties. This is especially practical in the case of a material containing several magnetic constituents. Absorbed photons excite the electrons to the localized 3d states as well as to the delocalized sp-states close to the Fermi level. In order to exclude the latter process, a background  $S(E)$  has to be subtracted from the experimental XAS:  $XAS_{\sigma\pm}(E) \rightarrow XAS_{\sigma\pm}(E) - S(E)$ , where  $S(E)$

is usually interpolated by a two-step function [105]:

$$S(E) = \frac{h}{3} \left( 1 + \frac{2}{\pi} \arctan \frac{E - E_{L3}}{\Delta E} \right) + \frac{h}{6} \left( 1 + \frac{2}{\pi} \arctan \frac{E - E_{L2}}{\Delta E} \right), \quad (3.7)$$

with  $h$  being the difference of the TEY signals at the pre-edge and the post-edge.  $\Delta E \sim 0.5$  eV is the spectrum broadening assumed to be equal at both edges. The ratio of the step heights is set to 2:1, which is proportional to the number of states at  $2p_{3/2}$  and  $2p_{1/2}$  levels.

The sum-rules allow for obtaining quantitative information about the magnetic moment per atom in a material from the XMCD data. Thole et al. [106] and Carra et al. [107] demonstrated that one can determine the orbital magnetic moment ( $\mu_L$ ) and the spin magnetic moment ( $\mu_S$ ) from integrals of the XAS and XMCD spectrum. The following notations appear useful for implementing the sum-rules, which are also illustrated in Fig. 3.7:

$$\begin{aligned} A &= \int_{L_3} XMCD(E) dE, \\ B &= \int_{L_2} XMCD(E) dE, \\ C &= \int \frac{XAS_{\sigma+}(E) + XAS_{\sigma-}(E)}{2} dE \propto N_d, \end{aligned} \quad (3.8)$$

where  $N_d$  is the number of d-holes [108]. The proper derivations of sum-rules can be found in the references [106; 107]. The result for the 3d transition materials, relevant for the present study, is

$$\begin{aligned} \mu_L &= -\frac{2(A+B)}{3C} N_d \mu_B, \\ \mu_S &= -\frac{A-2B}{C} N_d \mu_B, \end{aligned} \quad (3.9)$$

where the expectation value of the quadrupole operator  $\langle T_z \rangle$  is omitted. The values of the moments obtained with Eq. (3.9) have an error of  $\sim 10\%$  partly caused by jj-mixing of the  $2p_{3/2}$  and  $2p_{1/2}$  levels for the lighter 3d transition elements [109]. Therefore, an additional correction factor has to be added for compensating this error [110]. The second uncertainty arises from the assumption for the number of d-holes.

### 3.2.2 X-ray magnetic linear dichroism

#### Two models of X-ray magnetic linear dichroism

X-ray magnetic linear dichroism (XMLD) implies a difference in absorption of linearly polarized X-rays with different orientation of the electric field vector. A rigorous multiplet model of XMLD in a 3d material considers excitations from initial  $2p^6 3d^n (J_Z)$  states to excited  $2p^5 3d^{n+1} (J'_Z)$

states with  $J'_Z = J_Z \pm 0, 1$ , according to the selection rules. The degeneracy of the states with different  $J'_Z$  in the final state is lifted in a magnetic material due to Zeeman splitting caused by the Weiss field. It was shown by Thole et al. [111] that the matrix elements corresponding to absorption of linearly polarized photons with a certain final total momentum are proportional to the magnetization squared  $\langle M^2 \rangle$ . For experimental observation of the effect, the resolution has to be sufficient for separating transitions to the final states with different  $J'_Z$ .

Due to the quadratic dependence on the magnetization, not only FM having a net magnetic moment can be probed by XMLD, but also AFM with sign changing (staggered) magnetic moments. No sum-rules, analogous to XMCD, exist for the XMLD spectra to the best of my knowledge. However, XMLD still can provide valuable information about e.g. AFM order parameter temperature dependence [112] or the Néel vector orientation [113; 114].

A single electron model for an itinerant AFM containing a 3d-transition element is considered in Fig. 3.8. Please note, that the total DOS of an AFM is symmetric (see Fig. 7(b) in Section 1.2), which does not give rise to a circular dichroism.

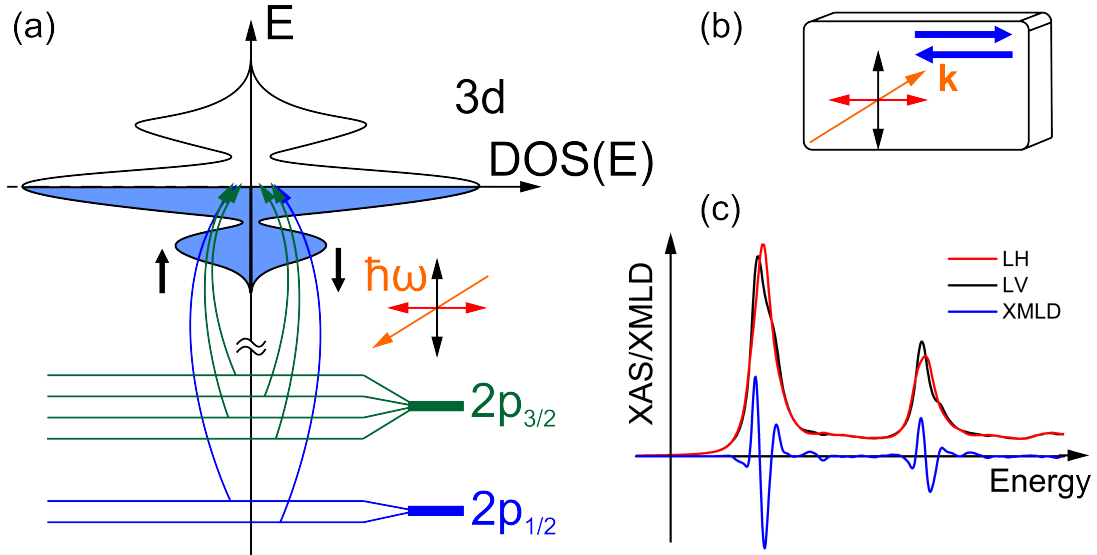


**Figure 3.8:** (a) Schematic DOS of a 3d transition antiferromagnetic material. (b) Experimental geometry for measuring XMCD. Blue arrows represent sublattice magnetizations. Red and black arrows indicate the electric field of horizontally and vertically polarized X-rays, respectively (c) XAS and XMLD calculated for Mn<sub>2</sub>Au using the FP-LAPW ELK software.

Exchange interaction splits the 2p<sub>3/2</sub> and 2p<sub>1/2</sub> core states into four and two sub-levels with different total momentum projections, respectively (Fig. 3.8 (a)). The transition matrix elements from the 2p sublevels to the 3d states are different for linear horizontal (LH) and vertical (LV) polarizations, which leads to the dichroism:

$$XMLD(E) = XAS_{LH}(E) - XAS_{LV}(E). \quad (3.10)$$

The chosen notations LH and LV correspond to the electric field of X-rays oriented in the ring plane and perpendicular to it. The resulting XMLD spectrum consists of narrow peaks with the separation corresponding to the energy splitting of  $2p_{3/2}$  ( $2p_{1/2}$ ) states (Fig. 3.8(c)).

### Crystal field effect

Within the multiplet model, the degeneracy lifting of the final states can be caused not only by the purely magnetic exchange interaction but also by a crystal field [115; 116; 117]. This effect is caused by a lower symmetry of a crystal lattice in comparison to the  $SO(3)$  group.

Fig. 3.9(a) shows energy splitting of 3d levels of a  $Dy^{3+}$  ion in environments having different symmetries. A magnetic field (either external or effective Weiss field) results in a set of equidistant levels with different  $J_Z$  values. An axially symmetric crystal field constructs degenerate pairs of levels with  $\pm J_Z$  unequally spaced in energy [116]. Therefore, X-ray linear dichroism having a non-magnetic origin appears due to the crystal field splitting (Fig. 3.9(b)). Moreover, the experimental polarization dependent XAS can be well described by both magnetic and crystal field based theories (Fig. 3.9(b)).

Two ways were proposed for distinguishing between magnetic and crystal field generated dichroism:

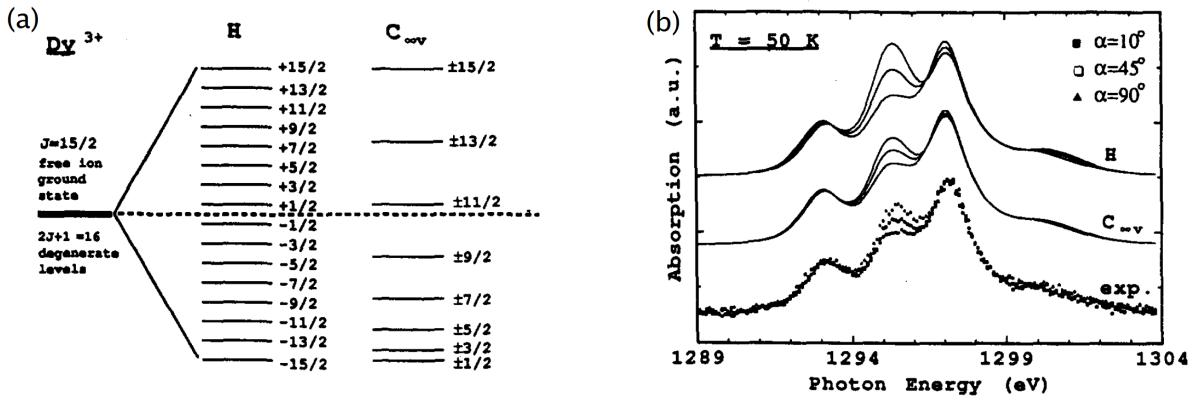


**Figure 3.9:** (a) Splitting of the  $Dy^{3+}$  ion levels caused by the Weiss field ( $H$ ) and by a crystal field having axial symmetry ( $C_{\infty v}$ ). (b) The theoretical polarization dependent XAS resulting from the splitting mechanisms shown in (a) and the experimental spectra for different angles ( $\alpha$ ) between the X-ray electric field and the quantization axis. Adapted from [116].

1) *Temperature dependent measurements.* The crystal field induced linear dichroism does not depend on temperature if there is no structural phase transition. In turn, the magnetic contri-

bution proportional to the squared order parameter decreases with increasing temperature (Fig. 3.10(a)). Thus, magnetic dichroism disappears above  $T_N$  [118].

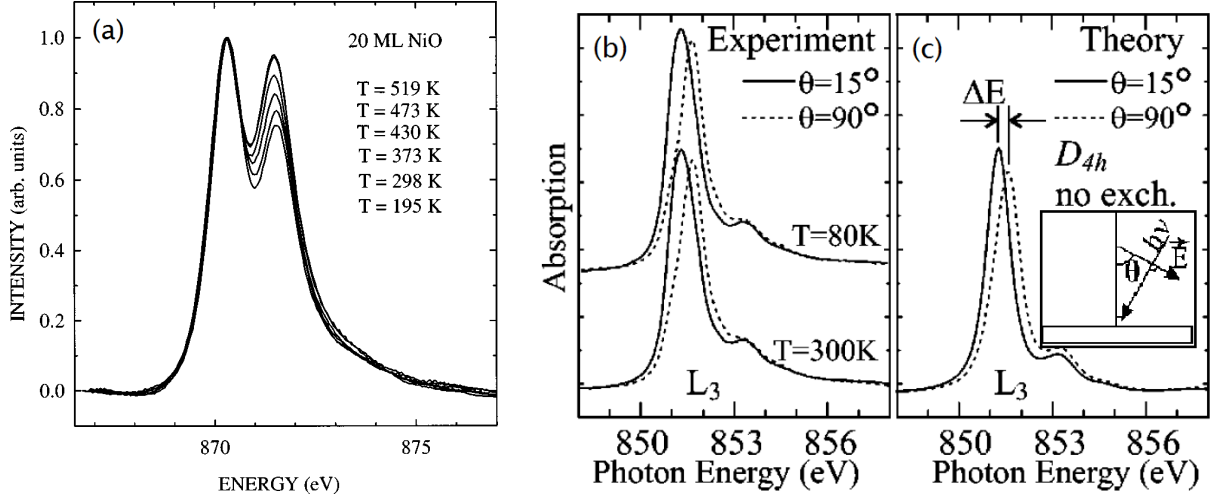


**Figure 3.10:** (a) Temperature dependent XAS of NiO measured at the Ni  $L_2$  edge with linearly polarized X-rays at normal incidence [118]. (b) Experimental and (c) theoretical XAS of NiO measured at the Ni  $L_3$  edge with linearly polarized X-rays at the incidence angles of  $\theta = 15^\circ$  and  $90^\circ$  [117]. The theoretical spectra are calculated assuming the crystal field originating from the  $D_{4h}$  symmetry with no exchange coupling. The inset in (c) shows the experimental geometry

2) *Polarization dependent measurements.* Varying the incidence angle changes the electric field direction with respect to the surface normal for a p-polarized beam (see the inset in Fig. 3.10(c)). Due to non-spherical p- and d-orbitals, different initial and final states are probed, which are shifted by the crystal field splitting. Redistribution of spectral weight within a multiplet causes a shift of the corresponding absorption peaks in the XAS (Figs. 3.10(b) and 3.10(c)).

The XMLD spectrum does not contain the crystal field contribution if the two consecutive XAS are measured with the X-rays polarized along the crystallographically equivalent directions, e.g.  $[110]$  and  $[\bar{1}\bar{1}0]$  in a tetragonal crystal.

### 3.3 Experimental methods for measuring X-ray absorption spectra

#### 3.3.1 Determining the absorption coefficient from transmission measurements

Absorption and scattering of X-rays lead to an intensity damping of a beam propagating within a material. Intensity due to these two processes after passing a distance  $d$  in a medium is given by the Beer-Lambert law:



$$I = I_0 \exp(-\mu d), \quad (3.11)$$

where  $I_0$  is the initial intensity. The attenuation coefficient ( $\mu$ ) can be represented as the sum of the absorption coefficient and the scattering coefficient  $\mu = \mu_A + \mu_S$ . In general,  $\mu(E)$ ,  $\mu_A(E)$ , and  $\mu_S(E)$  are material and energy dependent. In the case of a compound or a solution, the total attenuation coefficient is given by the sum of mass attenuation coefficients ( $(\mu/\rho)_i$ ):

$$\mu^{tot}(E) = \sum_i (\mu/\rho)_i \rho_i, \quad (3.12)$$

where  $\rho_i$  is the density of the corresponding constituent.

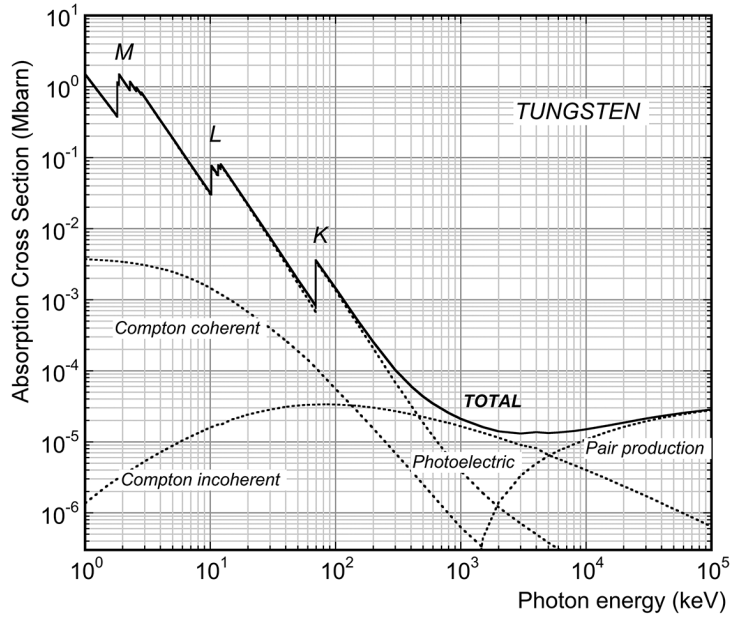


**Figure 3.11:** The energy dependence of the tungsten absorption cross section indicating contributions of different mechanisms [119].

Expressing  $\mu(E)$  from Eq. (3.11) results in

$$\mu(E) = -\frac{1}{t} \ln \left( \frac{I(E)}{I_0} \right). \quad (3.13)$$

Figure 3.11 shows the energy dependence of the absorption cross section ( $\sigma_A$ ), which determines the absorption coefficient  $\mu_A \propto \sigma_A$ , corresponding to different attenuation mechanisms in tungsten. For soft X-rays, the photoelectric (absorption) contribution is two orders of magnitude larger than the coherent scattering, and the incoherent scattering cross section remains negligibly small. This fact justifies the approximation  $\mu(E) \approx \mu_A(E)$ . The photoelectric cross section in a material with the atomic number  $Z$  decreases at higher frequencies as  $Z^n / (\hbar\omega)^3$ , where  $n =$

4 to 5. Therefore for hard X-rays, incoherent scattering dominates starting from  $\sim 100$  keV. At energies exceeding twice the electron rest mass  $2m_e c^2 \approx 1$  MeV, pair production occurs, which prevails at high photon energies.

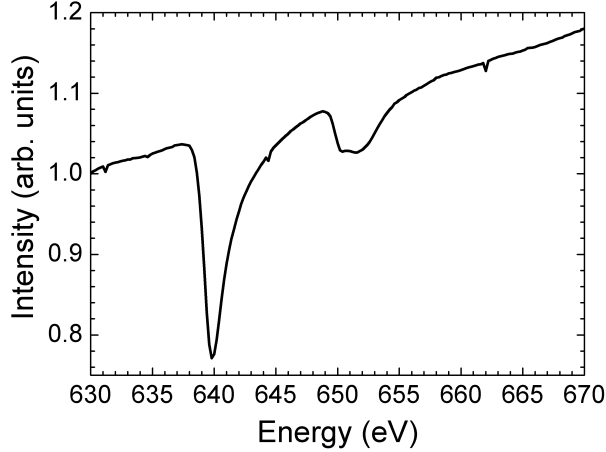


**Figure 3.12:** The normalized intensity of X-rays transmitted through the sample with the layer structure  $\text{Al}_2\text{O}_3/\text{Ta}$  18 nm/ $\text{Mn}_2\text{Au}$  10 nm/ $\text{AlO}_x$  2 nm.

The transmission of a 10 nm-thick  $\text{Mn}_2\text{Au}$  film measured with the ALICE instrument at BESSY II (HZB) is shown in Fig. 3.12. The investigated film was grown on a  $\text{Al}_2\text{O}_3(1\bar{1}02)$  substrate with a 18 nm-thick Ta buffer layer. The value plotted in Fig. 3.12, is the photoluminescence of the substrate, which is proportional to the transmitted X-ray intensity. The resonant enhancement of the absorption is distinctly visible at the photon energies corresponding to the  $L_3$ -edge and the  $L_2$ -edge of Mn. At the  $L_3$  edge, about 25 % of intensity are absorbed in the layer, which indicates an X-ray penetration depth  $\approx 35$  nm.

### 3.3.2 Determining the absorption coefficient from total electron yield measurements

The total electron yield (TEY) is based on the Auger process, which occurs due to recombination of the core hole appearing after photon absorption. The high-energy Auger electrons produce a cascade of secondary electrons (Fig. 3.13(a)), which escape to vacuum. The mean free path  $\lambda$  of the secondary electrons having an energy of several eV is in the nanometer regime according to the universal curve (Fig. 3.13(b)). This determines a probing depth of the method of  $\sim 3$  nm [25].

For a layer with a thickness much larger than  $\lambda$ , the photoelectron current ( $I$ ) is written as

$$I \propto \mu_A(E) \int_0^\infty e^{-\mu_A(E)z} e^{-z/\lambda} dz = -\frac{\mu_A(E)}{\mu_A(E) - 1/\lambda} \simeq \mu_A(E)\lambda, \quad (3.14)$$

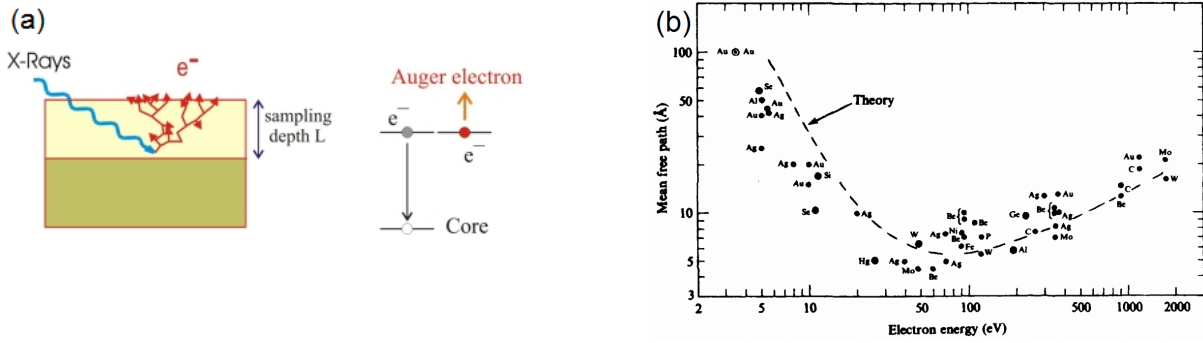


**Figure 3.13:** (a) Formation of a secondary electron cascade after absorption of an X-ray photon. The secondary electrons are excited by Auger electrons upon the core hole recombination (adapted from [120]). (b) The universal curve showing the mean free path of electrons depending on their kinetic energy [121].

where the condition  $\lambda \ll 1/\mu_A(E)$  is used. Thus, the absorption coefficient can be directly determined from the measured TEY current.

### 3.3.3 Determining the absorption coefficient from fluorescence measurements

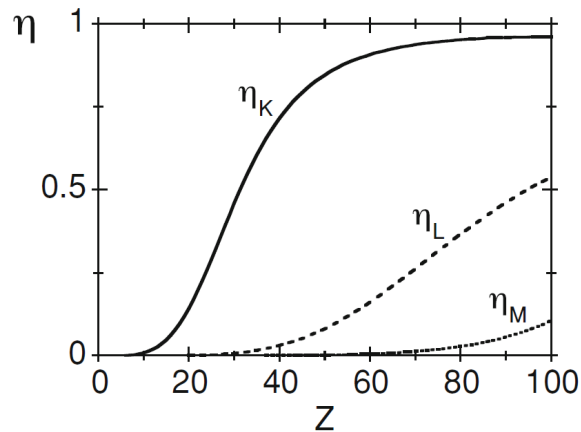


**Figure 3.14:** Fluorescence yield dependence on the atomic number for the holes in the K-, L-, and M-shells [101].

In addition to the discussed Auger process, core-hole recombination can be accompanied by the emission of a photon. The fluorescence method is based on detecting these photons instead of electrons. The relative probability of radiative versus non-radiative recombination process is described in terms of the fluorescence yield (FY), which is

$$\eta_s = \frac{X_s}{X_s + A_s}, \quad (3.15)$$

where  $X_s$  and  $A_s$  are the probabilities to emit a photon and an Auger electron, respectively, and the index  $s$  denotes the shell where the hole is created. The dependence of  $\eta_s$  on the atomic number is given in Figure 3.14. The value of  $\eta_s$  increases with  $Z$  and is largest for recombination with a hole in the K shell. For the L and M shells, FY is quite small and TEY remains the method of choice for measuring X-ray absorption in thin films containing transition metals or rare-earth elements.

### 3.4 Experimental setup for X-ray absorption spectroscopy and X-ray resonant magnetic scattering studies

All experiments with X-ray absorption are performed in vacuum since soft X-rays are strongly attenuated by air. High vacuum (HV) chambers and ultra-high vacuum (UHV) chambers are used at multiple beamlines all around the world. The HV chambers, e.g. ALICE at BESSY II (HZB), have an easily accessible sample stage providing freedom for installing additional equipment. However, the relatively high concentration of residual gases in combination with a high power beam illumination causes contamination of the sample surface during a measurement. In contrast, the UHV chambers, e.g. VEKMAG at BESSY II (HZB), preserve a clean sample surface but require a load-lock and a complicated transfer mechanics.

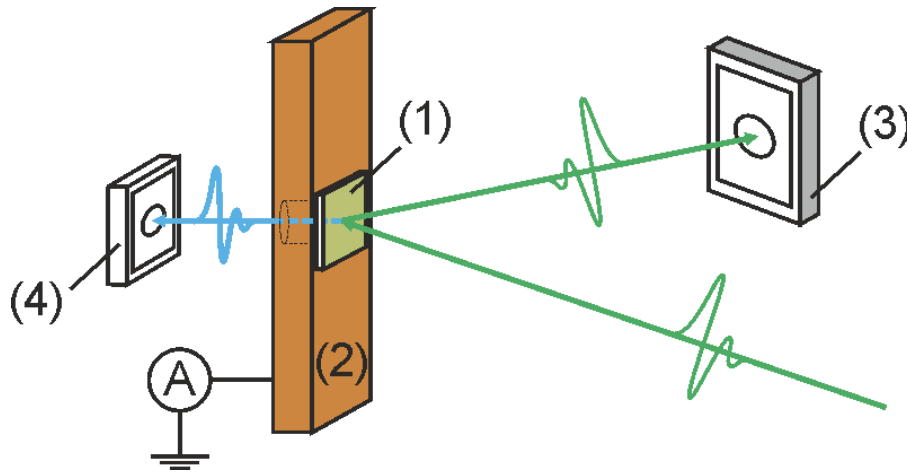


**Figure 3.15:** Scheme of a setup for X-ray absorption spectroscopy and X-ray resonant magnetic scattering measurements: (1) - sample, (2) - sample holder, (3) and (4) - photodiodes.

Typical equipment for X-ray absorption studies is presented in Figure 3.15. The layout allows simultaneous measurement of several parameters providing complementary information about

the investigated material properties. The sample (1) is mounted on a copper holder (2) with the investigated film being electrically connected to the holder. The amperemeter (A) monitors the total electron yield (TEY) current. The photodiode (3) detects the reflected X-ray intensity, and the photodiode (4) placed behind the sample acquires the substrate photoluminescence signal through a hole in the copper holder. Usually, the design of an experimental setup includes cooling equipment for performing the measurements at cryogenic temperatures and a magnet for applying an external field to the sample.

### **3.5 Low-energy electron microscopy and photoemission electron microscopy**

The spectroscopic techniques described in the previous section give the integral characteristic of a sample averaging the absorption coefficient over the X-ray spot size, which is typically  $\sim 10 \mu\text{m}$ . If magnetic inhomogeneities on this length scale are to be spatially resolved, a different approach is required. Several techniques exist providing a spatial resolution, among which are transmission X-ray microscopy (TXM) [122], scanning transmission X-ray microscopy (STXM) [123], X-ray holography [124], and X-ray photoemission electron microscopy (X-PEEM). The first three listed techniques are based on detecting the transmitted photons and are suitable for transparent samples. In contrast, the latter involves detecting the spatial distribution of the emitted secondary electrons with electron optics and does not require a transparent substrate or a complicated sample preparation procedure.

Two techniques for surface imaging are discussed in this chapter: photoemission electron microscopy (PEEM) and low-energy electron microscopy (LEEM). While LEEM is based on detecting the elastically backscattered electrons, PEEM deals with the electrons excited by either ultraviolet light or X-rays. The same detection optics can be utilized for LEEM and PEEM and usually, both methods are combined in one setup installed at a synchrotron for PEEM applications and having an additional electron gun for LEEM. One of the widely used solutions provided by Elmitec is installed at BESSY II (SPEEM beamline), DIAMOND (I06 beamline), and SLS (SIM beamline).

This section introduces the basic physical concepts underlying both methods and the typical instrumentation. Since the LEEM was used in the current work mainly for adjustment of the electron optics, only a brief description of the technique is given here.

#### **3.5.1 Interaction of low-energy electrons with matter**

In a LEEM, electrons approaching the sample surface typically have an energy in the interval from 0 to 100 eV. At these low-energies, backscattering occurs with a high probability [125] with the backscattering cross section depending on the electron energy and on the atomic number of the scattering atoms [126]. If scattering from a crystalline sample is considered, the highest

reflection coefficient is achieved for the electrons with the energies corresponding to a band gap of the sample, since there are no states which they can occupy. However, total reflection cannot be achieved due to several reasons such as the presence of surface states, electron-phonon interaction, etc. [126].

The inelastic processes for scattering from a metal are mainly connected with plasmonic excitations. For electrons with an energy smaller than the plasmon energy, the attenuation coefficient is mainly determined by elastic processes. Thus, low energy electrons can penetrate deeper into the material, which has a negative impact on the surface sensitivity. Bauer gives an optimal electron energy for electron-surface interaction of 20 to 30 eV [126].

### 3.5.2 Interaction of X-rays with matter

Interaction of X-rays with matter is discussed in detail in Section 3.2. The relevant process for PEEM is the resonant absorption of photons, which results in electronic excitations and creation of core holes. Subsequently, the high-energy Auger electrons produced in the recombination process generate secondary electrons (SE), which can propagate to a distance of several nm from the excitation point. For PEEM, this fact has two important consequences. Firstly, this implies a surface sensitivity of the technique with a probing depth of several nm. Secondly, the photoelectron current extracted from a sample area is proportional to the local excitation rate, which defines a high lateral resolution.

### 3.5.3 Instrumentation of a LEEM/PEEM microscope

Schematics of a typical LEEM/PEEM setup is shown in Fig. 3.16. In the PEEM mode, the X-ray beam impinges onto a sample under an angle of typically  $\approx 16^\circ$ . A small retarding voltage  $\sim 1$  eV cuts off the slow photoelectrons in the low energy part of the distribution and the rest is accelerated to an energy of 10 keV towards the objective lens. Passing the sector field, electrons enter the optical column, which transmits the image to the hemispherical analyzer, filtering the electrons according to the energy and improving the resolution. The projective optics magnifies the image and transfers it to the microchannel plate (MCP), which greatly enhances the photoelectron current. Then, the accelerated electrons bombard the luminescent screen imaged by the CCD camera. A resolution reaching 25 nm can be achieved with a modern PEEM [128].

In the LEEM mode, the electrons emitted from the electron gun pass through the beam separator towards the sample surface. The beam separator creates a homogeneous magnetic field inside of it, which deflects counter-propagating bunches of electrons to the opposite directions. This allows separating the incoming and the outgoing electrons. The anode of the electron gun is set under a high negative voltage of  $\sim -20$  keV. At the same time, the potential of the sample equal to  $\sim -20$  keV +  $U_{STV}$  is biased by a start voltage ( $U_{STV}$ ).  $U_{STV}$  can take values from -5 to 100 V. In the negative voltage regime, the electrons are reflected from the sample surface and

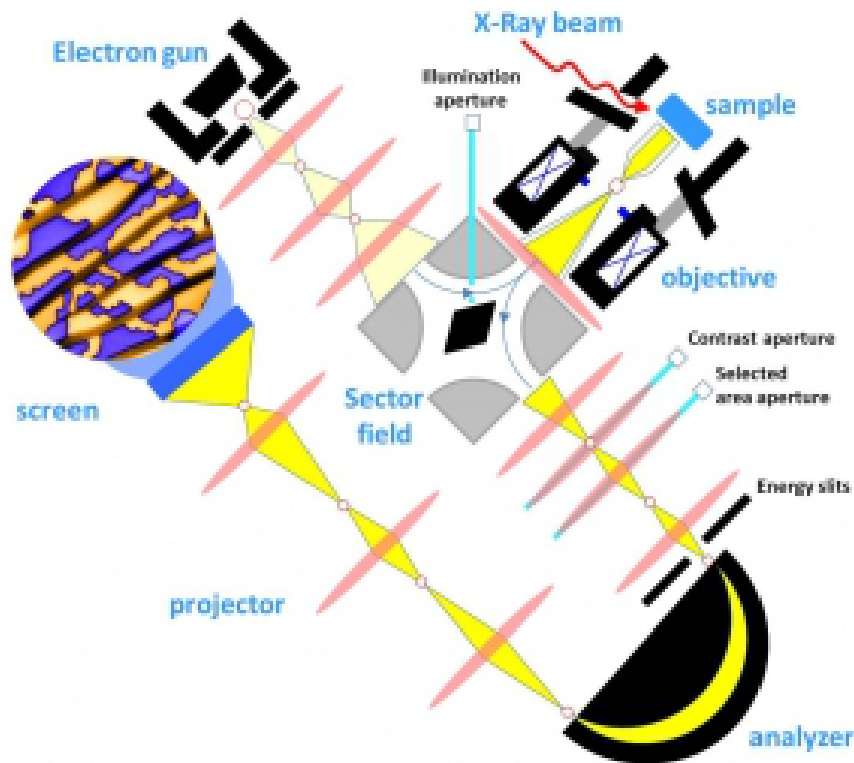


**Figure 3.16:** A schematic image of a low-energy electron microscope / photoemission electron microscope [127].

this operational mode is called mirror electron microscopy (MEM). For a positive  $U_{STV}$ , the electrons scattered from the surface atoms form a diffraction pattern in the focal plane of the extractor lens, similar to a conventional LEED experiment. The surface imaging can be then performed in the bright-field mode if the main (00)-reflex is chosen by the contrast aperture, or in the dark field mode in the case of a secondary reflex, e.g. (01).

Electrostatic and magnetic lenses are used for focusing the electrons in a microscope. Their operational principle is based on creating inhomogeneous electric (magnetic) fields, which curve the electron trajectories in the way as it is done with light beams in optical lenses. An electrostatic lens consists of several electrodes with apertures. A magnetic lens represents itself a solenoid wrapped around a yoke made out of a soft ferromagnetic material. The yoke can have a narrow slit for concentrating the magnetic field in a particular region of space and increasing its gradient.

Similar to visible light optics, electronic lenses also suffer from aberrations. The most important of them are spherical aberration, chromatic aberration, diffraction limit and astigmatism.

1) *Spherical aberration* is caused by the fact that the focal lengths are not equal for the electrons

propagating at different distances from the main optical axis (Fig. 3.17). The minimal spot diameter  $d_s$  for focusing a parallel beam is [129]

$$d_s = C_s \alpha^3. \quad (3.16)$$

Please note that  $C_s$  for electron optics is always positive (in contrast to light optics) and can therefore not be compensated by conventional means.

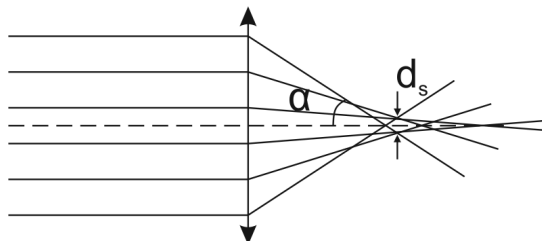


**Figure 3.17:** Illustration of spherical aberration in electronic optics.

2) *Chromatic aberration* results in different focal lengths for electrons with different kinetic energies (Fig. 3.18). Therefore, a parallel narrow non-monochromatic electron beam is focused to a spot having the diameter  $d_c$  [129]:

$$d_c = C_c \frac{\Delta E}{E} \alpha, \quad (3.17)$$

where  $E$  is the average energy of the electrons and  $\Delta E$  is the energy distribution width.

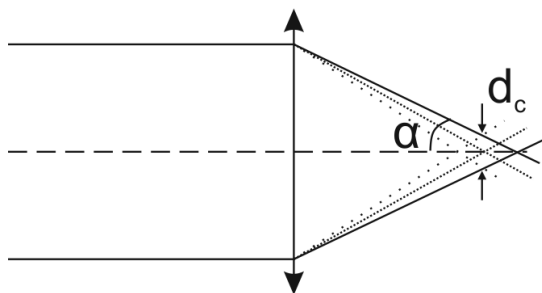


**Figure 3.18:** Illustration of chromatic aberration in electronic optics. Different lines correspond to the trajectories of the electrons with different energies.

3) Diffraction effects come into play when the wavefront is confined. The diffraction induced broadening  $d_D$  is given by the Abbe formula (Fig. 3.19):

$$d_D = \frac{1}{2} \frac{\lambda}{\alpha}, \quad (3.18)$$

where  $\lambda$  is the wavelength of the electrons.



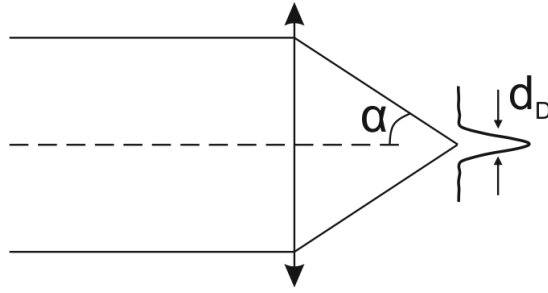


**Figure 3.19:** Illustration of diffraction limit related distortions in electronic optics.

The resolution, which can be achieved in an optical system, is limited by these three contributions  $d = \sqrt{d_s^2 + d_c^2 + d_D^2}$ . Figure 3.20 shows the dependence of  $d$  on the aperture  $r_A$ . The highest theoretical resolution for the considered parameters reaches 5 nm. In reality, the achievable resolution is several times lower [128]. This is explained by too optimistic parameters chosen for plotting Fig. 3.20 and other sources of aberrations, such as space charge caused by the pulsed illumination of the synchrotron light.

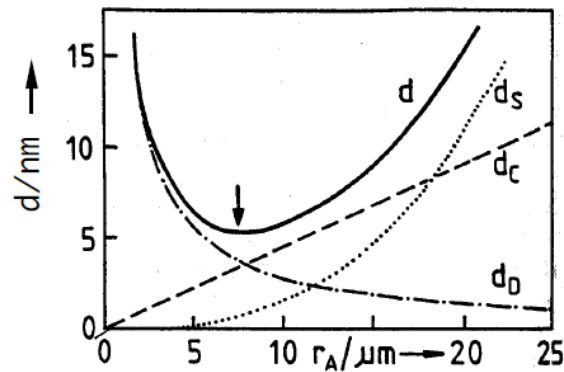


**Figure 3.20:** The total theoretically achievable resolution of an electronic lens ( $d$ ) as a function of the aperture width ( $r_A$ ):  $d_s$  - spherical aberration,  $d_c$  - chromatic aberration, and  $d_D$  - diffraction limit. The accelerating voltage is 25 kV, the field length is 3 mm, the start voltage is 2.5 eV, and the energy spread is 0.25 eV [130].

Another optical aberration, called axial astigmatism, is caused by flaws in axial symmetry of the electron optical elements. This leads to a variation of fields experienced by electrons at different  $\phi$  angles in the same cross-section of an optical element. As illustrated in Fig. 3.21(a), this results in a broadened image and elliptical distortions of the image before and after the image plane. For correcting this aberration, changes in the form of a (at the best round) spot on the sample surface are analyzed upon varying the objective focal length. In the presence of astigmatism, the image becomes elongated in two opposite directions, which is compensated by

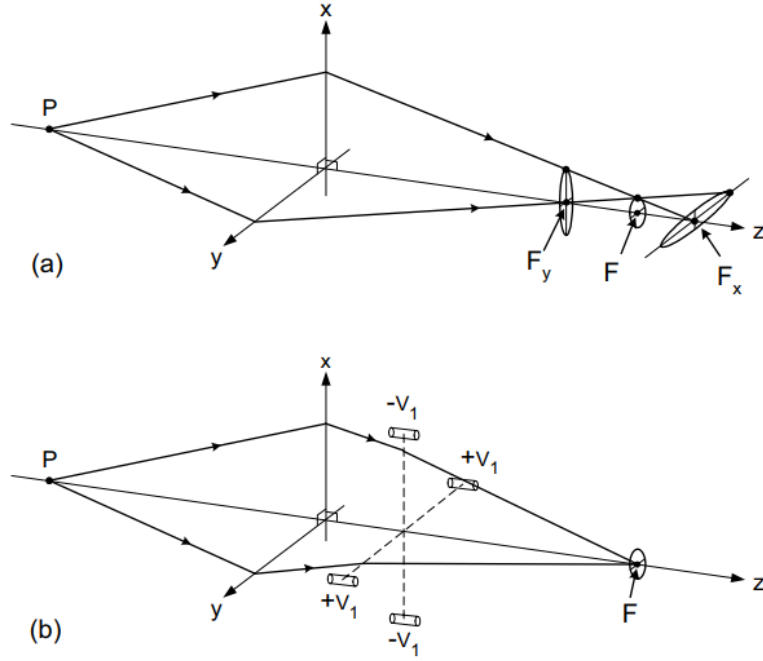


**Figure 3.21:** (a) The trajectories of electrons in a non-axial symmetric lens resulting in axial astigmatism. (b) Compensation of the aberration by the stigmators. The potentials of the opposite pairs of stigmators are  $\pm V_1$  [129].

the stigmators in live regime Fig. 3.21(b).

### 3.5.4 XMCD and XMLD spectromicroscopy

The current of the photoelectrons extracted from an area on the sample surface is proportional to the local  $\mu_A(E)$ . Therefore, the intensity of light caused by electrons bombarding the screen is also proportional to  $\mu_A(E)$ , which is then detected by the camera. For measuring the XAS of a sample with a PEEM, a series of images is taken at a range of energies close to the absorption edges of the investigated material. The absorption spectrum is then plotted as the sum of the gray-scale levels over the region of interest (ROI) in the obtained stack of images. This technique is called microspectroscopy since it allows for investigating the XAS over arbitrary ROIs.

In order to perform the surface composition analysis in a PEEM, two images are taken at the absorption edge of the investigated element and at an energy several eV lower. The ratio of these two images provides the element specific contrast in the near-surface region.

As it is shown above, the XMCD in a magnetic material is determined by the asymmetry of the DOS of the majority and minority electrons. In turn, it is proportional to the magnetic moment, projection on the chosen quantization axis (see Subsection 1.2.5). This leads to dependence of the XMCD on the mutual orientation of the X-ray wave vector and the magnetization [131]. This fact provides an opportunity for implementation of spectromicroscopy technique. For this,

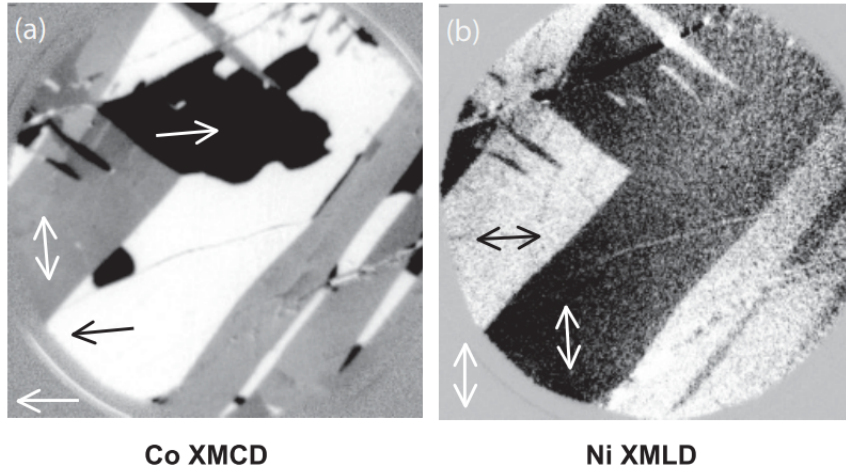


**Figure 3.22:** Magnetic domains measured by combination of XMCD and XMLD PEEM in a heterostructure NiO(100)/Co [132]. Field of view is 15  $\mu\text{m}$

the photon energy is set to the absorption edge, where the maximal dichroism is reached. The asymmetry of two images taken at circular right and left polarizations gives the ferromagnetic contrast. An example of Co domains imaged in a NiO(100)/Co 2.5 nm heterostructure is shown in Fig. 3.22(a) [132]. The white arrow in the left bottom corner shows the in-plane projection of the X-ray wave vector. Three colors can be distinguished in the picture, corresponding to parallel (white), perpendicular (grey), and antiparallel (black) orientation of the magnetization and the wave vector. The technique cannot distinguish between two perpendicular magnetization orientations, which is indicated by the double-headed arrow in the image.

The antiferromagnetic domains are imaged with linear polarization with the electric field vector in the film plane. For oxides exhibiting pronounced multiplet peaks in XAS, the magnetic contrast is obtained as the asymmetry of the images taken at the energies corresponding to different multiplet peaks. The conductive AFMs having a single maximum at every absorption edge require a different approach. In this case, a combination of spectroscopy and microscopy measurements provides the energies corresponding to the maximum and minimum of XMLD. The asymmetry of the images obtained at these energies provides magnetic contrast [76].

The AFM domains in the heterostructure NiO(100)/Co 2.5 nm discussed above are shown in Fig. 3.22(b). The probing depth of the X-ray PEEM allows for reaching buried layers at the depth of several nm under the sample surface. The white double-headed arrow in the left bottom corner indicates the X-ray electric field. Two types of AFM domains are visible in the image. It is worth mentioning that the shape of the Co domains and the NiO domains are very similar. A combination of XMCD and XMLD proved the  $90^\circ$  coupling between the FM moments and the AFM moments in a NiO/Co heterostructure.



# 4 Determination of the exchange constant and the loose spin concentration in $\text{Mn}_2\text{Au}$ epitaxial thin films

## 4.1 Introduction

Knowing the exchange constants  $J$  in AFMs is of high importance since they determine the spin-flop field [62], the DW profile [133], and the characteristic excitation frequencies [134]. Traditionally, the  $J$ s have been determined from the AFM magnon dispersion by inelastic neutron scattering [135]. However, these methods are not applicable to thin AFM films. Therefore, alternative methods are required as described in this chapter.

As mentioned in Section 2.3, the value of  $J$  depends on the distance between the interacting atoms, and usually, only a few nearest neighbors are considered. Three exchange constants are usually taken into account in  $\text{Mn}_2\text{Au}$ , which are responsible for the arrangement of spins within a unit cell (Fig. 4.1). Interaction between a Mn atom with its three nearest neighbors separated by  $2.750 \text{ \AA}$ ,  $2.846 \text{ \AA}$ , and  $3.328 \text{ \AA}$  is described by exchange constants  $J_1$ ,  $J_2$ , and  $J_3$ , respectively. The theoretical values of these constants calculated by density functional theory (DFT) are  $-34 \text{ meV}$ ,  $-46 \text{ meV}$  and  $10 \text{ meV}$ , respectively [136]. The negative values of  $J_1$  and  $J_2$  indicate the antiparallel coupling between the neighboring planes of Mn atoms, while the positive value of  $J_3$  implies parallel alignment of Mn moments within  $ab$ -planes.

One possible way for determining the exchange constants is to measure the perpendicular susceptibility of the AFM. While the exchange constants were determined by this method for a powder  $\text{Mn}_2\text{Au}$  sample in Ref. [55], measurements of  $J$  regarding thin films are lacking in the literature. XMCD suits perfectly for the susceptibility measurements in AFM thin films due to its element specificity and surface sensitivity in the TEY mode.

Epitaxial thin films contain structural defects, such as grain boundaries and substitutional atoms, which are caused by impurities, lattice mismatches between the layers, etc. In a magnetic

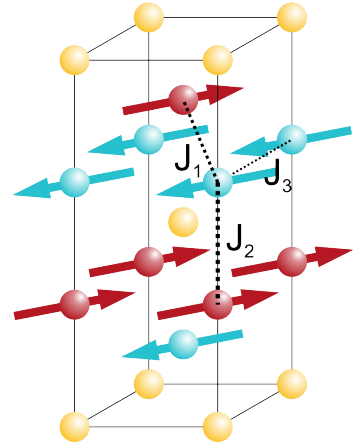


**Figure 4.1:** The elementary cell of  $\text{Mn}_2\text{Au}$  with Au atoms shown in yellow and Mn atoms belonging to different sublattices shown in red and blue. The exchange constants for the three nearest coordination spheres of a Mn atom are specified.

material, these defects also disturb the magnetic order leading to a weaker coupling of the moments to the neighbors. Thus in the case of a very weak residual coupling, the moments at the defect sites become loose and behave similarly to a paramagnet. A high magnetic field orients the paramagnetic spins at low temperatures, while at the high temperatures, the paramagnetic spin ensemble remains disordered. Therefore, the loose spin concentration can be determined from the perpendicular susceptibility measured at different temperatures.

This chapter is devoted to the discussion of the exchange constants and the loose spin concentration in epitaxial  $\text{Mn}_2\text{Au}$  thin films. Section 4.2 introduces the details about sample preparation and employed experimental techniques. Section 4.3 reports the field and temperature dependent perpendicular susceptibility accessed by XMCD and data analysis procedure, which allowed to determine the exchange constants and loose spin concentration of  $\text{Mn}_2\text{Au}$  thin films. The perpendicular susceptibility of  $\text{Mn}_2\text{Au}$  at room temperature (RT) originates solely from the response of the antiferromagnetically coupled spins (Section 4.3.1). Thus, it provides information on the exchange coupling constant (Subsections 4.3.2). In contrast, the susceptibility at low temperatures (Subsections 4.3.3) contains the contributions from coupled spins and from loose spins and sheds light on the loose spin concentration.

## 4.2 Experimental details

The epitaxial thin film samples discussed in this chapter have the layer sequence of  $\text{Al}_2\text{O}_3$  ( $1\bar{1}02$ )/ $\text{Ta}(001)$ / $\text{Mn}_2\text{Au}(001)$ / $\text{AlO}_x$ . The in-plane epitaxial relation probed by X-ray diffraction (XRD) is  $\text{Mn}_2\text{Au}(001)[100] \parallel \text{Ta}(001)[100]$ . The samples were grown by radio frequency magnetron sputtering in a UHV deposition cluster. A Ta buffer layer was deposited at the optimal temperature and Ar pressure assuring the best layer quality as verified afterward by reflection high energy electron diffraction (RHEED) and XRD. The heater temperature of  $600^\circ\text{C}$  in combination with the Ta buffer layer provided a high-quality  $\text{Mn}_2\text{Au}(001)$  film. The layer thicknesses were defined from the known deposition rates. An Al capping was used for oxidation protection.

The susceptibility measurements were performed at VEKMAG end station located at BESSY II (Helmholtz-Zentrum Berlin). The instrument is installed at beamline PM2 with a bending magnet as the X-ray source. The beam is monochromatized with a spherical grating monochromator and focused to a spot of  $40 \times 60 \mu\text{m}$ . The X-ray flux is  $5 \times 10^9$  photons/sec on the sample surface. The degree of circularity provided by the beamline is typically set to 77 %, which maximizes the figure of merit of the beamline. A beam analysis chamber installed in the beam path provides an outstanding beam stability. A load-lock and a mechanical transfer system allow a fast sample transfer to the experimental chamber, where the pressure is maintained lower than  $5 \times 10^{-10}$  mbar. The samples are mounted in the center of the superconducting vector magnet, providing  $\pm 8$  T along the beam,  $\pm 2$  T perpendicular to the beam and  $\pm 1$  T in the vertical direction. The sample stage allows conducting the measurements at temperatures from 7 K to

300 K. The X-ray absorption data in this work were acquired in TEY mode. Picoampermeters Keithley 6485 and 6487 were used for monitoring the currents. The total current extracted from the sample, which amounted to several picoamperes, was normalized to the current of a Pt mesh monitor located in the beam analysis chamber. This procedure allows for compensating the residual beam deviations caused by fluctuations of the storage ring current and the beamline equipment instabilities.

The sum rules in the following form were employed for determining the values of spin and orbital moment (see Subsection 3.2.1 for the definitions of  $A$ ,  $B$ , and  $C$ ):

$$\begin{aligned} m_S &= -\frac{Corr}{P} \frac{A - 2B}{C} N_d \mu_B, \\ m_L &= -\frac{Corr}{P} \frac{2(A + B)}{3C} N_d \mu_B, \end{aligned} \tag{4.1}$$

where  $N_d$  is the number of 3d holes in Mn,  $Corr = 1.5$  is the correction factor compensating for the  $jj$ -mixing [137], and  $P = 0.77$  is the degree of circular polarization provided by the beamline.

### 4.3 Determination of the exchange constant and the loose spin concentration in $Mn_2Au$

The exchange interaction determines the "rigidity" of the antiparallel spin alignment in an AFM. Therefore, it can be determined from the perpendicular susceptibility, which in the linear approximation is  $\chi_{\perp} = M_{\perp}/H$ . In a non-perfect AFM, the susceptibility contains contributions from the coupled and the loose spins:

$$\chi_{\perp} = \chi_{\perp}^{AFM} + \chi_{\perp}^{loose} = \frac{M_{\perp}^{AFM} + M_{\perp}^{loose}}{H}. \tag{4.2}$$

The susceptibility of antiferromagnetically coupled spins ( $\chi_{\perp}^{AFM}$ ) is determined by the strong exchange interaction and magnetic anisotropies favoring the antiparallel in-plane alignment (see Section 2.5). If the material of interest has a  $T_N$  much higher than the RT, as in the case of  $Mn_2Au$ , its magnetic properties do not significantly change upon cooling. Thus, the first term of Eq. (4.2) is assumed to be constant below RT. In contrast, the loose spin distribution in an external magnetic field is strongly temperature dependent, due to a weak coupling to the neighbors. Thus, susceptibility measurements performed at different temperature allow for separating two contributions in Eq. (4.2).

It is worth mentioning that for an easy plane antiferromagnetic  $Mn_2Au$ , an out-of-plane magnetic field results in the same induced magnetization in both types of antiferromagnetic domains. Therefore, the domain distribution in such a material does not affect the measured susceptibility.

### 4.3.1 Estimation of the loose spin contribution to the perpendicular susceptibility at different temperatures

In this work, the model of completely decoupled loose spins is employed. Therefore, they are treated as an ensemble of paramagnetic moments, which can be described by the Brillouin function:

$$\frac{M}{M_{loose}} = B_S(y) = \frac{2S+1}{2S} \coth\left(\frac{2S+1}{2S}y\right) - \frac{1}{2S} \coth\left(\frac{1}{2S}y\right), \quad (4.3)$$

where  $M_{loose}$  is the saturation magnetization of loose spins, and  $y = \mu_S^{Mn} \mu_0 H / k_B T$  is the dimensionless argument depending on the Mn magnetic moment  $\mu_S^{Mn} = 3.591 \mu_B$  (see Appendix 3). In Eq. (4.3) in comparison with the conventional Brillouin function, the total moment  $J$  is replaced by the spin moment  $S$ . This is justified in a crystalline solid due to orbital momentum quenching providing that  $J \approx S$ .

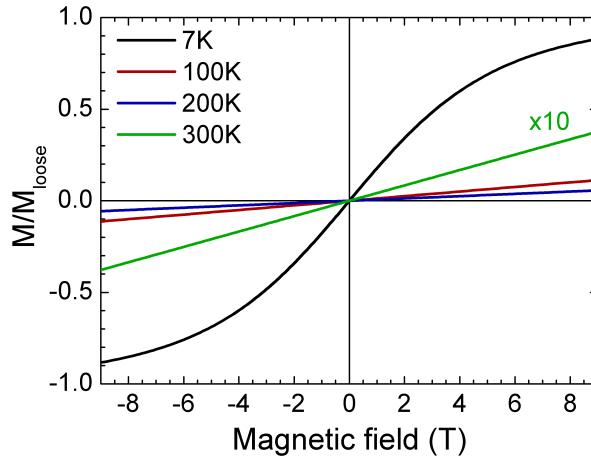


**Figure 4.2:** The graphical representation of the function in Eq. (4.3) for  $S=1.8$  at different temperatures. Please note that the plot corresponding 300 K is multiplied by 10.

For RT and the highest magnetic field of 8T, which was available during the XAS studies at VEKMAG, the Brillouin function provides  $M = 0.03M_{loose}$ . The same estimation at 7K gives the loose spin magnetization  $M = 0.74M_{loose}$ . A small concentration of loose spins in epitaxial films implies a small  $M_{loose}$  value. Thus, the contribution of loose spins to the perpendicular susceptibility can be neglected at RT but it has to be taken into account at low temperatures.

### 4.3.2 Room temperature measurements

Sample *MA1* with the stacking sequence  $\text{Al}_2\text{O}_3/\text{Ta } 18 \text{ nm}/\text{Mn}_2\text{Au } @600^\circ\text{C } 10 \text{ nm}/\text{AlO}_x 2 \text{ nm}$  was prepared for experiments on perpendicular susceptibility measurements. The absorption spectra



measured in *MA1* at RT in a field of 8 T indicate a sizable dichroism (Figs. 4.3(a) and 4.3(c)). The XMCD value at the  $L_2$  edge is small indicating a large induced orbital moment.

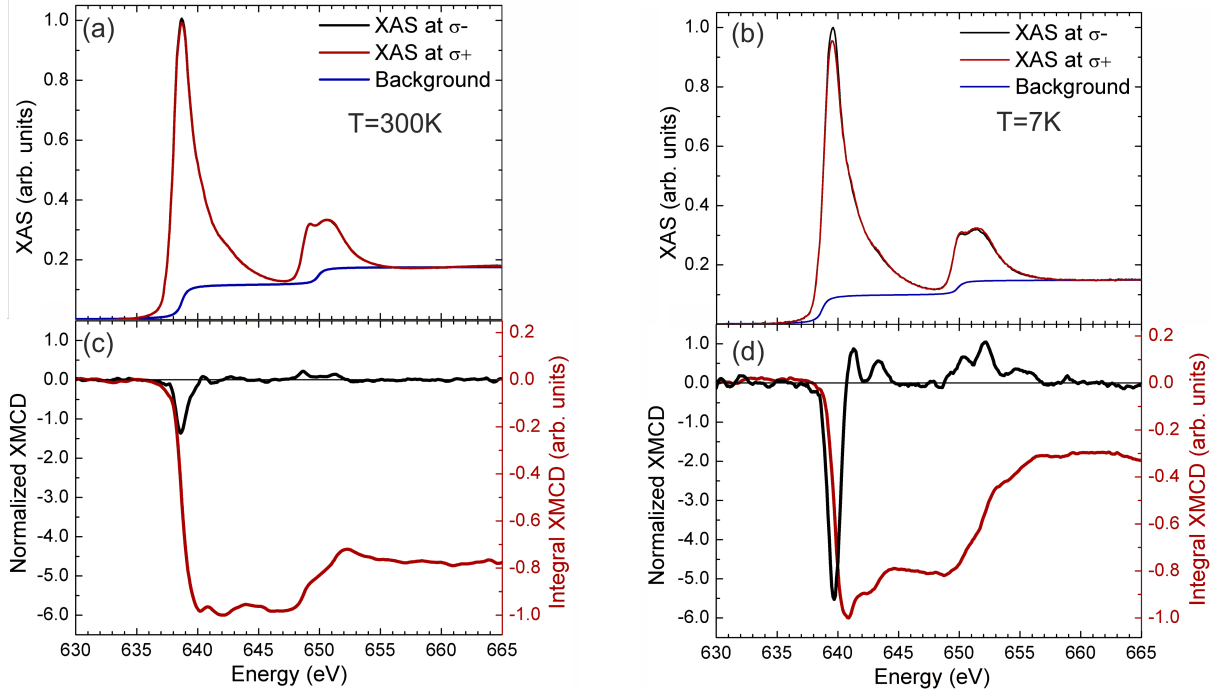


**Figure 4.3:** (a) XAS measured in *MA1* at 8 T and at 300 K. (b) The same measurement as in (a) but at 7 K. The blue line shows the contribution of the absorption to delocalized electron states. (c) and (d) The corresponding XMCD spectra calculated from the data shown in (a) and (b), respectively.

The blue curves in Fig. 4.3 represent the background associated with excitation of electrons from 2p states to delocalized states close to the Fermi level described by function  $S(E)$  with  $\Delta E = 0.35$  eV (see Subection 2.2.2).

Integration of the XAS and the XMCD spectrum provides  $A = -1.68 \pm 0.11$ ,  $B = 0.33 \pm 0.03$ , and  $C = 3.17 \pm 0.09$  (Fig. 4.3(c)). The resulting moments are  $\mu_S = (0.065 \pm 0.010) \mu_B/\text{atom}$  and  $\mu_L = (0.025 \pm 0.005) \mu_B/\text{atom}$  at 8 T. Please note that the ratio of  $\mu_L/\mu_S$  is surprisingly large, reaching 30%. The perpendicular susceptibility determined for the AFM coupled spins at RT is:

$$\chi_{\perp}^{AFM} = \frac{(\mu_S + \mu_L)n}{H} = (5.5 \pm 0.9) 10^{-3}, \quad (4.4)$$

where  $n = 4.2 \times 10^{28} \text{ m}^{-3}$  is the number density of Mn atoms in  $\text{Mn}_2\text{Au}$ .

A large experimental value of  $\mu_L$  can be interpreted with the following simple model. The spin magnetic moments of both sublattices ( $\mu_{S1}$  and  $\mu_{S2}$ ) are antiferromagnetically coupled via a strong exchange interaction. The magnetic field has to overcome the exchange torque to tilt the spin moments (left side of Fig. 4.4). In turn, the orbital magnetic moments ( $\mu_{L1}$  and  $\mu_{L2}$ )

are coupled to the corresponding  $\mu_{S_1}$  and  $\mu_{S_2}$  via SOC (the central part of the Fig. 4.4). The SOC constant is one order of magnitude smaller than the exchange constant [138]. Therefore, the external field rotates the orbital magnetic moments by a larger angle out of the equilibrium antiparallel position than the spin moments (see Fig. 4.4) and the projected perpendicular orbital moment is of the same magnitude as the projected spin moment. Our experimental finding point out that only the spin moments are coupled by the exchange interaction and not the orbital moments. A similar non-collinear arrangement of the spin moment and orbital moment has also been observed in FM [138].

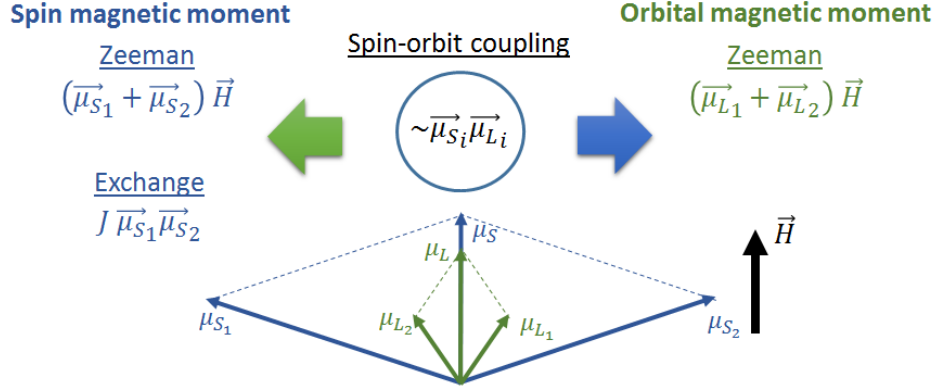


**Figure 4.4:** The spin ( $\mu_{S_1}$  and  $\mu_{S_2}$ ) and the orbital ( $\mu_{L_1}$  and  $\mu_{L_2}$ ) magnetic moments of two Mn<sub>2</sub>Au sublattices in external magnetic field. Spin-orbit coupling couples the spin and the orbital moment of the same sublattice.

The following energy density functional is employed for analyzing the field induced magnetization in Mn<sub>2</sub>Au, which takes into account exchange interaction, MAE, shape anisotropy, and Zeeman energy:

$$\epsilon = \epsilon_{exchange} + \epsilon_{MAE} + \epsilon_{shape} + \epsilon_{Zeeman}. \quad (4.5)$$

The exchange energy is given by (see Section 2.4):

$$\epsilon_{exchange} = \sum_{\{ij\}} -J_{ij} \mathbf{e}_i \mathbf{e}_j = \sum_{\{ij\}} J_{ij} \cos(\pi - 2\alpha), \quad (4.6)$$

where  $\mathbf{e}_i$  is a unit vector oriented along the spin vector  $\mathbf{S}_i$  and  $\alpha$  is the tilting angle of the Mn spins towards the film normal. In approximation that  $\alpha$  is small:

$$\epsilon_{exchange} = n J_{eff} 2\alpha^2, \quad (4.7)$$

where  $J_{eff} = (4J_1 + J_2)/2$  is the effective exchange constant (see Fig. 4.1) and  $n$  is the number of Mn atoms per unit volume. The parallel alignment of Mn spins within one *ab*-plane is preserved upon application of an out-of-plane magnetic field. Thus, the exchange constant  $J_3$  cannot be

determined from the present experiment. Using the notation from Ref. [56], the MAE is written as:

$$\epsilon_{MAE} = \frac{nK_{2\perp}}{2} \sin^2 \alpha \approx \frac{nK_{2\perp}}{2} \alpha^2. \quad (4.8)$$

The expression for shape anisotropy in thin films is [68]:

$$\epsilon_{shape} = \frac{1}{2} \mu_0 M_S^2 \sin^2 \alpha \approx \frac{1}{2} \mu_0 M_S^2 \alpha^2, \quad (4.9)$$

where  $M_S$  is the saturation magnetization of  $Mn_2Au$ . Combining Eqs. (4.7) to (4.9) and adding the Zeeman term  $n(\mu_S + \mu_L)\mu_0 H$  gives the total energy density:

$$\epsilon = (2nJ_{eff} + \frac{nK_{2\perp}}{2} + \frac{1}{2} \mu_0 M_S^2) \left( \frac{\mu_S}{\mu_{Mn}} \right)^2 - n(\mu_S + \mu_L)\mu_0 H, \quad (4.10)$$

where  $\alpha$  is replaced by  $\mu_S/\mu_{Mn}$ . Minimizing (4.10) with respect to the induced spin magnetic moment, the equation for  $J_{eff}$  is obtained:

$$J_{eff} = \frac{1}{4} \left( \mu_0 H \frac{\mu_{Mn}^2}{\mu_S} - K_{2\perp} - \frac{\mu_0 M_S^2}{n} \right). \quad (4.11)$$

Inserting values obtained from experiments at 300 K into Eq. (4.11) results in  $J_{eff} = (22 \pm 5)$  meV. This experimental value is considerably smaller than a theoretically predicted value of 90 meV [136] and the experimentally determined value of 75 meV for a powder sample [55]. One of the possible reasons for this discrepancy is the contribution of the weakly coupled moments at the surface and at the grain boundaries characterized by a reduced exchange constant.

### 4.3.3 Low temperature measurements

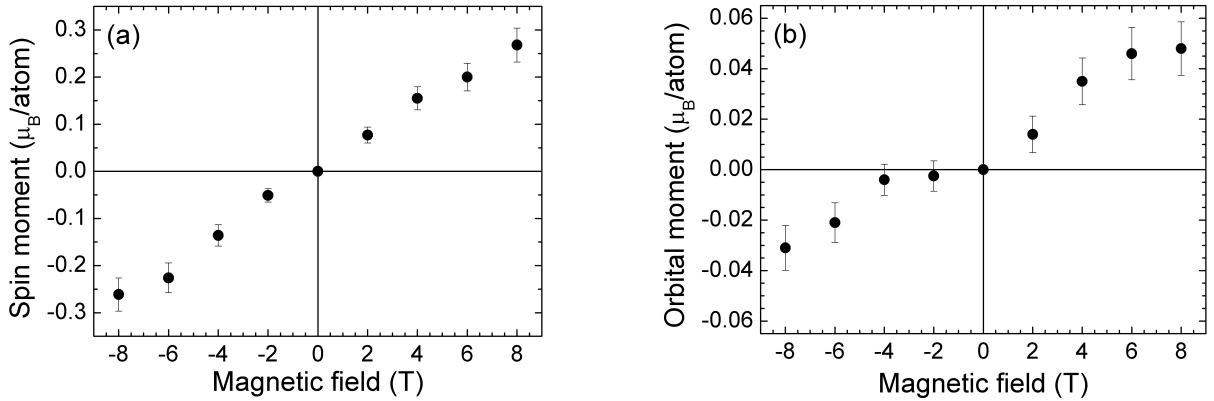


**Figure 4.5:** (a) The field dependence of the spin moment determined for *MA1* at the temperature of 7 K. (b) The same for the orbital moment.

The field dependent X-ray absorption measurements were performed after cooling *MA1* to 7 K

(Fig. 4.3(b)). The low-temperature XMCD spectrum reveals a higher dichroism values than measured at RT (compare with Fig. 4.3(a)). For these spectra we calculate  $A = -4.91 \pm 0.36$ ,  $B = 2.91 \pm 0.08$ ,  $C = 3.35 \pm 0.07$ . The spin moment determined according to the procedure described above reaches  $(0.27 \pm 0.04) \mu_B/\text{atom}$  at the external field of 8 T. The  $\mu_L = (0.048 \pm 0.015) \mu_B/\text{atom}$  is of the same order as the RT value. This fact corroborates the above-discussed model that the induced orbital moment originates mainly from the antiferromagnetically coupled moments.

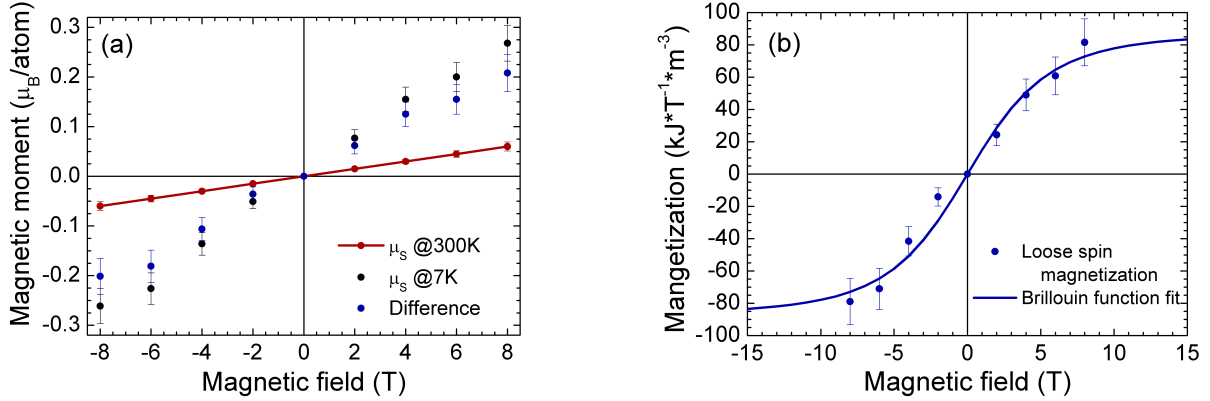


**Figure 4.6:** (a) The induced perpendicular spin magnetic moment in *MA1* at 7 K determined by XMCD (black dots), which is the sum of the loose spin contribution (blue dots) and the antiferromagnetically coupled spin contribution (red dots). The latter is the linear extrapolation of the data measured at RT. (b) The Brillouin function fit of the induced magnetization of loose spins.

For determining the concentration of loose spins, it is necessary to extract their contribution from the total low-temperature susceptibility. The moment of the antiferromagnetically coupled spins obtained at RT is linearly extrapolated to the range of magnetic field from -8 T to 8 T (Fig. 4.6(a) red dots and line) and subtracted from the total induced spin moment at the low temperature (Fig. 4.6(a) black dots). The difference (Fig. 4.6(a) blue dots) yields the loose spin contribution. The loose spin magnetization in the units of  $\text{J T}^{-1} \text{m}^{-3}$  (Fig. 4.6(b)) is fitted by the Brillouin function (Eq. 4.3) with the saturation magnetization ( $M_{\text{loose}}$ ) as the fit parameter. The blue line in Fig. 4.6(b) represents the best fit minimizing the root-mean-square deviation. The extracted  $M_{\text{loose}}$  is equal to  $86 \text{ kJ T}^{-1} \text{m}^{-3}$ . This value corresponds to a loose spin concentration of 6 % in the 3 nm surface region probed in the TEY mode.

## 4.4 Conclusion

The perpendicular susceptibility of a  $\text{Mn}_2\text{Au}(001)$  thin film in high magnetic fields up to 8 T has been measured by XMCD spectroscopy at RT and 7 K.

From the RT data, the exchange coupling constant was determined to be  $(4J_1 + J_2)/2 =$

$(22 \pm 5)$  meV. This value is lower than the theoretically predicted one of 90 meV, but still in the same order of magnitude. The obtained orbital magnetic moment is surprisingly large reaching about 30 % of the spin magnetic moment. A model is proposed for explaining this phenomenon, which includes exchange coupling acting solely on the spin moments of the sublattices in combination with a weaker spin-orbit coupling aligning spin and orbital moments of one sublattice. The effect results in similar projections of the spin and the orbital moment on the applied field direction.

The susceptibility measured at low temperatures contains two contributions, namely from the antiferromagnetically coupled moments and loose moments located at defect sites. A combined analysis of the data obtained at different temperatures provided the concentration of loose spins in the near-surface region, which for the investigated films is 6 % of the total amount of Mn spins.



# 5 Investigation of antiferromagnetic properties of $\text{Mn}_2\text{Au}$ via a ferromagnetic tracer layer

## 5.1 Introduction

In this chapter, a ferromagnetic tracer layer is used to gain information on the AFM properties of  $\text{Mn}_2\text{Au}$  films. The changes of the ferromagnetic hysteresis in a  $\text{Mn}_2\text{Au}$ /ferromagnet heterostructure due to exchange bias are analyzed to infer the properties of the AFM layer. The term exchange bias refers to an interface coupling between an AFM and a FM layer, where the Néel vector in the AFM is pre-oriented by cooling from above  $T_N$  in an external field or by growing the AFM on a FM layer in magnetic saturation [139]. The orientation of the AFM layer causes an additional effective field, the exchange bias field ( $H_{EB}$ ), that shifts the hysteresis loop of the ferromagnetic layer (see Section 2.7). Thus, the investigation of exchange bias can provide information about the interface properties. These include fixed and rotatable moments at the interface [87; 140] and magnetic anisotropy of the AFM [141].

Several studies were performed for imaging the domains in AFM/FM bilayers by the combination of XMLD-PEEM and XMCD-PEEM [24; 25]. It was found that an AFM underlayer strongly affects the FM domain pattern via interfacial exchange coupling. The shape of the resulting FM domains repeats the AFM domain pattern of the AFM layer.

In case of bulk  $\text{Mn}_2\text{Au}$ , direct alignment by field cooling is not possible because of the high  $T_N \sim 1500\text{ K}$  [55] since the material becomes structurally unstable below the  $T_N$  [142]. Nevertheless, Wu et al. measured an exchange bias induced by  $\text{Mn}_2\text{Au}$  in a Fe/ $\text{Mn}_2\text{Au}$  heterostructure grown on an MgO(001) substrate by molecular beam epitaxy (MBE) [143]. The  $\text{Mn}_2\text{Au}$  layer had a thickness of 10 nm, and the Fe layer was wedge-shaped with the thickness varying from 3 nm to 10 nm. This allowed investigating the dependence of exchange bias on the FM layer thickness. The samples were annealed in a field of 5 T at 380 K, which is much lower than the bulk material  $T_N$ , and subsequently cooled to cryogenic temperatures. After this procedure, a significant exchange bias was observed reaching 300 Oe for a 3 nm thick Fe layer at 5 K.

The aim of this chapter is to use a ferromagnetic layer as a tracer layer to detect the manipulation of the AFM Néel vector. It presents a systematic investigation of the magnetic properties of  $\text{Mn}_2\text{Au}$ /ferromagnet heterostructures. Section 5.2 contains the description of the sample preparation method and of the experimental setups used for field cooling, measuring the hysteresis loops, and imaging the domains. Section 5.3 shows the structural and magnetic characterization of the epitaxial  $\text{Mn}_2\text{Au}$ /Fe heterostructures. Subsection 5.3.1 reports the results obtained for

the high-quality epitaxial  $\text{Mn}_2\text{Au}$  layers deposited at the optimized growth conditions. Since no exchange bias was achieved in these films, we decided to prepare films with smaller grain sizes for decreasing the  $T_N$  (Subsection 5.3.2). The model employed for extracting the exchange coupling parameter and the fraction of fixed magnetic moments at the interface from the measured hysteresis loops is presented in Subsection 5.3.3. Subsection 5.3.4 introduces the results of fitting the experimental data. Section 5.4 describes the hysteresis loops measured for the sample having the reversed stacking sequence, i.e.  $\text{Mn}_2\text{Au}$  deposited on a *in-situ* magnetized Fe layer. The FM domain structure in the  $\text{Mn}_2\text{Au}/\text{Fe}$  heterostructures visualized by Kerr microscopy and by XMCD-PEEM are presented in Subsection 5.5.1 and Subsection 5.5.2 of Section 5.5, respectively.

## 5.2 Experimental details

The samples discussed in this chapter are grown by radio frequency magnetron sputtering. All samples are deposited at  $\text{Al}_2\text{O}_3(1\bar{1}02)$  substrates and have the layer sequence  $\text{Al}_2\text{O}_3/\text{Ta}(001)/\text{Mn}_2\text{Au}(001)/\text{Fe}(001)/\text{capping}$  or  $\text{Al}_2\text{O}_3/\text{Ta}(001)/\text{Mn}_2\text{Au}(001)/\text{Py}/\text{capping}$ . The in-plane epitaxial relation determined by XRD is  $\text{Ta}(001)[100] \parallel \text{Mn}_2\text{Au}(001)[100]$ . Additionally, orientation of the Fe layer with respect to the  $\text{Mn}_2\text{Au}$  layer is given by  $\text{Mn}_2\text{Au}(001)[100] \parallel \text{Fe}(001)[100]$ . The base pressure before deposition in the vacuum chamber was  $\sim 10^{-8}$  mbar. An epitaxial Ta buffer layer supported the epitaxial growth of the  $\text{Mn}_2\text{Au}$  layer in (001) orientation. A stoichiometric target was used for depositing  $\text{Mn}_2\text{Au}$ . The substrate temperature ( $T_{sub}$ ) during  $\text{Mn}_2\text{Au}$  deposition was chosen between  $450^\circ\text{C}$  and  $600^\circ\text{C}$  [75]. The layer thicknesses were defined from the previously determined deposition rates. Either Ta or Al is used as the capping layer to prevent oxidation.

The MOKE measurements were performed with an in-house developed instrument. The setup is equipped with a red laser diode (Coherent) generating a wavelength of 635 nm and an electromagnet (GMW 3470). The polarization rotation induced upon reflection from a magnetic medium is proportional to the sample magnetization [144; 145]. The implemented scheme for detecting the rotation based on Faraday modulator is described in Ref. [146]. A lock-in detector SR7225 and a pre-amplifier provided AC voltage for polarization modulation and DC voltage for compensating the Kerr rotation to the Faraday coil. The polarization after passing the Faraday coil was detected using a ThorLabs analyzer and a photodiode. The DC voltage dependence on the magnetic field was measured during the experiment. The samples were mounted either on a rotational stage, which allowed performing azimuthal scans at RT or on the copper cold finger of an Oxford cryostat placed between the pole shoes of the magnet for low-temperature investigations. During the measurements, the cryostat volume was pumped to  $10^{-7}$  mbar providing stable operation in the temperature range from 10 K to 450 K.

A separate vacuum heating stage equipped with a permanent magnet providing 0.2 T was used



for field cooling in the temperature range from 300 K to 500 K. The pressure in the vacuum chamber of the stage during the whole heating/cooling cycle did not exceed  $10^{-6}$  mbar. A Pt100 resistance thermometer was mounted on the copper sample holder for monitoring the temperature.

The Kerr microscopy measurements were performed using a Carl Zeiss Axio Imager.D2m equipped with a CCD camera Hamamatsu ORGA03G. The sample stage equipped with an electromagnet provides  $\pm 2000$  Oe. An array of light emitting diodes (LEDs) is used as a light source, which allows choosing between the longitudinal, transversal, and polar MOKE modes. The measurements presented here were performed in the longitudinal mode sensitive to the in-plane magnetization component [147]. Subtracting the background image taken at saturation field compensated for the surface morphology contribution. The utilized objective and the microscope settings provided a spatial resolution of 520 nm. The hysteresis loop was measured by taking a series of images at different magnetic fields from 1700 Oe to -1700 Oe and then from -1700 Oe to 1700 Oe with a step of 50 Oe.

The X-PEEM study was conducted at the SPEEM end station installed at beamline UE49\_PGM at the storage ring BESSY II (HZB, Berlin). The instrument provides a spatial resolution in the sub-100 nm range. The X-ray beam had a bandwidth of 0.4 eV during the measurement. A magnetic field of 250 Oe could be applied to a sample in the vacuum chamber between the measurement. An Ar-ion gun installed in the instrument allows sputtering materials from the sample surface for reaching buried layers. The X-ray beam incidence angle is kept constant during the experiment at  $16^\circ$  with respect to the sample surface. The XAS is measured prior to imaging the domains for determining the energies corresponding to the absorption edges. For that purpose, a series of images are acquired for a range of energies close to the  $L_3$  and  $L_2$  edges of the investigated material. The absorption is calculated as the integral of gray-scale levels over a region of interest. During the spectromicroscopy measurements, the photon energy is set at the  $L_3$  edge of the investigated material ( $E_{L_3}$ ) for achieving the maximal XMCD effect (see Subsection 3.2.1). For compensating a time-dependent drift, each measurement consists of three series. Firstly, 20 images are taken at circular right polarization ( $\sigma+$ ) followed by 40 images at circular left polarization ( $\sigma-$ ) and 20 more images at  $\sigma+$ . Afterward, the first and the third series are combined giving two sets for  $\sigma+$  and  $\sigma-$  with 40 images each. Ferromagnetic contrast is obtained as the asymmetry of the averaged images corresponding to  $\sigma+$  and  $\sigma-$ :

$$I_{XMCD} = \frac{I_{\sigma+}(E_{L_3}) - I_{\sigma-}(E_{L_3})}{I_{\sigma+}(E_{L_3}) + I_{\sigma-}(E_{L_3})} \quad (5.1)$$

## 5.3 Exchange bias in epitaxial $\text{Mn}_2\text{Au}/\text{Fe}$ heterostructures

### 5.3.1 Investigation of high-quality $\text{Mn}_2\text{Au}/\text{Fe}$ films

The first investigated sample *MA2* prepared at the optimal conditions for achieving a good crystal structure has the following stacking sequence:  $\text{Al}_2\text{O}_3/\text{Ta}$  18 nm/ $\text{Mn}_2\text{Au}$  @600°C 4 nm/ $\text{Fe}$  3 nm/ $\text{Ta}$  3 nm.

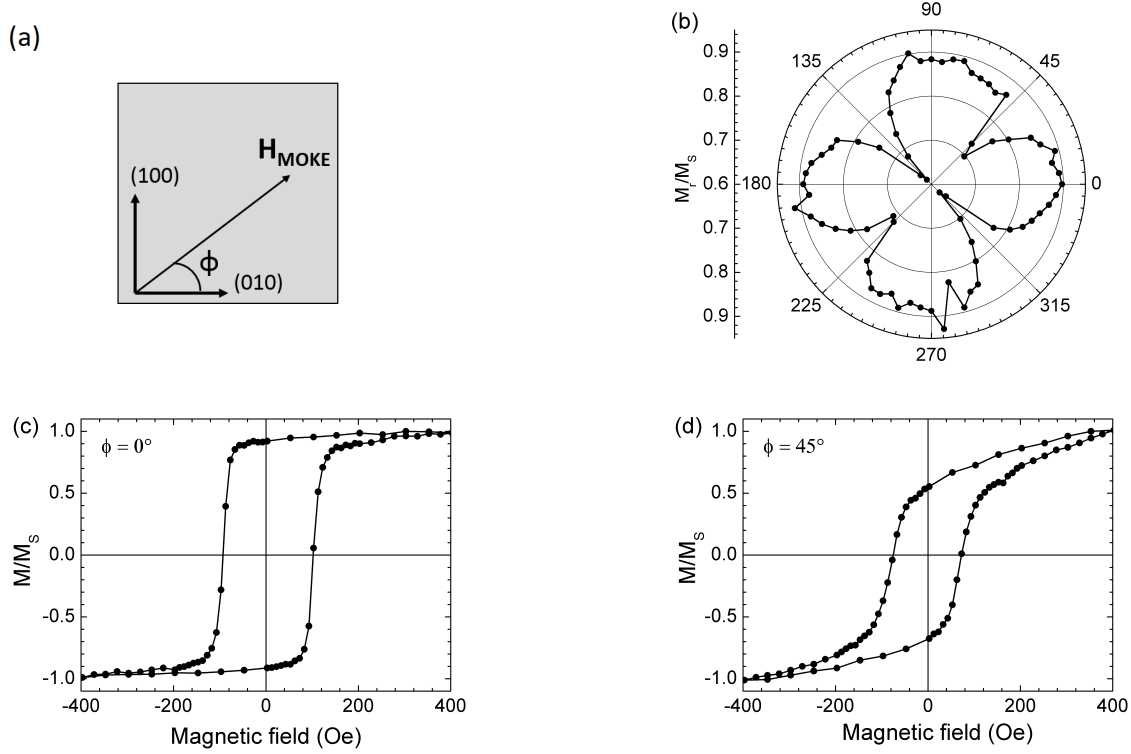


**Figure 5.1:** (a) Sketch of the experimental geometry.  $H_{MOKE}$  indicates the direction of the magnetic field and the plane of incidence during the MOKE measurements. (b) Angular dependence of remanence normalized to the saturation value for sample *MA2*. Examples of hysteresis loops at (c)  $\phi = 0^\circ$  and (d)  $\phi = 45^\circ$ .

The anisotropy of the Fe layer was characterized by measuring the hysteresis loops at different azimuthal orientations of the sample. The angular dependence of the residual magnetization ( $M_r$ ) reveals a four-fold magnetocrystalline anisotropy of the Fe layer grown on the epitaxial  $\text{Mn}_2\text{Au}$  film (Fig. 5.1(b)), where large and small values of  $M_r$  correspond to the easy and the hard magnetic axes of the ferromagnet, respectively. Therefore, the Fe  $\langle 100 \rangle$  easy-axes are rotated by  $45^\circ$  with respect to the  $\langle 110 \rangle$  easy-axes of bulk  $\text{Mn}_2\text{Au}$  [56]. The coercive field is found to be  $\sim 100$  Oe (Figs. 5.1(c) and 5.1(d)), which is one order of magnitude larger than in an epitaxial Fe film grown on a  $\text{MgO}(100)$  substrate [148]. This broadening is attributed to an exchange coupling between  $\text{Mn}_2\text{Au}$  and Fe (Section 2.7). The measured hysteresis loops are symmetric with respect to  $H = 0$ , indicating the absence of exchange bias in the as-prepared sample.

As mentioned above, an exchange bias in an AFM/FM heterostructure can be induced by field cooling (FC) through the  $T_N$ . Accordingly, the sample was cooled in the cryostat from 400 K to 10 K in a field of  $H_{FC} = 2000$  Oe. The field during FC was applied along the [100] crystallographic axis. The sample treatment protocol included annealing at 400 K in the magnetic field for 30 min before cooling. Please note that the applied field is much smaller than the spin-flop field of  $\text{Mn}_2\text{Au}$  and cannot directly influence the AFM Néel vector [55].

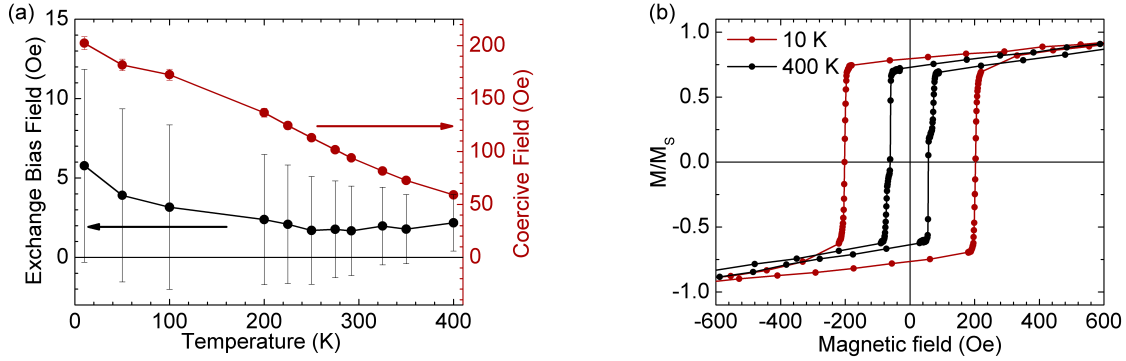


**Figure 5.2:** (a) The temperature dependence of the exchange bias and coercive field of sample *MA2* after field cooling from 400 K in a saturating magnetic field. (b) The corresponding hysteresis loops measured at 10 K and 400 K. Lines through the data points in (a) and (b) are for visual aid.

The temperature-dependent hysteresis loops were measured while heating the sample. The coercive field decreases with increasing temperature and becomes  $H_C = 50$  Oe at 400 K (Fig. 5.2(a)), which is still larger than the coercivity of an Fe layer grown on a paramagnetic substrate [148]. Since a loop broadening originates from AFM coupled rotatable spins at the interface (see Section 2.7), the  $\text{Mn}_2\text{Au}$  layer is in the AFM state in the investigated temperature region. This indicates that  $T_N$  is higher than 400 K. The determined  $H_{EB}$  is equal zero within error margins (Fig. 5.2(a)).

The external heating stage was used for achieving higher temperatures with the aim of exceeding  $T_N$ . Field cooling was performed in two steps. Firstly, sample *MA2* was cooled from 500 K to RT in a saturating magnetic field of 2000 Oe in the heating stage. Then the sample was transferred to the cryostat and cooled further to 10 K while applying a field of the same magnitude. The determined coercivity and the exchange bias are plotted in Fig. 5.3. For estimating  $T_N$ , the assumption is made that the coercivity is proportional to the AFM order parameter  $H_C \propto L$  and approaches zero at  $T_N$  because of a small intrinsic coercivity of an uncoupled epitaxial Fe film. Accordingly, the temperature-dependent coercivity data are fitted by Eq. (2.17) in Section 2.3 with  $\beta = 1/2$ :

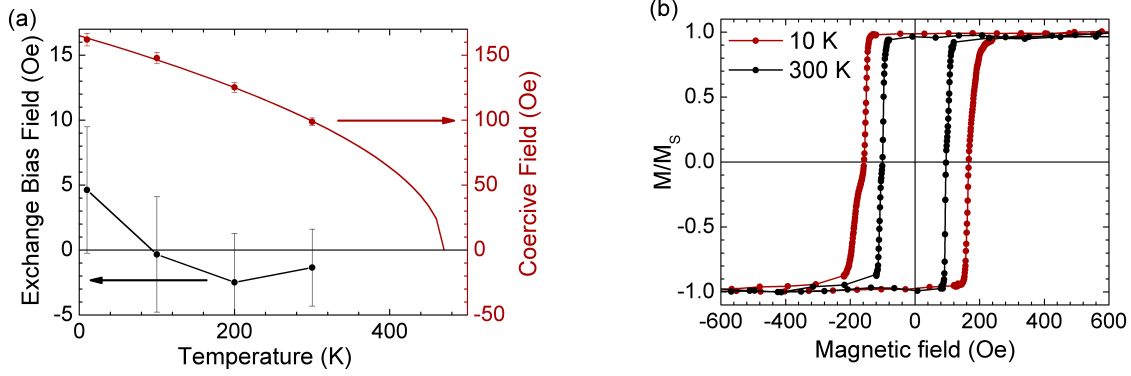


**Figure 5.3:** (a) The temperature dependence of the exchange bias and coercive field of sample *MA2* after field cooling from 500 K in a saturating magnetic field (see text for details). Red curve corresponds to the best fit of the experimental data by Eq. (5.2). The black lines are guides to the eye. (b) The corresponding hysteresis loops measured at 10 K and 300 K. Lines through the data points are guides to the eye.

$$H_C(T) = H_C(0) \sqrt{1 - \frac{T}{T_N}} \quad (5.2)$$

depending on two parameters  $H_C(0)$  and  $T_N$ . The best fit is shown by the red line in Fig. 5.3(a). The fit parameters are  $H_C(0) = 165$  Oe and  $T_N = 470$  K, which is smaller than the maximal temperature of 500 K reached during the field cooling. On the other hand, no significant exchange bias is observed, which can be explained by a too weak anisotropy of the AFM layer that fails to stabilize the interface moments.

In an attempt to increase the anisotropy, a thicker  $\text{Mn}_2\text{Au}$  sample *MA3* was prepared with the stacking sequence  $\text{Al}_2\text{O}_3/\text{Ta}$  18 nm/ $\text{Mn}_2\text{Au}$  @600 °C 7 nm/ $\text{Fe}$  3 nm/ $\text{Ta}$  3 nm. The same field cooling and measurement protocol utilizing the heating stage and the cryostat were applied as described above.

The  $H_C$  for sample *MA3* is larger than that for sample *MA2* (Fig. 5.4(a)). The best fit by Eq. (5.2) is shown by the red line in Fig. 5.4(a) corresponds to  $H_C(0) = 235$  Oe and  $T_N = 550$  K. The exchange bias is again equal to zero within the error bars. Most likely, the absence of exchange bias is caused by the fact that  $T_N$  was not reached before field cooling.

Heating of the  $\text{Mn}_2\text{Au}/\text{Fe}$  heterostructures above 500 K leads to interdiffusion of the atoms at the interface, which is evidenced by non-reversible changes of a  $\text{Mn}_2\text{Au}/\text{Fe}$  sample resistance introduced after overcoming this temperature. Accordingly, field cooling from above 500 K was not performed to avoid deterioration of the interface. An interesting question is why a considerable exchange bias effect has been observed before for similar  $\text{Fe}/\text{Mn}_2\text{Au}$  layers in Ref. [143]. The RHEED XRD data provided in the article indicate a considerable disorder at the interface and a substantial proportion of admixture phases in  $\text{Mn}_2\text{Au}$ . This fact suggests that

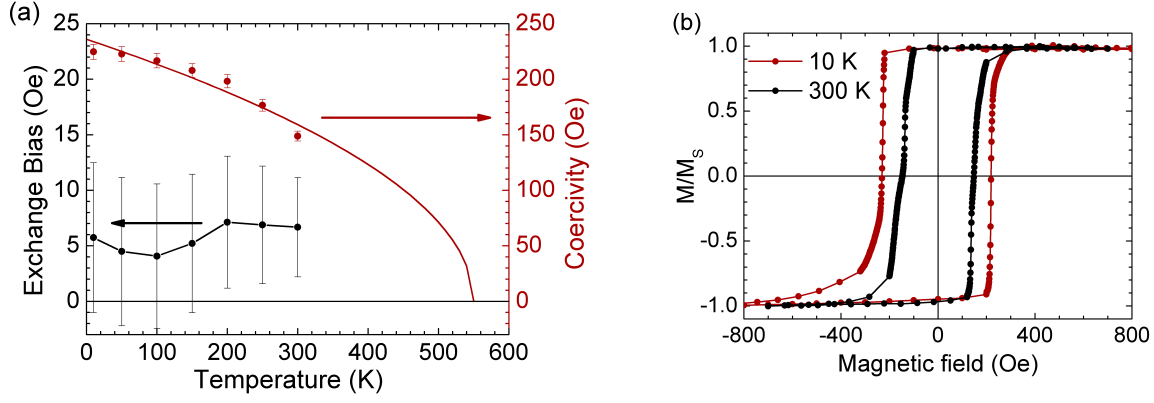


**Figure 5.4:** (a) The temperature dependence of the exchange bias and coercive field of sample *MA3* after field cooling from 500 K in a saturating magnetic field (see text for details). Red curve corresponds to the best fit of the experimental data by Eq. (5.2). The black lines are guides to the eye. (b) The corresponding hysteresis loops measured at 10 K and 300 K. Lines through the data points are guides to the eye.

the observed exchange bias can originate from uncompensated moments at the interface and does not reflect the intrinsic magnetic order within  $\text{Mn}_2\text{Au}$  [149].

In summary, the anisotropy of a  $\text{Mn}_2\text{Au}$  film with a thickness  $\lesssim 7$  nm is too small for sustaining an exchange bias and thicker films have a  $T_N > 500$  K. A proper field cooling process of a thick  $\text{Mn}_2\text{Au}$  films requires a temperature exceeding 500 K, which introduces defects at the interface between the  $\text{Mn}_2\text{Au}$  and a FM layer.

### 5.3.2 Dependence of the exchange bias field on the $\text{Mn}_2\text{Au}$ grain size

This subsection addresses the issue of decreasing the  $T_N$  by tailoring the crystallite size of the epitaxial film for achieving a sizable exchange bias effect. The Néel temperature of a polycrystalline AFM depends on the grain size [150], which can be reduced by lowering the substrate temperature during deposition. In order to investigate the exchange bias dependence on the grain size, two samples, *MA4* and *MA5*, were prepared at purposely non-optimal growth conditions. Both samples have the same structure  $\text{Al}_2\text{O}_3/\text{Ta}$  18 nm/ $\text{Mn}_2\text{Au}$  @( $T_{sub}$  °C) 10 nm/ $\text{Fe}$  3 nm/ $\text{Ta}$  3 nm, where  $T_{sub}$  is 500 °C and 450 °C for samples *MA4* and *MA5*, respectively.

The crystal structure of the films was investigated by XRD. The experimental peak positions in the  $\theta$ - $2\theta$  scans in Fig. 5.5 are close to the theoretical values with the lattice parameters from [136]. The majority of the  $\text{Mn}_2\text{Au}$  crystallites have (001)-orientation with the proportion of (101)-phase increasing at lower  $T_{sub}$ . In order to extract the grain size, the peaks in the  $\theta$ - $2\theta$  spectra were fitted by Lorentzian functions and the corresponding rocking curves by Gaussian functions (Table 5.1). The Scherrer equation was used for calculating the average crystallite size [151]. The size of the (001) crystallites is reduced for the sample deposited at a lower tempera-

ture. At the same time, the size of the (101) crystallites increases. For the further analysis, only the (001) crystallites are assumed to provide an exchange bias due in-plane magnetic moments at the surface, in contrast to the (101) crystallites with predominantly out-of-plane moment direction. Therefore, sample *MA5* has smaller exchange bias-creating crystallites than sample *MA4*.

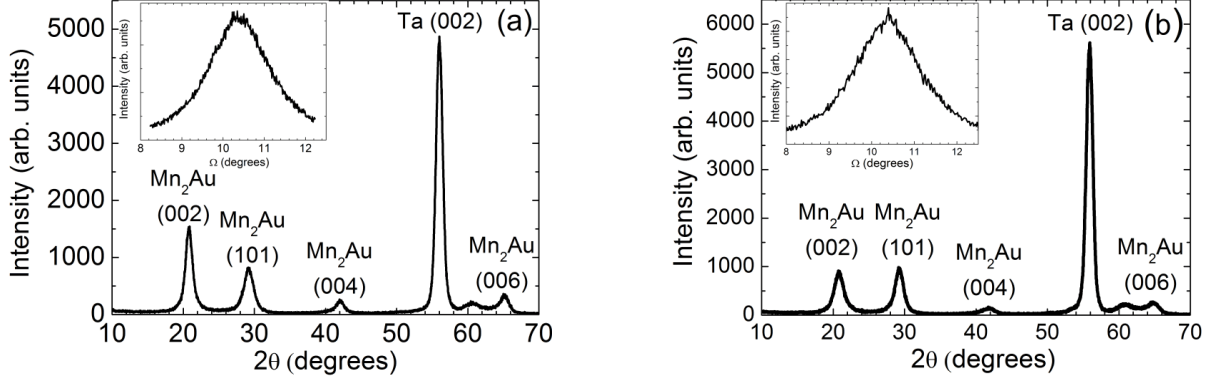


**Figure 5.5:** (a)  $\theta - 2\theta$  spectrum measured for sample *MA4* grown at  $500^\circ\text{C}$ . (b) The same for sample *MA5* deposited at  $450^\circ\text{C}$ . The insets in (a) and (b) show the rocking curves obtained at  $2\theta$  corresponding to (002)-peak of  $\text{Mn}_2\text{Au}$ .

Sample	The size of (001) crystallites (nm)	The size of (101) crystallites (nm)	Rocking curve width (degrees)
MA4 ( $500^\circ\text{C}$ )	8.4(1)	6.1(1)	0.68(1)
MA5 ( $450^\circ\text{C}$ )	6.4(1)	7.3(1)	0.77(1)

**Table 5.1:** The grain size and the rocking curve width for samples *MA4* and *MA5*. The values in parentheses indicate the fit errors.

Both samples were field cooled from 500 K to RT in a saturating magnetic field of 2000 Oe. The  $H_{FC}$  was applied along the [100] crystallographic axis. The angle-dependent MOKE measurements conducted for sample *MA5* at RT show a dominating two-fold anisotropy that may be induced by an interfacial exchange coupling. In order to prove that the two-fold anisotropy is induced by field cooling, the experiment was repeated for  $H_{FC}$  directed along the [010] axis (Fig. 5.7). The subsequently measured hysteresis loops exhibit the easy and hard axis behavior for opposite angles compared to the results shown in Figure 5.6. In fact, no shift of the hysteresis loops could be detected at RT in either case.

Temperature-dependent MOKE measurements were performed for both samples after further FC in the Oxford cryostat from RT to 20 K in a field of 2000 Oe (Figs. 5.8 and 5.9). A significant exchange bias was observed for reaching 140 Oe and 210 Oe at 20 K in samples *MA4* and *MA5*,

respectively. The presence of an exchange bias indicates that the  $T_N$  of both samples is smaller than 500 K. The coercivity of the polycrystalline Fe films in these samples is unknown for the absence of exchange coupling and can significantly exceed that of an epitaxial layer [148]. Therefore, estimation of the  $T_N$  including the fitting by Eq. (5.2) as presented in Figs. 5.3 and 5.4 cannot be implemented here.

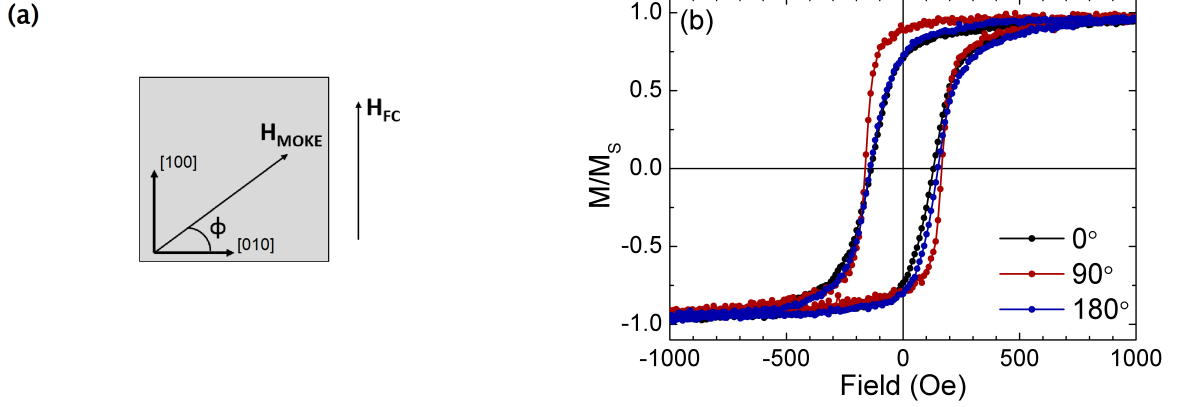


**Figure 5.6:** (a) The experimental geometry indicating the field direction during field cooling ( $H_{FC}$ ). (b) The hysteresis loops measured in sample *MA5* at different  $\phi$  values.

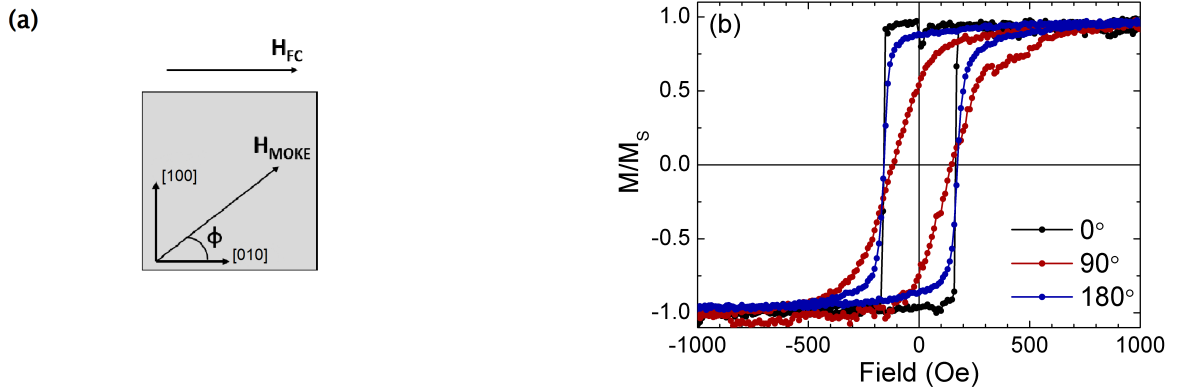


**Figure 5.7:** (a) The experimental geometry indicating the field direction during field cooling ( $H_{FC}$ ). (b) The hysteresis loops measured in sample *MA4* at different  $\phi$  values.

The blocking temperature ( $T_B$ ) characterizes the interface energy ( $E_{int}$ ) of an AFM/FM heterostructure, which determines the exchange coupling. At high temperatures the thermal energy reduces the interface energy according to  $E_{int}(T) = E_{int}(0) - k_B T_B$  [152], and the exchange bias approaches zero at  $T_B$ . Obviously, the blocking temperature of an AFM cannot exceed Néel temperature  $T_B \leq T_N$ . The values of  $T_B$  obtained from Figs. 5.8(b) and 5.9(b) for samples *MA4* and *MA5* are 250 K and 200 K, respectively.

The remagnetization mechanism determines the shape of the hysteresis loop. An abrupt tran-

sitional region of the descending branch (negative fields) of the 20 K-loop in Figure 5.9(a) indicates remagnetization via the domain wall formation and propagation. A smoother change of the magnetization at the ascending branch (positive fields) implies remagnetization via (partial) coherent moment-rotation. The same behavior, however less pronounced, is also observed at low temperatures for sample *MA4* (Fig. 5.8(a)).

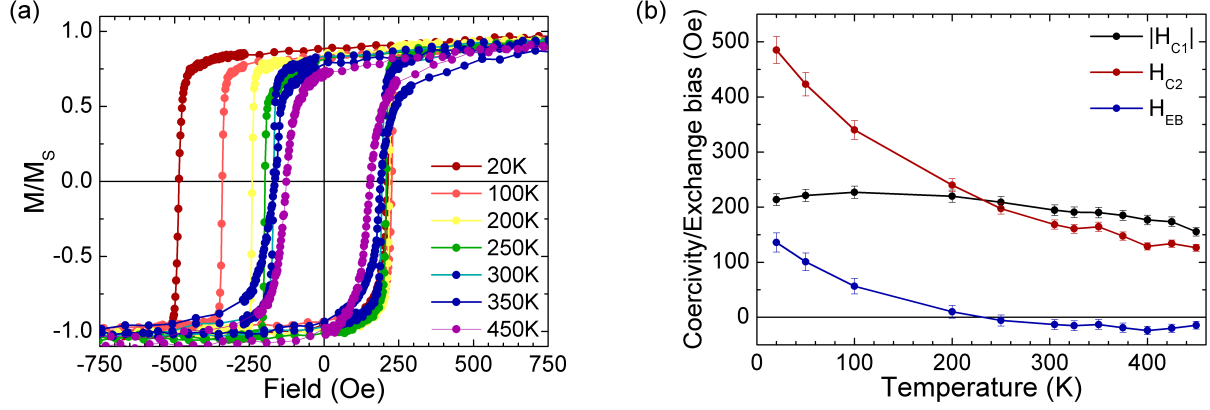


**Figure 5.8:** (a) The temperature-dependent hysteresis loops measured for sample *MA4* after FC. (b) Coercivities and exchange bias fields extracted from the loops in (a).

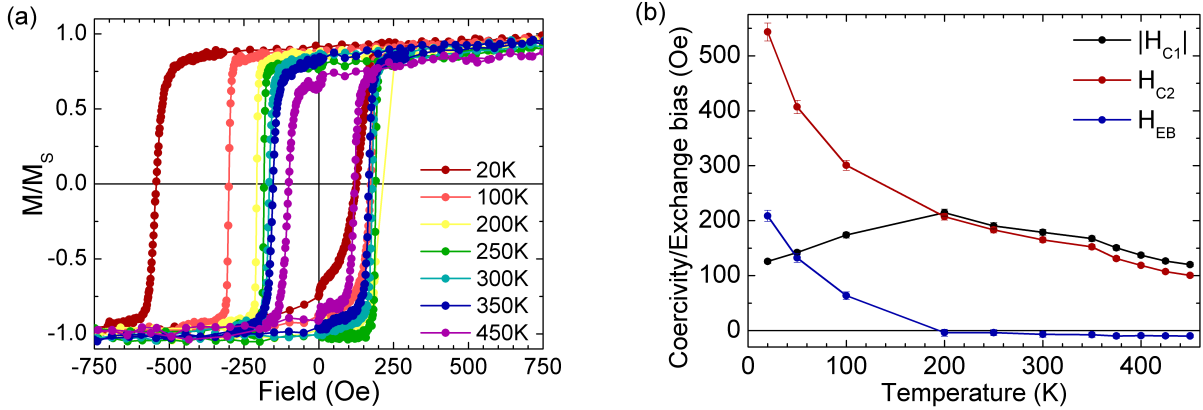


**Figure 5.9:** (a) The temperature-dependent hysteresis loops measured for sample *MA5* after FC. (b) Coercivities and exchange bias fields extracted from the loops in panel (a).

Summarizing the presented results, a significant exchange bias in a  $Mn_2Au/Fe$  heterostructure can be achieved for a higher degree of disorder in the  $Mn_2Au$  film via lowering the growth temperature. In order to get a deeper insight into the exchange bias mechanism in non-perfect  $Mn_2Au$  layers, the experimentally obtained hysteresis loops were simulated using the spin glass model. The results are presented in the next section.



### 5.3.3 Spin glass theory of coupled antiferromagnet/ferromagnet heterostructures

The spin glass model accounts for important features observed in the experimental loops such as 1) the shift of the loop, caused by fixed interfacial AFM spins, 2) the increase of  $H_C$  originating from rotatable interfacial AFM spins, and 3) an asymmetric shape of the hysteresis loops due to different remagnetization mechanisms at  $H_{C1}$  and  $H_{C2}$  [153].

The model is based on the Stoner-Wolfarth macrospin approach [154] with the additional assumption that the interface contains a layer of low anisotropy spins having a thickness of  $t_{SD}$  and magnetization  $M_{SD}$ . The coupling strength between the FM and the interfacial spins is characterized by exchange constant  $J$ . A certain fraction  $f$  of the interfacial spins is assumed to be fixed and  $(1-f)$  to be rotatable. This leads to an additional uniaxial anisotropy with the coefficient  $K_{SD}^{eff} = J(1-f)$  and an unidirectional anisotropy characterized by  $J_{SD}^{eff} = Jf$ . Please note that both parameters,  $K_{SD}^{eff}$  and  $J_{SD}^{eff}$ , describe the interface effects and have dimensions of  $[J\text{ m}^{-2}]$ . The total energy functional within the spin glass model has the form:

$$\begin{aligned}
E = & -\mu_0 H M_{FM} t_{FM} \cos(\theta - \beta) + K_{FM} t_{FM} \sin^2(\beta) \cos^2(\beta) + \\
& + K_{AFM} t_{AFM} \sin^2(\alpha + \pi/4) \cos^2(\alpha + \pi/4) - \mu_0 H M_{SD} t_{SD} \cos(\theta - \beta) + \\
& + K_{SD}^{eff} \sin^2(\beta - \gamma) - J_{SD}^{eff} \sin(\beta - \alpha), \quad (5.3)
\end{aligned}$$

where angles  $\alpha$ ,  $\beta$ , and  $\theta$  correspond to the orientation of AFM moments, FM moments, and magnetic field respectively.  $t_{FM}$  and  $t_{AFM}$  are the thicknesses of the FM and AFM layers. The first term in Eq. (5.3) is the Zeeman energy depending on the magnetization of the FM layer. The second and the third terms represent the four-fold in-plane anisotropy of Fe and  $\text{Mn}_2\text{Au}$  characterized by the constants  $K_{FM}$  and  $K_{AFM}$ , respectively. The additional factor  $\pi/4$  accounts for the different easy directions of Fe and  $\text{Mn}_2\text{Au}$ . The last three terms are related to the spin glass at the interface and represent the Zeeman energy and the additional anisotropies discussed above.

In the following, the  $\text{Mn}_2\text{Au}$  anisotropy is considered to be larger than the Fe anisotropy. This allows neglecting the second term in Eq. 5.3. The fourth term in Eq. (5.3) is omitted since  $t_{SD}$  is usually much smaller than  $t_{FM}$  [153]. Accordingly, one obtains the condition for the energy minimum:

$$\begin{aligned}
\frac{\partial E}{\partial \alpha} &= K_{AFM} t_{AFM} \sin(2\alpha) - J_{SD}^{eff} \cos(\beta - \alpha) = 0, \\
\frac{\partial E}{\partial \beta} &= -\mu_0 H M_{FM} \sin(\theta - \beta) + K_{SD}^{eff} \sin(2\beta - \gamma) - J_{SD}^{eff} \cos(\beta - \alpha) = 0.
\end{aligned} \quad (5.4)$$

### 5.3.4 Fitting of experimental data using theoretical models

The temperature-dependent hysteresis loops measured in samples *MA4* and *MA5* were simulated according to Eq. (5.4) with  $J$  and  $f$  left as the fitting parameters. Angle  $\gamma = \pi/9$  was chosen for all calculations [153].

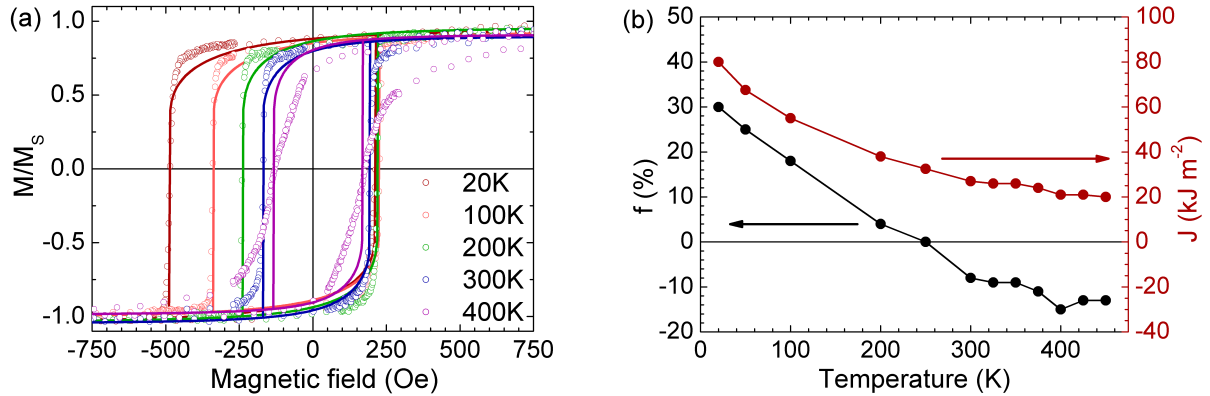


**Figure 5.10:** (a) Temperature-dependent hysteresis loops measured for sample *MA4* (circles) and corresponding simulated hysteresis loops (solid lines). (b) The coupling constant ( $J$ ) and the fraction of the rotatable interfacial spins ( $f$ ) corresponding to the best fit curves shown in (a).

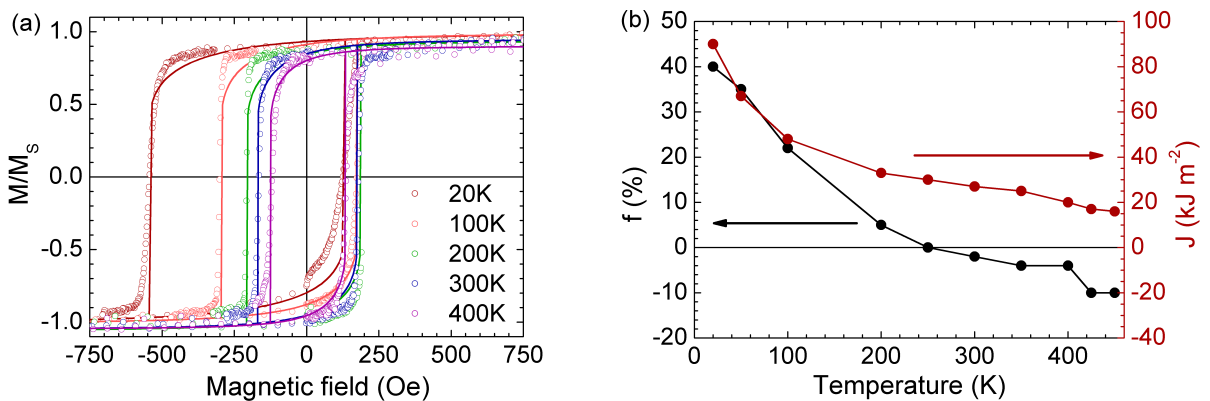


**Figure 5.11:** (a) Temperature-dependent hysteresis loops measured for sample *MA5* (circles) and corresponding simulated hysteresis loops (solid lines). (b) The coupling constant ( $J$ ) and the fraction of the rotatable interfacial spins ( $f$ ) corresponding to the best fit curves shown in (a).

The determined coupling parameters  $J$  are very close for both samples (Figs. 5.10(b) and 5.11(b)). Consequently, larger exchange bias values in sample *MA5* stem from a larger amount of fixed spins, which reaches 40 % at 10 K in comparison with 30 % for sample *MA4*. The value of  $f$  is reduced at higher temperatures and approaches zero at  $T_B$ . Negative values of  $f$  above  $T_B$  are caused by the offset of the measured hysteresis loops due to a systematic error (see blue curves

Figs. 5.8(b) and 5.9(b)). The model fails to properly describe the hysteresis loops for sample *MA4* at temperatures above 300 K (Fig. 5.10(a)). This is presumably caused by an increasing ratio of the FM and the AFM anisotropy constants  $K_{FM}/K_{AFM}$  at higher temperatures. In this case, the second term in Eq. (5.3) has to be taken into account.

## 5.4 Exchange bias induced by $Mn_2Au$ deposited on an Fe layer

An alternative to field cooling is the deposition of the AFM layer on a previously magnetized FM layer. In this case the Néel vector is oriented during the growth of the AFM layer as soon as  $T_N$  exceeds the growth temperature. The advantage is that a high temperature annealing step is not required.

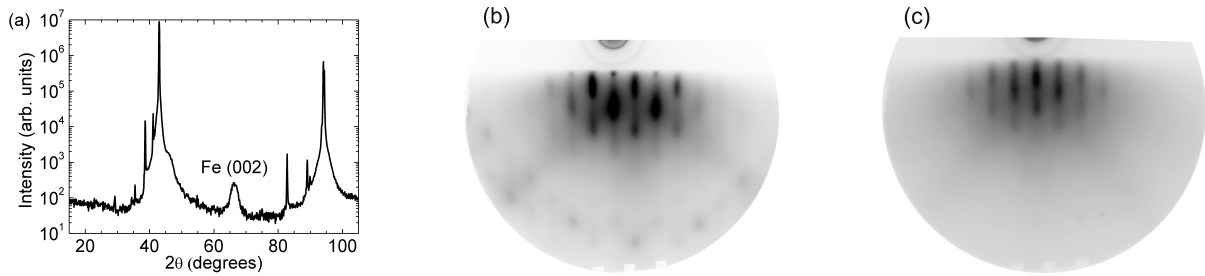


**Figure 5.12:** (a) XRD spectrum of sample *MA6*. (b,c) RHEED images measured *in-situ* after deposition of the Fe layer (b) and the  $Mn_2Au$  layer (c).

Sample *MA6* with the following structure MgO(001)/Fe(001) 5 nm/ $Mn_2Au$  @RT 10 nm/Ta 3 nm was used for investigating exchange bias induced by a ferromagnetic buffer layer. For this purpose, the Fe layer was magnetized *in-situ* by a permanent magnet before depositing  $Mn_2Au$ . The XRD analysis of the sample indicated no peaks corresponding to  $Mn_2Au$  (Fig. 5.12(a)). The presence of weak spots in the RHEED image of the  $Mn_2Au$  surface indicates a textured structure of the AFM layer (Fig. 5.12(c)).

The angle-dependent hysteresis loops of the as-prepared sample are presented in Figure 5.13. The loops are much more narrow than for Fe deposited on an epitaxial  $Mn_2Au$  and exhibit an anisotropic behavior featuring steps at  $H_C$ . These steps indicate a superposition of the Fe four-fold magnetocrystalline anisotropy and a uniaxial anisotropy originating from an exchange interaction at the interface [155]. Please note that the easy axis for the uniaxial anisotropy coincides with the Fe magnetization direction ( $\mathbf{M}_{FE}$ ), which means that the  $Mn_2Au$  moments are oriented by the underlying FM. No shift of the hysteresis curves is observed in Fig. 5.13(b). The low-temperature hysteresis loops measured after field cooling from RT in a magnetic field of 2000 Oe are significantly broadened and shifted in the direction opposite to the magnetic field applied during field cooling (Fig. 5.14(a)). In contrast to epitaxial  $Mn_2Au$  films, both  $H_{C1}$  and  $H_{C2}$  decrease uniformly with increasing temperature. The  $T_N$  of sample *MA6* is close to 300 K, which is evidenced by a vanishing width of the Fe hysteresis curve at this temperature. The

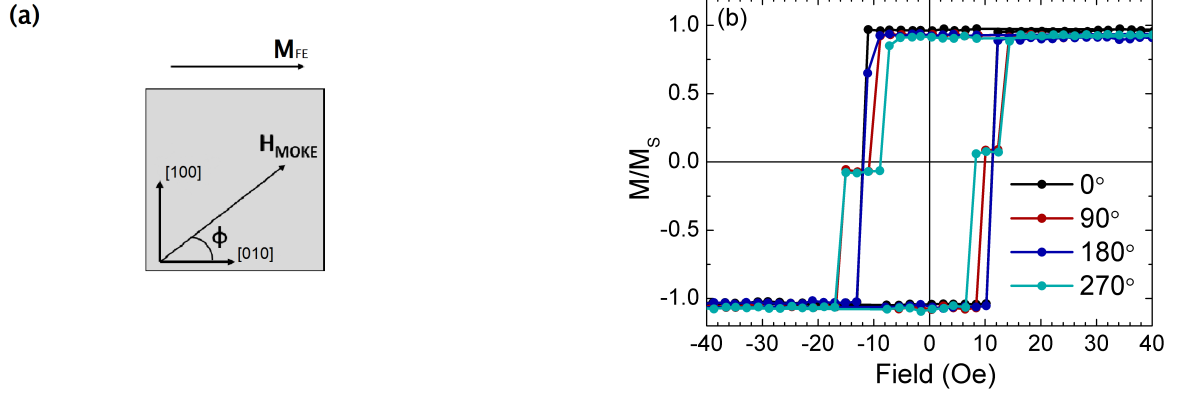


**Figure 5.13:** (a) The experimental geometry indicating the Fe magnetization direction during  $\text{Mn}_2\text{Au}$  deposition.  $H_{MOKE}$  denotes the direction of the magnetic field and the plane of incidence during the MOKE measurements. (b) The hysteresis loops measured for sample *MA6* at different  $\phi$  values.

absolute value of  $H_{EB}$  is significantly smaller than for samples *MA4* and *MA5*, which can be caused by a smaller fraction of the fixed spins at the interface.  $T_B$  of the textured  $\text{Mn}_2\text{Au}$  layer is estimated to be  $\sim 200$  K, which is comparable to the epitaxial  $\text{Mn}_2\text{Au}$  films.

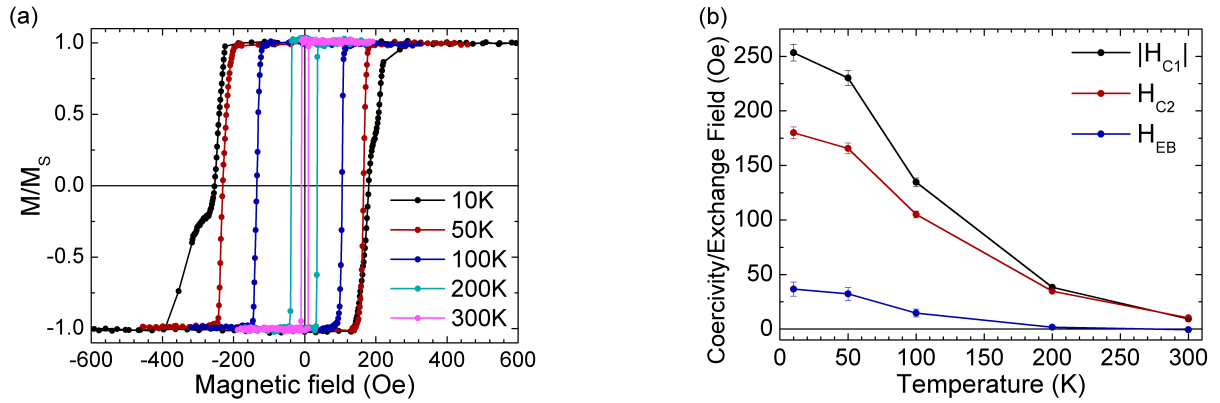


**Figure 5.14:** (a) The temperature-dependent hysteresis loops measured for sample *MA6* after FC. (b) Coercivities and exchange bias fields extracted from the loops in (a).

In summary, the reversed growth process indeed produces a sizable exchange bias indicating the antiferromagnetic order in the  $\text{Mn}_2\text{Au}$  film. However, the growth of  $\text{Mn}_2\text{Au}$  on the FM Fe layer causes a decreased quality of the crystal structure, resulting in a considerably reduced Néel temperature in comparison with the epitaxial  $\text{Mn}_2\text{Au}$  films.

## 5.5 Investigation of ferromagnetic domains in $\text{Mn}_2\text{Au}$ /ferromagnet heterostructures

In order to investigate the domain structure in an as-grown high quality  $\text{Mn}_2\text{Au}$  film, a ferromagnetic layer deposited on  $\text{Mn}_2\text{Au}$  was used as a tracer. The exchange coupling is expected to transfer the AFM domains on the FM, whose domain pattern is then visualized by Kerr microscopy (Subsection 5.5.1) and XMCD-PEEM (Subsection 5.5.2).

### 5.5.1 Kerr microscopy investigation of ferromagnetic domains in $\text{Mn}_2\text{Au}/\text{Py}$

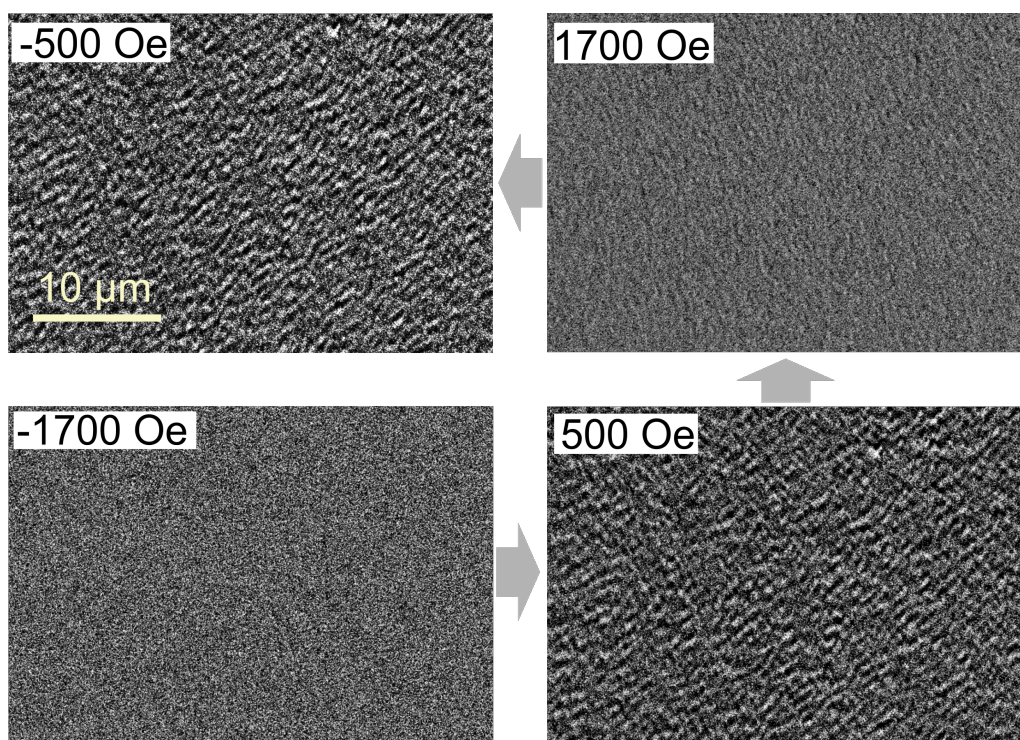


**Figure 5.15:** The Kerr microscopy images for sample *MA7* taken consecutively at the field values specified in the insets. The background image acquired at -1700 Oe was subtracted from each of the images.

Permalloy (Py) was chosen for this experiment since it forms a polycrystalline layer on  $\text{Mn}_2\text{Au}$  and has a negligible magnetocrystalline anisotropy. In this case, the FM domain distribution is supposed to be mainly determined by the AFM. Correspondingly, Py is a good tracer layer for studying the exchange coupling and the AFM domains. Sample *MA7* with a layer structure of  $\text{Al}_2\text{O}_3/\text{Ta}$  18 nm/ $\text{Mn}_2\text{Au}$  @600 °C 66 nm/Py 4 nm/Ta 3 nm was prepared for Kerr microscopy studies. The hysteresis loop measured using the Kerr microscope exhibits a significant broadening with a coercivity of  $\sim 500$  Oe, which is two orders of magnitude larger than the coercivity

of a Py thin film grown on a paramagnetic substrate [156]. This indicates a strong interfacial exchange coupling between  $\text{Mn}_2\text{Au}$  and Py.

Afterward, a series of images were taken while sweeping the in-plane field from a negative saturation value of -1700 Oe to the positive field of the same magnitude (Fig. 5.15). The background image taken at -1700 Oe is subtracted from the images in Fig. 5.15. The image taken at a positive coercivity of +500 Oe shows a pronounced domain contrast with fine domains. The domain size is at the limit of the instrumental resolution and cannot be determined from the image. At the positive saturation field (+1700 Oe), the image becomes homogeneously gray, proving the white/black contrast to be magnetic. After decreasing the external field to the negative coercivity, a similar domain pattern is obtained. Since the size of the observed domains is much smaller than in a Py layer not coupled to an AFM [157], the observed domain pattern is presumably caused by the AFM domains via exchange coupling.

### 5.5.2 XMCD-PEEM investigation of ferromagnetic domains in $\text{Mn}_2\text{Au}/\text{Fe}$

In order to obtain a better spatial resolution for analyzing the domain shape and size, XMCD-PEEM has been applied. The XMCD-PEEM experiments were performed with sample *MA8*, consisting of the following layers:  $\text{Al}_2\text{O}_3/\text{Ta}$  18 nm/ $\text{Mn}_2\text{Au}$  @600°C 60 nm/ $\text{Fe}$  10 nm /Al 5 nm. Fe is a preferable material for this experiment since it provides a higher XMCD asymmetry than Py. The Al capping layer was sputtered with the Ar gun prior to the measurements in order to enhance the contrast from the underlying FM layer. For sputtering, an acceleration voltage of 1.2 keV was used and the Ar pressure was set to  $2 \times 10^{-5}$  mbar. The sputtering time amounted to 15 min.

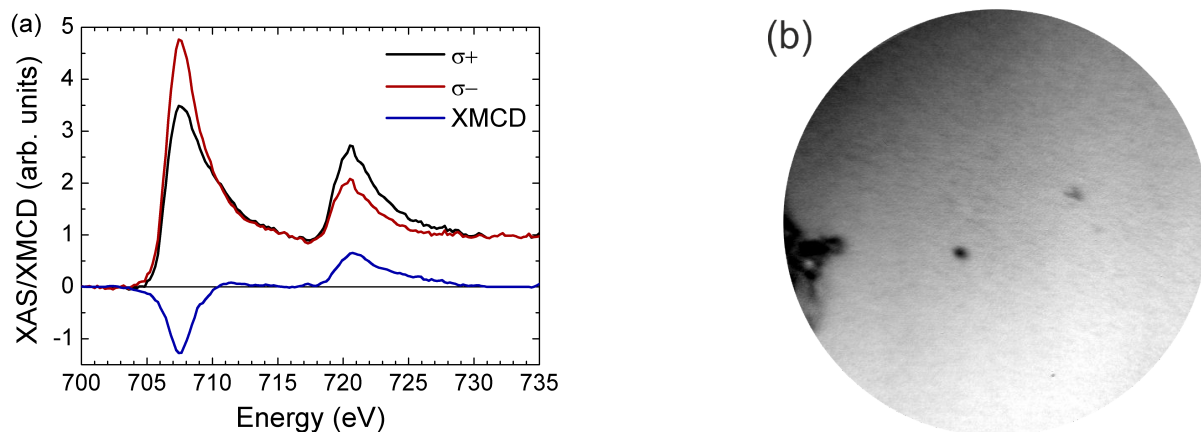


**Figure 5.16:** (a) The XAS and corresponding XMCD measured for sample *MA8*. (b) The element contrast obtained as the ratio of the images taken at the Fe  $L_3$  edge (707.5 eV) and pre-edge (700.0 eV). The black areas on the left and in the center of the image are due to structural defects used for alignment. The FOV is 15  $\mu\text{m}$ .

The XAS and XMCD spectrum of Fe measured after removing the capping layer are shown in

Fig. 5.16(a). The  $L_3$  and the  $L_2$  edges corresponds to the energies of 707.5 eV and 720.7 eV, respectively. The surface morphology and the Fe content in the near-surface region are revealed in ratio of the images taken at the  $L_3$  edge (707.5 eV) and a pre-edge (700.0 eV) shown in Figure 5.16(b). The homogeneous intensity over the whole image implies the capping layer to be uniformly sputtered.

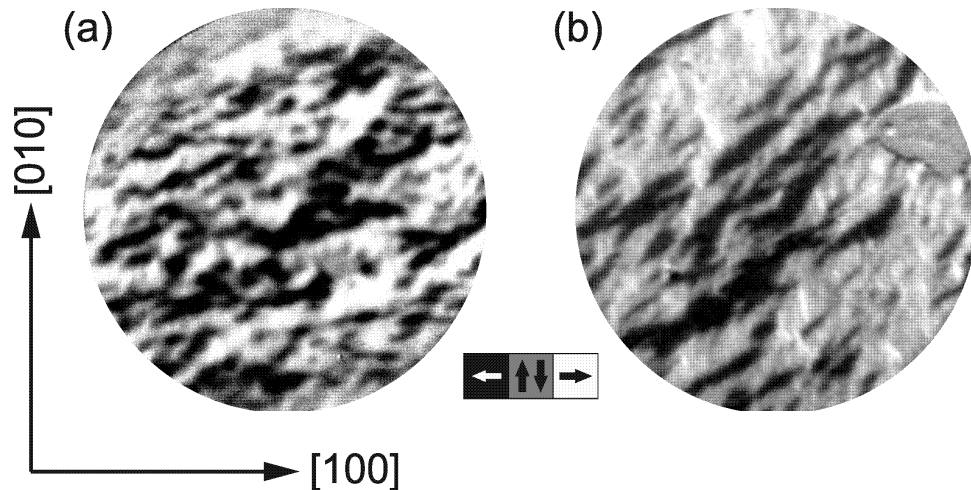


**Figure 5.17:** The asymmetry of the images taken at  $\sigma+$  and  $\sigma-$  in sample *MA8*. The FOV is (a) 25  $\mu\text{m}$  and (b) 10  $\mu\text{m}$ .

The images shown in Figure 5.17 represent the XMCD asymmetry for sample *MA8* indicating the FM contrast. The Fe domains have irregular shapes and are elongated in the [110] direction, which is the easy axis of  $\text{Mn}_2\text{Au}$ . The average size of the domains is  $\sim 1 \mu\text{m}$  being in line with the previously obtained Kerr microscopy data.

The maximal magnetic field available with the used sample holder was 250 Oe. However, it was possible to conduct the measurements only in 200 Oe field because of the photoelectron trajectories distortions caused by magnetic fields. In order to investigate the influence of moderate magnetic fields on the domain distribution, a field of 250 Oe (-250 Oe) was applied to the sample before the measurements and reduced to 200 Oe (-200 Oe) during the measurements. In both cases, the domain structure did not exhibit any visible changes (Fig. 5.18). This observation is in agreement with the large coercive field measured for  $\text{Mn}_2\text{Au}/\text{Fe}$  heterostructures.

Subsequently, an attempt was made to sputter the Fe layer and measure the AFM domains directly using the XMLD effect to compare them with their ferromagnetic counterpart. However, we were not able to obtain any magnetic contrast, most likely because of the deterioration of the sample surface caused by the sputtering process.

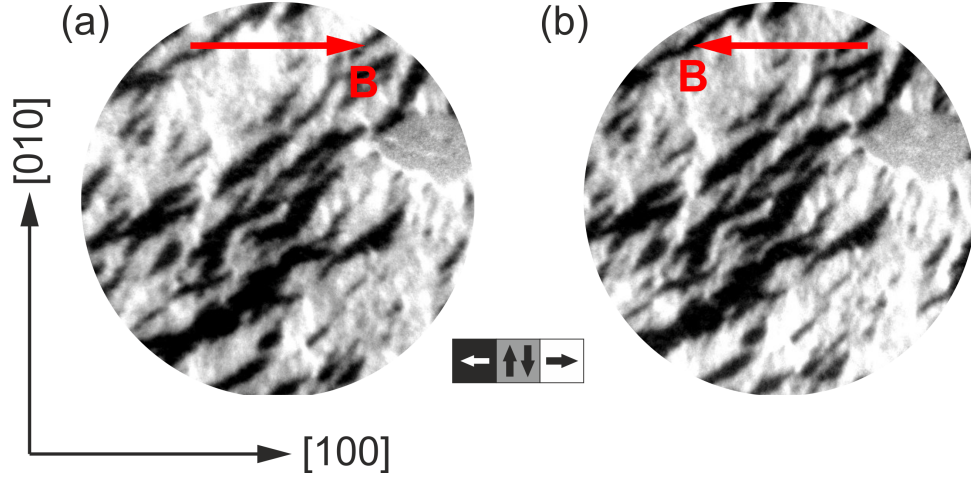


**Figure 5.18:** The ferromagnetic domain in sample *MA8* exposed to an external magnetic field. (a) a field of +250 Oe was applied to the sample prior to the measurement and the set of images was taken at a field of +200 Oe. (b) The negative field of the same amplitudes were applied before and during the measurement.

## 5.6 Conclusion

The main findings presented in this chapter are as follows.

- High-quality  $\text{Mn}_2\text{Au}$  films with a thickness  $\lesssim 7$  nm grown at an optimized deposition temperature have a low anisotropy and turn out to be inefficient for generating exchange bias in  $\text{Mn}_2\text{Au}/\text{Fe}$  heterostructures. Thicker  $\text{Mn}_2\text{Au}$  layers are characterized by an increased Néel temperature  $T_N > 500$  K. Exchange bias in such samples cannot be induced by field cooling, since it requires heating the sample to temperatures above  $T_N$ . At this conditions, interdiffusion occurs at the AFM/FM interface, which results in its deterioration.
- In order to lower the  $T_N$  of  $\text{Mn}_2\text{Au}$ , samples with a reduced grain size were prepared. In the current work, control of the crystallite size is achieved by depositing the material at different substrate temperatures. Two samples were prepared at the substrate temperatures 100 °C and 150 °C lower than the optimal temperature of 600 °C. A lower deposition temperature corresponds to smaller (001)-crystallites as it was evidenced by XRD. After performing field cooling, a significant exchange bias was measured reaching 140 Oe in the former and 210 Oe in the latter. The value of  $T_B$  for the samples is lower than RT and amounts to  $\sim 250$  K and  $\sim 200$  K, respectively. A broadening of the hysteresis loop is observed, which is induced by a strong uniaxial anisotropy created at the interface by the AFM.
- The spin glass theory is used for fitting the experimental hysteresis loops of the  $\text{Mn}_2\text{Au}/\text{Fe}$  heterostructures grown at a decreased substrate temperature. Within the model, the interfacial exchange constant is found to be equal in both samples. The larger value of  $H_{EB}$  in a sample corresponding to a lower growth temperature and smaller crystallites originates from a larger



fraction of fixed AFM moments at the interface.

- A  $\text{Mn}_2\text{Au}$  film deposited on an epitaxial and magnetically saturated Fe layer has a textured structure and also generates an exchange bias of  $\sim 40$  Oe upon cooling to 10 K, which is smaller than for the epitaxial samples. The studied sample is characterized by  $T_B = 200$  K and a low  $T_N$  of 300 K. The reduction of the Néel temperature is attributed to a low crystalline quality of the  $\text{Mn}_2\text{Au}$  layer.
- The domains in epitaxial high-quality  $\text{Mn}_2\text{Au}/\text{Py}$  and  $\text{Mn}_2\text{Au}/\text{Fe}$  heterostructures with thick AFM layers were imaged by Kerr microscopy and XMCD-PEEM. The acquired ferromagnetic domain patterns consist of fine random domains with an average size of  $\sim 1$   $\mu\text{m}$ , which is significantly smaller than the domain size in a Py or Fe film on a non-magnetic substrate. This result indicates that the ferromagnetic domains follow the domain pattern of the underlying  $\text{Mn}_2\text{Au}$  film. Consequently, a FM layer can be used as a tracer layer for investigating the non-easily accessible AFM domains of  $\text{Mn}_2\text{Au}$  thin films, which is otherwise only possible by the XMLD effect.



# 6 Antiferromagnetic domains in $\text{Mn}_2\text{Au}$ and domain reorientation in a high magnetic field

## 6.1 Introduction

It is known that, in analogy to FM, AFM may also form domains with a uniform Néel vector within one domain. However since AFMs do not have a net magnetization and do not produce stray fields, the AFM domains remained elusive for investigators longer than their FM counterpart. First observations of domains in bulk insulating AFMs were made by neutron tomography [158; 159; 160] and optical microscopy [161; 73]. An important breakthrough in research on domains in AFM thin films was made after discovery of XMLD, which is the difference between absorption of X-rays with various linear polarizations [131]. Subsequently, a series of exciting experiments were performed in AFM and AFM/FM heterostructures [24; 25; 162; 163] with the help of XMLD combined with PEEM. It was shown that in thin AFM films the domains have a size of  $\sim 1 \mu\text{m}$  [164; 24; 165] and usually show irregular shapes with curved boundaries. Menon et al. demonstrated imaging of domains in NiO by LEEM [166]. Since NiO has a magnetic periodicity twice larger than the structural periodicity, half-order Bragg reflexes appear in the back focal plane of the objective. Choosing one of these reflexes by the contrast aperture allows obtaining the domain images in the dark-field mode. The virtues of this technique are a high surface sensitivity and a lateral resolution reaching 10 nm. However, the method is not universal and requires different spatial and magnetic periods resulting in separate magnetic Bragg peaks. In AFM spintronics, a bit of information can be encoded by the direction of the Néel vector. Therefore a concept of AFM memory requires efficient methods for writing and reading the Néel vector orientation, in other words, changing and detecting its direction. The emergence of current induced NSOT in AFMs with non-centrosymmetric magnetic sublattices was theoretically predicted in Ref. [40]. This torque can change the orientation of the Néel vector, which was, indeed, recently demonstrated for CuMnAs [21; 41] and  $\text{Mn}_2\text{Au}$  [22; 167]. However, the threshold current densities for Néel vector reorientation are, in general, close to the sample destruction limit. To this end, the characterization of the AFM domain structure is of major importance for further material optimization, which allows for reducing the necessary current.

Two equivalent bulk types of domains exist in  $\text{Mn}_2\text{Au}$  with staggered magnetization oriented along  $[110]$  and  $[1\bar{1}0]$  directions. However, there are four possible surface terminations with the topmost magnetic moments pointing along  $\pm[110]$  and  $\pm[1\bar{1}0]$  (Fig. 6.1). Little is known about the domains in  $\text{Mn}_2\text{Au}$  thin films. Results presented in the previous chapter obtained

by XMCD-PEEM for a  $\text{Mn}_2\text{Au}/\text{Fe}$  heterostructure provide an estimated AFM domain size of  $\sim 1\ \mu\text{m}$ . To this end, measurements directly probing the AFM domain structure of  $\text{Mn}_2\text{Au}$  are required.

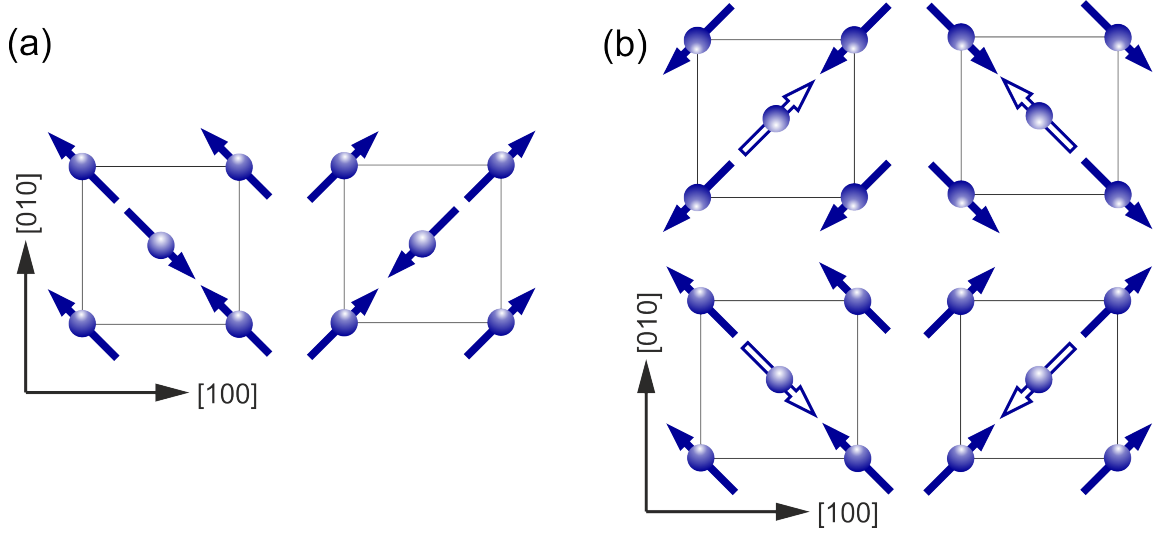


**Figure 6.1:** (a) Two types of bulk AFM domains in  $\text{Mn}_2\text{Au}$ . (b) Four possible structures at the surface of a  $\text{Mn}_2\text{Au}$  bulk single crystal. Filled and empty arrows correspond to the topmost moments and the second layer of Mn atoms, respectively.

The region separating two magnetic domains is called a domain wall (DW), where the Néel vector ( $\mathbf{L}$ ) direction changes smoothly from  $\mathbf{L}_1$  in the first domain to  $\mathbf{L}_2$  in the second domain. The DW structure is determined by the bulk and interface properties of the magnetic layers, such as exchange coupling, anisotropy coefficients, and Dzyaloshinskii-Moriya interaction [133]. Information about the AFM DWs is lacking in the literature. Only a few articles exist concerning NiO domain walls, which provide different estimations for the domain wall width [168; 27]. The analysis of the DW profiles in AFMs is interesting because it can provide information about the above-mentioned parameters of AFM samples. For example, information about the magnetocrystalline anisotropy determining the switching current value is required for lowering its threshold density [40]. Moreover, a recent study of NSOT in CuMnAs indicated a crucial role of domain walls for current switching [42].

Spin-flop manifests itself in a reorientation of sublattice magnetizations in an AFM by a strong magnetic field. This effect was for the first time experimentally investigated in  $\text{MnF}_2$ , an AFM with a uniaxial magnetocrystalline anisotropy having  $T_N = 67\ \text{K}$  [30]. The susceptibility measurements in a pulsed magnetic field performed at  $4.2\ \text{K}$  indicated a sudden increase of the induced magnetic moment at  $H_{SF} = 9.3\ \text{T}$ . The transition region became broader for the external field misaligned with the easy axis direction. As it is also pointed out in Section 2.8, the spin-flop field is proportional to the square root of the product of exchange field and the

anisotropy field  $\propto \sqrt{H_E H_A}$ . The materials with a high Néel temperature are characterized by a large  $H_E$  and, as a consequence, a large  $H_{SF}$ . Generally, fields of several tens of Tesla are necessary to achieve spin-flop. These high fields are available only in pulsed mode, which hinders direct experimental investigation of this phenomenon. The  $H_{SF}$  can also be determined by performing a field dependent antiferromagnetic resonance measurement since the collective mode frequency depends on the external field as  $f_{AFMR} \propto (\sqrt{2H_E H_A} - H)$  and goes to zero when  $H = H_{SF} = \sqrt{2H_E H_A}$  [30]. However, this approach is also fraught with difficulties for AFMs with high  $T_N$  since it requires extremely high magnetic fields available only in the pulsed mode for reducing  $f_{AFMR}$  to the measurable values.

This chapter presents the investigation of the domain structure in epitaxial  $\text{Mn}_2\text{Au}$  thin films and orientation of the AFM domains in high magnetic fields. Section 6.2 shows the details of the sample preparation and the employed experimental techniques including XMLD and XMLD-PEEM. Section 6.3 introduces the XMLD spectra obtained in as-prepared  $\text{Mn}_2\text{Au}$  samples and samples exposed to high magnetic fields. The AFM domains in an as-prepared  $\text{Mn}_2\text{Au}$  film imaged by XMLD-PEEM are discussed in Section 6.4. Section 6.5 presents the changes in the  $\text{Mn}_2\text{Au}$  domain structure caused by high external magnetic field via spin-flop transition. Antiferromagnetic DWs in  $\text{Mn}_2\text{Au}$  are discussed in Section 6.6. Finally, Section 6.7 introduces the measurements of the  $\text{Mn}_2\text{Au}$  magnetoresistance. The obtained results confine the field range, at which the spin-flop transition occurs in  $\text{Mn}_2\text{Au}$ .

## 6.2 Experimental details

The epitaxial thin films discussed in this chapter have the layer stacking sequence  $\text{Al}_2\text{O}_3(1\bar{1}02)/\text{Ta}(001)/\text{Mn}_2\text{Au}(001)/\text{AlO}_x$  with the in-plane epitaxial relation  $\text{Mn}_2\text{Au}(001)[100] \parallel \text{Ta}(001)[100]$ . The samples were grown by radio frequency magnetron sputtering in a UHV cluster. The base pressure before the deposition was  $10^{-8}$  mbar. First, a Ta buffer layer was deposited at an optimal substrate temperature of  $710^\circ\text{C}$  and an Ar pressure of 0.03 mbar assuring the best layer quality. These growth parameters correspond to a 2D-RHEED pattern and the narrowest Ta (001)  $\theta - 2\theta$  peak as well as the rocking curve measured by XRD. A stoichiometric target was used for depositing  $\text{Mn}_2\text{Au}$ . During the  $\text{Mn}_2\text{Au}$  deposition, the Ar pressure was set to 0.1 mbar and the RF source power to 25 W. A substrate temperature of  $600^\circ\text{C}$  in combination with the Ta buffer layer provided a  $\text{Mn}_2\text{Au}(001)$  epitaxial thin film [75]. The layer thicknesses were defined from the known deposition rates. An Al capping was used for oxidation protection.

High magnetic fields were applied to the samples at the High Magnetic Field Laboratory of the Helmholtz Zentrum Dresden Rossendorf (HZDR) (courtesy of Dr. Yurii Scourski). A set of samples prepared according to the same protocol was exposed to pulsed magnetic fields having a maximal value from 30 T to 70 T with an increment of 10 T. The direction of the external field was parallel to either [110] or [100] crystallographic axis of  $\text{Mn}_2\text{Au}$ .

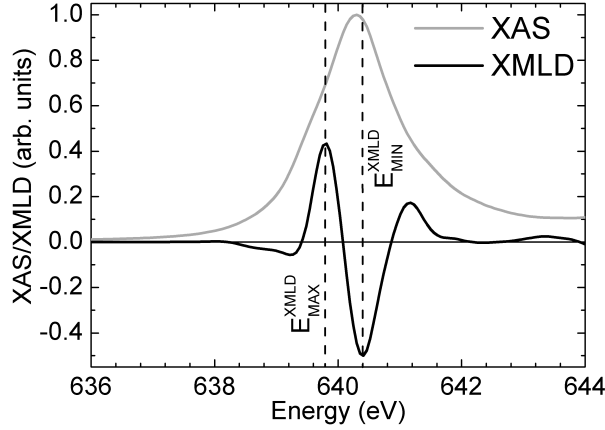


**Figure 6.2:** The XAS and the corresponding XMLD spectrum of  $\text{Mn}_2\text{Au}$  calculated with FP-LAPW ELK software [60]. The energies  $E_{XMLD}^{max}$  and  $E_{XMLD}^{min}$  corresponding to the maximum and the minimum of XMLD are indicated.

The spectroscopic X-ray absorption studies were performed with the ALICE chamber at the synchrotron facility BESSY II (HZB). During the experiments, the instrument was installed at the beamline UE52\_SGM with an implemented APPLE II undulator providing variable circular and linear beam polarizations. The X-ray beam was incident normal to the sample surface and focused to a spot of  $60\ \mu\text{m} \times 80\ \mu\text{m}$ . The film was connected to the ground through a Keithley 6485 picoamperemeter. Crystallographic  $\langle 110 \rangle$  axes were oriented horizontal and vertical, i.e. in the X-ray polarization planes. A deviation of  $[110]$  axis from the X-ray electric field direction amounting to a few degrees is to be expected. The XAS were measured in TEY mode, detecting the current flowing to the ground to compensate the photocurrent. The monitor current measured at a Pt mesh located in the beam path was used for normalization. The XMLD spectrum was calculated as the difference of the corresponding XAS spectra measured at linear horizontal (LH) and linear vertical (LV) polarizations:

$$XMLD(E) = \frac{XAS_{LH}(E) - XAS_{LV}(E)}{XAS_{LH}^{max} + XAS_{LV}^{max}}, \quad (6.1)$$

where LH and LV correspond to the electric field vectors oriented in the ring plane and perpendicular to it, respectively.

The XMLD-PEEM studies were performed at beamline I06 at Diamond Light Source and SPEEM at BESSY II (HZB) both equipped with Elmitec photoemission electron microscopes. The setup allows obtaining images with the field of view of 5 to  $80\ \mu\text{m}$  and a spatial resolution of  $\sim 50\ \text{nm}$ . The energy resolution was  $\sim 0.4\ \text{eV}$ . The X-ray beam incidence angle was kept constant during the experiment and equal to  $16^\circ$ . All measurements were conducted at linear vertical (LV) polarization with the electric field vector oriented in the sample plane. The XAS were obtained with PEEM by taking pictures at a series of energies in the vicinity of the Mn

$L_3$  edge and averaging the gray scale levels over a selected area in the pictures. Comparing it with the spectroscopy XAS measured with ALICE, the energies corresponding to the maximum ( $E_{XMLD}^{max}$ ) and the minimum ( $E_{XMLD}^{min}$ ) of XMLD were experimentally determined (Fig. 6.2). The AFM contrast was obtained from the difference between pictures at the energies of ( $E_{XMLD}^{min}$ ) and ( $E_{XMLD}^{max}$ ) normalized by their sum:

$$I_{XMLD} = \frac{I_{LV}(E_{XMLD}^{max}) - I_{LV}(E_{XMLD}^{min})}{I_{LV}(E_{XMLD}^{max}) + I_{LV}(E_{XMLD}^{min})}. \quad (6.2)$$

A stack of 20 pictures at  $E_{XMLD}^{max}$  followed by 40 pictures at  $E_{XMLD}^{min}$  and another 20 pictures at  $E_{XMLD}^{max}$  with an exposition time of 3 seconds were taken. These measurements were repeated 4 times. An averaging procedure including background correction and drift correction allowed to obtain a sharp magnetic contrast in the averaged image [169]. The measurements were performed at different angles of rotation around the sample normal. For a tetragonal easy plane AF, a magnetic contrast is expected when the electric field of the X-ray beam is parallel to an easy axis. The contrast is supposed to disappear after rotating the sample by  $45^\circ$  and to change sign after  $90^\circ$  rotation [76].

Transport measurements were performed in a cryostat (Oxford) providing magnetic fields up to 16 T. The resistance of a square  $10\text{ mm} \times 10\text{ mm}$  sample was detected in the van der Pauw geometry.

### 6.3 Orienting the Néel vector of a $\text{Mn}_2\text{Au}$ thin film by a spin-flop transition in a high magnetic field

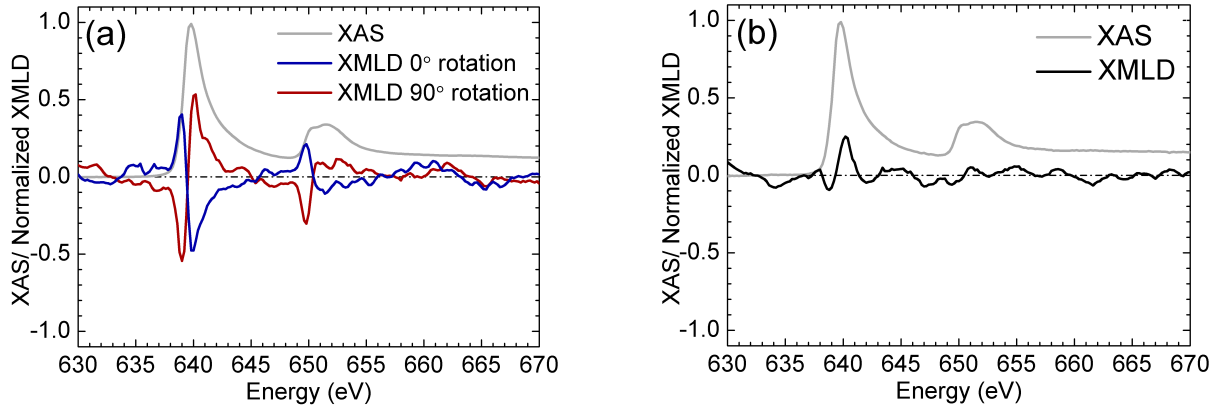


**Figure 6.3:** (a) The XAS and the corresponding XMLD spectrum measured in sample *MA9* previously exposed to a pulsed field of 70 T along the [110] direction. The sample was rotated by  $0^\circ$  (blue) and by  $90^\circ$  around its normal (red). (b) The XAS and the corresponding XMLD spectrum for reference sample *MA9ref*.

The first experiment was aimed at investigating the possibility to orient the AFM domains

in  $\text{Mn}_2\text{Au}$  via spin-flop transition. Two samples *MA9* and *MA9ref* with the layer sequence  $\text{Al}_2\text{O}_3/\text{Ta}$  15 nm/ $\text{Mn}_2\text{Au}$  @500 °C 10 nm/ $\text{Fe}$  1 nm/ $\text{AlO}_x$  2 nm were prepared for this experiment. The growth temperature was decreased in comparison to the optimal 600 °C [75] for reducing the spin-flop field value, which is achieved by decreasing the grain size. A smaller grain size results in a lower Néel temperature and lower exchange interaction strength [170], which determines the spin-flop field (see Section 2.8). Sample *MA9* was exposed to a magnetic field of 70 T along the [110] crystallographic direction. The Fe layer, which was deposited for magneto-optical Kerr effect (MOKE) investigations, is assumed to have no influence on the spin-flop process [171]. The XMLD spectra measured in *MA9* after exposure to a 70 T magnetic field are shown in Fig. 6.3(a). The XMLD at the  $L_3$  edge reaches 0.5% and changes sign after rotating the sample by 90°. The as-prepared sample *MA9ref*, which was not exposed to a high magnetic field, does not exhibit an XMLD effect (Fig. 6.3(b)). Thus, the external field reoriented the magnetic moments in  $\text{Mn}_2\text{Au}$ , resulting in a net XMLD signal for *MA9*, in contrast to *MA9ref*. The experiments on imaging the AFM domains presented in the next chapters shed light on the changes in the domain structure caused by spin-flop transition and explain the obtained data in more detail. The XAS spectrum reaches its maximum at the Mn  $L_3$  edge at an energy of 639.8 eV. The maximum and minimum XMLD value at 0° rotation (blue curve in Fig. 6.3(a)) correspond to 639.0 eV and 639.8 eV and are separated from the  $L_3$  absorption edge by 0.8 eV and 0.0 eV, respectively.

## 6.4 Imaging AFM domains in an as-prepared $\text{Mn}_2\text{Au}$

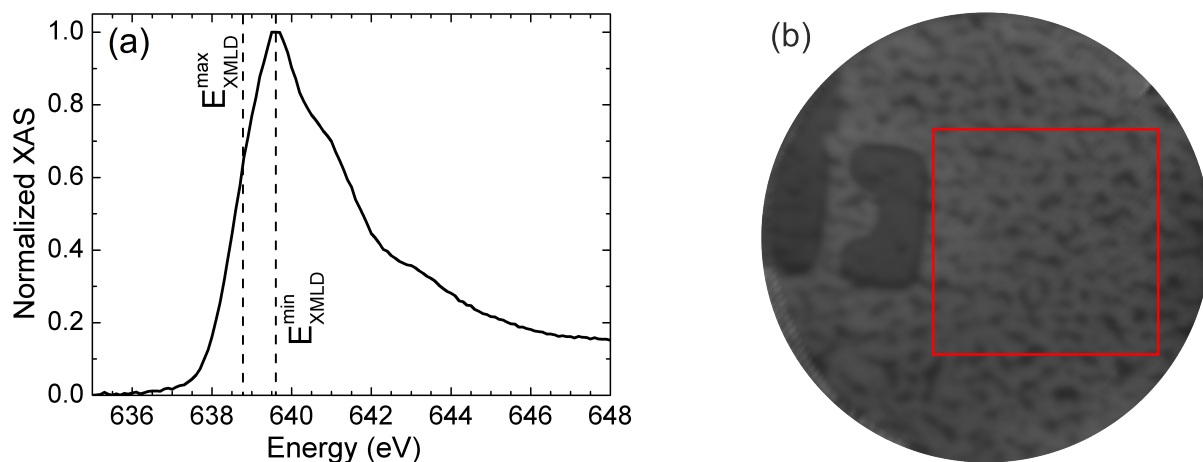


**Figure 6.4:** (a) The XAS measured in *MA10*. (b) The spectrum is averaged over the area marked with the red box. The field of view is 8  $\mu\text{m}$ .

The AFM domains in the as-prepared sample *MA10* with the layer sequence of  $\text{Al}_2\text{O}_3/\text{Ta}$  30 nm/ $\text{Mn}_2\text{Au}$  @600 °C 240 nm/ $\text{AlO}_x$  2 nm were studied by XMLD-PEEM. The XAS spectrum



(Fig. 6.4(a)) was measured over the region of interest (ROI) with the dimensions  $250 \text{ pixel} \times 250 \text{ pixel}$  indicated by the red box in Figure 6.4(b). Comparing the Mn  $L_3$  absorption edge energy  $E_{L_3} = 639.6 \text{ eV}$  (Fig. 6.4(a)) with the spectroscopy data (Fig. (6.3(a))), the energies  $E_{XMLD}^{max}$  and  $E_{XMLD}^{min}$  were found to be  $638.8 \text{ eV}$  and  $639.6 \text{ eV}$ , respectively. The asymmetry was calculated from the pictures taken at the above given energies  $E_{XMLD}^{max}$  and  $E_{XMLD}^{min}$  according to Eq. (6.2). The same procedure for measuring XAS and determining the energies was repeated for each sample discussed below.

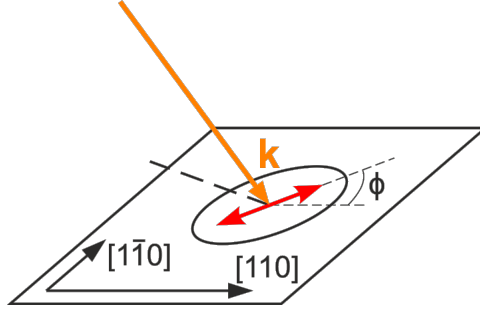


**Figure 6.5:** The XMLD-PEEM experimental geometry. The X-ray wave vector (orange) forms an angle of  $16^\circ$  with the sample plain,  $\phi$  is the angle between the X-ray electric field (red) and the  $[110]$  crystallographic direction in  $\text{Mn}_2\text{Au}$ .

The asymmetry image obtained at the X-ray electric field pointing along the  $[110]$  crystallographic axis exhibits light/dark areas with a size of  $1 \mu\text{m}$  (Fig. 6.6(a)). Figure 6.6(c) shows that the contrast changes sign after rotating the sample from  $\phi = 0^\circ$  to  $\phi = 90^\circ$ . This leads to the conclusion that the light and dark contrast correspond to the areas with different orientations of the Néel vector. For  $45^\circ$  rotation, when the X-ray polarization is along the  $[100]$  direction, no contrast is visible (Fig. 6.6(b)). Thus, there are two magnetic domains in  $\text{Mn}_2\text{Au}$  with the Néel vector pointing along  $[110]$  and  $[1\bar{1}0]$  directions with the AFM axis orientation indicated below the images. The domains in an as-grown sample have an irregular shape and a size of  $1 \mu\text{m}$ . The XMLD effect detected by spectroscopy methods in *MA9ref* (Fig. 6.3(b)) is averaged over multiple domains with the perpendicularly oriented Néel vectors within the X-ray spot having a size of about  $50 \mu\text{m}$ . The contributions from these domains cancel out resulting in a vanishing dichroism.

## 6.5 Spin-flop induced changes in the AFM domain structure in $\text{Mn}_2\text{Au}$ epitaxial thin films

For the investigation of the changes in the domain structure caused by spin-flop, samples with the layer structure  $\text{Al}_2\text{O}_3 / \text{Ta } 30 \text{ nm} / \text{Mn}_2\text{Au } @600^\circ\text{C } 240 \text{ nm} / \text{AlO}_x 2 \text{ nm}$  exposed to high magnetic fields were studied. Sample *MA11* exposed to a field of  $30 \text{ T}$  along the  $[110]$  direction exhibits a

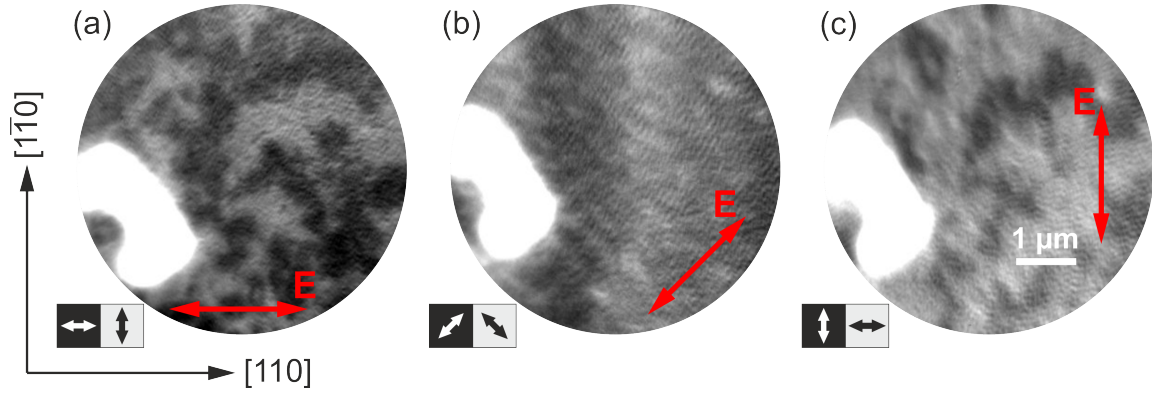


**Figure 6.6:** Asymmetry images for the as-prepared sample *MA10*. The in-plane angle of the X-ray electric field vector is (a)  $0^\circ$ , (b)  $45^\circ$  and (c)  $90^\circ$ . The red double-headed arrow indicates the X-ray polarization. The white feature on the left side of the figures is caused by the gold marker.

fundamentally different asymmetry pattern, in comparison with the as-prepared sample, which consists predominantly of light areas incorporating smaller dark areas (Fig. 6.7). Increase of the AFM domain size occurs at a field less than 30 T, specifying the upper boundary for the spin-flop field in  $\text{Mn}_2\text{Au}$ .

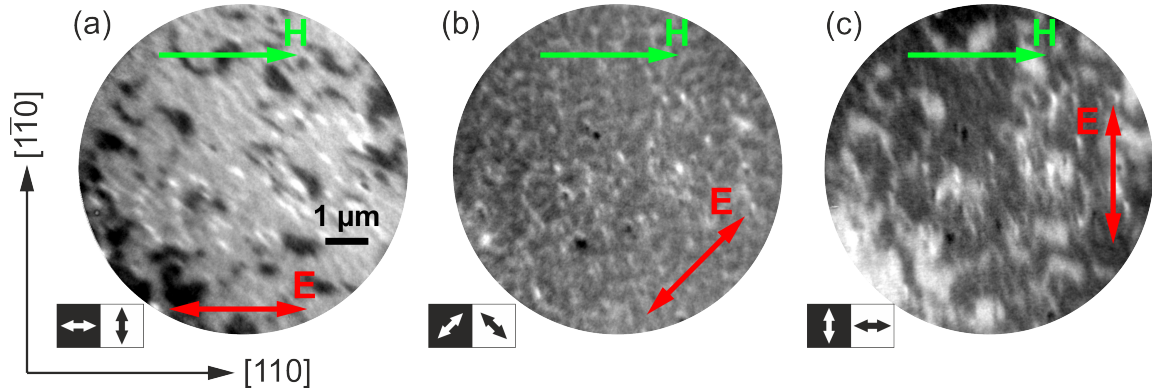


**Figure 6.7:** Asymmetry images for the sample *MA11*, which was exposed to a magnetic field of 30 T along the  $[110]$  direction (green arrow). The in-plane angle of the X-ray electric field vector is (a)  $0^\circ$ , (b)  $45^\circ$ , and (c)  $90^\circ$ . The red double-headed arrow indicates the X-ray polarization.

Sample *MA12* was exposed to 50 T along the  $[110]$  in-plane direction. An asymmetry in the images is present if the electric field is directed along one of the  $\langle 110 \rangle$  directions (Fig. 6.8). In panel (a) we recognize large light gray areas that have Néel vectors pointing along the  $\pm[1\bar{1}0]$  directions. These areas indicate that the high external field has wiped out domains with the Néel vector oriented parallel to the applied magnetic field direction (Fig. 6.10). Residual dark lines are also present having a width of  $\sim 100$  nm with the Néel vector predominantly oriented along

$\pm[110]$  directions. These regions can either be due to AFM domains formed by locally enhanced magnetostriction or due to  $180^\circ$  domain walls. A detailed investigation of these features requires a technique with a resolution of  $\sim 10$  nm and is out of the scope of this research.

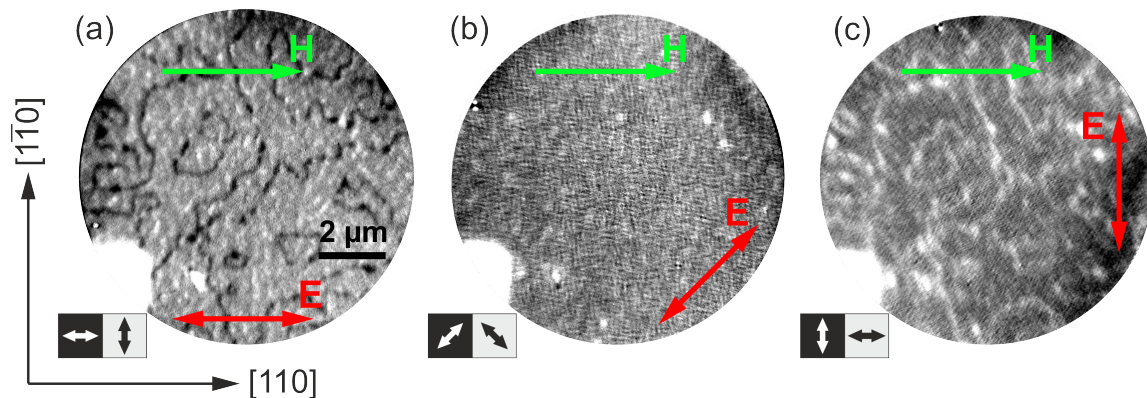


**Figure 6.8:** Asymmetry images for the sample *MA12*, which was exposed to a magnetic field of 50 T along the  $[110]$  direction (green arrow). The in-plane angle of the X-ray electric field vector is (a)  $0^\circ$ , (b)  $45^\circ$ , and (c)  $90^\circ$ . The red double-headed arrow indicates the X-ray polarization.

Finally, the effect of a 70 T magnetic field applied to sample *MA13* along  $[100]$  axis is investigated. Also here, a sign change is observed after rotating the sample by  $\phi = 90^\circ$ , which proves the magnetic origin of the contrast (Fig. 6.9). Both types of AFM domains have a size from  $1 \mu\text{m}$  to  $3 \mu\text{m}$  and occupy comparable areas signifying a symmetric domain distribution.

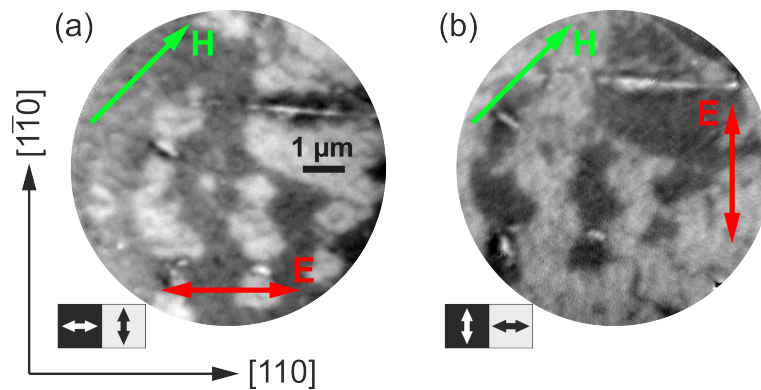


**Figure 6.9:** Asymmetry images for the sample *MA13*, which was exposed to a magnetic field of 70 T along the  $[100]$  direction (green arrow). The in-plane angle of the X-ray electric field vector is (a)  $0^\circ$  and (b)  $90^\circ$ . The red double-headed arrow indicates the X-ray polarization.

The changes in the domain structure resulting from a spin-flop transition can be explained by

the following simple model. An as-prepared  $\text{Mn}_2\text{Au}$  sample has two types of AFM domains equally distributed in the sample (Fig. 6.10(a)). A high external field applied along an easy axis induces a spin-flop transition, if the field is higher than the spin-flop field (Fig. 6.10(b)). After switching the field off, the oriented magnetic moments keep their direction due to magneto-crystalline anisotropy preventing them from flipping back. Thus if the magnetic field is oriented along an easy axis, the spin-flop transition is accompanied by a dramatic increase of the size of one type of domain and an elimination of the other type of domains almost completely. This change in the magnetic domain distribution is proven by the presented experimental images and manifests itself in the appearance of an XMLD spectrum. It is worth mentioning that some magnetic moments can restore their original direction after the spin-flop transition due to local magnetoelastic effects prevailing over the magnetocrystalline anisotropy (dark lines in Fig. 6.8(a)).

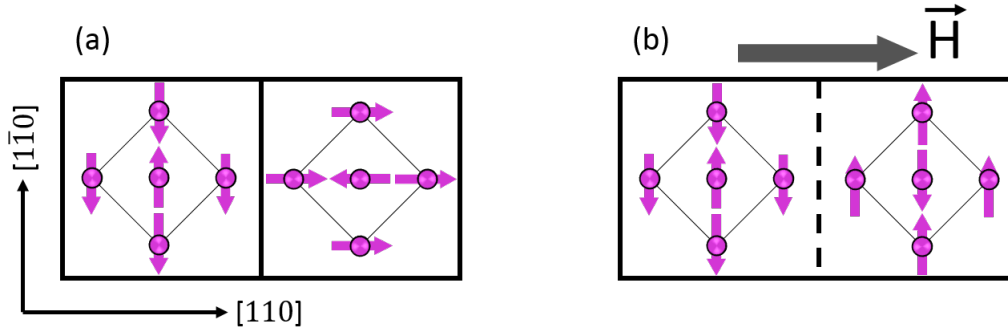


**Figure 6.10:** (a) A schematic representation of two equivalent antiferromagnetic domains in an as-prepared  $\text{Mn}_2\text{Au}$  sample. (b) By applying a high external magnetic field along an easy direction, the magnetic moments are rotated via a spin-flop transition. The moments show along the easy axis perpendicular to the applied field direction.

An external field higher than the spin-flop field applied along a hard axis leads to orthogonal orientation of the staggered magnetization (Fig. 6.11(b)). After reducing the magnetic field magnitude, the magnetic moments pointing along a hard axis are arranged back to the easy axes, which can result in a larger domain size keeping the areas occupied by the equivalent AFM domains almost equal.

The experimentally determined limit for the spin-flop field in  $\text{Mn}_2\text{Au}$  allows estimating the in-plane anisotropy constant using the equation for the spin-flop field  $H_{SF} = \sqrt{2H_{ex}H_a^{IP}}$  [89]. Using an exchange field of  $\mu_0 H_{ex} = 1300$  T from Ref. [55], the anisotropy field  $\mu_0 H_a^{IP}$  results in  $\mu_0 H_a^{IP} = 0.35$  T. For the in-plane moments with  $\theta = \pi/2$ , the expression for the tetragonal anisotropy from Section 2.8 becomes  $K_{4||} \cos 4\phi_i$ . With this notation, the obtained anisotropy field corresponds to  $K_{4||} = 17.5$   $\mu\text{eV}/\text{f.u.}$ , which roughly agrees with the theoretically predicted value of 10  $\mu\text{eV}/\text{f.u.}$  [56].

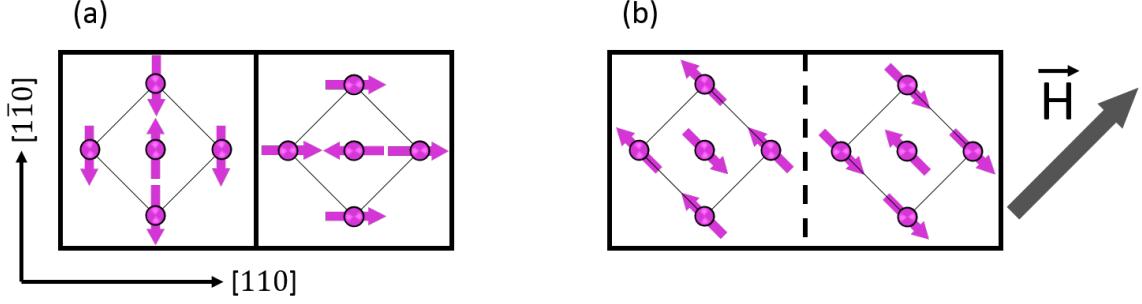


**Figure 6.11:** (a) A schematic representation of two equivalent antiferromagnetic domains in an as-prepared  $\text{Mn}_2\text{Au}$  sample. (b) By applying a high external magnetic field along a hard direction, the magnetic moments are rotated via a spin-flop transition. The moments show along the hard axis perpendicular to the applied field direction.

## 6.6 Domain walls in $\text{Mn}_2\text{Au}$

It was predicted theoretically by Shick et al. [56] that the out-of-plane anisotropy constant  $K_{2\perp}$  in  $\text{Mn}_2\text{Au}$  is several orders of magnitude larger than the constant  $K_{4\parallel}$  associated with the four-fold in-plane anisotropy. Therefore, Néel type DWs with the Néel vector rotating in-plane are energetically more favorable in our thin films. The width of a DW can be determined by minimizing the total DW energy per unit area containing exchange interaction and magnetocrystalline anisotropy terms [172].

In the following, the exchange energy functional is derived for [100] (Fig. 6.12(a)) and [110] (Fig. 6.12(b)) domain walls. In the first case, the functional is given by:

$$E = \sum_i (2J_1 \cos(\phi_{i+1} - \phi_i) + J_3 \cos(\phi_{i+2} - \phi_i)) = \int_{-\infty}^{\infty} \frac{J_1 + 2J_3}{4} a^2 \left( \frac{d\phi}{dx} \right)^2 dx, \quad (6.3)$$

where  $i$  numbers the rows of atoms in the [100] direction,  $n$  is the volume density of Mn atoms, and  $a$  is the  $\text{Mn}_2\text{Au}$  lattice constant. For the [110] DW, the exchange energy is

$$E = \sum_i (J_1 + 2J_3) \cos(\phi_{i+1} - \phi_i) = \int_{-\infty}^{\infty} \frac{J_1 + 2J_3}{4} a^2 \left( \frac{d\phi}{dx} \right)^2 dx, \quad (6.4)$$

where  $i$  numbers the rows of atoms in the [110] direction. Identity of the Eqs. (6.3) and (6.4) implies the same properties of a [100]-DW and a [110]-DW in  $\text{Mn}_2\text{Au}$ .

The total energy of the DW is given by

$$E[\phi(x)] = \int_{-\infty}^{\infty} \left( J a^2 \left( \frac{d\phi}{dx} \right)^2 + K_{4\parallel} (1 - \cos 4\phi) \right) dx, \quad (6.5)$$

where  $J = (J_1 + 2J_3)/4$  for both types of domain walls (see Fig. 6.12) and  $K_{4\parallel}$  is the four-fold

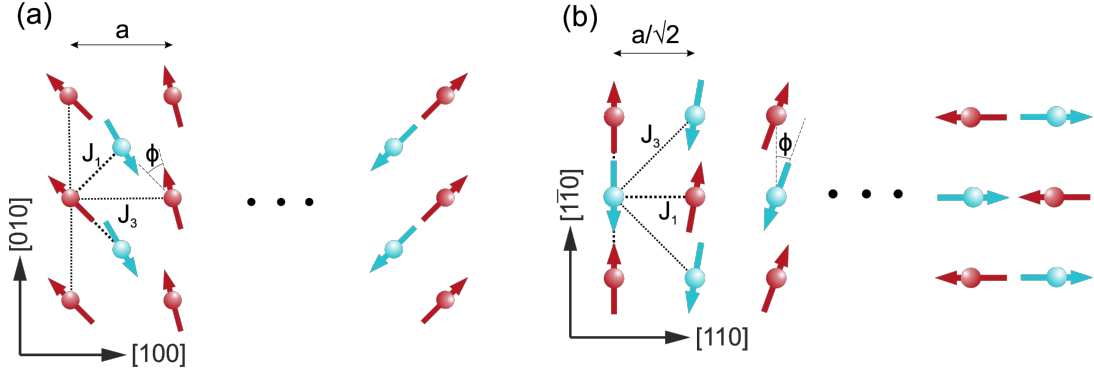


**Figure 6.12:** (a) A schematic image of the [100]-Néel type domain wall in  $\text{Mn}_2\text{Au}$  with the exchange constants specified for the nearest Mn atoms. (b) The same for the [110]-Néel type domain wall.

anisotropy constant. The chosen angular dependence of the anisotropy term corresponds to angle  $\phi$  between  $[\bar{1}10]$  easy axis and the staggered magnetization direction (Fig. 6.12). Minimizing the functional in Eq. (6.5) with the boundary conditions  $\phi(-\infty) = 0$  and  $\phi(\infty) = \pi/2$  for a  $90^\circ$  DW provides the dependence  $\phi(x)$ :

$$\phi(x) = \arctan \exp \left( \sqrt{\frac{8K_{4\parallel}}{Ja^2}} x \right), \quad (6.6)$$

The DW width results from the profile gradient in the center of the DW. Using Eq. (6.6), the DW width is derived as:

$$w = \frac{\pi}{2} \frac{1}{d\phi/dx(x=0)} = \frac{\pi}{2} \sqrt{\frac{J}{2K_{4\parallel}}} a. \quad (6.7)$$

Since the XMLD does not change the sign upon Néel vector inversion, the normalized XMLD-PEEM contrast across a DW is proportional to the cosine squared of the angle between the Néel vector and the X-ray electric field  $I_{DW}(x) \propto \cos^2 \phi(x)$  [173]. Thus in analogy with Eq. (6.7), the apparent antiferromagnetic DW width observed in the experiment is:

$$w_{exp} = \frac{1}{dI_{DW}/dx(x=0)} = \sqrt{\frac{J}{2K_{4\parallel}}} a. \quad (6.8)$$

This result indicates that a DW appears  $\pi/2$  times more narrow in an XMLD-PEEM image in comparison with the actual width.

In an XMLD-PEEM experiment, the DW image is broadened due to a finite instrumental reso-

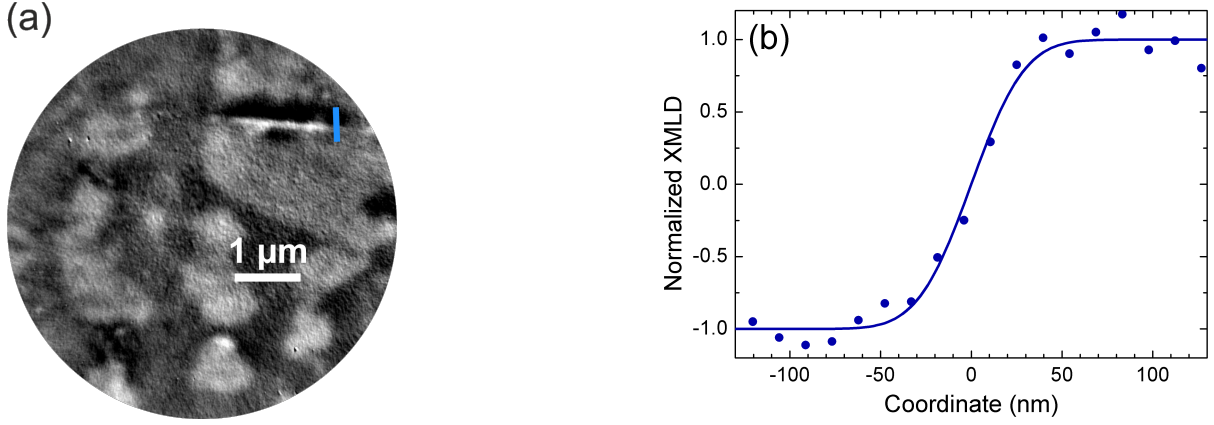


**Figure 6.13:** (a) Asymmetry image obtained for the sample *MA13*. The path used for calculating the line profile across the topographical structure is indicated by the blue line. (b) Line profile across a domain wall (dots) and fits by Eq. (6.10) (solid line).

lution, which can be represented as a Gaussian function:

$$Res_{\sigma}(x) = \frac{1}{\sqrt{2\pi\sigma^2}} \exp\left(-\frac{x^2}{2\sigma^2}\right), \quad (6.9)$$

where parameter  $2\sigma$  defines the resolution. A sharp element on the sample surface will appear smeared, with the boundary described by the Gauss error function, which is the convolution of the step-function and the Gauss function:

$$I_{Res}(x) = Erf\left(\frac{x}{\sqrt{2}\sigma}\right), \quad (6.10)$$

For determining  $2\sigma$ , the intensity profile was calculated across the defect in the top right part of Fig. 6.9(a), which is shown in Fig. 6.13(a). Each point is averaged over 150 nm perpendicular to the line. The profile was fitted by the Gauss error function (Fig. 6.13(b)). The obtained value for  $2\sigma$  from the fit is 47 nm.

A domain wall profile was determined across a straight section of a domain wall in sample *MA13* (green line in Fig. 6.13(a)) with every point being averaged over 300 nm perpendicular to the line, as depicted in Fig. 6.13(c). The profile was fitted by a convolution of the instrumental resolution and the domain wall profile:

$$I_{DW}^{exp}(x) = (I_{DW} * Res_{\sigma})(x) \quad (6.11)$$

with  $2K_{4||}/J$  being the fit parameter. The value of  $2K_{4||}/J$  providing the best fit is  $2 \times 10^{-4}$ , with the lower limit estimated to be  $0.5 \times 10^{-4}$  (see Fig. 6.13(c)). According to Eq. (6.7), this value corresponds to a domain wall width of 80 nm, which is of the same order of magnitude as

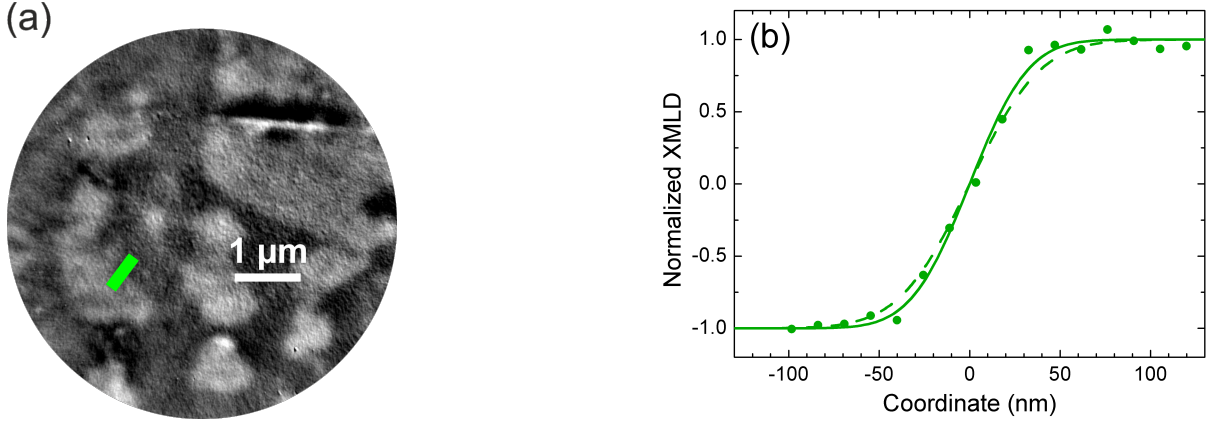


**Figure 6.14:** (a) Asymmetry image obtained for sample *MA13*. The path used for calculating the line profile across the straight domain wall section is indicated by a green line. (b) Line profile across a domain wall (dots) and fits by Eq. (6.11) for  $2K_{4\parallel}/J = 2 \times 10^{-4}$  (solid line) and  $2K_{4\parallel}/J = 0.5 \times 10^{-4}$  (dashed line).

the instrumental resolution. Considering the expected DW width, a high spatial resolution of better than 10 nm is necessary for a detailed investigation of DWs in  $\text{Mn}_2\text{Au}$ . Please note, that our analysis relies on the assumption of a perfect straight domain wall section. In FM thin films, straight DW sections are favored because they minimize the stray-field energy, which is absent in AFM. Therefore, the apparently straight DW section in an AFM might show a variation of the position perpendicular to the profile, thereby increasing the apparent domain wall width. Substituting  $J$  equal to 13.5 meV from Ref. [136] results in  $K_{4\parallel} = 1.5 \text{ meV/f.u.}$ , which is the lower estimation for  $K_{4\parallel}$ . This value corresponds to an anisotropy field of 0.02 T and  $H_{SF} = 7 \text{ T}$ .

## 6.7 Transport measurement of spin-flop in $\text{Mn}_2\text{Au}$

In order to investigate changes in the magnetic structure of a  $\text{Mn}_2\text{Au}$  thin film at lower fields, transport measurements in a cryostat equipped with a superconducting magnet were performed (courtesy of Dr. Lorenzo Baldrati). Reorientation of the Néel vector was read-out by AMR measurements.

AMR is a change of the material resistance depending on the relative orientation of the magnetic moments and the electric current. Since the effect is invariant with respect to the magnetic moment inversion [174], the material resistance depends evenly on the angle ( $\alpha$ ) between the order parameter ( $\mathbf{M}$  for a FM and  $\mathbf{L}$  for an AFM) and the current direction. For a single domain state one obtains:

$$R = R_0 + \Delta R \sin^2 \alpha, \quad (6.12)$$



where  $R_0$  is the resistance for  $\mathbf{M}$ (or  $\mathbf{L}$ ) parallel to the current direction,  $\Delta R$  is the AMR magnitude. In the case of a  $\text{Mn}_2\text{Au}(001)$  thin film in the multidomain state, the AMR contributions from different domains are summed up. Let  $x$  be the fraction of the  $[1\bar{1}0]$  domains. For the current applied along the  $[1\bar{1}0]$  direction, the measured resistance is given by (see Fig. 6.15)

$$R = R_0 + \Delta R \times x, \quad (6.13)$$

where the the domain wall contribution to the resistance is neglected. Thus, AMR allows for measuring the domain distribution.

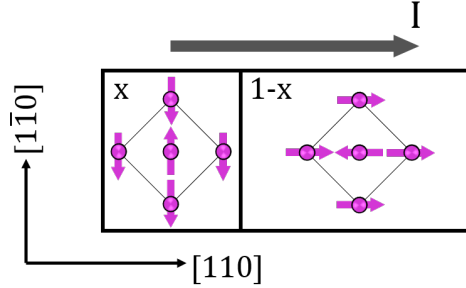


**Figure 6.15:** To the calculation of AMR in a  $\text{Mn}_2\text{Au}$  film in a multidomain state. The fraction of  $[1\bar{1}0]$  domains and of  $[110]$  domains is  $x$  and  $1-x$ , respectively

The transport investigations were performed in sample *MA14* with the layer sequence of  $\text{Al}_2\text{O}_3/\text{Ta}$  18 nm/  $\text{Mn}_2\text{Au}$  @600°C 80 nm/  $\text{TaO}_x$  3 nm. The measurement protocol included ramping the magnetic field to 12 T then decreasing it to  $-12$  T and increasing it back to 0 T. In the first experiment, the field was oriented along the  $[110]$  easy direction. The field dependence of the relative resistance change is shown in Fig. 6.16(a). A resistance drift was corrected assuming its linear increase with time. No significant change of the resistance is observed in the accessed field range. According to the recent data,  $\Delta R$  in  $\text{Mn}_2\text{Au}$  reaches 6 % [22], which corresponds to a resistance change of 3 % with respect to the as-prepared state upon reorienting half of the AFM domains via the spin-flop transition. A small measured  $\Delta R/R_0$  not exceeding 0.2 % indicates that the applied magnetic field does not invoke any significant change in the domain structure. Subsequently, the sample was taken out of the cryostat and rotated by  $90^\circ$  such that the  $[1\bar{1}0]$  axis became parallel to the field direction. The measurement was repeated for the maximal field increased to 16 T. Again, a variation of the resistance smaller than 0.2 % is observed (Fig. 6.17(a)). The initial increase of the resistance is caused by the temperature instabilities (compare with Fig. 6.17(b)). The measurements were stopped while decreasing the external field at  $-10$  T due to technical reasons. The conclusion can be made that no spin-flop transition occurs at fields less than 16 T.

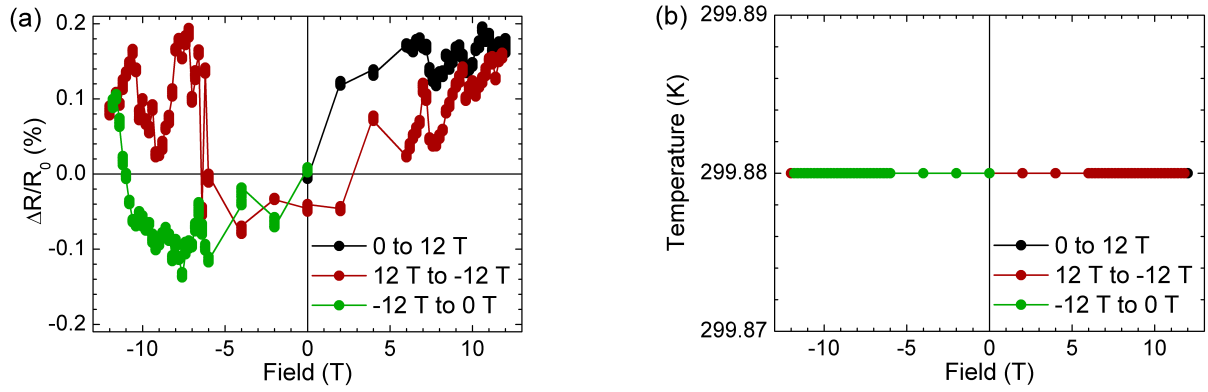


**Figure 6.16:** (a) Field dependence of  $\Delta R/R_0$  measured in *MA14* while applying an external field along the  $[110]$  direction. (b) The corresponding temperature values during the measurements.

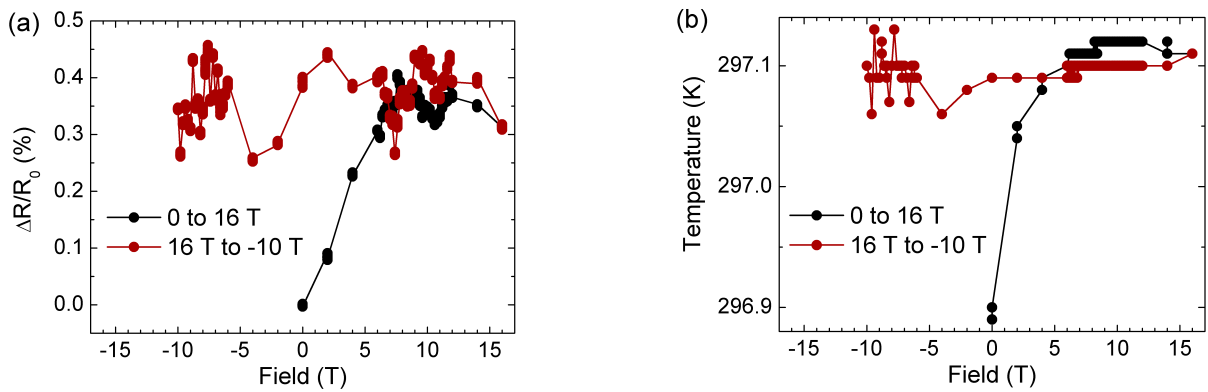


**Figure 6.17:** (a) Field dependence of  $\Delta R/R_0$  measured in *MA14* after  $90^\circ$  rotation while applying an external field along the  $[1\bar{1}0]$  direction. (b) Corresponding temperature values during the measurements.

## 6.8 Conclusion

In this chapter, the effect of large external fields on the AFM domain distribution in epitaxial  $\text{Mn}_2\text{Au}(001)$  thin films is discussed.

The absorption spectroscopy studies show an XMLD of 0.5 % in a  $\text{Mn}_2\text{Au}$  sample exposed to a pulsed magnetic field of 70 T along an in-plane easy axis. In contrast, no dichroism is measured in an as-prepared  $\text{Mn}_2\text{Au}$  sample. The obtained XMLD spectrum provided the energies corresponding to the maximum and the minimum dichroism values for  $\text{Mn}_2\text{Au}$ , which were subsequently exploited for obtaining an AFM contrast in PEEM. XMLD-PEEM was employed for imaging the AFM domains in  $\text{Mn}_2\text{Au}$  films. Small and irregular domains with a size of  $\sim 1 \mu\text{m}$  were found in an as-prepared sample. This result is in line with the domain size determined

from the XMCD-PEEM measurements using an Fe tracer layer deposited on  $\text{Mn}_2\text{Au}$ .

The sample exposed to a high external field of 30 T along an easy-axis prior to the measurement exhibits large domains with the Néel vector oriented perpendicular to the field. This is an indication of the spin-flop transition resulting in the domain reorientation. The sample exposed to a field of 50 T also shows large domains with the Néel vector oriented perpendicular to the field separated by  $180^\circ$  domain walls (narrow domains). The domain pattern measured after exposure to a field of 70 T along a hard axis consists of both types of AFM domains with the Néel vectors rotated by  $90^\circ$ . A simple model is proposed for explaining the changes in the domain distribution caused by a spin-flop transition upon application of a magnetic field along easy and hard magnetic directions.

The microscopy data provide insight into the magnetic structure of the AFM materials upon the spin-flop transition and allow comprehending the dichroism spectra. The XMLD averaged over an X-ray spot size of  $50\ \mu\text{m}$  has a finite value only if the sample has been subjected to a pulsed magnetic field generating large domains. In an as-grown sample, the magnetic domains are much smaller than the spot size and the resulting dichroism is negligible.

The rotation of the Néel vector within a Néel type DW in  $\text{Mn}_2\text{Au}$  was calculated by solving the variational problem for the energy density functional. The instrumental resolution was determined to be  $\sim 50\ \text{nm}$  by fitting the profile of a structural defect image. A corresponding fit of a line profile across a DW provided the DW width of less than 80 nm. This value is at the limit of the instrumental resolution and should be considered as a rough approximation for the average DW width in  $\text{Mn}_2\text{Au}$ .

Combination of the XMLD-PEEM data obtained in the samples exposed to high magnetic fields and of the transport data provided the spin-flop field ranging between 16 T and 30 T. From these values, the four-fold in-plane anisotropy constant is inferred to be in the range from  $5\ \mu\text{eV}/\text{f.u.}$  to  $17.5\ \mu\text{eV}/\text{f.u.}$ , which is in agreement with the theoretical predictions [56].



# 7 Magnetoelastic effect in $\text{Mn}_2\text{Au}$ epitaxial thin films

## 7.1 Introduction

Magnetoelastic effects are considered to play an important role in the magnetic structure of an AFM. Due to the absence of stray fields in AFMs, the AFM domain pattern is expected to be mainly determined by magnetoelastic interactions [16]. An AFM with a uniform Néel vector has the maximal magnetostriction energy and splitting into domains reduces this energy within the film. Additionally, a mechanical strain imposed by epitaxial or external forces should cause a magnetic anisotropy analogous to the well-known strain anisotropy in ferromagnets. If the magnetic strain anisotropy is strong enough, it will even change the domain structure of the AFM film. Consequently, the phenomenon of strain anisotropy can be exploited to actively manipulate the Néel vector [171].

An influence of epitaxial strains on the magnetization structure in AFM films has been investigated using substrates or buffer layers with different lattice constants [79; 78; 175]. The epitaxial tensile strain generated in CoO sandwiched between two MgO layers induces the preferential out-of-plane orientation of the moments in contrast to the compressively strained CoO grown on Ag(100) with in-plane orientation of magnetic moments. Besides the Néel vector orientation, strain also changes the  $T_N$ . A Ag/MgO/CoO/MgO sample has  $T_N = 290$  K and for a Ag/CoO sample one obtains  $T_N = 310$  K [79]. In AFM/FM heterostructures, an epitaxial strain can produce a dramatic change of the interfacial exchange coupling. The epitaxial strain causes an enhanced exchange bias in  $\text{Fe}_x\text{Mn}_{1-x}/\text{Fe}$  [78] or even a spin-reorientation transition Co/Mn films depending on the Mn layer thickness [175]. These observations prove that strain has an effect on the magnetization structure in AFMs, however, an epitaxial strain is always fixed, once the film has been deposited.

In order to reversibly manipulate the magnetization structure, external forces must be applied. Piezoelectric substrates provide an elegant way to produce external forces by applying an electrical potential. The manipulation of magnetization structures by piezoelectric substrates has been demonstrated for FM films and AFM/FM heterostructures. The additional anisotropy contribution in an epitaxial  $\text{Fe}_3\text{O}_4$  thin film has been monitored by ferromagnetic resonance measurements [176], and changes of the domain pattern in Ni nanostructures were imaged by XMCD-PEEM [177]. Modulation of the perpendicular exchange coupling in IrMn[Co/Pt] was demonstrated in Ref. [178]. The piezo-induced strain opens a pathway to a full electric control of magnetism, which is relevant for low power-consumption electronics [179; 180].

Theoretical predictions suggested that the magnetic easy directions in  $\text{Mn}_2\text{Au}$  can be altered

from  $\langle 110 \rangle$  to one particular  $[100]$  direction, along which a mechanical strain is applied [56]. The authors calculated the additional uniaxial anisotropy resulting from the mechanical strain characterized by the parameter  $K_{2\parallel}^*$ . The reorientation of the magnetic moments occurs when  $K_{2\parallel}^* \times \epsilon > 2K_{4\parallel}$ , where  $\epsilon$  is the strain value and  $K_{4\parallel}$  is the four-fold in-plane anisotropy constant. Substituting  $K_{4\parallel}$  from Ref. [56] results in a minimal strain of  $\sim 0.3\%$  that is necessary for altering the easy-axes. The contribution of the Au atoms to  $K_{2\parallel}^*$  is prevailing over the Mn contribution. This fact is connected with the anisotropy mechanism in  $\text{Mn}_2\text{Au}$ , where the Mn atoms polarize the Au orbitals, which are coupled to the lattice due to the strong SOC of 5d-electrons. Therefore, the Mn compounds containing a heavy-element with a high SOC are favorable for investigating magnetoelastic effects [181].

This chapter presents the study of magnetoelastic effects in AFM  $\text{Mn}_2\text{Au}$  films. Section 7.2 introduces the sample preparation method and the setups used for investigating strain-induced changes of the magnetic structure by transport measurements and XMLD spectroscopy. Two sample stages designed for applying a controllable value of strain are introduced. Section 7.3 reports experimental results of the domain manipulation by strain and monitoring the domain distribution by AMR. A reference experiment was performed for a Ni film (Subsection 7.3.2) to demonstrate the feasibility of the method. Analogous AMR measurements conducted for epitaxial  $\text{Mn}_2\text{Au}$  thin films are reported in Subsection 7.3.3. Section 7.4 deals with the synchrotron-based investigation of magnetoelastic effects in  $\text{Mn}_2\text{Au}$  using XMLD, which yields more direct information on the AFM order.

## 7.2 Methods

The FM and AFM thin films were grown by radio frequency magnetron sputtering.  $\text{MgO}$  (100) and  $\text{Al}_2\text{O}_3(1\bar{1}02)$  10 mm  $\times$  14 mm-substrates were utilized for depositing the samples for the transport experiments. The FM sample has the layer structure  $\text{MgO}/\text{Ni}/\text{TaO}_x$  with a polycrystalline Ni layer grown at RT. The AFM sample with the stacking sequence  $\text{Al}_2\text{O}_3/\text{Ta}(001)/\text{Mn}_2\text{Au}(001)/\text{TaO}_x$  and the reference sample  $\text{Al}_2\text{O}_3(1\bar{1}02)/\text{Ta}(001)/\text{TaO}_x$  not containing a  $\text{Mn}_2\text{Au}$  layer were used for investigating the magnetoelastic effects in AFM  $\text{Mn}_2\text{Au}$ . The sample for the X-ray studies grown at a standard  $\text{Al}_2\text{O}_3(1\bar{1}02)$  10 mm  $\times$  10 mm-substrate has the layer structure  $\text{Al}_2\text{O}_3/\text{Ta}(001)/\text{Mn}_2\text{Au}(001)/\text{AlO}_x$ . The base pressure in the vacuum chamber before deposition was  $10^{-8}$  mbar. All layers were deposited at the optimal temperature and Ar pressure [75]. A stoichiometric target was used for depositing  $\text{Mn}_2\text{Au}$ . The layer thicknesses were defined from the previously determined deposition rates. The Ta and Al layers served as the oxidation protection.

Two setups for applying a mechanical strain have been developed (see Appendix 4). The setup for the strain-dependent AMR measurements contains a sample stage, which can be moved in the vertical direction by a micrometer screw, and a piezoelectric actuator PA 90/14 with a lifting range of 100  $\mu\text{m}$  (Fig. 7.1). The base side of a triangular sample is fixed at the stage. A strain is generated by lifting the loose vertex of the sample by the piezoelectric actuator. Combined manipulation of the micrometer stage and the piezoelectric actuator allow achieving high values of strain reaching 0.3 %. The voltage to the piezoelectric actuator was applied by a Keithley 6487 Picoammeter/Voltage source. The resistance of the sample was measured in the four-point van der Pauw scheme while applying the current with a Knick J41 current source and monitoring the voltage with a Keithley 182 Digital voltmeter.

For the X-ray absorption studies, the device described above is too large to be implemented on the sample manipulator of the ALICE chamber (BESSY II, HZB). Therefore, a smaller bending device has been developed shown in Fig. 7.2(a) (see also Appendix 4). The operational principle of the device is based on generating a strain by a force applied in the center line of a substrate that is fixed at both ends (see Fig. 7.2(b)). The force is produced by a rod with an eccentric rotation axis. In the lowest state, the surface of the rod is on one level with the substrate. If rotated by an angle, the rod presses on the substrate inducing a mechanical strain, which is transmitted to the film deposited on the upper face of the substrate. In this case, the strain is less homogeneous across the film area with the maximum in the film center. A strain gauge SS-080-050-500P-S4 from ME-Meßsysteme was attached to each sample with epoxy glue M-Bond-600 for monitoring the strain value.

The spectroscopic X-ray absorption studies were performed with the ALICE chamber at the synchrotron facility BESSY II (HZB). During the experiments, the instrument was installed at the beamline UE52\_SGM with an implemented APPLE II undulator providing variable linear beam polarizations. The X-ray beam was incident normally on the sample surface and focused to a spot of 60  $\mu\text{m}$   $\times$  80  $\mu\text{m}$ . Crystallographic  $\langle 110 \rangle$  axes were oriented horizontal and vertical, i.e. in the X-ray polarization planes. A deviation of the [110] axis from the X-ray electric field direction amounting to a few degrees is to be expected. The XAS were measured in the TEY mode. The current of a Pt mesh monitor placed in the beam path is used for normalizing the TEY current. The XMLD spectrum was calculated as the normalized difference of the corresponding XAS

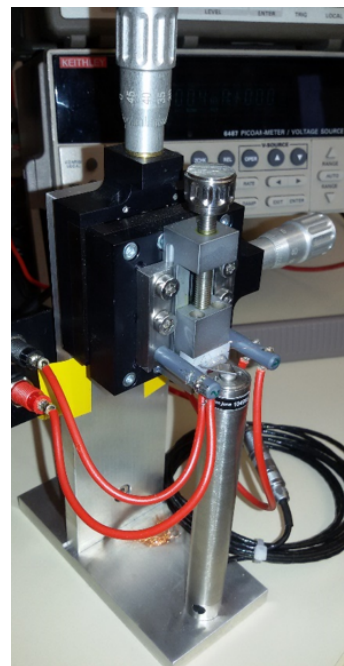


**Figure 7.1:** A photograph of the bending device used for the transport measurements.

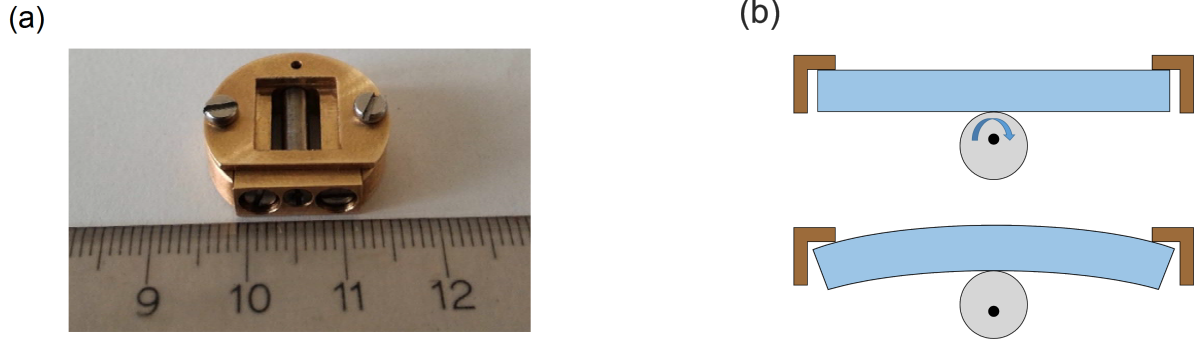


**Figure 7.2:** (a) A photograph of the vacuum compatible bending device used for the XAS studies. (b) Schematic representation of the operational principle of the bending device.

spectra measured at linear vertical (LV) and linear horizontal (LH) polarizations:

$$XMLD(E) = \frac{XAS_{LV}(E) - XAS_{LH}(E)}{XAS_{LV}^{max} + XAS_{LH}^{max}}, \quad (7.1)$$

where  $XAS_{LV}^{max}$  and  $XAS_{LH}^{max}$  are the maxima of the corresponding XAS spectra.

## 7.3 Investigation of the magnetoelastic effects by transport measurements

### 7.3.1 Optimization of the sample geometry for achieving a homogeneous strain

In order to prove the constant strain distribution in a triangular sample, the following model is considered. A film having a thickness much smaller than the substrate thickness ( $t_s$ ) is solidly bonded to the substrate. Thus, the film elongation is equal to the elongation of the substrate upper face.

A small deformation depicted in Fig. 7.3(b) is considered, for which

$$\sigma_{YY}(z, Y) = \varepsilon_{YY}(z, Y)E = \frac{zE}{R(Y)}, \quad (7.2)$$

where  $E$  is the Young modulus,  $R(Y)$  is the curvature radius, and  $z$  is the coordinate over the substrate cross-section. The torques acting on the substrate have to be equal for every cross-section:

$$F(L - Y) = \int_{-t_s/2}^{t_s/2} \int_{-(L-Y)\tan\alpha}^{(L-Y)\tan\alpha} \frac{EZ}{R(Y)} z dX dz. \quad (7.3)$$

Performing the integration results in the following expression for  $R(Y)$ :



$$R(Y) = R = \frac{Et_S^3}{6F} \tan(\alpha). \quad (7.4)$$

Thus, the strain is constant over the sample having a triangular shape. Taking notice that the curvature radius depends on the coordinate of the middle line  $R = Z''_{YY}$  and  $Z(Y) = R(L - Y)^2/2$ , the strain on the upper face of the substrate with  $z = t_S/2$  is given by:

$$\varepsilon_{YY} = \frac{t_S Z_{piezo}}{L^2}. \quad (7.5)$$

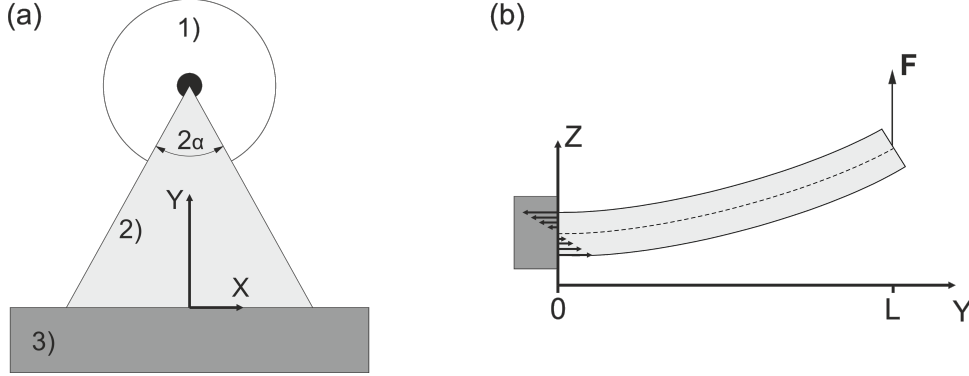


**Figure 7.3:** (a) Schematic representation of the in-house developed setup for strain-dependent transport measurements. The piezoelectric actuator (1) presses on the vertex of the triangular substrate (2) fixed in the movable stage (3). (b) The substrate cross-section featuring the acting forces.

### 7.3.2 Magnetoelastic effects in a Ni thin film

We investigate the AMR of a Ni film as a reference experiment on a well-known FM material showing a sizable AMR effect and also exhibiting a strong magnetoelastic anisotropy [182]. Sample *Ni1* with the structure MgO/Ni 35 nm/TaO<sub>x</sub> 3 nm was prepared for measuring the strain-induced AMR. Firstly, the magnetic field induced AMR was measured for determining the magnitude of the effect in the unstrained Ni film. A saturating magnetic field was applied to the sample with the help of a permanent magnet. The magnet was held close to the sample (saturation) and then was removed (remanence) along the Y-direction. Afterward, the experiment was repeated while moving the magnet along the X-direction (Fig. 7.4(a)). An AMR of 0.8 % was detected from the resistance in both saturated states, which is a typical value for Ni [183].

Knowing the expected AMR value, the strain-dependent transport measurements were performed without applying an external magnetic field. The strain-induced changes of the AMR reached 0.5 % (Fig. 7.4(b)). The resistance saturates at a strain of 0.1 % and almost recovers

to its initial value after relaxing the sample. This indicates a high degree of reversibility of the strain induced changes in the Ni domain structure. A small discrepancy between two resistance values in the unstrained state can be caused either by a time-dependent drift or by the presence of irreversible domains.

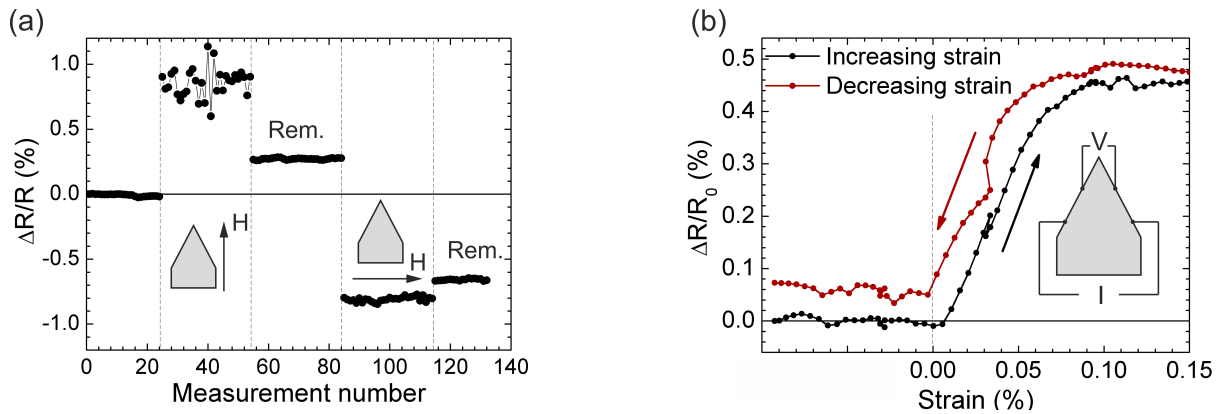


**Figure 7.4:** (a) Magnetic field induced AMR measured in sample *Ni1* for different directions of the saturating external field (shown in the insets) and at the remanent states with  $H = 0$  (denoted as Rem.). (b) Strain-dependent change of the resistance of sample *Ni1*. The inset shows the four point measurement scheme

### 7.3.3 Magnetoelastic effects in a $Mn_2Au$ thin film

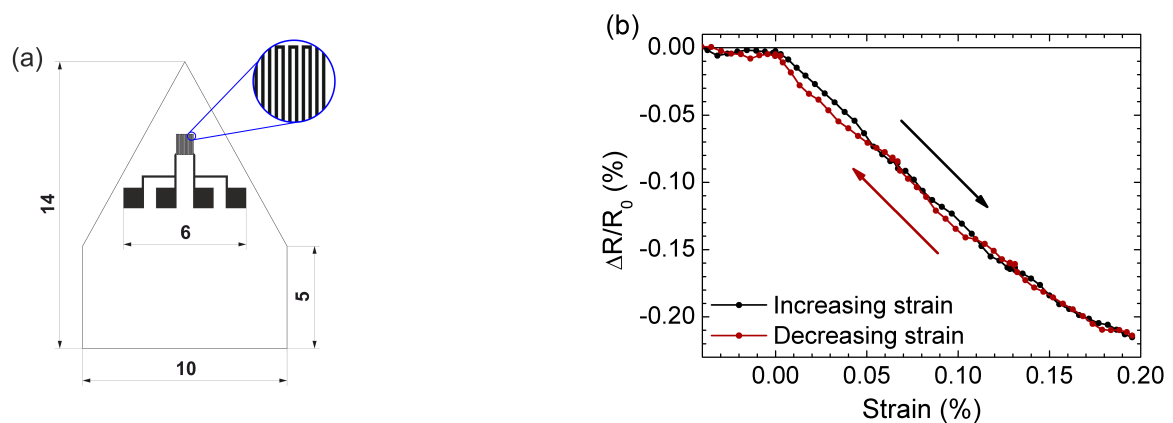


**Figure 7.5:** (a) The lithographic structure patterned on the samples *MA15ref* and *MA15* used for the transport measurements. (b) Strain-dependent changes of the resistance of sample *MA15ref* upon increasing and decreasing strain.

All  $Mn_2Au$  films are grown on Ta buffer layers, and the strain induced changes of resistance are expected in both metallic layers. Therefore, reference sample *MA15ref* with a layer structure

$\text{Al}_2\text{O}_3/\text{Ta } 10 \text{ nm}/ \text{TaO}_x 3 \text{ nm}$  was studied prior to the samples containing  $\text{Mn}_2\text{Au}$ . Please note that all films discussed in the current subsection were patterned by optical lithography (courtesy of S. Yu. Bodnar) as shown in Fig. 7.5(a). The meander structure is oriented along the strain direction, providing a more precise value of AMR. The periphery and the central contact pads are used for applying current and for measuring the voltage in the four-probe measurement scheme, respectively.

The resistance of sample *MA15ref* in the unstrained state is  $(65\,816 \pm 10) \Omega$ . Upon application of elastic strain, the resistance changes linearly with increasing  $\varepsilon$  and reaches 0.22 % at  $\varepsilon = 0.2 \%$  (Fig. 7.5(b)). A fully reversible behavior is observed when decreasing the strain.

Afterward, sample *MA15* with the stacking sequence of  $\text{Al}_2\text{O}_3/\text{Ta } 10 \text{ nm}/ \text{Mn}_2\text{Au } 75 \text{ nm}/ \text{AlO}_x 2 \text{ nm}$  was investigated. The sample resistance at zero strain is  $R_{0\text{MA15}} = 4825.0 \pm 7.2 \Omega$ . The dependence of  $\Delta R/R_0$  on the strain value is reversible (Fig. 7.6(a)) indicating that any changes in the domain structure disappear after relaxing the sample. In order to extract  $\Delta R/R_0$  for the  $\text{Mn}_2\text{Au}$  layer, the Ta contribution shown in Fig. 7.5(b) was subtracted according to:

$$\Delta R_{\text{Mn}_2\text{Au}} = R_{0\text{Mn}_2\text{Au}}^2 \left( \frac{\Delta R_{\text{MA15}}}{R_{0\text{MA15}}^2} - \frac{\Delta R_{\text{MA15ref}}}{R_{0\text{MA15ref}}^2} \right), \quad (7.6)$$

where  $R_{0\text{Mn}_2\text{Au}} = R_{0\text{MA15}} R_{0\text{MA15ref}} / (R_{0\text{MA15ref}} - R_{0\text{MA15}}) = 5206.7 \pm 8.9 \Omega$ . No saturation of the  $\text{Mn}_2\text{Au}$  layer resistance with increasing strain is observed (see Fig. 7.6(b)) in contrast to the case of Ni (Fig. 7.4(b)). Therefore, it is not possible to distinguish between the strain induced AMR and the non-magnetic contributions caused by lattice distortions. A different method much more sensitive to the magnetic order, such as XMLD, is necessary for analyzing the magnetoelastic effects in  $\text{Mn}_2\text{Au}$ .

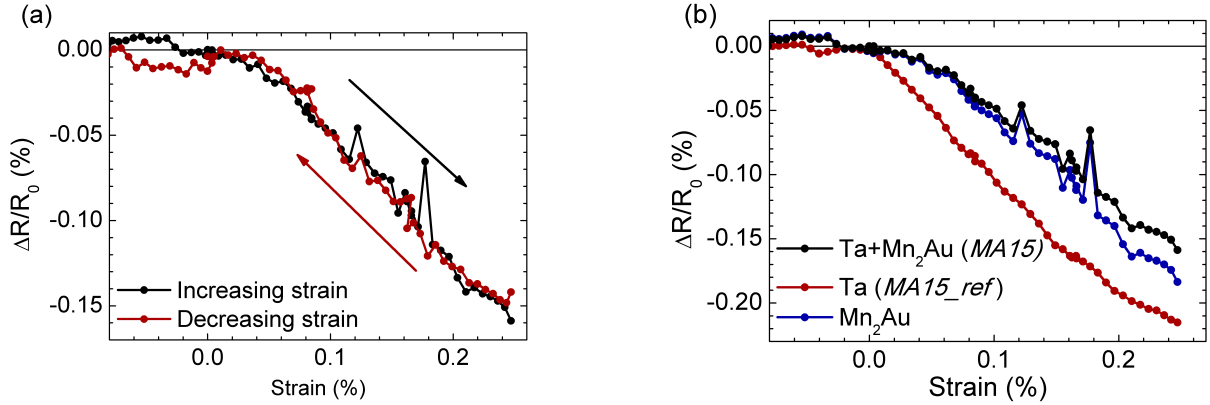


**Figure 7.6:** (a) Strain-dependent changes of the resistance of sample *MA15* upon increasing and decreasing strain. (b)  $\Delta R/R_0$  of the  $\text{Mn}_2\text{Au}$  layer determined according to Eq. (7.6).

## 7.4 Investigation of the magnetoelastic effects in $\text{Mn}_2\text{Au}$ by XMLD measurements

Sample *MA16* with the stacking sequence of  $\text{Al}_2\text{O}_3/\text{Ta}$  10 nm/  $\text{Mn}_2\text{Au}$  60 nm/  $\text{AlO}_x$  2 nm was used for strain-dependent XMLD experiments. The sample was mounted to the small bending device and fixed to the sample holder in the ALICE chamber. The XMLD measurements were performed at several values of strain. Increasing the strain was accomplished outside of the vacuum chamber by manually rotating the eccentric rod. The resistance of the strain gauge was monitored before and after each XMLD measurement. The difference in the readings did not exceed  $1\ \Omega$ , corresponding to an absolute strain variation of  $0.003\ \%$  during a measurement. The total error of the determined strain did not exceed  $0.01\ \%$ .

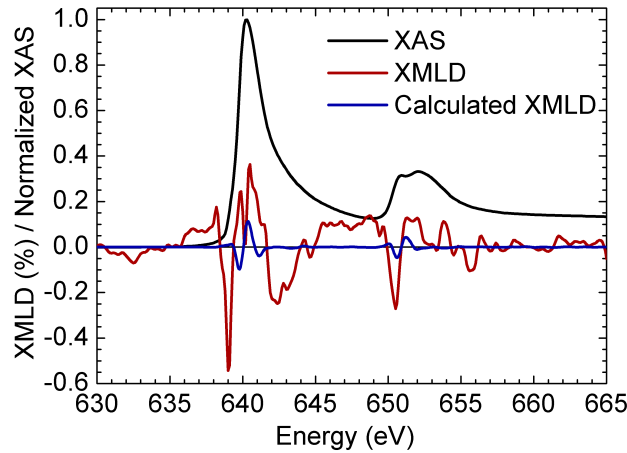


**Figure 7.7:** The XAS and corresponding XMLD spectrum measured in the unstrained sample *MA16*.

The XMLD spectrum measured in the unstrained sample does not show a clear XMLD minus/plus feature at the  $L_3$  edge (Fig. 7.7). This is a clear sign that the  $\langle 110 \rangle$ -domains are equally distributed. Next, the XMLD measurements were performed for several values of strain up to  $0.16\ \%$ . A higher strain value caused a destruction of the  $\text{Al}_2\text{O}_3$  substrate. The tensile strain during this experiment was applied along the easy  $[110]$  direction. The representative strain-dependent spectra are shown in Figure 7.8.

The difference of two XAS spectra corresponding to the electric field parallel and perpendicular to the Néel vector gives an XMLD spectrum with the characteristic minus/plus-pattern at the  $L_3$ -edge of Mn (see Appendix 3). The XMLD spectra presented in Figure 7.8, which are calculated according to Eq. (7.1), exhibit the expected minus/plus-pattern. Accordingly, the Néel vector in the strained state is oriented in the vertical direction, perpendicular to the horizontally applied strain.

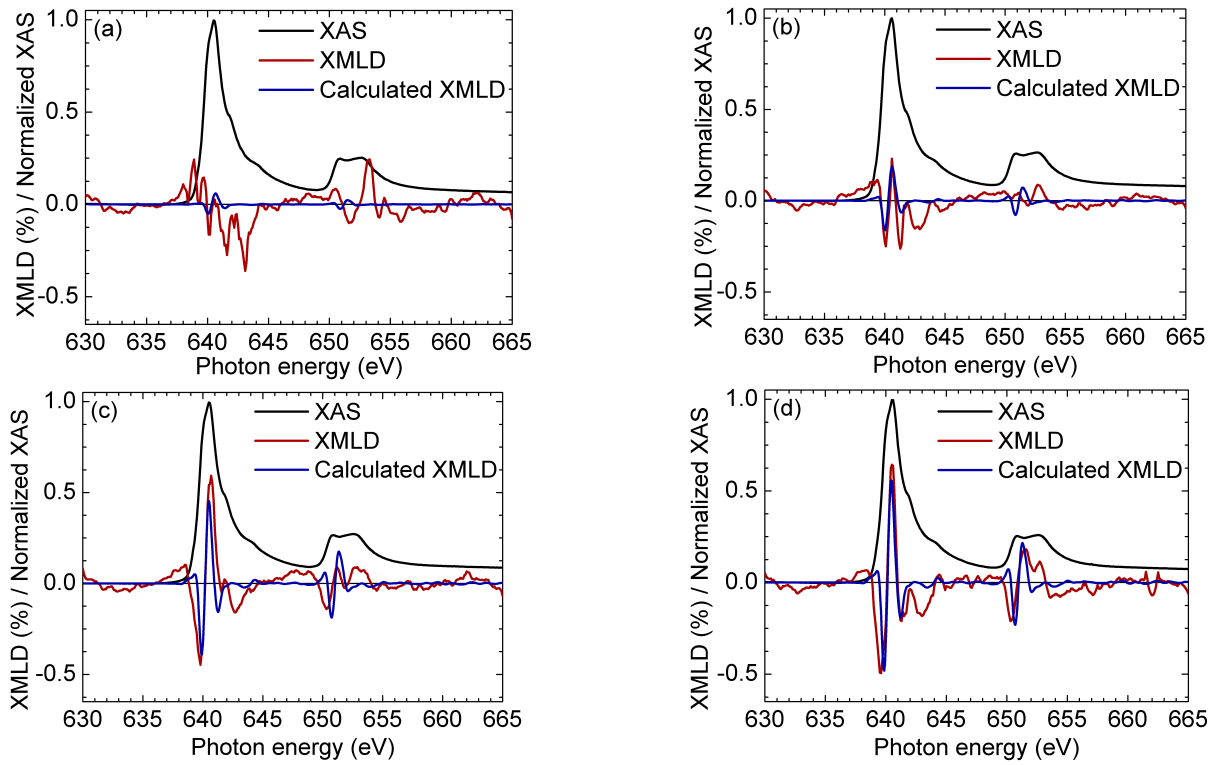


**Figure 7.8:** XAS and corresponding XMLD spectra measured in *MA16* at a strain of (a) 0.06 %, (b) 0.08 %, (c) 0.10 %, and (d) 0.16 %

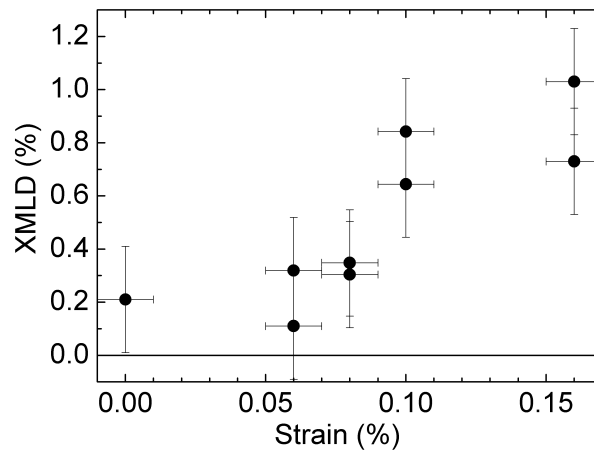


**Figure 7.9:** Strain-dependent difference of the maximum and the minimum of XMLD. The dots indicate the XMLD values measured at different points at the sample surface (see the text).

The theoretical spectrum calculated by the density functional theory (DFT) methods (see Appendix 3) multiplied by a factor ( $F \times XMLD_{th}(E)$ ) was used for fitting the experimental XMLD

( $XMLD_{exp}(E)$ ) spectra with  $F$  being the fitting parameter. The magnitude of the XMLD effect was determined as the difference of the maximal and the minimal value of  $F \times XMLD_{th}(E)$  providing the best fit at the  $L_3$  edge (Fig. 7.9). A pair of data points for each of the strain values in Figure 7.9 represent the XMLD obtained at two points on the sample surface separated by 0.5 mm. The difference between the obtained XMLD values may be caused by the residual growth induced strain in the film, inhomogeneous distribution of the actual strain, or by growth inhomogeneities of the  $Mn_2Au$  layer. In spite of the noisy data, there is, beyond any doubt, an increase of the XMLD effect with increasing strain, which reaches 1% at  $\varepsilon = 0.16\%$ .

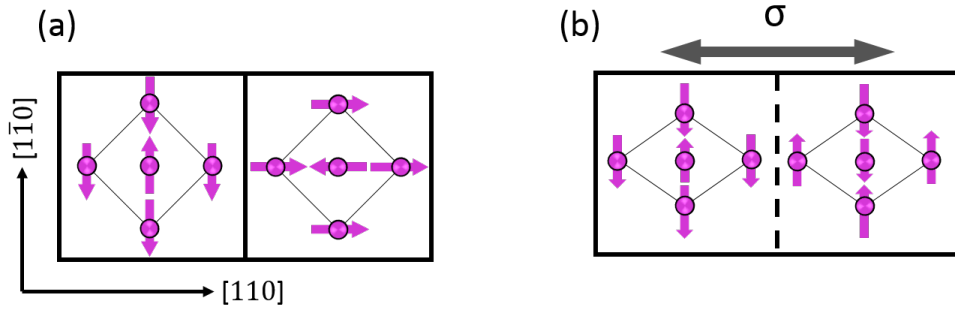


**Figure 7.10:** (a) Two equivalent AFM domains in unstrained  $Mn_2Au$ . (b) Schematic representation of the strain induced lattice distortion resulting in a uniaxial anisotropy. The relative deformation in (b) is strongly exaggerated.

The observed experimental results can be described by the following simple model (Fig. 7.10). The AFM structure of an unstrained sample consists of two types of domains with the Néel vector rotated by  $90^\circ$  and the expected XMLD signal, as averaged over both types of domains, is zero (Fig. 7.10(a)). A mechanical strain distorts the tetragonal  $Mn_2Au$  lattice. The imposed uniaxial anisotropy may favor one direction on the expense of the other one resulting in a finite XMLD signal. Only one in-plane easy axis perpendicular to the strain direction is expected to remain in the material after reaching the saturation value of strain.

## 7.5 Conclusion

An experimental stage for strain-dependent transport measurements in thin magnetic films was constructed and assembled, with a piezoelectric actuator providing a controllable strain value. For demonstrating the feasibility of the method and for testing the equipment, the dependence of the AMR in a Ni thin film on the applied strain was measured. The detected resistance change reaches a saturation value of 0.5% at a strain level of  $\varepsilon = 0.1\%$ , which is consistent with the field induced AMR data obtained in the same sample. This experiment confirms that a change of the magnetic domain distribution in a metallic thin film can indeed be detected by

AMR measurements.

With this positive test, the dependence of the  $\text{Mn}_2\text{Au}$  thin-film resistance on the applied strain was determined. Experimental data were obtained for a  $\text{Mn}_2\text{Au}$  grown on a Ta buffer layer and for a reference sample containing only the Ta layer. The resistance changes linearly for  $\varepsilon$  up to 0.25 % with no saturation achieved. Presumably, non-magnetic strain-dependent contributions to the resistance dominate in this experiment. The sensitivity of the experimental method to the AFM order can be enhanced by growing  $\text{Mn}_2\text{Au}$  on the  $\text{Al}_2\text{O}_3$ -substrate without a buffer layer, which was suggested in Ref. [184].

Please note that a control experiment based on reorienting the magnetic moments by an external field, as done for the Ni film, was not possible for the  $\text{Mn}_2\text{Au}$  sample. The reason for that is an extremely high magnetic field value necessary for orienting the AFM moments in  $\text{Mn}_2\text{Au}$ .

In order to directly probe the changes in the domain distribution upon applying a mechanical strain, XMLD measurements were performed in a  $\text{Mn}_2\text{Au}$  thin film. The external strain was applied using a vacuum compatible bending device and monitored by semiconductor strain gauges. An increase of the XMLD effect up to 1 % proves the possibility to reorient AFM moments (domains) at a strain level of 0.1 %. A model is proposed for explaining the experimental data, which predicts the emergence of an additional uniaxial anisotropy due to lattice distortions. This leads to a single domain state at a high strain value instead of two equivalent intrinsic domains in the tetragonal unstrained  $\text{Mn}_2\text{Au}$ .

The XMLD effect turns out to be slightly different when measured in different areas on the sample surface. This variation is presumably caused by an inhomogeneous strain distribution in the film plane. Unfortunately, this renders a quantitative analysis of the experimental data difficult. Precise investigation of the magnetoelastic effect in  $\text{Mn}_2\text{Au}$  requires means of measuring the strain locally. Moreover, a flexible substrate able to sustain higher values of strain would also be favorable for further analysis. In any case, the present XMLD results confirm that reorientation of AFM domains in  $\text{Mn}_2\text{Au}$  by application of strain is feasible.





## 8 Summary and Outlook

In this work, we investigated the magnetic properties of epitaxial  $\text{Mn}_2\text{Au}$  thin films, which is a promising candidate for antiferromagnetic spintronics. Also, we scrutinized the possibility of manipulating the AFM domains in this material by extremely high magnetic fields and by elastic strain.

The first experiments were aimed at determining the exchange constant, an important parameter of an AFM, which among other things characterizes the ordering temperature of the material and the spin-flop field value. For this, we measured the perpendicular susceptibility in magnetic fields up to 8 T by XMCD spectroscopy. The sum-rule analysis of the XMCD spectra measured at RT provided the value of induced spin and orbital moments. Using these values the exchange constant  $J = (22 \pm 5)$  meV was calculated. The large ratio of induced perpendicular orbital moment and spin moment reaching 30 % is explained based on a simplified model for the effect of an external field on magnetic moments in a solid. Within this model, the external field has a smaller effect on the spin moment because it is strongly coupled to the neighbors via exchange interactions. In contrast, the orbital moment, that is coupled more weakly by the spin-orbit coupling, is rotated to a larger angle towards the field. Taking into account different absolute values of spin moment and of orbital moment, this results in similar projected values on the field axis. Comparing the field induced perpendicular spin moments measured at RT and at 7 K granted the loose spin concentration in the near-surface region of our thin  $\text{Mn}_2\text{Au}$  films. A relatively high obtained value of 6 % is due to a contribution of defects in thin films including antisite disorder and grain boundaries. The employed experimental technique can be used for characterizing a wide variety of AFM thin films. Moreover, for materials with a lower  $T_N$ , larger induced moments are expected, which serves decreasing the experimental error.

Furthermore, a ferromagnetic layer deposited on top of a  $\text{Mn}_2\text{Au}$  film was used for extracting information about the magnetic properties of the AFM from the exchange bias measurements. High-quality epitaxial  $\text{Mn}_2\text{Au}$  films grown at optimal deposition conditions induce a broadening of the FM hysteresis loop with no shift. This is explained by a small anisotropy of thin  $\text{Mn}_2\text{Au}$  layers with a thickness  $\leq 7$  nm and a very high Néel temperature of the thicker films preventing a non-destructive field cooling protocol, usually required for inducing an exchange bias effect. For the purpose of lowering the  $T_N$ , samples with a smaller crystallite size were prepared. The reduction of the crystallite size was achieved by changing the substrate temperature during the  $\text{Mn}_2\text{Au}$  deposition resulting in a Néel temperature below 500 K. The maximum value of exchange bias measured for such a sample at 10 K reaches 210 Oe. A  $\text{Mn}_2\text{Au}$  film deposited on an epitaxial Fe layer in magnetic saturation also induces an exchange bias, which is, however, smaller than that for the above-discussed films. This behavior is most likely due to a lower

crystalline quality of the  $\text{Mn}_2\text{Au}$  layer grown on Fe as compared to normal layer sequence: Fe on top of  $\text{Mn}_2\text{Au}$ .

A ferromagnetic tracer layer deposited on top of the AFM film was used for investigating the AFM domains in  $\text{Mn}_2\text{Au}$ . The FM domains were visualized in a  $\text{Mn}_2\text{Au}/\text{Py}$  sample by Kerr microscopy. A small size of the observed domains, very unusual for Py, indicates that this domain pattern is, indeed, imprinted by the AFM layer. However, the limited resolution of an optical microscope does not allow to investigate the details of the domain size and shape. In order to improve the resolution, XMCD-PEEM measurements were performed for  $\text{Mn}_2\text{Au}/\text{Fe}$  samples. In general, the obtained domain images agree with the findings of the Kerr microscopy. The FM domains have irregular shapes and presumably follow those of the AFM. The average size of antiferromagnetic domains estimated from this experiment is  $\sim 1 \mu\text{m}$ .

XMLD-PEEM provides an opportunity to directly visualize the AFM domains in thin films.  $\text{Mn}_2\text{Au}$  thin films covered with a thin Al capping layer for oxidation protection, which is favorable for total electron yield photoemission measurements, were prepared for such experiments. Combined spectroscopy and microscopy measurements are necessary to maximize the magnetic contrast in an XMLD-PEEM experiment for conductive AFMs without a multiplet structure at the absorption edges. Using laterally integrated XMLD spectra for a  $\text{Mn}_2\text{Au}$  sample with oriented magnetic moments, the energies corresponding to the maximum and minimum of the XMLD were determined. The magnetic contrast was obtained from the asymmetry of the images taken at these energies. The magnetic domains in an as-grown sample have an average size of  $\sim 1 \mu\text{m}$ . From the similarity of the directly measured  $\text{Mn}_2\text{Au}$  domains and those obtained by XMCD-PEEM in the  $\text{Mn}_2\text{Au}/\text{Fe}$  heterostructure we infer that a thin FM layer can indeed be used as a tracer for investigating the AFM domains.

After characterizing the magnetic properties of our AFM thin films, we addressed the question of manipulating the magnetic moments in  $\text{Mn}_2\text{Au}$ . The first experiment was aimed at orienting the magnetic domains by applying a high external field via a spin-flop transition. For the samples exposed to a field higher than 30 T along an easy axis, we observed a significant increase of the size of the domain with the Néel vector pointing perpendicular to the field. Application of a very high pulsed magnetic field of 70 T aligned along a hard axis of the sample causes a slight increase of the domain size, while the areas covered by two equivalent in-plane domains remain similar. An important aspect is the non-reversibility of the field-induced Néel vector reorientation in  $\text{Mn}_2\text{Au}$ , which is still present after several months passed between applying the magnetic field and performing the microscopy measurements.

These findings pave the way for investigating the changes in the  $\text{Mn}_2\text{Au}$  caused by current pulses via Néel spin-orbit torque (NSOT) using XMLD-PEEM [22]. Such experiments have already been performed in  $\text{CuMnAs}$ , another conductive AFM material where NSOT can be realized [76; 42]. To this end, the PEEM studies shed light on numerous important aspects of the current-switching effect in  $\text{CuMnAs}$ . The established procedure for imaging the  $\text{Mn}_2\text{Au}$  domains will

provide a deeper understanding of NSOT in  $\text{Mn}_2\text{Au}$  thin films and lead to further optimization for a reliable Néel vector switching for future spintronics devices.

The second method for manipulating the AFM order addressed in this work is magneto-elastic coupling, which links the magnetic and the mechanical properties of a material. In this work, a controllable strain was applied to magnetic thin films by bending the substrate, which caused an elongation of the film along an easy magnetic axis. The strain induced changes in the domain structure of a conductive material can be studied by measuring AMR, i.e. changes of the material resistance caused by reorientation of the magnetic moments. This method was successfully applied to ferromagnetic Ni samples but did not provide convincing evidence for domain reorientation in  $\text{Mn}_2\text{Au}$ . Nevertheless, optimization of the sample structure can improve this method into a reliable tool for investigating magnetoelastic effects in  $\text{Mn}_2\text{Au}$ . The Néel vector orientation in strained  $\text{Mn}_2\text{Au}$  thin films was directly probed by XMLD spectroscopy. An increase of XMLD measured at strain values above 0.1% was observed. Analysis of the experimental spectra involving DFT calculations performed by the FP-LAPW ELK software proves that the change of XMLD is due to a reorientation of magnetic moments in the material, which orient themselves perpendicular to the elongation direction.



# 9 Appendix

## 9.1 The list of samples

The substrate is either  $\text{Al}_2\text{O}_3$  (1 $\bar{1}$ 02) or  $\text{MgO}$  (100). All deposited layers consist predominantly of (001) oriented crystallites with the in-plane epitaxial relation  $\text{Ta}$  (001)[100]  $\parallel$   $\text{Mn}_2\text{Au}$  (001)[100]  $\parallel$   $\text{Fe}$  (001)[100], if not specified otherwise.

Sample	Layer sequence	$\text{Mn}_2\text{Au}$ deposition temperature	Comment
MA1	$\text{Al}_2\text{O}_3/\text{Ta}$ 18 nm/ / $\text{Mn}_2\text{Au}$ 10 nm/ $\text{TaO}_x$ 3 nm	600 °C	
MA2	$\text{Al}_2\text{O}_3/\text{Ta}$ 18 nm/ / $\text{Mn}_2\text{Au}$ 4 nm/ $\text{Fe}$ 3 nm/ $\text{TaO}_x$ 3 nm	600 °C	
MA3	$\text{Al}_2\text{O}_3/\text{Ta}$ 18 nm/ / $\text{Mn}_2\text{Au}$ 7 nm/ $\text{Fe}$ 3 nm/ $\text{TaO}_x$ 3 nm	600 °C	
MA4	$\text{Al}_2\text{O}_3/\text{Ta}$ 18 nm/ / $\text{Mn}_2\text{Au}$ 10 nm/ $\text{Fe}$ 3 nm/ $\text{TaO}_x$ 3 nm	500 °C	
MA5	$\text{Al}_2\text{O}_3/\text{Ta}$ 18 nm/ / $\text{Mn}_2\text{Au}$ 10 nm/ $\text{Fe}$ 3 nm/ $\text{TaO}_x$ 3 nm	450 °C	
MA6	$\text{MgO}/\text{Fe}$ 5 nm/ / $\text{Mn}_2\text{Au}$ 10 nm/ $\text{TaO}_x$ 3 nm	RT	
MA7	$\text{Al}_2\text{O}_3/\text{Ta}$ 18 nm/ / $\text{Mn}_2\text{Au}$ 66 nm/ $\text{Py}$ 4 nm/ $\text{TaO}_x$ 3 nm	600 °C	
MA8	$\text{Al}_2\text{O}_3/\text{Ta}$ 18 nm/ / $\text{Mn}_2\text{Au}$ 60 nm/ $\text{Fe}$ 10 nm/ $\text{AlO}_x$ 5 nm	600 °C	
MA9	$\text{Al}_2\text{O}_3/\text{Ta}$ 15 nm/ / $\text{Mn}_2\text{Au}$ 10 nm/ $\text{Fe}$ 1 nm/ $\text{AlO}_x$ 2 nm	500 °C	Exposed to a field of 70 T along [110] direction

Sample	Layer sequence	Mn <sub>2</sub> Au deposition temperature	Comment
MA9ref	Al <sub>2</sub> O <sub>3</sub> /Ta 15 nm/ /Mn <sub>2</sub> Au 10 nm/Fe 1 nm/AlO <sub>x</sub> 2 nm	500 °C	
MA10	Al <sub>2</sub> O <sub>3</sub> /Ta 30 nm/ /Mn <sub>2</sub> Au 240 nm/AlO <sub>x</sub> 2 nm	600 °C	
MA11	Al <sub>2</sub> O <sub>3</sub> /Ta 30 nm/ /Mn <sub>2</sub> Au 240 nm/AlO <sub>x</sub> 2 nm	600 °C	Exposed to a field of 30 T along [110] direction
MA12	Al <sub>2</sub> O <sub>3</sub> /Ta 30 nm/ /Mn <sub>2</sub> Au 240 nm/AlO <sub>x</sub> 2 nm	600 °C	Exposed to a field of 50 T along [110] direction
MA13	Al <sub>2</sub> O <sub>3</sub> /Ta 30 nm/ /Mn <sub>2</sub> Au 240 nm/AlO <sub>x</sub> 2 nm	600 °C	Exposed to a field of 70 T along [100] direction
MA14	Al <sub>2</sub> O <sub>3</sub> /Ta 18 nm/ /Mn <sub>2</sub> Au 80 nm/TaO <sub>x</sub> 3 nm	600 °C	
MA15	Al <sub>2</sub> O <sub>3</sub> /Ta 10 nm/ /Mn <sub>2</sub> Au 75 nm/TaO <sub>x</sub> 3 nm	600 °C	Substrate size 10 mm × 14 mm
MA15ref	Al <sub>2</sub> O <sub>3</sub> /Ta 10 nm/ /TaO <sub>x</sub> 3 nm	600 °C	Substrate size 10 mm × 14 mm
MA16	Al <sub>2</sub> O <sub>3</sub> /Ta 10 nm/ /Mn <sub>2</sub> Au 60 nm/AlO <sub>x</sub> 2 nm	600 °C	
Ni1	MgO/Ni 35 nm/ /TaO <sub>x</sub> 3 nm	600 °C	Substrate size 10 mm × 14 mm

RT - room temperature

## 9.2 Collective magnonic modes in a tetragonal easy plane antiferromagnet

The out-of-plane hard axis is  $z$ , the easy axes are  $x$  and  $y$ . The spins in equilibrium point along  $\pm x$ -axis. The following expression for the anisotropy energy density is used (see Section 1.4):

$$\epsilon_A = \sum_{\alpha=1,2} K_{2\perp} \beta_{\alpha z}^2 + K_{4\perp} \beta_{\alpha z}^4 + K_{4\parallel} (\beta_{\alpha x}^4 + \beta_{\alpha y}^4), \quad (9.1)$$

where the sum over the atom number  $i$  is replaced by the sum over the sublattice number  $\alpha$ . In the linear approximation, considering that in the excited material  $\beta_{1x} \approx 1$  and  $|\beta_{1y}|, |\beta_{1z}| \ll 1$  and  $\beta_{2x} \approx -1$  and  $|\beta_{2y}|, |\beta_{2z}| \ll 1$ :

$$\epsilon_A = \sum_{\alpha=1,2} K_{2\perp} \beta_{\alpha z}^2 - 2K_{4\parallel} \beta_{\alpha z}^2 - 2K_{4\parallel} \beta_{\alpha y}^2 \approx \sum_{\alpha=1,2} K_{2\perp} \beta_{\alpha z}^2 + 2K_{4\parallel} \beta_{\alpha y}^2. \quad (9.2)$$

The total energy is the sum of the exchange, the anisotropy, and the Zeeman energy:

$$\epsilon_{total} = J_{eff} \beta_1 \beta_2 + \sum_{\alpha=1,2} K_{2\perp} \beta_{\alpha z}^2 + 2K_{4\parallel} \beta_{\alpha y}^2 + \mu_0 H M_S (\beta_{1x} + \beta_{2x}), \quad (9.3)$$

where magnetic field  $H$  is directed along the  $x$ -axis. Landau-Lifshitz equation, with  $\gamma=1$  is given by:

$$M_S \frac{d\beta_\alpha}{dt} = \gamma \left[ \beta_\alpha \times \frac{\partial \epsilon_{total}}{\partial \beta_\alpha} \right], \quad (9.4)$$

where  $M_S$  is the sublattice magnetization. For different components of the vectors  $\beta_1$  and  $\beta_2$ , Eq. (9.4) takes the form:

$$\begin{aligned} \frac{M_S}{\gamma} \frac{d\beta_{1y}}{dt} &= -(\mu_0 H M_S + 2K_{2\perp} + J_{eff}) \beta_{1z} - J_{eff} \beta_{2z}, \\ \frac{M_S}{\gamma} \frac{d\beta_{2y}}{dt} &= J_{eff} \beta_{1z} - (\mu_0 H M_S - 2K_{2\perp} - J_{eff}) \beta_{2z}, \\ \frac{M_S}{\gamma} \frac{d\beta_{1z}}{dt} &= (\mu_0 H M_S + 4K_{4\parallel} + J_{eff}) \beta_{1y} + J_{eff} \beta_{2y}, \\ \frac{M_S}{\gamma} \frac{d\beta_{2z}}{dt} &= -J_{eff} \beta_{1y} + (\mu_0 H M_S - 4K_{4\parallel} - J_{eff}) \beta_{2y}. \end{aligned} \quad (9.5)$$

Using the notations  $H_E = J_{eff}/(\mu_0 M_S)$ ,  $H_A^\parallel = 4K_{4\parallel}/(\mu_0 M_S)$ , and  $H_A^\perp = 2K_{2\perp}/(\mu_0 M_S)$ , Eq. (9.5) can be written as:

$$\frac{1}{\gamma} \frac{d}{dt} \begin{pmatrix} \beta_{1y} \\ \beta_{2y} \\ \beta_{1z} \\ \beta_{2z} \end{pmatrix} = \hat{\Omega} \begin{pmatrix} \beta_{1y} \\ \beta_{2y} \\ \beta_{1z} \\ \beta_{2z} \end{pmatrix}, \quad (9.6)$$

where  $\hat{\Omega}$  is given by the expression:

$$\hat{\Omega} = \begin{pmatrix} 0 & 0 & -(H + H_E + H_A^\perp) & -H_E \\ 0 & 0 & H_E & -(H - H_E - H_A^\perp) \\ H + H_E + H_A^\parallel & H_E & 0 & 0 \\ -H_E & H - H_E - H_A^\parallel & 0 & 0 \end{pmatrix}. \quad (9.7)$$

The frequencies of the harmonic modes  $\beta_{\alpha i} = \beta_{\alpha i}^0 e^{i\omega t}$  are given by the eigenvalues of Eq. (9.7):

$$\begin{aligned} \omega_1 &= \gamma H \pm \gamma \sqrt{2H_E H_A^\perp}, \\ \omega_2 &= \gamma H \pm \gamma \sqrt{2H_E H_A^\parallel}, \end{aligned} \quad (9.8)$$

where the anisotropy fields are considered to be much smaller than the exchange field.

The resonance frequencies approach zero at the spin-flop field. Therefore,  $H_{SF} = \sqrt{2H_E H_A^\perp}$  for the out-of-plane field and  $H_{SF} = \sqrt{2H_E H_A^\parallel}$  for the in-plane field.

## 9.3 Density functional theory calculation of density of states and of X-ray magnetic linear dichroism in Mn<sub>2</sub>Au

### 9.3.1 A short introduction to density functional theory

Density functional theory (DFT) is a universal method for calculating the electronic structure of different classes of materials including atoms, molecules, and crystals. The calculation of the electronic structure starts with the stationary Schrödinger equation:

$$\hat{\mathcal{H}}\psi(\mathbf{r}_1, \dots, \mathbf{r}_n, \mathbf{R}_1, \dots, \mathbf{R}_m) = E\psi(\mathbf{r}_1, \dots, \mathbf{r}_n, \mathbf{R}_1, \dots, \mathbf{R}_m), \quad (9.9)$$

where  $\hat{\mathcal{H}}$  is the Hamiltonian of the system and  $\psi$  is the wave function, depending on the coordinates of  $n$  electrons and  $m$  nuclei. The Hamiltonian in Eq. (9.9) contains the terms corresponding to the kinetic energies of the electrons and the nuclei and to the electron-electron, electron-nucleus, and to the nucleus-nucleus Coulomb interactions:



$$\hat{\mathcal{H}} = \hat{T}_e + \hat{T}_i + \hat{V}_{ee} + \hat{V}_{ei} + \hat{V}_{ii}. \quad (9.10)$$

The Born-Oppenheimer approximation takes into account that the electron mass is several orders of magnitude smaller than the mass of a nucleus. Therefore, the nuclei are considered to be immobilized creating the constant external potential for the electrons  $\hat{V}_{ext} = \hat{V}_{ei}$ . This assumption allows omitting the second and the third terms in Eq. (9.10):

$$\hat{\mathcal{H}} = \hat{T}_e + \hat{V}_{ee} + \hat{V}_{ext}. \quad (9.11)$$

The DFT approach is based on two theorems formulated by Hohenberg and Kohn [185]. The first theorem states that the external potential  $V_{ext}(\mathbf{r})$  is uniquely determined by the ground-state density distribution  $\rho(\mathbf{r})$ . This statement indicates that there is a one-to-one correspondence between the Hamiltonian in Eq. (9.11), depending on  $V_{ext}(\mathbf{r})$  and the number of electrons  $n$  and  $\rho(\mathbf{r})$ . Consequently, the energy calculated for Eq. (9.10) is the functional of the electron density:

$$E[\rho] = T[\rho] + V_{ee}[\rho] + V_{ext}[\rho]. \quad (9.12)$$

The second Hohenberg-Kohn theorem states that the  $E[\rho]$  is minimal for the density corresponding to the ground state of the system, which directly follows from the variational principle of quantum mechanics.

A further step to an efficient implementation of DFT methods was introduced by Kohn and Sham. They suggested to replace the kinetic energy  $T[\rho]$  with the energy of a system of  $n$  non-interacting electrons  $T_S[\rho] = \sum_i \langle \phi_i | \nabla^2 | \phi_i \rangle$  using the wave functions providing the necessary electron density  $\rho(\mathbf{r}) = \sum_i \langle \phi_i | \phi_i \rangle$ . The classical Hartree term in the form:

$$V_H[\rho] = \int \int \frac{\rho(\mathbf{r}_i)\rho(\mathbf{r}_j)}{|\mathbf{r}_i - \mathbf{r}_j|} d\mathbf{r}_i d\mathbf{r}_j \quad (9.13)$$

is separated from  $V_{ee}[\rho]$  resulting in:

$$E[\rho] = T_S[\rho] + V_H[\rho] + V_{ext}[\rho] + E_{xc}[\rho], \quad (9.14)$$

$$E_{xc}[\rho] = (T[\rho] - T_S[\rho]) + (V_{ee}[\rho] - V_C[\rho]),$$

where  $E_{xc}[\rho]$  is exchange correlation energy. Varying Eq. (9.14), one obtains the Kohn-Sham equations:

$$-\frac{1}{2}\nabla^2\psi_{i\sigma}(\mathbf{r}) + \left[ V_{ext}(\mathbf{r}) + \int \frac{\rho(\mathbf{r}')}{|\mathbf{r} - \mathbf{r}'|} + \frac{\delta E_{xc}[\rho]}{\delta \rho(\mathbf{r})} \right] \psi_{i\sigma} = E_{i\sigma}\psi_{i\sigma}. \quad (9.15)$$

The explicit form of  $V_{xc}(\mathbf{r}) = \delta E_{xc}[\rho]/\delta \rho(\mathbf{r})$  is not known and different approaches are used for evaluating it. These include the local density approximation (LDA), where  $V_{xc}(\rho(\mathbf{r}))$  is assumed to depend only on  $\rho(\mathbf{r})$ , and the generalized gradient approximation (GGA) with

$V_{xc}(\rho(\mathbf{r}), \nabla\rho(\mathbf{r}))$ .

### 9.3.2 A short introduction to the linear augmented plane wave method

One of the important tasks for implementing the DFT methods is to properly choose the basis wave functions for the potential  $V_{ext}(\mathbf{r})$ . One of the possible choices is to specify a muffin-tin potential. Within this approximation, each nucleus is surrounded by a sphere (S) with a spherically symmetric potential within S and a constant potential in the interstitial region (I). Full potential approaches do not require such restrictions and deal with the atomic potential in the whole space. Correspondingly, the wave functions are represented as atomic orbitals in S and Bloch functions in I:

$$\left\{ \begin{array}{ll} \frac{1}{\sqrt{V}} \sum_{\mathbf{G}} C_{\mathbf{G}} e^{i(\mathbf{k}+\mathbf{G})\mathbf{r}} & \mathbf{r} \text{ in } I, \\ \sum_{lm} A_{lm} u_l(r; E_l) Y_{lm}(\theta, \phi) & \mathbf{r} \text{ in } S. \end{array} \right. \quad (9.16)$$

Please note that the Bloch functions are expanded in a Fourier row. This choice of the wave function is the base of the augmented plane wave method (APW). The function  $u_l(r; E_l)$  is the solution of the Schrödinger equation  $(-\frac{1}{2}\nabla^2 + V(r) - E_l)u_l(r; E_l) = 0$ . Since  $u_l(r; E_l)$  depends on  $E$ , the Schrödinger equation provides the correct wave function if  $E = E_{\mathbf{k}}$  in accordance with the dispersion relation for a electronic band. Absence of variational freedom with respect to  $E$  increases the necessary computational power if  $E_{\mathbf{k}}$  is unknown.

An extension of the APW method called linear augmented plane wave (LAPW) method adds the derivative of the wave function with respect to  $E$ :

$$\left\{ \begin{array}{ll} \frac{1}{\sqrt{V}} \sum_{\mathbf{G}} C_{\mathbf{G}} e^{i(\mathbf{k}+\mathbf{G})\mathbf{r}} & \mathbf{r} \text{ in } I, \\ \sum_{lm} (A_{lm} u_l(r; E_l) + B_{lm} \dot{u}_l(r; E_l)) Y_{lm}(\theta, \phi) & \mathbf{r} \text{ in } S. \end{array} \right. \quad (9.17)$$

In this case, the wave function for an arbitrary energy is  $u_l(r; E) = u_l(r; E_l) + (E - E_l)\dot{u}_l(r; E_l) + O((E - E_l)^2)$ , which results in an error of  $O((E - E_l)^4)$  in the band energy.

For some problems, e.g. for calculating the X-ray absorption spectra, it is necessary to explicitly take into account the core atomic states. Since the core states are strongly localized near the nucleus, it is convenient to describe them in terms of local orbitals, which exist only in S and do not expand into I:

$$\left\{ \begin{array}{ll} 0 & \mathbf{r} \text{ in } I, \\ \sum_{lm} u_l^{LO}(r; E_l) Y_{lm}(\theta, \phi) & \mathbf{r} \text{ in } S. \end{array} \right. \quad (9.18)$$

### 9.3.3 The results obtained for Mn<sub>2</sub>Au

The DFT simulations were performed with the ELK full-potential linear augmented plane wave (FP-LAPW) software [60]. The valence band density of states (DOS) was calculated for bct Mn<sub>2</sub>Au with the fixed lattice parameters  $a = 3.328 \text{ \AA}$  and  $c = 8.539 \text{ \AA}$ . The spin of Mn atoms was calculated self-consistently by setting a high external magnetic field with the opposite directions on each Mn atom in the basis. The field value was reduced at each iteration to improve convergence. The high-quality setting of ELK was activated, which specifies the summation cut-off for the APW  $lmaxapw = 10$ , maximal length of  $|\mathbf{G} + \mathbf{k}|$  in units of reciprocal muffin-tin sphere radius  $rgkmax = 8$ . Also, the maximal  $|\mathbf{G}|$  is set  $gmaxvr = 20$  and the angular momentum cut-off for the muffin-tin density and potential  $lmaxo = 8$ . Broyden mixing is implemented for facilitating convergence. A  $12 \times 12 \times 12$  mesh of k-points uniformly distributed within the Brillouin zone (BZ) was used. Perdew-Burke-Ernzerhof GGA approach is chosen for calculating the  $E_{xc}[\rho]$ .

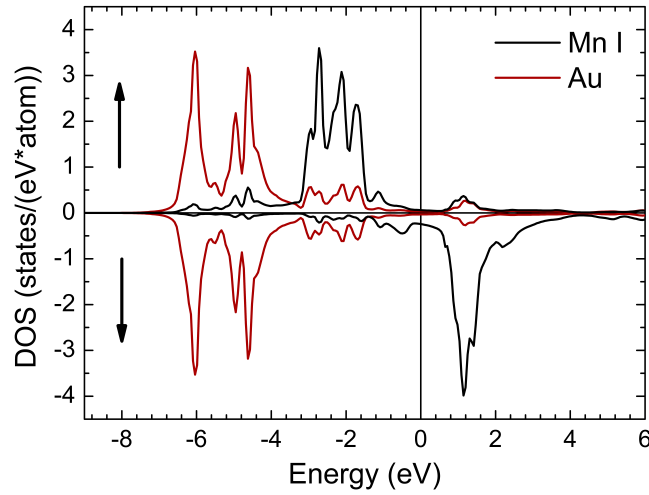


**Figure 9.1:** Element resolved DOS of Mn<sub>2</sub>Au. Positive and negative DOS values correspond to spin-up (majority) and spin-down (minority) electrons, respectively.

The calculated Mn<sub>2</sub>Au DOS indicates that the Mn atoms carry a magnetic moment (Fig. 9.1), whereas the Au atoms do not possess a magnetic moment, confirmed by the identical DOS for majority and minority electrons. The DOS of MnII atoms (not shown) is found to be opposite to the DOS of MnI atoms. The simulation provides the following Mn spin moment  $\mu_S^{Mn} = \pm 3.591 \mu_B$  and orbital moment  $\mu_L^{Mn} = \mp 0.002 \mu_B$ . The value of  $\mu_L^{Mn}$  is much smaller than  $\mu_S^{Mn}$ , which is typical for transition metal elements due to orbital moment quenching [186]. It is worth mentioning that the  $\mu_L^{Mn}$  is oriented oppositely to  $\mu_S^{Mn}$ . Another important property of Mn<sub>2</sub>Au obtained from the DOS is the number of d-holes per Mn atom  $N_d$ , which amounts to 5.0.

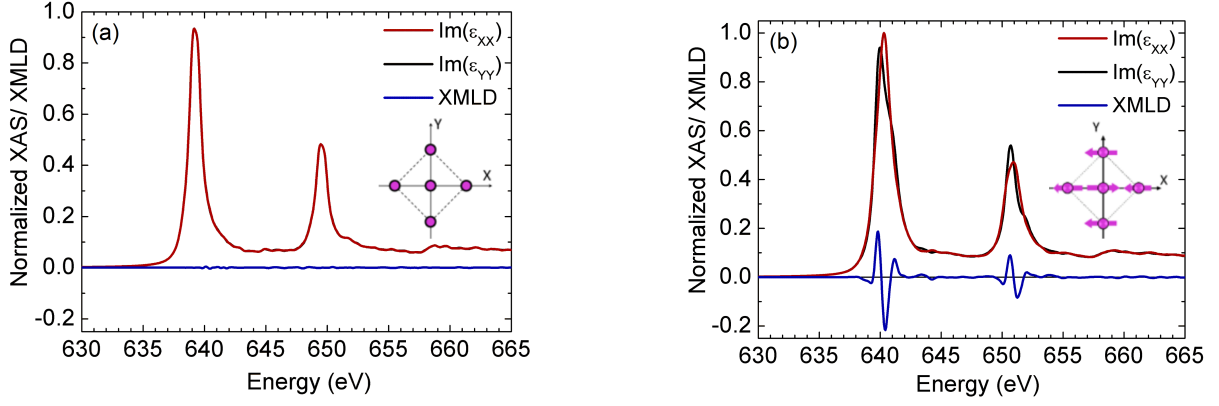


**Figure 9.2:** (a) Theoretical XMLD spectra calculated for non-magnetic tetragonal  $\text{Mn}_2\text{Au}$ . (b) The same for the AFM  $\text{Mn}_2\text{Au}$  with the moments pointing along the  $\pm[110]$  directions. The insets show the schematic basal-plane view of the modeled compounds.

In order to obtain the X-ray absorption spectra, local orbitals were added at Mn sites in order to account for exchange splitting of the  $2p_{3/2}$  and  $2p_{1/2}$  core states. The linear optical response tensor  $(\epsilon_{ij})$  was simulated based on the momentum matrix elements. The absorption coefficient for linearly polarized X-rays with the polarization vector along  $\hat{e}_i$  is expressed as

$$\mu_i = \Im m(\epsilon_{ii}). \quad (9.19)$$

The theoretical spectra presented in Fig. 9.2(a) were calculated for a non-magnetic  $\text{Mn}_2\text{Au}$  by setting the Mn spins equal to zero. The XMLD spectrum calculated as

$$XMLD = \Im m(\epsilon_{xx}) - \Im m(\epsilon_{yy}). \quad (9.20)$$

is vanishingly small. In contrast to the non-magnetic compound, the tetragonal  $\text{Mn}_2\text{Au}$  with magnetic moments oriented along the  $\langle 110 \rangle$  axes shown Fig. 9.2(b) exhibits a significant dichroism.

It is important for the interpretation of the strain-dependent measurements of the Néel vector in  $\text{Mn}_2\text{Au}$  to know the non-magnetic contribution to the linear dichroism originating from a reduced lattice symmetry. For this purpose, non-magnetic  $\text{Mn}_2\text{Au}$  with a distorted lattice was modeled by setting the elongation along the X-axis to 0.1% together with a compression along the Y-axis to keep the unit cell volume. The numerical result indicates that the dichroism due to the pure lattice distortion without magnetism is much smaller than the XMLD of a single-domain antiferromagnetic  $\text{Mn}_2\text{Au}$ .

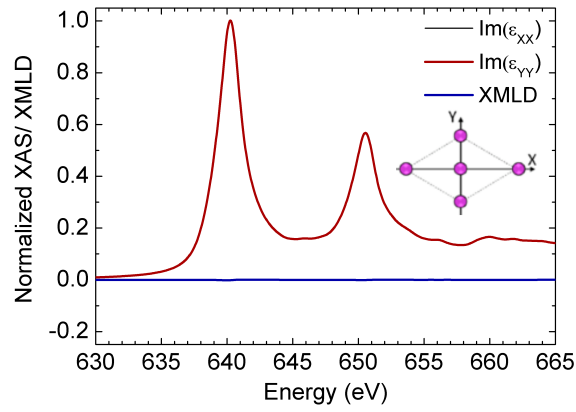


**Figure 9.3:** (a) Theoretical XMLD spectra calculated for non-magnetic  $\text{Mn}_2\text{Au}$  strained to a value of 0.1% in the  $[110]$  direction. The inset shows the schematic basal-plane view of the modeled compound (the deformation is strongly exaggerated).

## 9.4 Technical drawings of the equipment for the bending experiments

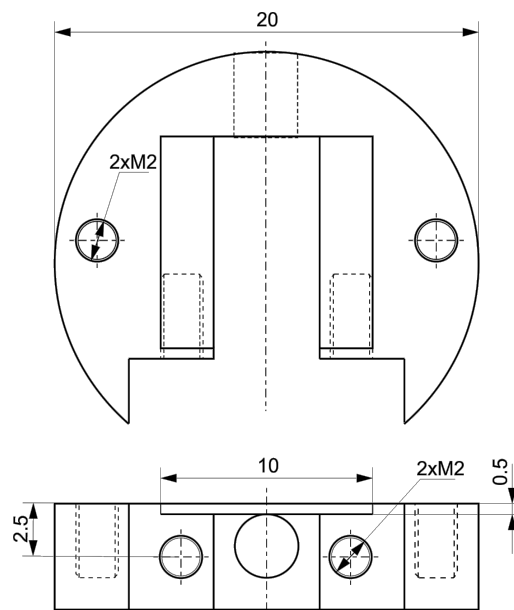


**Figure 9.4:** The drawing of the base of the miniature vacuum-compatible bending device. The material is oxygen-free copper.

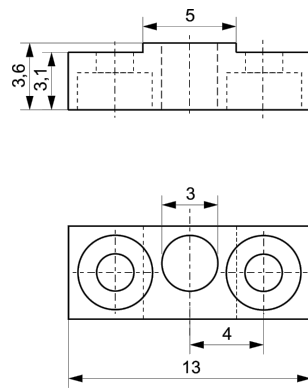


**Figure 9.5:** The drawing of the fixing part. The material is oxygen-free copper.

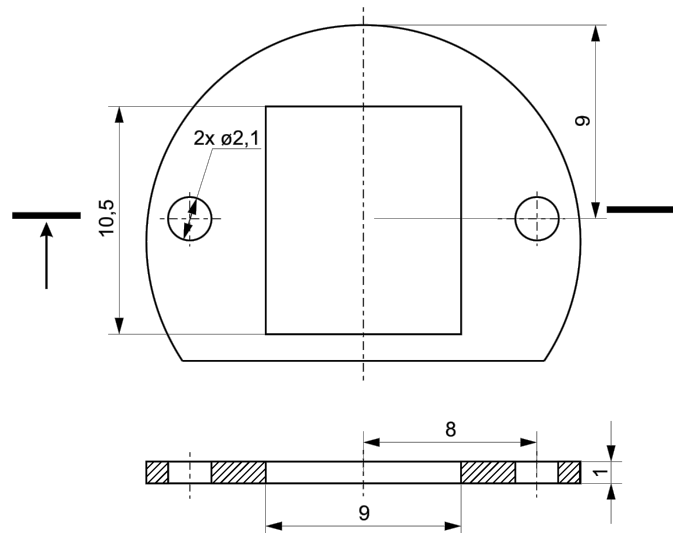


**Figure 9.6:** The drawing of the frame. The material is oxygen-free copper.

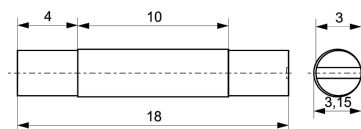


**Figure 9.7:** The drawing of the eccentric rod. The material is titan.

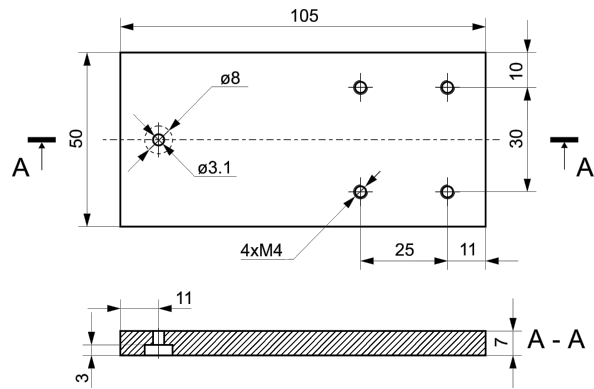


**Figure 9.8:** The first part of the bending device with a piezo element. The material is aluminum.

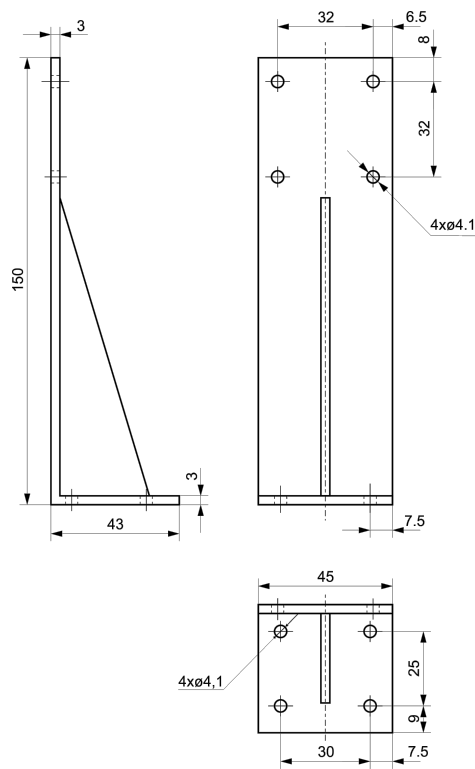


**Figure 9.9:** The second part of the bending device with a piezo element. The material is aluminum.





# List of used abbreviations

FM - ferromagnet  
AFM - antiferromagnet  
XMCD - X-ray magnetic circular dichroism  
XMLD - X-ray magnetic linear dichroism  
PEEM - photoemission electron microscopy  
X-PEEM - X-ray photoemission electron microscopy  
LEEM - low-energy electron microscopy  
GMR - giant magnetoresistance  
TMR - tunneling magnetoresistance  
HDD - hard disc drive  
STT - spin transfer torque  
SHE - spin Hall effect  
MRAM - magnetoresistive random-access memory  
SMR - spin Hall magnetoresistance  
NSOT - Néel spin-orbit torque  
 $T_N$  - Néel temperature  
 $T_C$  - Curie temperature  
 $T_B$  - Blocking temperature  
TAMR - tunneling anisotropic magnetoresistance  
SHA - spin Hall angle  
RE - rare-earth  
RKKY - Ruderman-Kittel-Kassiya-Yoshida  
DOS - density of states  
FP-LAPW - full potential linear augmented plane wave  
NN - nearest neighbor  
SQUID - superconducting quantum interference device  
VSM - vibrating sample magnetometry  
MOKE - magneto-optic Kerr effect  
DMI - Dzyaloshinskii-Moriya interaction

MAE - magnetocrystalline anisotropy energy  
SOC - spin-orbit coupling  
DW - domain wall  
FEL - free electron laser  
XAS - X-ray absorption spectrum  
TEY - total electron yield  
FY - fluorescence yield  
 $\sigma+$  - circular right (X-ray polarization)  
 $\sigma-$  - circular left (X-ray polarization)  
LH - linear horizontal (X-ray polarization)  
LV - linear vertical (X-ray polarization)  
HZB - Helmholtz-Zentrum Berlin  
HV - high vacuum  
UHV - ultra-high vacuum  
TXM - transmission X-ray microscopy  
STXM - scanning transmission X-ray microscopy  
SE - secondary electrons  
MCP - microchannel plate  
MEM - mirror electron microscopy  
ROI - region of interest  
DFT - density functional theory  
 $J$  - exchange constant  
RHEED - reflection high energy electron diffraction  
XRD - X-ray diffraction  
 $H_C$  - coercivity  
 $H_{EB}$  - exchange bias field  
 $H_{FC}$  - field applied during field cooling  
 $M_r$  - remanent magnetization  
RT - room temperature  
RF - radio frequency  
AMR - anisotropic magnetoresistance

# Bibliography

- [1] L. Néel, *Ann. de physique* **10**, 5 (1932).
- [2] L. Néel, *Ann. de physique* **11**, 232 (1936).
- [3] F. Bitter, *Phys. Rev.* **54**, 79 (1938).
- [4] C. G. Shull and J. S. Smart, *Phys. Rev.* **76**, 1256 (1949).
- [5] W. H. Meiklejohn and C. P. Bean, *Phys. Rev.* **105**, 904 (1957).
- [6] M. N. Baibich, J. M. Broto, A. Fert, F. N. Van Dau, F. Petroff, P. Etienne, G. Creuzet, A. Friederich, and J. Chazelas, *Phys. Rev. Lett.* **61**, 2472 (1988).
- [7] G. Binasch, P. Grünberg, F. Saurenbach, and W. Zinn, *Phys. Rev. B* **39**, 4828(R) (1989).
- [8] B. Dieny, V. S. Speriosu, S. S. P. Parkin, B. A. Gurney, D. R. Wilhoit, and D. Mauri, *Phys. Rev. B* **43**, 1297(R) (1991).
- [9] D. C. Ralph and M. D. Stiles, *J. Magn. Magn. Mater.* **320**, 1190 (2008).
- [10] J. Sinova, S. O. Valenzuela, J. Wunderlich, C. H. Back, and T. Jungwirth, *Rev. Mod. Phys.* **87**, 1213 (2015).
- [11] R. Cheng, D. Xiao, and A. Brataas, *Phys. Rev. Lett.* **116**, 207603 (2016).
- [12] O. Gomonay, T. Jungwirth, and J. Sinova, “Narrow-band tunable THz detector in anti-ferromagnets via Néel spin-orbit torque and spin-transfer torque,” arXiv:1712.02686 .
- [13] R. Cheng, J. Xiao, Q. Niu, and A. Brataas, *Phys. Rev. Lett.* **113**, 057601 (2014).
- [14] S. M. Wu, W. Zhang, A. KC, P. Borisov, J. E. Pearson, J. S. Jiang, D. Lederman, A. Hoffmann, and A. Bhattacharya, *Phys. Rev. Lett.* **116**, 097204 (2016).
- [15] A. H. MacDonald and M. Tsoi, *Philos. Trans. R. Soc. A* **369**, 3098 (2011).
- [16] E. V. Gomonay and V. M. Loktev, *Low Temp. Phys.* **40**, 17 (2014).
- [17] T. Jungwirth, X. Marti, P. Wadley, and J. Wunderlich, *Nat. Nanotechnol.* **11**, 231 (2016).
- [18] O. Gomonay, T. Jungwirth, and J. Sinova, *Phys. Status Solidi RRL* **11**, 1700022 (2017).
- [19] V. Baltz, A. Manchon, M. Tsoi, T. Moriyama, T. Ono, and Y. Tserkovnyak, *Rev. Mod. Phys.* **90**, 015005 (2018).

- [20] B. G. Park, J. Wunderlich, X. Martí, V. Holý, Y. Kurosaki, M. Yamada, H. Yamamoto, A. Nishide, J. Hayakawa, H. Takahashi, A. B. Shick, and T. Jungwirth, *Nat. Mat.* **10**, 347 (2011).
- [21] P. Wadley, B. Howells, J. Železný, C. Andrews, V. Hills, R. P. Champion, V. Novák, K. Olejník, F. Maccherozzi, S. S. Dhesi, S. Y. Martin, T. Wagner, J. Wunderlich, F. Freimuth, Y. Mokrousov, J. Kuneš, J. Chauhan, M. J. Grzybowski, A. W. Rushforth, K. W. Edmonds, B. L. Gallagher, and T. Jungwirth, *Science* **351**, 587 (2016).
- [22] S. Yu. Bodnar, L. Šmejkal, I. Turek, T. Jungwirth, O. Gomonay, J. Sinova, A. A. Sapozhnik, H.-J. Elmers, M. Kläui, and M. Jourdan, *Nat. Commun.* **9**, 348 (2018).
- [23] J. Fischer, O. Gomonay, R. Schlitz, K. Ganzhorn, N. Vlietstra, M. Althammer, H. Huebl, M. Opel, R. Gross, S. T. B. Goennenwein, and S. Geprägs, *Phys. Rev. B* **97**, 014417 (2018).
- [24] F. Nolting, A. Scholl, J. Stöhr, J. W. Seo, J. Fompeyrine, H. Siegart, J.-P. Locquet, S. Anders, J. Lüning, E. E. Fullerton, M. F. Toney, M. R. Scheinfein, and H. A. Padmore, *Nature(London)* **405**, 767 (2000).
- [25] H. Ohldag, T. J. Regan, J. Stöhr, A. Scholl, F. Nolting, J. Lüning, C. Stamm, S. Anders, and R. L. White, *Phys. Rev. Lett.* **87**, 247201 (2001).
- [26] T. Kampfrath, A. Sell, G. Klatt, A. Pashkin, S. Mährlein, T. Dekorsy, M. Wolf, M. Fiebig, A. Leitenstorfer, and R. Huber, *Nat. Photonics* **5**, 31 (2010).
- [27] K. Arai, T. Okuda, A. Tanaka, M. Kotsugi, K. Fukumoto, T. Ohkochi, T. Nakamura, T. Matsushita, T. Muro, M. Oura, Y. Senba, H. Ohashi, A. Kakizaki, C. Mitsumata, and T. Kinoshita, *Phys. Rev. B* **85**, 104418 (2012).
- [28] R. Masrour, E. K. Hlil, M. Hamedoun, A. Benyoussef, O. Mounkachi, and H. El Mousaoui, *J. Supercond. Nov. Magn.* **28**, 3045 (2015).
- [29] H.-Ch.. Ding and Ch...D. Duan, *Europhys. Lett.* **97**, 57007 (2012).
- [30] I. S. Jacobs, *J. Appl. Phys.* **32**, 61S (1961).
- [31] F. M. Johnson and A. H. Nethercot, *Phys. Rev.* **114**, 705 (1959).
- [32] R. C. Ohlmann and M. Tinkham, *Phys. Rev.* **123**, 425 (1961).
- [33] J. Nogués, D. Lederman, T. J. Moran, and I. K. Schuller, *Phys. Rev. Lett.* **76**, 4624 (1996).

- [34] T. Zhao, A. Scholl, F. Zavaliche, K. Lee, M. Barry, A. Doran, M. P. Cruz, Y. H. Chu, C. Ederer, N. A. Spaldin, R. R. Das, D. M. Kim, S. H. Baek, C. B. Eom, and R. Ramesh, *Nat. Mater.* **5**, 823 (2006).
- [35] A. V. Kimel, A. Kirilyuk, A. Tsvetkov, R. V. Pisarev, and Th.. Rasing, *Nature (London)* **429**, 850 (2004).
- [36] A. V. Kimel, B. A. Ivanov, R. V. Pisarev, P. A. Usachev, A. Kirilyuk, and Th.. Rasing, *Nat. Phys.* **5**, 727 (2009).
- [37] P. Wadley, V. Hills, M. R. Shahedkhah, K. W. Edmonds, R. P. Champion, V. Novák, B. Ouladdiaf, D. Khalyavin, S. Langridge, V. Saidl, P. Nemeč, A. W. Rushforth, B. L. Gallagher, S. S. Dhesi, F. Maccherozzi, J. Železný, and T. Jungwirth, *Sci. Rep.* **5**, 17079 (2015).
- [38] P. Wadley, V. Novák, R. Champion, C. Rinaldi, X. Martí, H. Reichlová, J. Železný, J. Gazquez, M. Roldan, M. Varela, D. Khalyavin, S. Langridge, D. Kriegner, F. Mác, J. Mašek, R. Bertacco, V. Holý, A. Rushforth, K. Edmonds, B. Gallagher, C. Foxon, J. Wunderlich, and T. Jungwirth, *Nat. Commun.* **4**, 2322 (2013).
- [39] D. Kriegner, K. Výborný, K. Olejník, H. Reichlová, V. Novák, X. Martí, J. Gazquez, V. Saidl, P. Němec, V. V. Volobuev, G. Springholz, V. Holý, and T. Jungwirth, *Nat. Commun.* **7**, 11623 (2016).
- [40] J. Železný, H. Gao, K. Výborný, J. Zemen, J. Mašek, A. Manchon, J. Wunderlich, J. Sinova, and T. Jungwirth, *Phys. Rev. Lett.* **113**, 157201 (2014).
- [41] K. Olejník, V. Schuler, X. Martí, V. Novák, Z. Kašpar, P. Wadley, R. P. Champion, K. W. Edmonds, B. L. Gallagher, J. Garces, M. Baumgartner, P. Gambardella, and T. Jungwirth, *Nat. Commun.* **8**, 15434 (2017).
- [42] P. Wadley, S. Reimers, M. J. Grzybowski, C. Andrews, M. Wang, J. Chauhan, B. Gallagher, R. Champion, K. Edmonds, S. Dhesi, F. Maccherozzi, V. Novák, J. Wunderlich, and T. Jungwirth, “Current-polarity dependent manipulation of antiferromagnetic domains,” [arXiv:1711.05146](https://arxiv.org/abs/1711.05146) .
- [43] F. Mác, J. Kudrnovský, V. Drchal, I. Turek, O. Stelmakhovych, P. Beran, A. Llobet, and X. Marti, *Phys. Rev. B* **94**, 094407 (2016).
- [44] N. Kunitomi, Y. Hamaguchi, and Sh.. Anzai, *J. Phys. France* **25**, 568 (1964).
- [45] E. Fawcett, *Rev. Mod. Phys.* **60**, 209 (1988).
- [46] A. Arrott, S. A. Werner, and H. Kendrick, *Phys. Rev. Lett.* **14**, 1022 (1965).

- [47] P. Bödeker, A. Schreyer, and H. Zabel, *Phys. Rev. B* **59**, 9408 (1999).
- [48] J.-Ph. Hanke, F. Freimuth, S. Blügel, and Yu. Mokrousov, *Sci. Rep.* **7**, 41078 (2017).
- [49] E. Mancini, F. Pressacco, M. Haertinger, E. E. Fullerton, T. Suzuki, G. Woltersdorf, and C. H. Back, *J. Phys. D: Appl. Phys.* **46**, 245302 (2013).
- [50] W. Zhang, M. B. Jungfleisch, W. Jiang, J. E. Pearson, A. Hoffmann, F. Freimuth, and Yu. Mokrousov, *Phys. Rev. Lett.* **113**, 196602 (2014).
- [51] X. Marti, I. Fina, C. Frontera, J. Liu, P. Wadley, Q. He, R. J. Paull, J. D. Clarkson, J. Kudrnovský, I. Turek, J. Kuneš, D. Yi, J.-H. Chu, C. T. Nelson, L. You, E. Arenholz, S. Salahuddin, J. Fontcuberta, T. Jungwirth, and R. Ramesh, *Nat. Mat.* **13**, 367 (2014).
- [52] M. G. Loving, R. Barua, C. Le Graët, J. Kinane, D. Heiman, S. Langridge, C. H. Marrows, and L. H. Lewis, *J. Phys. D: Appl. Phys.* **51**, 024003 (2017).
- [53] P. Wells and J. H. Smith, *Acta Cryst.* **A26**, 379 (1970).
- [54] S. Abe, M. Matsumoto, T. Kaneko, Y. H., H. Morita, and T. Kanomata, *J. Magn. Magn. Mater.* **140-144**, 103 (1995).
- [55] V. M. T. S. Barthem, C. V. Colin, H. Mayaffre, M.-H. Julien, and D. Givord, *Nat. Commun.* **4**, 2892 (2013).
- [56] A. B. Shick, S. Khmelevskiy, O. N. Mryasov, J. Wunderlich, and T. Jungwirth, *Phys. Rev. B* **81**, 212409 (2010).
- [57] V. M. T. S. Barthem, C. V. Colin, R. Haettel, D. Dufeu, and D. Givord, *J. Magn. Magn. Mater.* **406**, 289 (2016).
- [58] E. Pavarini, E. Koch, R. Scalettar, and R. M. e. Martin, *The Physics of Correlated Insulators, Metals, and Superconductors Modeling and Simulation, Vol. 7* (Verlag des Forschungszentrum Jülich, 2017).
- [59] M. A. Ruderman and C. Kittel, *Phys. Rev.* **96**, 99 (1954).
- [60] <http://elk.sourceforge.net>.
- [61] W. Heisenberg, *Zeitschrift für Physik* **49**, 611 (1928).
- [62] M. Getzlaff, *Fundamentals of magnetism* (Springer-Verlag Berlin Heidelberg, 2008).
- [63] H. E. Stanley, *Introduction to Phase Transitions and Critical Phenomena* (Oxford Science Series, 1971).

- [64] J. Stöhr and H. C. Siegman, *Magnetism from fundamentals to nanoscale dynamics* (Springer-Verlag Berlin Heidelberg, 2006).
- [65] I. Dzyaloshinsky, *J. of Phys. and Chem. of Solids* **4**, 241 (1960).
- [66] T. Moriya, *Phys. Rev.* **120**, 91 (1958).
- [67] A. Fert, N. Reyren, and V. Cros, *Nat. Rev. Mater.* **2**, 17031 (2017).
- [68] A. Aharoni, *Introduction to the theory of ferromagnetism* (Oxford university press, 2007).
- [69] R. Koch, M. Weber, K. Thürmer, and K. H. Rieder, *J. Magn. Magn. Mater.* **159**, L11 (1996).
- [70] R. C. O'Handley and S.-W. Sun, *J. Magn. Magn. Mater.* **104**, 1717 (1992).
- [71] L. Breitenstein, R. Lendecke, S. Bohlens, G. Meier, and U. Merkt, *J. Appl. Phys.* **104**, 083909 (2008).
- [72] H. Zijlstra, *IEEE Trans. Magn.* **15(5)**, 1246 (1979).
- [73] S. Saito, M. Miura, and K. Kurosawa, *J. Phys. C: Solid State Phys.* **13**, 1513 (1980).
- [74] A. Scholl, J. Stöhr, J. Lüning, J. W. Seo, J. Fompeyrine, H. Siegwart, J.-P. Locquet, F. Nolting, S. Anders, E. E. Fullerton, M. R. Scheinfein, and H. A. Padmore, *Science* **287**, 1014 (2000).
- [75] M. Jourdan, H. Bräuning, A. Sapozhnik, H.-J. Elmers, H. Zabel, and M. Kläui, *J. Phys. D: Appl. Phys.* **48**, 385001 (2015).
- [76] M. J. Grzybowski, P. Wadley, K. W. Edmonds, R. Beardsley, V. Hills, R. P. Campion, B. L. Gallagher, J. S. Chauhan, V. Novak, T. Jungwirth, F. Maccherozzi, and S. S. Dhesi, *Phys. Rev. Lett.* **118**, 057701 (2017).
- [77] S. N. Klausen, P.-A. Lindgård, K. Lefmann, F. Bødker, and S. Mørup, *Phys. Stat. Sol. (a)* **189**, 1039 (2002).
- [78] W.-C. Lin, W. B.-Y., T.-Y. Chen, L.-C. Lin, Y.-W. Liao, W. Pan, N.-Y. Jih, K.-J. Song, and M.-T. Lin, *Appl. Phys. Lett.* **90**, 052502 (2007).
- [79] S. I. Csiszar, M. W. Haverkort, Z. Hu, A. Tanaka, H. H. Hsieh, H.-J. Lin, C. T. Chen, T. Hibma, and L. H. Tjeng, *Phys. Rev. Lett.* **95**, 187205 (2005).
- [80] H. V. Gomonay and V. M. Loktev, *Phys. Rev. B* **75**, 174439 (2007).
- [81] O. Gomonay, S. Kondovych, and V. Loktev, *J. Magn. Magn. Mater.* **354**, 125 (2014).

- [82] R. H. Kodama, A. E. Berkowitz, E. J. McNiff, Jr., and S. Foner, *Phys. Rev. Lett.* **77**, 394 (1996).
- [83] M. J. Benitez, O. Petravic, E. L. Salabas, F. Radu, H. Tüysüz, F. Schüth, and H. Zabel, *Phys. Rev. Lett.* **101**, 097206 (2008).
- [84] J. McCord, H. Zolla, and H. Grimm, *IEEE Trans. Magn.* **39**, 2384 (2003).
- [85] F. Radu and H. Zabel, In Zabel H., Bader S.D. (eds) *Magnetic Heterostructures*. Springer Tracts in Modern Physics **227**, 97 (2008).
- [86] F. Radu, S. K. Mishra, I. Zizak, A. I. Erko, H. A. Dürr, W. Eberhardt, G. Nowak, S. Buschhorn, H. Zabel, K. Zhernenkov, M. Wolff, D. Schmitz, E. Schierle, E. Dudzik, and R. Feyerherm, *Phys. Rev. B* **79**, 184425 (2009).
- [87] H. Ohldag, A. Scholl, F. Nolting, E. Arenholz, S. Maat, A. Young, M. Carey, and J. Stöhr, *Phys. Rev. Lett.* **91**, 017203 (2003).
- [88] N. C. Koon, *Phys. Rev. Lett.* **78**, 4865 (1997).
- [89] F. L. A. Machado, P. R. T. Ribeiro, J. Holanda, R. L. Rodríguez-Suárez, A. Azevedo, and S. M. Rezende, *Phys. Rev. B* **95**, 104418 (2017).
- [90] D. Attwood, *Soft X-rays and extreme ultraviolet radiation: Principles and applications* (Cambridge University Press, 1999).
- [91] <http://www.diamond.ac.uk/PressOffice/MediaResources.html>.
- [92] H. A. Dürr, T. Eimüller, H.-J. Elmers, S. Eisebitt, M. Farle, W. Kuch, F. Matthes, M. Martins, H. C. Mertins, P. M. Oppeneer, L. Plucinski, C. M. Schneider, H. Wende, W. Wurth, and H. Zabel, *IEEE Trans. Magn.* **45**, 15 (2009).
- [93] J. Schwinger, *Phys. Rev.* **75**, 1912 (1949).
- [94] P. Willmot, *An introduction to synchrotron radiation* (Wiley, 2011).
- [95] [http://photon-science.desy.de/research/students\\_\\_teaching/sr\\_and\\_fel\\_basics/fel\\_basics/tdr\\_spectral\\_characteristics/index\\_eng.html](http://photon-science.desy.de/research/students__teaching/sr_and_fel_basics/fel_basics/tdr_spectral_characteristics/index_eng.html).
- [96] A. Thompson *et al.*, *X-ray data booklet* (Lawrence Berkeley National Laboratory, University of California, 2009).
- [97] R. Abrudan, F. Brüßing, R. Salikhov, J. Meermann, I. Radu, H. Ryll, F. Radu, and H. Zabel, *Rev. Sci. Instr.* **86**, 063902 (2015).
- [98] [https://www.helmholtz-berlin.de/pubbin/igama\\_output?modus=\\einzel\&gid=1639\&sprache=en](https://www.helmholtz-berlin.de/pubbin/igama_output?modus=\\einzel\&gid=1639\&sprache=en).



- [99] G. van der Laan and A. I. Figueora, *Coord. Chem. Rev.* **277-278**, 95 (2014).
- [100] <https://nau.edu/cefns/labs/electron-microprobe/glg-510-class-notes/signals/>.
- [101] S. Mobilio, F. Boscherini, and C. Meneghini, *Fundamentals of nanoscale film analysis* (Springer Verlag Berlin Heidelberg, 2015) pp. 181–221.
- [102] <http://ssrl.slac.stanford.edu/dichroism/xas.html> ().
- [103] J. L. Erskine and E. A. Stern, *Phys. Rev. B* **12**, 5016 (1975).
- [104] G. Schütz, W. Wagner, W. Wilhelm, P. Kienle, R. Zeller, R. Frahm, and G. Materlik, *Phys. Rev. Lett.* **58**, 737 (1987).
- [105] M. Kallmayer, P. Klaer, H. Schneider, G. Jacob, H. J. Elmers, D. Legut, and P. M. Oppeneer, *Phys. Rev. B* **84**, 054448 (2011).
- [106] B. T. Thole, P. Carra, F. Sette, and G. van der Laan, *Phys. Rev. Lett.* **68**, 1943 (1992).
- [107] P. Carra, B. T. Thole, M. Altarelli, and X. Wang, *Phys. Rev. Lett.* **70**, 694 (1993).
- [108] C. T. Chen, Y. U. Idzerda, H.-J. Lin, N. V. Smith, G. Meigs, E. Chaban, G. H. Ho, E. Pellegrin, and F. Sette, *Phys. Rev. Lett.* **75**, 152 (1995).
- [109] C. Piamonteze, P. Miedema, and F. M. F. de Groot, *Phys. Rev. B* **80**, 184410 (2009).
- [110] E. Goering, *Philos. Mag.* **85**, 2895 (2005).
- [111] B. T. Thole, G. Van Der Laan, and G. A. Sawatzky, *Phys. Rev. Lett.* **55**, 2086 (1985).
- [112] H. Ohldag, H. Shi, E. Arenholz, J. Stöhr, and D. Ledermann, *Phys. Rev. Lett.* **96**, 027203 (2006).
- [113] J. Zhu, Q. Li, J. X. Li, Z. Ding, J. H. Liang, X. Xiao, Y. M. Luo, C. Y. Hua, H.-J. Lin, T. W. Pi, Z. Hu, C. Won, and Y. Z. Wu, *Phys. Rev. Lett.* **90**, 054403 (2014).
- [114] Q. Li, J. H. Liang, Y. M. Luo, Z. Ding, T. Gu, Z. Hu, C. Y. Hua, H.-J. Lin, T. W. Pi, S. P. Kang, C. Won, and Y. Z. Wu, *Sci. Rep.* **6**, 22355 (2016).
- [115] M. Sacchi, O. Sakho, and G. Rossi, *Phys. Rev. B* **43**, 1276(R) (1991).
- [116] M. Sacchi, F. Sirotti, and G. Rossi, *Solid State Commun.* **81**, 977 (1992).
- [117] M. W. Haverkort, S. I. Csiszar, Z. Hu, S. Altieri, A. Tanaka, H. H. Hsieh, H.-J. Lin, C. T. Chen, T. Hibma, and L. H. Tjeng, *Phys. Rev. B* **69**, 020408(R) (2004).

- [118] D. Alders, L. H. Tjeng, F. C. Voogt, T. Hibma, G. A. Sawatzky, C. T. Chen, J. Vogel, M. Sacchi, and S. Iacobucci, *Phys. Rev. B* **57**, 11623 (1998).
- [119] F. Sauli, *Gaseous Radiation Detectors* (Cambridge University Press, 2014).
- [120] <http://www-ssrl.slac.stanford.edu/nexafs.html> ().
- [121] A. Zangwill, *Physics at surfaces* (Cambridge University Press, 1988).
- [122] P. Fisher, *J. Phys. D: Appl. Phys.* **50**, 313002 (2017).
- [123] A. L. D. Kilcoyne, T. Tylizszczak, W. F. Steele, S. Fakra, P. Hitchcock, K. Franck, E. Anderson, B. Harteneck, E. G. Rightor, G. E. Mitchell, A. P. Hitchcock, L. Yang, T. Warwick, and H. Ade, *Journal of Synchrotron Radiation* **10**, 125 (2003).
- [124] S. Eisebitt, J. Lüning, W. F. Schlotter, M. Lörger, O. Hellwig, W. Eberhardt, and J. Stöhr, *Nature (London)* **432**, 885 (2004).
- [125] A. Méndez-Vilas and J. E. Díaz, *Modern Research and Educational Topics in Microscopy*. (Verlag des Forschungszentrum Jülich, 2007) pp. 795–804.
- [126] E. Bauer, *Rep. Prog. Phys.* **57**, 895 (1994).
- [127] <https://www.synchrotron-soleil.fr/en/beamlines/hermes>.
- [128] F. Kronast and S. Valencia Molina, *Journal of large-scale research facilities* **2**, A90 (2016).
- [129] R. Egerton, *Physical Principles of Electron Microscopy* (Springer, 2016).
- [130] E. Bauer, *Surf. Rev. and Lett.* **5**, 1275 (1998).
- [131] J. Stöhr, H. A. Padmore, S. Anders, T. Stammler, and M. R. Scheinfein, *Surf. Rev. and Lett.* **5**, 1297 (1998).
- [132] G. van der Laan, N. D. Telling, A. Potenza, S. S. Dhesi, and E. Arenholz, *Phys. Rev. B* **83**, 064409 (2011).
- [133] T. Shiino, S.-H. Oh, P. M. Haney, S.-W. Lee, G. Go, B.-G. Park, and K.-J. Lee, *Phys. Rev. Lett.* **117**, 087203 (2016).
- [134] F. Keffer and C. Kittel, *Phys. Rev.* **85**, 329 (1952).
- [135] L. Passell, O. W. Dietrich, and J. Als-Nielsen, *Phys. Rev. B* **14**, 4897 (1976).
- [136] S. Khmelevskiy and P. Mohn, *Appl. Phys. Lett.* **93**, 162503 (2008).
- [137] P. Klaer, B. Balke, V. Alijani, J. Winterlik, G. H. Fecher, C. Felser, and H. J. Elmers, *Phys. Rev. B* **84**, 144413 (2011).

- [138] H. A. Dürr, G. Y. Guo, G. van der Laan, J. Lee, G. Lauhoff, and J. A. C. Bland, *Science* **277**, 213 (1997).
- [139] J. Nogués and I. K. Schuller, *J. Magn. Magn. Mater.* **192**, 203 (1999).
- [140] S.-W. Chen, X. Lu, E. Blackburn, V. Lauter, H. Ambaye, K. T. Chan, E. E. Fullerton, A. E. Berkowitz, and S. K. Sinha, *Phys. Rev. B* **89**, 094419 (2014).
- [141] M. Takahashi and M. Tsunoda, *J. Phys. D: Appl. Phys.* **35**, 2365 (2002).
- [142] H. Okamoto and T. B. Massalski, *Phase diagrams of binary gold alloys* (Metals Park, Ohio: ASM International, 1997).
- [143] H.-C. Wu, Z.-M. Liao, R. G. Sumesh Sofin, G. Feng, X.-M. Ma, A. B. Shick, O. N. Mryasov, and I. V. Shvets, *Adv. Mater.* **24**, 6374 (2012).
- [144] J. Zak, E. R. Moog, C. Liu, and S. D. Bader, *J. Magn. Magn. Mater.* **89**, 107 (1990).
- [145] Z. Q. Qui and S. D. Bader, *Rev. Sci. Instr.* **71**, 1243 (2000).
- [146] H. Hornauer, T. M. Atmono, and K. Röhl, *J. Magn. Magn. Mater.* **83**, 551 (1990).
- [147] A. Hubert and R. Schäfer, *Magnetic domains the analysis of magnetic microstructures* (Springer-Verlag Berlin Heidelberg, 2009).
- [148] Y. Cao, K. Xu, W. Jiang, T. Droubay, P. Ramuhalli, D. Edwards, B. R. Johnson, and J. McCloy, *J. Magn. Magn. Mater.* **395**, 361 (2015).
- [149] A. P. Malozemoff, *J. Appl. Phys.* **63**, 3874 (1988).
- [150] H. N. Fuke, K. Saito, M. Yoshikawa, H. Iwasaki, and M. Sashiki, *Appl. Phys. Lett.* **75**, 3680 (1999).
- [151] P. Scherrer, *Göttinger Nachrichten Math. Phys.* **2**, 98 (1918).
- [152] X. Y. Lang, W. T. Zheng, and Q. Jiang, *Nanotechnology* **18**, 155701 (2007).
- [153] F. Radu, A. Westphalen, K. Theis-Bröhl, and H. Zabel, *J. Phys. Cond. Mat.* **18**, L29 (2006).
- [154] E. C. Stoner and E. P. Wohlfarth, *Philos. Trans. R. Soc. A* **240**, 599 (1948).
- [155] S. Trudel, G. Wolf, J. Hamrle, B. Hillebrands, P. Klaer, M. Kallmayer, H.-J. Elmers, H. Sukegawa, W. Wang, and K. Inomata, *Phys. Rev. B* **83**, 104412 (2011).
- [156] C. W. T. McLyman, *Transformer and Inductor Design Handbook* (CRC Press, 2011).

- [157] W. Szmaja, J. Balcerski, W. Kozłowski, M. Cichomski, J. Grobelny, M. Smolny, and P. J. Kowalczyk, *J. Alloys Compd.* **521**, 174 (2012).
- [158] J. Baruchel, M. Schlenker, and W. L. Roth, *J. Appl. Phys.* **48**, 5 (1977).
- [159] M. Schlenker and J. Baruchel, *J. Appl. Phys.* **49**, 1996 (1978).
- [160] J. Baruchel, M. Schlenker, and B. Barbara, *J. Magn. Magn. Mater.* **15-18**, 1510 (1980).
- [161] W. L. Roth, *J. Appl. Phys.* **31**, 2000 (1960).
- [162] F. U. Hillebrecht, H. Ohldag, N. B. Weber, C. Bethke, U. Mick, M. Weiss, and J. Bahrtdt, *Phys. Rev. Lett.* **86**, 3419 (2001).
- [163] J. Wu, J. Choi, A. Scholl, A. Doran, E. Arenholz, Y. Z. Wu, C. Won, C. Hwang, and Z. Q. Qiu, *Phys. Rev. B* **80**, 012409 (2009).
- [164] J. Stöhr, A. Scholl, T. J. Regan, S. Anders, J. Lüning, M. R. Scheinfein, H. A. Padmore, and W. R. L., *Phys. Rev. Lett.* **83**, 1862 (1999).
- [165] I. P. Krug, F. U. Hillebrecht, M. W. Haverkort, A. Tanaka, L. H. Tjeng, H. Gomonay, A. Fraile-Rodriguez, F. Nolting, S. Cramm, and C. M. Schneider, *Phys. Rev. B* **78**, 064427 (2008).
- [166] K. S. R. Menon, S. Mandal, J. Das, T. O. Montes, M. A. Niño, A. Locatelli, and R. Belkhou, *Phys. Rev. B* **84**, 132402 (2011).
- [167] M. Meinert, D. Graulich, and T. Matalla-Wagner, “Electrical switching of antiferromagnetic Mn<sub>2</sub>Au and the role of thermal activation,” arXiv:1706.06983 .
- [168] N. B. Weber, H. Ohldag, H. Gomonaj, and F. U. Hillebrecht, *Phys. Rev. Lett.* **91**, 237205 (2003).
- [169] M. Guizar-Sicarios, S. T. Thurman, and J. R. Fienup, *Opt. Lett.* **33**, 156 (2008).
- [170] C. Won, Y. Z. Wu, H. W. Zhao, A. Scholl, A. Doran, W. Kim, T. L. Owens, X. F. Jin, and Z. Q. Qiu, *Phys. Rev. B* **71**, 024406 (2005).
- [171] A. A. Sapozhnik, R. Abrudan, Yu. Skourski, M. Jourdan, H. Zabel, M. Kläui, and H.-J. Elmers, *Phys. Status Solidi RRL* **11**, 1600438 (2017).
- [172] T. Yamada, *J. Phys. Soc. Jpn.* **21**, 650 (1966).
- [173] D. Alders, J. Vogei, C. Levelut, S. D. Peacor, T. Hibma, M. Sacchi, L. H. Tjeng, C. T. Chen, G. van der Laan, B. T. Thole, and G. A. Sawatzky, *Europhys. Lett.* **32**, 259 (1995).

- [174] R. Galceran, I. Fina, J. Cisneros-Fernández, B. Bozzo, C. Frontera, L. López-Mir, H. Deniz, K.-W. Park, B.-G. Park, Ll. Balcells, X. Martí, T. Jungwirth, and B. Martínez, *Sci. Reports* **6**, 35471 (2016).
- [175] B.-Y. Wang, J.-Y. Hong, N.-Y. Jih, K.-H. Ou Yang, L.-R. Chen, H.-J. Lin, Y.-L. Chan, D.-H. Wei, and M.-T. Lin, *Phys. Rev. B* **90**, 224424 (2014).
- [176] A. Brandlmaier, S. Geprägs, M. Weiler, A. Boger, M. Opel, H. Huebl, C. Bihler, M. S. Brandt, B. Botters, D. Grundler, R. Gross, and S. T. B. Goennenwein, *Phys. Rev. B* **77**, 104445 (2008).
- [177] S. Finizio, M. Foerster, M. Buzzi, B. Krüger, M. Jourdan, C. A. F. Vaz, J. Hockel, T. Miyawaki, A. Tkach, S. Valencia, F. Kronast, G. P. Carman, F. Nolting, and M. Kläui, *Phys. Rev. Appl.* **1**, 021001 (2014).
- [178] Y. Y. Wang, C. Song, J. Y. Zhang, and F. Pan, *J. Magn. Magn. Mater.* **428**, 431 (2017).
- [179] S. M. Wu, S. A. Cybart, D. Yi, J. M. Parker, R. Ramesh, and R. C. Dynes, *Phys. Rev. Lett.* **110**, 067202 (2013).
- [180] W. Echtenkamp and Ch. Binek, *Phys. Rev. Lett.* **111**, 187204 (2013).
- [181] C. Song, Y. You, X. Chen, X. Zhou, Y. Wang, and F. Pan, *Nanotechnology* **29**, 112001 (2018).
- [182] D. Sander, *Rep. Prog. Phys.* **62**, 809 (1999).
- [183] T. R. McGuire and R. Potter, *IEEE Trans. Magn.* **11**, 1018 (1975).
- [184] M. Arana, F. Estrada, D. S. Maior, J. B. S. Mendes, L. E. Fernandez-Outon, W. A. A. Macedo, V. M. T. S. Barthem, D. Givord, A. Azevedo, and S. M. Rezende, *Appl. Phys. Lett.* **111**, 192409 (2017).
- [185] P. Hohenberg and W. Kohn, *Phys. Rev.* **136**, 864 (1964).
- [186] I. Galanakis, *Phys. Rev. B* **71**, 012413 (2005).



# Publications

Part of this work has been published in:

- *Epitaxial Mn<sub>2</sub>Au thin films for antiferromagnetic spintronics.*  
M. Jourdan, H. Bräuning, A. Sapozhnik, H. J. Elmers, H. Zabel, and M. Kläui, J. Phys. D Appl. Phys. **48**, 385001 (2015)
- *Manipulation of antiferromagnetic domain distribution in Mn<sub>2</sub>Au by ultrahigh magnetic fields and by strain.*  
A. A. Sapozhnik, R. Abrudan, Yu. Skourski, M. Jourdan, H. Zabel, M. Kläui, and H. J. Elmers, Phys. Stat. Solidi RRL **11**, 1600438 (2017)
- *Direct imaging of antiferromagnetic domains in Mn<sub>2</sub>Au manipulated by high magnetic fields.*  
A. A. Sapozhnik, M. Filianina, A. Lamirand, M.-A. Mawass, Yu. Skourski, H. J. Elmers, H. Zabel, M. Kläui, and M. Jourdan, Phys. Rev. B (in press)
- *Experimental determination of exchange constants in antiferromagnetic Mn<sub>2</sub>Au.*  
A. A. Sapozhnik, C. Luo, H. Ryll, R. Florin, M. Jourdan, H. Zabel, and H. J. Elmers, Phys. Rev. B (manuscript submitted for publication)

Further publications:

- *Analyzing the enforcement of a high-spin ground state for a metallocrown single-molecule magnet.*  
P. Happ, A. Sapozhnik, J. Klanke, P. Czaja, A. Chernenkaya, K. Medjanik, S. Schuppler, P. Nagel, M. Merz, E. Rentschler, H. J. Elmers, Phys. Rev. B **93**, 174404 (2016)
- *Writing and reading antiferromagnetic Mn<sub>2</sub>Au: Néel spin-orbit torques and large anisotropic magnetoresistance.*  
S. Yu. Bodnar, L. Šmejkal, I. Turek, T. Jungwirth, H. Gomonay, J. Sinova, A. A. Sapozhnik, H. J. Elmers, M. Kläui, and M. Jourdan, Nature Commun. **9**, 348 (2018)
- *Néel Spin Orbit Torque driven antiferromagnetic resonance in Mn<sub>2</sub>Au probed by time-domain THz spectroscopy.*  
N. Bhattacharjee, A. A. Sapozhnik, S. Yu. Bodnar, V. Yu. Grigorev, Steinn Agustsson, J. Cao, D. Dominko, M. Obergfell, H. Gomonay, J. Sinova, M. Kläui, H. J. Elmers, M. Jourdan, and J. Demsar, Phys. Rev. Lett. (manuscript submitted for publication)





# Curriculum Vitae

## Personal information

Name: Alexey Sapozhnik  
Date of birth: 08.05.1991  
Place of birth: Irkutsk, USSR  
Citizenship: Russian Federation  
Private address: Richard-Schirrmann-Str. 14  
D-55122 Mainz, Germany  
Parents: Olga (née Shulgina) and Alexander Sapozhnik  
Family status: Single

## Education

Sept. 1998 - June 2005 Elementary school (School No. 28, Irkutsk)  
Sept. 2005 - June 2008 Junior and senior high school (Lyceum No. 36, Irkutsk)

## Studies

Sept. 2008 - June 2012 Bachelor's studies in physics (Novosibirsk State University)  
Jan. 2012 - June 2012 Bachelor's thesis in experimental physics  
Title: *Development of a spectrometer for measuring the longitudinal and transversal components of photoelectron velocities*  
Supervisor: Prof. Dr. Alexander Terekhov  
Sept. 2012 - June 2014 Master's degree in Physics (Novosibirsk State University)  
Sept. 2013 - June 2014 Master's thesis in experimental physics  
Title: *Scattering of photoelectrons emitted from p-GaAs(Cs,O)*  
Supervisor: Prof. Dr. Alexander Terekhov

Nov. 2014 - Oct. 2018    Dissertation in experimental physics  
Title: *Magnetic Properties of Antiferromagnetic Mn<sub>2</sub>Au:  
Exchange Interaction and Domain Manipulation*  
Supervisors:  
Prof. Dr. Hans-Joachim Elmers and Prof. Dr. Hartmut Zabel

### **Scholarships**

Nov. 2014 - Nov. 2017    Scholarship of the Graduate school of Excellence  
Materials Science in Mainz (MAINZ)